University de Granada

Department of Electronics and Computer Technology

Diseño de sistemas multisensores para monitorización ambiental

Design of multisensor systems for environmental monitoring

Tesis Doctoral

Almudena Rivadeneyra Torres

Juan Antonio López Villanueva, Catedrático de Universidad, y Alberto J Palma López, Catedrático de Universidad, ambos del Departamento de Electrónica y Tecnología de Computadores de la Universidad de Granada,

CERTIFICAMOS:

Que el trabajo de investigación recogido en la presente memoria, titulada "Diseño de sistemas multisensores para monitorización ambiental", y presentada por Almudena Rivadeneyra Torres para optar al grado de Doctor por la Universidad de Granada, ha sido realizado en su totalidad bajo nuestra dirección en el Departamento de Electrónica y Tecnología de Computadores de la Universidad de Granada.

Granada, Julio de 2014

Dr. Juan Antonio López Villanueva   Dr. Alberto J. Palma López

Catedrático de Universidad   Catedrático de Universidad

La doctoranda Almudena Rivadeneyra Torres y los directores de la tesis Juan Antonio López Villanueva y Alberto J. Palma López, garantizamos, al firmar esta tesis, que el trabajo ha sido realizado por el doctorando bajo la dirección de los directores de la tesis y hasta donde nuestro conocimiento alcanza, en la realización del trabajo, se han respetado los derechos de otros autores a ser citados, cuando se han utilizado sus resultados o publicaciones

Granada, Julio de 2014

Director/es de la Tesis   Doctoranda

Fdo.: Alberto J. Palma López   Fdo.:Almudena Rivadeneyra Torres

    Juan Antonio López Villanueva

Agradecimientos

Me gustaría que estas líneas sirvieran para expresar mi sincero agradecimiento a todas aquellas personas que con su ayuda han colaborado directa o indirectamente en la realización del presente trabajo.

En especial a mis directores, Alberto y Juan Antonio, por la orientación, el seguimiento y la supervisión recibida a lo largo de estos años. Quisiera mostrar también mi gratitud a mis compañeros del Departamento de Electrónica y Tecnología de Computadores así como al grupo de investigación ECSens, especialmente a Fermín por la ayuda que me ha prestado. Muy especialmente quiero agradecer la ayuda y el apoyo de Manuel. También me gustaría mostrar mi agradecimiento a mis supervisores en las estancias realizadas en el extranjero, Alan Mathewson del Insitituto Tyndall (Irlanda) y Danick Briand de la Escuela Politéncia Federal de Lausana (Suiza), por acogerme en sus grupos así como a mis compañeros en ambos centros.

A mi familia y especialmente a mi madre por la comprensión, paciencia y el ánimo recibido. Así como a todos mis amigos, mención especial a mis "pavas" que tantos años llevan confiando en mí.

Por último, me faltan palabras para agradecer el apoyo, la ayuda y la paciencia de Pepe. Sin él no habría llegado hasta aquí.

A todos ellos, muchas gracias.

Index

Figures Index

Table Index

Acronyms

AC	Alternating current
DABCO	1,4-Diazabicyclo[2.2.2]octane
AIBN	2,2′-Azobis(2-methylpropionitrile)
DMHD	2,5-Dimethyl-2,5-hexanediol
ADS	Advanced Design Simulator
ADC	Analog-Digital converter
CAB	Cellulose acetate butyrate
ClB	Chlorobenzene
CLK	Clock
CMOS	Complementary metal-oxide-semiconductor
CAD	Computer-aided design
CH	Cyclohexanol
DRIE	Deep reactive-ion etching
DAE	Differential algebraic equation
DC	Direct current
Dtd	Drop to drop space
ENL	Effective Noise Level
EM	Electromagnetic
EPC	Electronic Product Code
ENA	Enable
Eq	Equation
EDGMA	Ethylene glycol dimethylacrylate
FE	Finite element
FEA	Finite element analysis
FEM	Finite element method
HEXSIL	Hexagonal Silicon
HF	High frequency
ISS	Impedance Substrate Standard
IR	Infrared
IC	Integrated circuit
IDE	Interdigitated electrodes
IOT	Internet of Things
LIFT	Laser-induced forward transfer
PZT	lead zirconate titanate
LED	light-emitting diode
LIGA	lithography plating and molding

LPCVD	Low Pressure Chemical Vapor Deposition
MFC	Mass flow controller
MMA	Methyl methacrylate
MEMS	Micro-electro mechanical system
MWCNT	Multi-walled carbon nanotubes
NPG	Neopentyl glycol or 2,2-Dimethyl-1,3-propanediol
ODE	Ordinary differential equation
PDE	Partial differential equation
PSE	Partial isobutyl/methyl mixed ester
Ppb	Parts per billion
Ppm	Parts per million
PO	Photodectector output
PECVD	Plasma-enhanced chemical vapor deposition
PDMS	Polydimethylsiloxane
PtOEP	Platinum octaethylporphyrin
PLF	Polarization Loss Factor
PMMA	Poly(methyl methacrylate)
PES	Polyethersulphone
PET	Polyethylene terephthalate
PI	Polyimide
PolyMUMPs	Polysilicon Multi-User MEMS Processes
PS	Polystyrene
PVA	Polyvinyl acetate
PVC	Polyvinyl chloride
PCB	Printed circuit board
PE	Printed electronics
PG	Propylene glycol
PWM	Pulse-width modulation
RF	Radiofrequency
RFID	Radiofrequency identification
RH	Relative humiditye
RMS	Root mean square
SEM	Scanning electron microscope
SFM	Scanning force microscope
SFE	Sensor Front End
SER	Serpentine electodes
SOLT	Short-Open-Load-Thru
SDA	Signal data

SOG	Spin-On-Glass
SMA	SubMiniature version A
SMD	Surface Mount Device
THF	Tetrahydrofurane
TFT	Thin film transistors
TME	Trimethylolethane
TMP	Trimethylolpropane
UHF	Ultra High Frequency
USB	Universal Serial Bus
VNA	Vector Network Analyzer
VOC	Volatile Organic Compounds
WSN	Wireless Sensors network

Resumen

Este trabajo se centra en el diseño, fabricación y caracterización de diferentes tipos de sensores ambientales y su unión para formar sistemas multisensores compactos.

Se entiende por sensor cualquier tipo de dispositivo que recibe una señal o estímulo de su entorno y responde con otra señal que puede convertirse en una eléctrica. Los sensores no funcionan independientemente sino que forman siempre parte de sistemas más complejos que pueden incluir muchos otros detectores, procesadores de señal, acondicionadores de señal, memorias y actuadores.

En la introducción de este trabajo se describen las principales características de los sensores así como las técnicas de fabricación más frecuentes para el desarrollo de sensores.

Inicialmente, se han descrito estructuras interdigitales como sensores de humedad. Dichos sensores han sido previamente modelados para optimizar sus dimensiones y sensibilidad y posteriormente fabricados por inyección de tinta sobre substrato flexible. Los sensores han sido caracterizados en función de la humedad relativa, temperatura y frecuencia. A continuación, se ha presentado una estructura capacitiva novedosa, incluyendo una sección de simulación detallada y comparada con los electrodos interdigitales. Además, estos sensores han sido fabricados y caracterizados como sensores de humedad para directamente poder compararlos con los sensores interdigitales. Se han analizado electrodos dispuestos en forma de espiral enrollada, incluyendo su simulación, fabricación y caracterización. Estos tres tipos de electrodos siguen el mismo proceso de fabricación basado en utilizar substratos sensibles al analito de interés, por lo que solo es necesario imprimir los electrodos sin necesidad de depositar otro material sensible. El último sensor capacitivo de humedad presentado sigue un proceso de fabricación diferente. En este caso, el proceso es más complejo ya que combina varias etapas de serigrafía y un material más que los anteriores pero el ratio capacidad-área aumenta sustancialmente.

En el siguiente capítulo se presenta una estructura mixta capaz de medir dos magnitudes distintas. Dicha estructura integra un sensor capacitivo y otro

resistivo. La parte capacitiva sigue el mismo principio de fabricación que los sensores presentados en el primer capítulo mientras que la parte resistiva requiere la impresión de una capa sensora extra. Este sensor doble ha sido probado como sensor capacitivo de humedad y sensor resistivo de concentración de tolueno al mismo tiempo. Además, se muestra un estudio detallado de los parámetros de diseño principales de la película sensible al tolueno como son la influencia de la composición de la resina, la densidad de la pantalla de serigrafía empleada y la forma de los electrodos.

En el capítulo cuarto, se muestran diferentes estructuras diseñadas con distintas tecnologías y para diferentes finalidades pero con la característica común de poseer alguna parte suspendida. Primero se han diseñado micro-palancas impresas siguiendo distintas estrategias de fabricación. A continuación, se han estudiado dos dispositivos que usan tecnología MEMS: un recolector de energía piezoeléctrico con el objetivo de ampliar su factor de calidad y sintonizar su frecuencia de resonancia; y un micrófono capacitivo para optimizar su sensibilidad en función de sus parámetros geométricos. Estas últimas estructuras no han sido fabricadas todavía pero se ha llevado a cabo un profundo modelado basado en simulación numérica.

Finalmente se muestras distintas estrategias de integración de sensores de humedad, tanto de sensores desarrollados por nosotros como de sensores disponibles comercialmente, en sistemas electrónicos para proporcionar una funcionalidad completa al usuario final. Primero, se muestra una sonda edáfica multisensora. Dicha sonda mide humedad, temperatura y concentración de oxígeno en las inmediaciones de las raíces de las plantas. Para ello se ha empleado un sensor comercial de humedad y temperatura y un sensor de oxígeno previamente desarrollado en este grupo de investigación. A continuación, se ha presenta una etiqueta RFID que proporciona la lectura de dos parámetros ambientales: humedad y temperatura. La humedad proviene de un sensor capacitivo impreso en la etiqueta como los presentados previamente en este trabajo mientras que la temperatura viene dada por un sensor integrado en el chip RFID de la etiqueta. Ambos parámetros son leídos con una alta precisión. El último prototipo desarrollado es otra etiqueta RFID que incluye también un sensor capacitivo impreso de humedad. Esta etiqueta puede ser leída con cualquier lector RFID pero solo proporciona un valor umbral de la humedad, es decir, la lectura o no lectura del identificador

de la etiqueta en cuestión está asociada a un rango de humedades concreto. En caso de no incluir chip RFID esta configuración puede ser empleada directamente como sensor de humedad en el que los cambios en la frecuencia de resonancia están asociados a la humedad relativa.

1.   Motivation, objectives and background of this work

This work is centred in the design, fabrication and characterization of different types of sensors.

A sensor is any device that receives a signal or stimulus from its environment and responds with another signal that can be converted into an electrical one. (Fraden 2004).

A sensor does not function independently, but it is always a part of a more complex system which can include many other detectors, signal processor, signal conditioners, memory devices, data recorders and actuators (Figure 1).
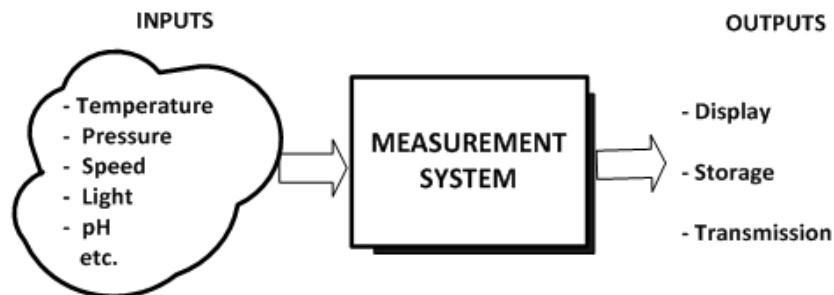
Figure 1. Schema of a measurement system.

The objectives encompassed in this work are the following:

- Design, fabrication and characterization of capacitive sensors by using printing techniques on flexible substrates.
- Design, fabrication and characterization of double capacitive-resistive sensors by using printing techniques on flexible substrates.
- Design, fabrication and characterization of cantilevers by using printing techniques on flexible substrates.
- Modelling of cantilevers as piezoelectric harvesters by microelectromechanical systems (MEMS) technology to tune its resonance frequency and optimize its quality factor.

- Modelling of capacitive microphone by Micro-Electro-Mechanical Systems (MEMS) technology to optimize its sensitivity.
- Design and fabrication of a multisensor soil probe capable of measuring temperature, humidity and oxygen concentration at the root depth.
- Integration of printed capacitive sensors in radiofrequency identification (RFID) tags.

1.1 Sensors classification

Many different classifications for sensors can be found; here we summarize the most common ones.

Chemical, physical and biological sensors

- A chemical sensor is a device that transforms chemical information into an analytically useful signal.
- A physical sensor is a device that provides information about a physical property of the system.
- A biological sensor or biosensor combines a biological component with a physic-chemical detector.

Active and passive sensors

- Active sensors require an external source of power to provide the majority of the output power of the signal.
- Passive sensors do not require an excitation voltage, the output power is almost entirely provided by the measured signal.

Digital and analog sensors

- Digital sensors produce or reflect a binary signal.
- Analog sensors provide a continuous signal related to the measurand signal.

Sensors according to the transduction effect

Table 1 classifies the transduction effect according to the input and output nature.

Table 1. Classification of transduction effects.

OUT IN	Radiant	Mechanical	Thermal	Electrical	Magnetic	Chemical
Radiant	Photo-luminescence	Radiation by pressure	Thermal radiation	Photo-conductivity	Photo-magnetism	Photo-chemical reaction
Mechanical	Photoelastic effect	Momentum conservation	Heat by friction	Piezoelectric effect	Magneto-striction	Reaction by pressure
Thermal	Incandescence	Thermal expansion	Thermal conductivity	Seedbeck effect	Curie-Weiss law	Endothermic reaction
Electrical	Electro-luminescence	Piezoelectric effect	Peltier effect	PN union	Ampere law	Electrolysis
Magnetic	Faraday effect	Magneto-striction	Ettling-Hausen effect	Hall effect	Magnetic induction	
Chemical	Chemi-luminescence	Explosive reaction	Exothermic reaction	Volta effect		Chemical reaction

1.2   Sensors characteristics

Sensors are normally designed to operate under well-defined conditions for specified circumstances. Therefore, it is not always necessary that a sensor responds specifically to a certain physical or chemical property. Under carefully controlled operating conditions, the measurand signal may be independent of other sample components, thus allowing the determination of the property of interest without any major preliminary treatment. Otherwise unspecific but satisfactory reproducible sensors can be used in series for multicomponent analysis using multivariate calibration software and signal processing. Such systems for multicomponent analysis are called sensor arrays (Adam, Stanisław and Folke 1991). The main characteristics to take into account in the selection of a sensor to a specific application are summarized below (Kalantar-zadeh and Fry 2008, Fraden 2004):

Range is the maximum and minimum value range over which a sensor works properly. Often sensors could work well outside this range, but require special or additional calibration.

Accuracy is measured as a ratio of the highest deviation of a value obtained by the sensor to the ideal value, that is, how good the data is when compared with a recognized standard.

Resolution is the ability of a sensor to discriminate well between small differences in readings.

Repeatability corresponds to the ability of a sensor to repeat a measurement when is placed in the same environment. It is often directly related to accuracy, but a sensor can be inaccurate, yet be repeatable in making observations.

Stability or drift is referred as to the low frequency change in a sensor in time, that is, the degree to which sensor characteristics remain constant over time. It is often associated with electronic aging of components or reference standards in the sensor.

Hysteresis reflects the variations between the ascending and descending response of the sensor.

Sensitivity is the ratio of incremental change in the output of the sensor to its incremental change of the measurand in input.

Selectivity corresponds to the sensor's ability to measure a single component in the presence of others.

Precision relates to how carefully the final measurement can be read but not how accurate the measurement is.

Error is the difference between the true value of the quantity being measured and the actual value obtained from the sensor. Errors can be classified in systematic and random errors.

1. Systematic errors. Errors which can be avoided or whose magnitude can be determined. Systematic error can be further classified as

operational and personal error; instrumental error; errors of method and additive or proportional error.

2. Random errors. They occur accidentally or randomly.

Noise refers to random fluctuations in the output signal when the measurand is not changing. It can be caused either internal or external to the sensor. Examples of external noise are mechanical vibrations, electromagnetic signals or ambient temperatures. Internal noises can be classified as: thermal noise (it results from random variations in current or voltage originated from thermal energy), shot noise (random fluctuations in a measured signal caused by the signal carrier's random arrival time), generation-recombination noise (it arises from the generation and recombination of electrons and holes in semiconductors) and pink noise (it is associated with a non-uniform frequency spectrum of a signal, and has equal power per octave).

Response time is the time taken by a sensor to approach its true output when subjected to a step input. The s**ettling time** is the time for the sensor to reach a stable output once it is turned on whereas the **fall time** is the time for the sensor to reach the null value once it is turned off, both within a given tolerance

1.3   Technologies of sensor fabrication

1.3.1 Micro-Electro-Mechanical Systems

MEMS is the acronym of Micro-Electro-Mechanical Systems. M points out the device size: micrometer. E and M correspond to electrical and mechanical, respectively, because these devices incorporate electrical and/or moving parts. S encompasses the idea of a set of these devices working together in an integrated whole. The majority of these devices are tiny machines. This term covers a wide variety of applications, such as sensors included in air-bags in cars, gyroscopes to aerospace use, radio frequency (RF) switches for mobile cells, chemical and biological detectors and so on.

Many physical phenomena that are neglected at macroscale can be the dominant characteristic at microscale. These systems take ingeniously advantage of these phenomena, resulting in operation modes totally different

to their homologous at macroscale. Furthermore, the fabrication processes of a 100-µm length structure are markedly different to the techniques used at macroscale.

There are numerously advantages to use this technology. First, less material is required to fabricate them, therefore, fewer resources are consumed and their cost is also reduced. In addition, their manufacturing process is based on batches, that is, many devices are produced in a batch, saving fabrication time. Also, many devices can be introduced in the same area thanks to their tiny size. Thus, the reliability is enhanced as a result of the increased redundancy of the system. Moreover, their dimensions below 1 mm make them minimally invasive.

The inclusion of one or more layers of mechanical materials is a requirement of a MEMS process flow. Then, unit process to shape these materials and other unit processes to release some part of the structural materials are also indispensable to manufacture MEMS devices. The choice of micromachining process depends on the specification of device dimensions and tolerances: structures over 10 µm thickness normally follow bulk micromachining, whereas structures under 10 µm are based on surface micromachining or hybrid bulk/surface micromachining.

MEMS materials can be categorized in 4 groups (Fedder 2003).

- Substrate and surface material. These layers must resist different process steps. Surface material can be used to protect either the substrate or the structural layers from certain etching steps. Another function of surface material can be the achievement of electrical insulation.
- Spacer. This layer is released completely or partially during the manufacturing process. They are commonly known as sacrificial layers.
- Structural material. The main properties of these layers are mass density, electrical and thermal conductivity, stress gradients, Young's modulus, etc.
- Active material. These layers are included to take advantage of their special electromechanical properties, for example: piezoelectric effect in PZT, ZnO, AlN as sensing and/or actuating elements;

silicon piezoresistance for stress measurements; some magnetic materials to mechanically couple to magnetic fields.

There are many different processes to cover all possible MEMS designs, the majority of them are techniques developed and adapted in the fabrication of integrated circuits and semiconductor processing. Such techniques create structures on thin and smooth substrates (usually silicon) on batch processes. MEMS fabrication can be made using the substrate itself as a part of the structure of the MEMS device (known as bulk micromachining) or builds microstructures by deposition and etching of different structural layers (usually polysilicon) on top of the substrate (known as surface micromachining).

A. Surface micromachining

Surface micromachining is a method of producing MEMS by depositing, patterning and etching a sequence of thin films. The thickness is typically about 1–100 μm. One of the most important processing steps required for dynamic MEMS devices is the selective removal of an underlying sacrificial layer, without attacking an overlying structural film. Figure 2 illustrates a typical surface micromachining process (Bustillo, Howe and Muller 1998).
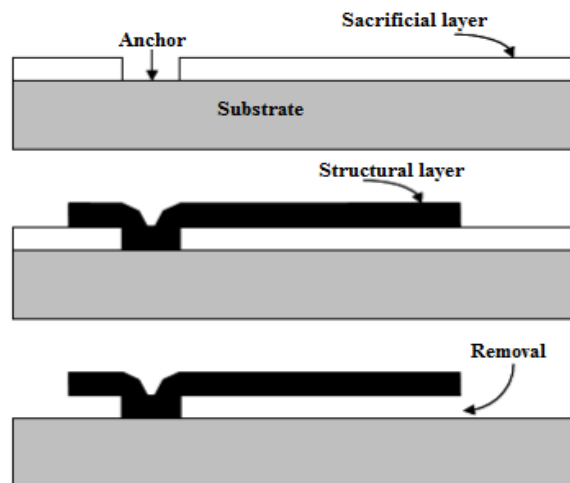
Figure 2. Surface micromachining including sacrificial layer technique (Judy 2001).

The advantages of surface micromachining are:

1. The size of the structural and spacer features, especially thicknesses can be below 10 μm.
2. The micromachined device footprint can often be much smaller than bulk wet-etched devices.
3. The electronics integration results easier below surface microstructures.
4. The tolerance of surface microstructures generally is superior compared with bulk wet-etched devices.

The main drawback is the fragility of surface microstructures to handling, particulates and condensation during manufacturing. The most common form of surface micromaching is based on polysilicon (polycrystalline silicon) whose mechanical properties are similar to single-crystal silicon.

B. Bulk micromachining

The main difference between bulk and surface micromachining is the fact that the substrate material in bulk micromachining is directly patterned and shaped to form an important functional component of the resulting device. An illustration of a typical bulk micromachining process is given in Figure 3. The substrate is typically single-crystal silicon by exploiting the predictable anisotropic etching characteristics of this material, many high-precision complex three-dimensional shapes, such as V-grooves, channels, pyramidal pits, membranes, vias and nozzles, can be formed (Kovacs 1998, Petersen 1982).
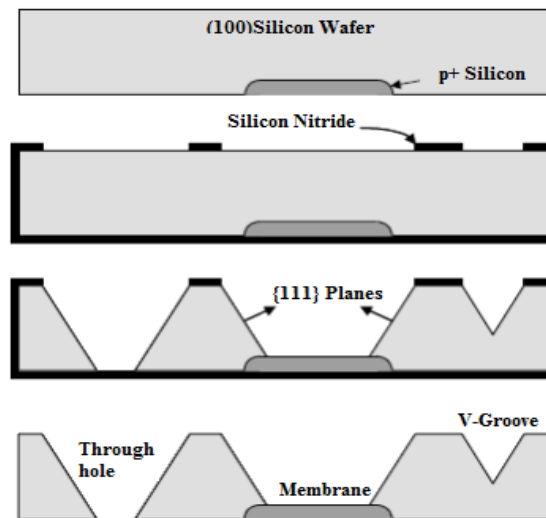
Figure 3. Bulk micromachining along crystallographic planes (Judy 2001).

- *Deep reactive ion etching (DRIE)* process was patented by the Robert Bosch Corp (Laermer and Schilp 1996). This procedure allows deeply etch into a silicon wafer while leaving vertical sidewalls, independently of the crystallographic orientation. The mask is usually either photoresist or silicon oxide; nevertheless other mask materials can be used.

- *Micromolding (HEXSIL).* HEXSIL combines HEXagonal honeycomb geometries for making rigid structures with thin-films and SILicon for surface micromachining and complementary metal-oxide-semiconductor (CMOS) electronics. Micromolded structures can be fabricated by combination of DRIE and conformal deposition processes, such as low pressure chemical vapor deposition (LPCVD) polysilicon and silicon dioxide. First, a pattern is bulk-etched in the silicon substrate by DRIE (Figure 4a). Next, sequential conformal depositions are performed (Figure 4 b and Figure 4 c), such as undoped polysilicon, doped polysilicon or plated nickel. The access to the sacrificial silicon dioxide can be then achieved either by etching or polishing. Lastly, the sacrificial layer is removed and the microstructure that has been built to the substrate is expelled. This process can be repeated with the recycled substrate (Figure 4d). Thick microstructures (about 500 µm thick) can be fabricated with

thin-film depositions and only one deep etching step following this procedure.
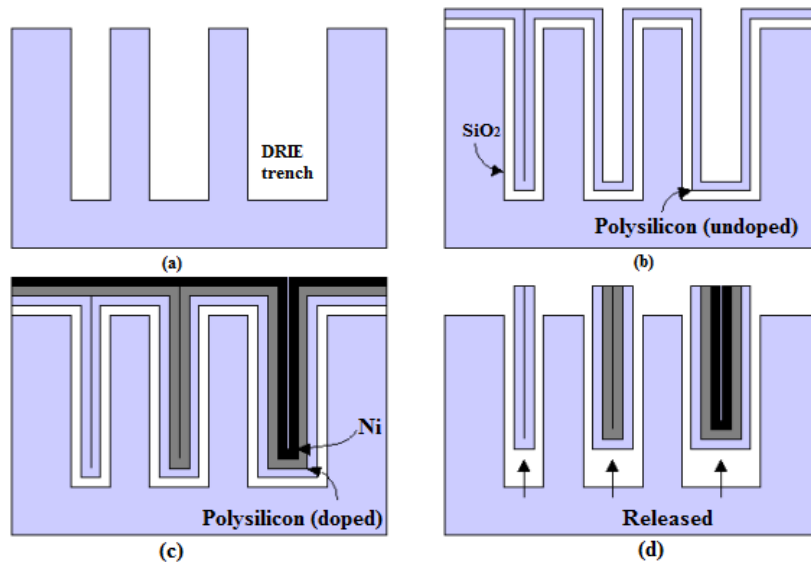
Figure 4. Micromolding process (Keller and Ferrari 1994).

C. Substrate bonding

Different substrates can be bonded together through several processes (Madou 2002), such as fusion bonding (Barth 1990), anodic bonding (Wallis and Pomerantz 2003), eutectic bonding (Cohn and Howe 2000) and adhesive bonding (Maas et al. 1996). Generally, at least one of the bonded substrates has been previously micromachined either by wet etching with an anisotropic silicon etchant or DRIE. The reasons to work with substrate bonding are to either mold a structure that is almost impossible otherwise (for example: large cavities that may be hermetically sealed, a complex system of enclosed channels) or to simply add mechanical support and protection.

D. Non-silicon microfabrication

The development of MEMS has contributed significantly to advance in non-silicon microfabrication techniques; we comment some examples as follows:

- *LIGA*. LIGA is a German acronym standing for lithography plating and molding (Ehrfeld et al. 1987). Basically, this process combines utterly tick resist (normally above 1 mm) and high-energy x-ray lithography (approximately 1 GeV). This lithography is able to

pattern thick resist with high accuracy. One disadvantage of this technique is the use of high energy X-ray sources. These sources are expensive and limited.

- *SU-8.* It is a cheap alternative to LIGA with similar performance. It is based on the use of a special epoxy-resin-based optical resist, called SU-8. This resist can be spun on in thick layers (above 500 μm) and patterned with commonly available lithography tools. Vertical sidewalls can also be obtained following this procedure (Lorenz et al. 1997).

- *Plastic molding with Polydimethylsiloxane* (PDMS). PDMS is a transparent elastomer that can be poured over a mold, polymerized and then removed easily by peeling it from the mold substrate (Xia and Whitesides 1998). The advantages of this process are: many inexpensive PDMS parts can be fabricated from a single mold, PDMS faithfully reproduce even submicron features, PDMS is biocompatible and tissues, cells and other materials can be easily imaged through PDMS due to its transparency. Common uses of PDMS in biomedical applications include microstamping of biological compounds and microfluidic systems (Xia and Whitesides 1998, Duffy et al. 1998, Jo et al. 2000).

D. CMOS MEMS

The term "CMOS MEMS" refers to as processes that build microstructures directly out of the metal/dielectric interconnect stack in foundry complementary metal-oxide-semiconductor (CMOS). The metallization and dielectric layers, normally used for electrical interconnect, can serve as structural layers. There is significant motivation for making MEMS out of CMOS. Electronics can be placed directly next to microstructures, enabling complete systems on chip. The integrated circuit (IC) fabrication must be willing to allow non-standard fabrication steps but many foundries are reluctant to that because their objective is to maximize yield. Despite these difficulties, Analog Devices Inc. produces their commercially successful MEMS products, such as inertial sensors, using this methodology.

1.3.2 Printing techniques

Printed Electronics (PE) is a technology based on printing techniques to create electronic circuits. In this sense, high-quality electronic products can be manufactured providing new features to the traditional electronics, such as the ability to produce thin, flexible, wearable, lightweight, ultra-cost-effective, and environmentally friendly structures. The main benefits of PE technology are summarized below:

1. It must be thin, lightweight, and useable in large electronic devices. Printing can make large products up to several tens of meters wide. This could be applied to, for example, TV, solar, and lighting equipment being larger than those made with conventional silicon technology.

2. It reduces production cost and time. Silicon technology is reaching its ultimate fine pitch resolution, 13 nm, and the establishment of the production foundry requires a huge investment. Printing production requires less than approximately 10 or 100 times the investment, and time is also considerably reduced.

3. It achieves true wearable devices. Traditional "wearable" devices are easily characterized by their size, heavy weight, stiffness, and fast power consumption. But truly wearable devices should be lightweight, thin, and comfortable and must power themselves; these requirements can be fulfilled by PE.

4. All products tend to be smart: they will be equipped with some sort of intelligent device capable of communicating with the outside world wirelessly. Traditional silicon dyes are not profitable in many cases due to their high cost.

5. All electronic devices should be environmentally friendly that means free of toxins and rare earth elements and requiring low energy, both in the manufacturing process and in operation. In conventional production of electronic equipment, complex processes are required in the production of both silicon devices and printed circuit boards, discarding much solid and liquid waste in the environment. The considerable reduction of solid and liquid waste in manufacturing is a key feature of PE technology, as well as the fact that it uses less energy.

Thus, there are many reasons to explore PE technology not only to supplant conventional electronics but also to expand its applications and markets (Suganuma 2014). There are different printing techniques applied in PE, we will indicate the main technologies and explain their characteristics.

A. Screen printing

In screen printing, the process is performed at low pressure using a screen mesh with the designed pattern with uniform thickness (Figure 5). The ink is transferred onto the substrate through the open areas of this mesh. A fill blade or flexible metal squeegee or rubber squeegee is moved across the screen for squeezing paste through the mesh. The typical materials used for the mesh are polyamide, polyester, or stainless steel. The mesh pattern is defined by photolithography of an emulsion on the mesh. A metal screen can also be used instead of a mesh screen with an emulsion pattern.
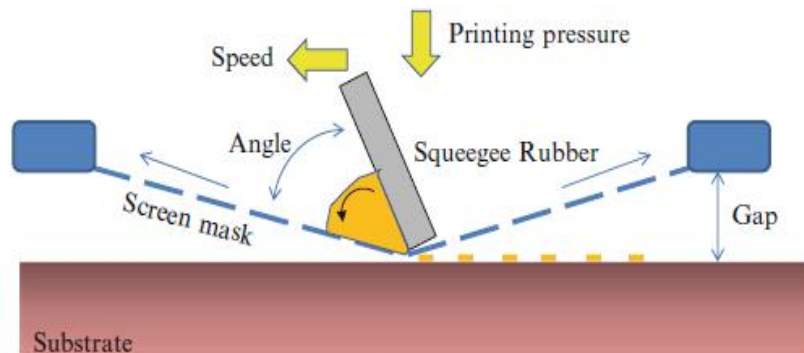
Figure 5. Schema of screen printing fabrication (Suganuma 2014).

The usual thickness of a screen printed pattern is in the range of microns, but in case of a thick screen mesh, the thickness can exceed 100 μm with one layer of printing. This thickness value cannot be achieved by any other printing method. The pattern resolution obtained by screen printing is higher than 100 μm. The viscosity of the ink has to be at least 1000 mPa·s.

B. Inkjet Printing

The traditional continuous jet printer used electrostatic plates to deposit drops on the substrate. These have been replaced by drop-on-demand systems. Canon and Hewlett-Packard developed systems where a heated plate causes a vapour bubble to form and eject a droplet of ink through a

nozzle. Epson printers use an array of piezoelectric plates which drive the droplet in bend or push mode (Calvert 2001). In order to obtain a wiring homogeneous fine line, the inkjet parameters should be controlled for each nozzle at each step. The droplet size, shape, speed, and uniformity of an inkjet printer differ from one nozzle to another.

The distance between the substrate and a nozzle is usually about 1–2 mm, but during flight, air resistance can affect the droplet shape. Furthermore, the solvent evaporation happens at the same time. The viscosity of the ink should be lower than 5 mPa·s. The pattern resolution is about 20-30 µm and the thickness achieved can be lower than 100 nm.

C. Flexography

Flexography (often abbreviated to flexo) uses a flexible relief plate. The printing pressure involved is very low and the process results very fast. The ink viscosity is about 50-500 mPa·s, the resolution achieved is above 30 µm and the thickness with a single layer is about 0.5-8 µm. The printing mechanism is described in Figure 6. The main parts of this printing process are:

1. Fountain roller. This roller transfers the ink that is located in the ink pan to the second roller, which is the anilox or ceramic roller.
2. Plate cylinder. This plate holds the printing plate, which is soft flexible rubber.
3. Anilox or Ceramic roller. This roller meters the predetermined ink that is transferred for uniform thickness. It has engraved cells that carry a certain capacity of inks. These rollers are responsible to transfer the inks to the flexible-plates that are already mounted on the Plate Cylinders
4. Impression cylinder. The impression cylinder applies pressure to the plate cylinder, where the image is transferred to the substrate
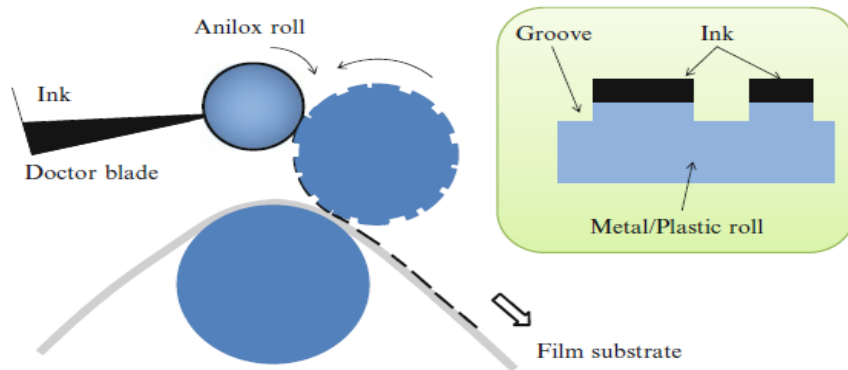
Figure 6. Flexography process (Suganuma 2014).

D. Gravure

The mechanism of offset-gravure or gravure printing is schematically presented in Figure 7. First, ink is placed on a gravure roll of metal and the excess of ink is grazed with a doctor blade. In the offset process, ink is transferred to a transfer roll, and then ink is finally deposited onto the substrate under pressure. The ink viscosity is about 10-200 mPa·s, the resolution achieved is below 20 µm and the thickness with a single layer is about 0.8-0.1 µm.
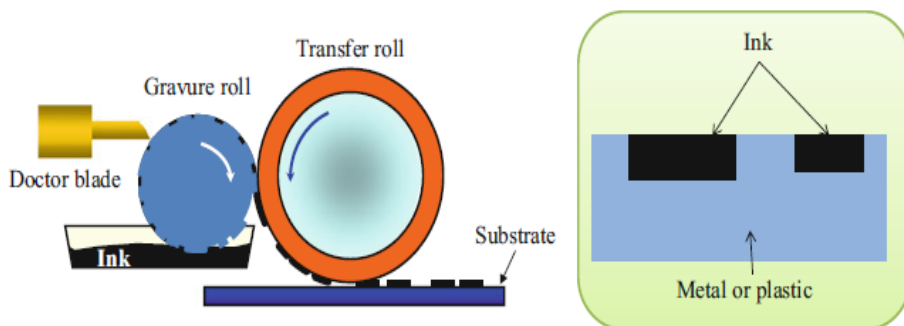
Figure 7. Gravure process flow (Suganuma 2014).

Ideally, all of the ink on the flexo/gravure plate should be ultimately deposited onto the substrate surface. Some of the key parameters of these printing techniques are enumerated as follows:

- Material and state of roll/plate: affinity with inks, swelling, hardness.

- Ink characteristics, such as type of solute and its content, viscosity, solvent type/volatility/ amount.
- Depth and pattern/shape of relief.
- Wetting and affinity between each roll and ink, surface state of substrate.
- Contact pressure of print and transfer roll.
- Materials and hardness state of plate and doctor blade.

E. Laser-Induced Forward Transfer

Laser-induced forward transfer (LIFT) is based on a metal ablation phenomenon by high-power laser irradiation developed in 1986 (Soeda et al. 2011). An object film defined on an optically transparent support is transferred to a substrate by a high-energy focused laser pulse, as schematically illustrates in Figure 8. The resolution can be on the order of a few microns depending on the focus of the laser beam.
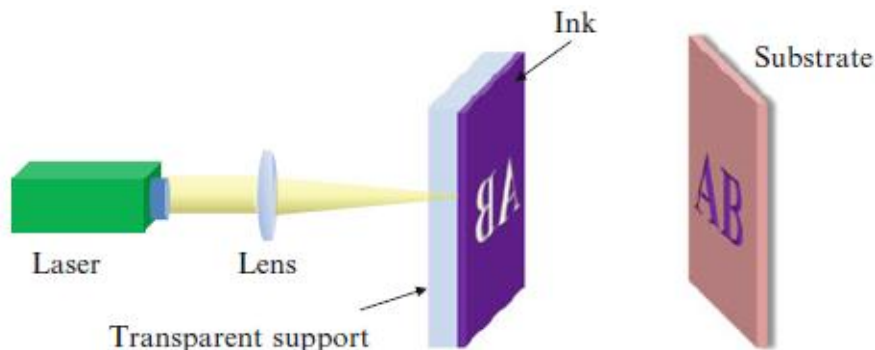
Figure 8. Laser-induced forward transfer technology (Suganuma 2014).

The pattern is uniform and it has a very sharp edge. This technique is characterized by non-contact, direct-multilayer printing in a solvent-free single step, without requiring any shadowing mask or vacuum installation.

1.4 Outline of this thesis

This thesis encompasses the design of different sensors following MEMS and printing technology in each particular case. In chapter 2, several capacitive structure without moving parts are reported. These structures have

been modelled as humidity sensors and are fabricated with printing technology. We have manufactured and characterized them, showing the main differences.

In chapter 3, we cover the design, manufacturing and characterization of printed resistive sensors to detect toluene. In addition to this, we illustrate a double structure that allows a capacitive measurement and a resistive one, improving the performance of this area.

Another kind of devices is described in chapter 4. The common aspect between all of them is the inclusion of suspended structures that results in moving parts. First, we show two different processes to develop printed cantilevers, one based on sacrificial layer and the other one on substrate layer. The, we model a silicon energy harvester with the aim of tuning its resonance frequency and broadening its quality factor. In this sense, different strategies are presented. Finally, we analyse a capacitive MEMS microphone in order to enhance its performance.

Finally, we integrate some sensors to constitute complete multisensory applications with commercial and fabricated sensors in chapter 5. First, a multisensor probe is presented with the capability of sensing temperature, humidity and oxygen in soils. Then, an ultra-high frequency (UHF) RFID tag with sensing capabilities is shown. In this case, not only the antenna and interconnections are printed but also the humidity sensors. Lastly, a high frequency (HF) RFID tag is depicted to act as threshold humidity tag.

2.   Capacitive sensors

A capacitor is a physical device which stores energy when it is polarized by an electric field by applying a suitable voltage across it (Sukhija and Nagsarkar 2010). Its simplest form consists of two parallel plates separated by a dielectric material. Capacitance indicates the ability of these two plates to hold this charge. A large capacitance is capable of storing more charge than a small capacitance. The amount of existing charge defines how much current must be used to change the voltage on the plate.

Capacitive sensors measure the capacitance between two or more conductors in a dielectric environment, usually air or liquid (Baxter 1996). When we use a capacitive sensor, the sensing surface of the probe is often the electrified plate and the target is the other plate. The driver electronics continually change the voltage on the sensing surface. This is called the excitation voltage. The amount of current required to change the voltage is measured by the circuit and indicates the amount of capacitance between the probe and the target. Or, conversely, a fixed amount of current is pumped into and out of the probe and the resulting voltage change is measured (Precision 2006).

Capacitive sensors are widely used for many different applications; some examples are explained below (Baxter 1996):

- Proximity sensing:
    - Personnel detection. Safety shutoff/opening when a person is too far/ close.
    - Vehicle detection. Traffic lights use inductive loops for vehicle detection. Capacitive detectors can also do this function, with better response to slow-moving vehicles.
- Measurement:
    - Flow. Capacitive flow meters can measure the displacement directly or convert pressure to displacement with a diaphragm.
    - Pressure. Variations in pressure can be directly measure as a dielectric constant change or loss tangent change.

o Chemical concentration. Capacitive chemical sensors can measure the content of an analyte directly as a dielectric constant change.

- Switch: Limit switches can detect the proximity of a metal machine component as an increase in capacitance, or the proximity of a plastic component by virtue of its increased dielectric constant over air.
- Communication: RF propagation in the near filed can be sensed by a receiver with a capacitive plate antenna.

One classification of this kind of sensors can be made according to the sensitive variable, that is, which part of a specific structure is the responsible of the behaviour as a concrete sensor (Figure 9). In this sense, we can point out the following categories:

- Electrical properties of the constitutive materials. The most common is a dependence of the electrical permittivity of the dielectric with the sensing variable.
- Displacement of the electrodes. A displacement in any of the electrodes axes by the sensing variable.

$$C_x = \frac{\varepsilon A}{x}$$

$$C_x = \frac{\varepsilon}{d}(A - wx)$$

$$C_x = \frac{\varepsilon_0 w}{d}\left[\varepsilon_2 l - (\varepsilon_2 - \varepsilon_1)x\right]$$
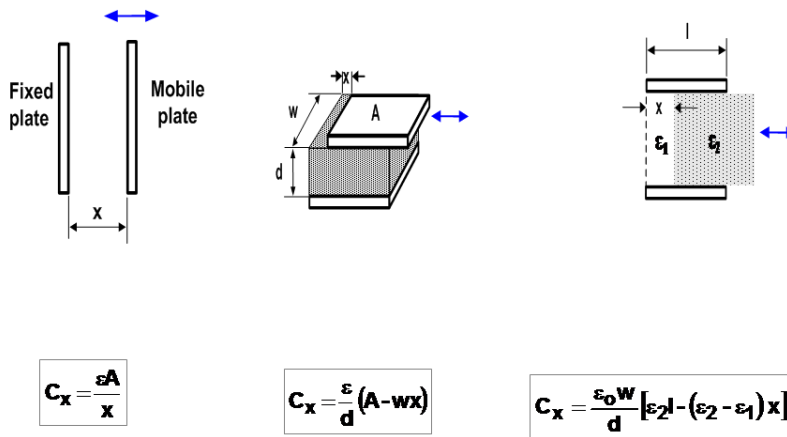
Figure 9. Summary of parameters that can vary the capacitance.

In this chapter, we present different topologies to develop capacitive sensors based on a change in the electrical permittivity of the dielectric layer. Firstly, the interdigitated electrode structure as humidity sensor are described, including a modelling section and its fabrication by inkjet printing as well as

its characterization. Secondly, a novel capacitive structure is explained. We have included a complete simulation section with a comparison with the interdigitated electrodes and, after that, its manufacturing and characterization processes as humidity sensor are shown. In addition, spiral electrodes are analysed, including the modelling part, their fabrication and characterization.

These three capacitive structures follow the same principle of fabrication process based on using the substrate as sensing material; therefore we only print the electrodes without other deposited layer. Finally, a new structure is presented with a different manufacturing procedure. In this case, the printed process is more complex but the ratio capacitance-area is substantially enhanced. We present the modelling part of this design and the first approach to its fabrication.

2.1   Materials and methods

2.1.1   Simulation

We have used COMSOL Multiphysics 4.2a (www.comsol.com, COMSOL, Inc. USA) to optimize the capacitive designs. This is a powerful interactive environment for solving problems based on partial differential equations with the finite element method.

This software has previously been used to calculate distributions of potential field in this kind of structures (Mohd Syaifudin, Mukhopadhyay and Yu 2012, Oikonomou et al. 2012). The equations solved in the determination of the capacitance in each finite element are:

$$-\nabla \varepsilon_0 \varepsilon_r \nabla V = \rho \qquad\qquad (\,1\,)$$

$$\boldsymbol{D} = \varepsilon_0 \varepsilon_r \mathbf{E} \qquad\qquad (\,2\,)$$

where ρ is the charge density, $\mathbf{D}$ is the electric displacement, and $\mathbf{E}$ is the electric field. The electrostatic energy density needed to charge a capacitor is equal to that energy of the electrostatic field, and is given by:

$$W_e = \int_\Omega DE d\Omega \qquad\qquad (3)$$

Then, the total capacitance is determined by the integral of the electric energy density through the relation:

$$C = \frac{2}{V_{port}^2} \int_\Omega W_e d\Omega \qquad\qquad (4)$$

where V_{port} is the value of the applied voltage in the port of the sensor. The other electrode is connected to ground. The electrical parameters of the substrate given by the manufacturer and the printed and cured conductive silver ink according to our characterization procedure were included in the numerical simulator (Dupont™ Kapton® polyimide film datasheet).

2.1.2 Printing techniques

A. Inkjet printing

The DMP-2831™ Dimatix printer (Fujifilm Dimatix Inc, Santa Clara, USA) has been used for inkjet printing. This printed works with piezo-based inkjet print cartridges. The printable area depends on the substrate thickness. Below 0.5 mm, this area is about 210 mm x 315 mm; between 25 mm and 0.5 mm it is 210 mm x 260 mm. The repeatability is ± 25 μm.

The substrate holder contains a vacuum platen to fix the substrate. Furthermore, the temperature is adjustable from ambient value to 60ºC. This printer has been used for the first three prototypes of sensors described in this chapter.

B. Screen printing

A Serfix III screen printing machine (Seglevint SL, Barcelona, Spain) has been used for the last prototype of sensor described in this chapter. The screen used to manufacture the patterns by screen printing had a mesh density of 120 Nylon thread per centimetre (T/cm) in an aluminium rectangular structure of 50 cm of width and 35 cm of length to fabricate them with only a single-layer screen printed. A more detailed description of this technique will be provided in Chapter 3.

2.1.3 Materials

A. Inks

Two silver inks have been used: an ink of silver nanoparticles (U5603 SunTronic Technology, San Diego, USA) which has a solid content of 20% of silver nanoparticles dispersed in ethanol/ethanediol, and a conductive silver ink CRSN 2569 (Sun Chemical Corporation, Parsippany, USA).

In order to know the thickness of the printed layer, a theoretical model (Salmerón et al. 2014) has been used based on the one reported in (Molina-Lopez, Briand and de Rooij 2012) . In the case of inkjet printing, the theoretical thickness of a printed layer of dry silver can be estimated as the ratio of the volume of dry silver, V_{Ag}, to the surface area, S, that it occupies as:

$$t = \frac{V_{Ag}}{S} \tag{5}$$

Knowing that one single inkjetted drop volume, V_D, is composed by a certain volume of silver, V_{Ag}, and certain volume of solvent, V_S, then:

$$V_D = V_{Ag} + V_S = \frac{m_{Ag}}{\rho_{Ag}} + \frac{m_S}{\rho_S} \tag{6}$$

where ρ_{Ag} (m_{Ag}) and ρ_S (m_S) are the mass density of the silver and solvent, respectively. The total volume of every drop is fixed by the cartridge used in the printing process and is set to 10 pL in the present work. Inks suppliers usually provide the solid ratio or mass fraction, χ_{Ag}, of silver inside a total ink mass, m_T, from where it is possible to establish the relationship between total mass and the mass of each ink component as follows:

$$m_{Ag} = \chi_{Ag} m_T \tag{7}$$

$$m_S = \chi_S m_T = (1 - \chi_{Ag}) m_T \tag{8}$$

Dividing both equations by the corresponding density and replacing them in equation (6) the following expression is found for the volume contained in one jetted drop in terms of its mass:

$$V_D = \frac{\chi_{Ag} m_T}{\rho_{Ag}} + \frac{(1 - \chi_{Ag}) m_T}{\rho_S} \tag{9}$$

Isolating m_T in the equation (9) and introducing it in the term $\chi_{Ag}m_T/\rho_{Ag}=V_{Ag}$ we obtain:

$$V_{Ag} = \frac{V_D}{1 + \dfrac{\rho_{Ag}}{\rho_S}\dfrac{(1-\chi_{Ag})}{\chi_{Ag}}}$$ (10)

The total number of drops deposited on a certain surface area, *S*, at every printed layer can be estimated from the drop to drop space, *dtd*. The printed head deposits one drop every *dtd* distance in both *x* and *y* directions, thus every surface area equal to *dtd*^{2} accommodates the volume of one single drop.
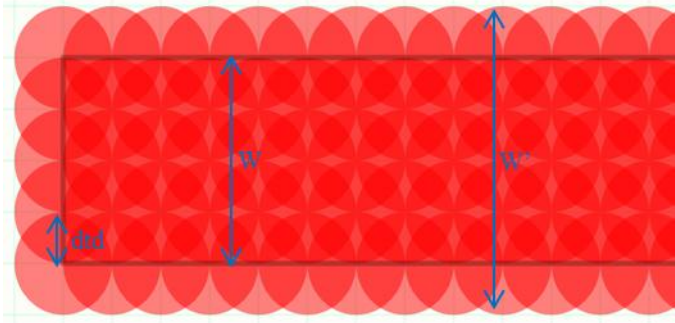
Figure 10. Sketch of the size of a printed line of real width W' compared with the size established in the layout with width W.

This relation is fulfilled everywhere except at the edge of the printed line where the amount of ink is smaller (see Figure 10). This irregularity in the contribution of the outer part of the lines to the average thickness has to be taken into account only if the printed element is comparable in size with the diameter of one printed drop. Therefore, special care has to be taken to the amount of ink deposited along the width of the lines. We can still consider a linear drop density of one drop per *dtd* distance along the length direction. The number of drops printed along the line width are *(W/dtd +1)*, with *W* the width established on the layout of the pattern, so that a surface *S=W'dtd*, where *W'* is the real measured width, would correspond to a number of *(W/dtd +1)* drops. Then, combining (5) and (10) and assuming that the thickness of dry silver adds up linearly at every printed layer, the total theoretical thickness of a line composed of *n* layers is given by the following expression where all the parameters are known.

$$t = n \frac{(\frac{W}{dtd} + 1)}{S} V_{AG} = n \frac{(\frac{W}{dtd} + 1)}{W'dtd} \frac{V_D}{1 + \frac{\rho_{Ag}}{\rho_S} \frac{(1 - \chi_{Ag})}{\chi_{Ag}}} \qquad (11)$$

All the parameters in the expression above are known or can be estimated. If layers are printed with different *dtd* space, the total thickness is easily calculated by using equation (11) independently for each layer. This model has been checked with the experimental data obtained from the interferometry study.

B. Substrate

A polyimide film with 75 µm thickness (Kapton® HN, Dupont™, Wilmington, DE, USA) has been used as a substrate. This polyimide is a well-known and broadly used material whose electrical permittivity, ε_r shows a high sensitivity to the relative humidity, according to the following expression given by the manufacturer of the substrate, see equation (12).

$$\varepsilon_r = 3.05 + 0.008 \cdot RH(\%) \quad at\ 1\ kHz, 23°C \qquad (12)$$

where RH(%) is the relative humidity in percentage. This relative permittivity also depends on frequency and temperature among other parameters which could interfere with the measurement of the humidity (Dupont™ Kapton® polyimide film datasheet).

2.1.4   Characterization

The geometrical characterization, the roughness of printed patterns as well as the thickness of the patterns has been done using a Wyko NT1100 Optical Profiling System (VEECO, Tucson, AZ, USA), and a Dektak XT™ Stimulus Surface Profiling System (Bruker Corporation, Conventry, UK).

The AC electrical characterization for the different fabricated capacitors has been performed by measuring their capacitance and dissipation factor, using the four-wire measurement technique with a precision Impedance Analyser 4294A and an impedance probe kit (4294A1) (Agilent Tech., Santa Clara, CA, USA). Two LCR-meters (HP 4284L and Agilent E4980A, Agilent Tech., Santa Clara, CA, USA) have also been used to measure the capacitance.

In most of the prototypes, one of the end sides has been enlarged to facilitate its connection to any analyser. A SMA (SubMiniature version A) male connector has been glued to these ends points using silver-filled epoxy EPO-TEK® H20E (Epoxy Technology, Inc., Billerica, USA). A complete compensation method has been implemented to eliminate the contribution of parasitic capacitances by measuring several commercial capacitances placed in the same configuration as the devices under test with the 16034G surface mount device (SMD) Test Fixture (Agilent Tech., Santa Clara, CA, USA).

The stationary humidity and temperature responses of the sensors have been measured in a climatic chamber VCL 4006 (Vötsch Industrietechnik GmbH, Germany). Due to the slow response of the mentioned climatic chamber, the dynamic response has been measured in a customized humidity measurements set-up (9 cm x 3 cm), which has automatically controlled wet and dry airflow inside a small gas cell at room temperature.

The data acquisition and analysis have been automated using Labview 2012 software (National Instruments Corporation, Texas, USA) (Figure 11).
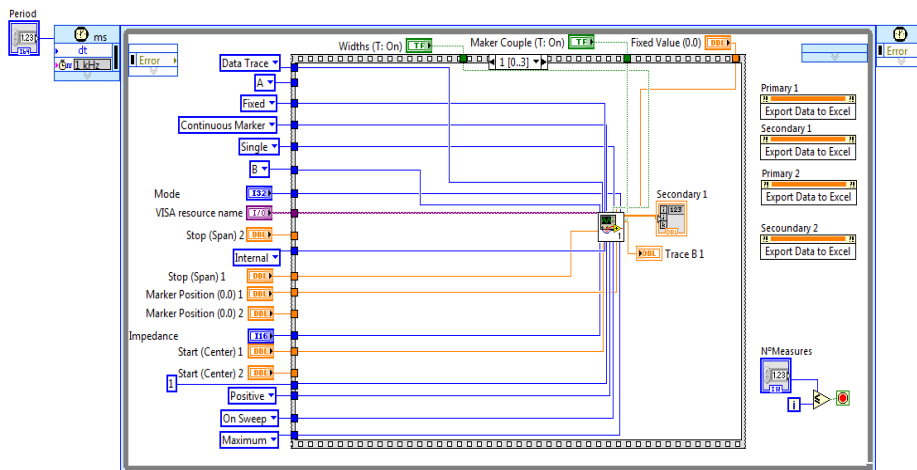
Figure 11. Caption of Labview program to automate measurements.

2.2   Interdigitated Electrode Structure

In recent years, printed and flexible electronic devices have become increasingly attractive due to their potential low-cost per surface area, mechanical flexibility and feasibility of large scale processing. The main

advantage of printed electronics is a simplified manufacturing process, which results in lower cost processes and shorter cycle time.

On another front, today there is a very strong and growing demand in world trade for humidity sensors. In fact, the field of smart packaging including sensor capabilities opens new challenges in the development of flexible and printed humidity sensors compatible with this kind of technologies. An important additional advantage of printed sensors is the possibility of integrating them with printed radio frequency identification (RFID) tags. There is a lot of interest at present in converging RFID tags and sensing capabilities that are able to save and store the acquired information related to both identity and measured parameters, see for example(Babar et al. 2012, Oprea et al. 2009a, Potyrailo et al. 2012b). The introduction of RFID and the Electronic Product Code (EPC) standard as a substitute of popular barcodes in packaging has advanced markets in intelligent packaging. It will be possible to read not only many packages at the same time but also environmental parameters extracted from sensors incorporated into the containers. There is a special interest in the capability of tracking the condition of a package through the whole supply chain to certify that products in their packages have not been endangered because of being exposed to wrong environmental conditions.

Great efforts and very valuable advances have been made in the design of flexible and printed humidity (Potyrailo et al. 2012b, Unander and Nilsson 2009a, Andersson et al. 2012, Virtanen et al. 2010) and other gases sensors (Briand et al. 2011b, Subramanian, Chang and Liao 2013, Potyrailo et al. 2009). Related to the requirement of low energy consumption, the classic transduction mechanism of these humidity sensors is capacitive, specifically through changes in the electrical permittivity of some component of the capacitor and the dielectric thickness. This requires the use of chemicals (usually polymers) whose electrical permittivity changes with the relative humidity of the environment.

The most common sensing capacitive structures are the planar parallel plate and the interdigitated electrode (IDE). The former is characterized by the simplicity of its geometry and the ease of modelling and calculation. However, IDE structure present very different and interesting features such

as one-side access (the other side can be open to the ambient), control of signal strength by changing easily its dimensions, multiple physical effects in the same structure (electric, magnetic, acoustic), simplified modelling in 2D when the aspect ratio of the electrode finger length to the spatial wavelength is large, and a wide frequency spectrum of use (Mamishev et al. 2004). Moreover, it has been fabricated with multiple materials and following different manufacturing process, from integration in semiconductor dices to printing on flexible substrates (Reddy et al. 2011, Yang et al. 2011, Jalkanen et al. 2012).

Many efforts have been devoted to the characterization of the IDE. Igreja et al. (Igreja and Dias 2004) developed a theoretical model of the capacitance of this structure. These capacitors have also been simulated using different simulations tools (Mohd Syaifudin et al. 2012, Molina-Lopez et al. 2012, Oikonomou et al. 2012). This structure has been typically adopted as sensor because of the low energy consumption of the capacitive transduction mechanism and its compactness, high contact area and relative ease of manufacturing. Some authors have analysed other constructions such as spiral electrodes and concentric rings in order to improve the performance of this design (Yang et al. 2011, Boltshauser, Azeredo Leme and Baltes 1993).

Different fabrication processes have been used to develop this kind of sensors, such as gravure, screen printing and inkjet-printing; and different strategies have been applied to include the sensing capability in the capacitor. The most common approach has been to deposit the sensing layer over the IDE capacitor (Molina-Lopez et al. 2012, Weremczuk, Tarapata and Jachowicz 2012, Starke et al. 2011). Some frequently used polymers are cellulose acetate butyrate (CAB), polymethylmethacrylate (PMMA) and polyvinylchloride (PVC), among others. Another possibility is to use the flexible substrate as the sensing element. In this case, polyimide (Virtanen et al. 2010) and photographic paper (Andersson et al. 2012) have already been described, saving fabrication steps compared with the former approach. Despite all the previous work, these capacitive sensors have a high thermal drift as one of the main challenges to be overcome in order to obtain an accurate humidity measurement. Differential measurements with reference capacitors (not sensitive to humidity) (Oprea et al. 2009a) or including additional temperature sensors (Molina-Lopez et al. 2013b, Courbat et al.

2011) are some of the used strategies to reduce the interference due to thermal drift. Both solutions imply the addition of other devices, consuming more area and energy.

In this section, we present the design, fabrication and characterization of a capacitive humidity sensor which uses the flexible substrate as sensitive element (Almudena Rivadeneyra 2014). This capacitor has been printed with silver nanoparticles by inkjet-printing on a polyimide thin film. Our aim has been to obtain a very small device with optimized dimensions based on numerical simulation, minimal fabrication steps and a very low thermal drift without additional components, useful in many applications. Furthermore, we have analysed the influence of the number of printed layers on the sensor performance.

2.2.1 Design

The devices analysed in this study are planar IDE capacitors which allow more direct interaction between the sensor and the surrounding environment compared to other structures (Molina-Lopez et al. 2012). The usual approach for providing humidity (or other gases) sensitivity is to deposit a sensing layer on this structure with some humidity-dependent electrical property. The variation of this property with the humidity produces changes in the capacitance of the whole device. But here, we have skipped this deposition step and directly have used the flexible substrate made of polyimide as the sensing element to simplify the fabrication process (Figure 12). The polyimide is a well-known chemical whose electrical behaviour shows a high sensitivity to the relative humidity. Specifically, the relationship between the electrical permittivity of this polyimide and the relative humidity has already made it interesting to test it as a humidity sensor (Virtanen et al. 2010). This relationship is given by:

$$\varepsilon_r = \varepsilon_{r0} + \alpha \cdot RH(\%) \qquad (13)$$

where RH(%) is the relative humidity in percentage and ε_{r0} and α are material dependent parameters. This relative permittivity also depends on frequency and temperature among other parameters which could interfere with the measurement of the humidity. These dependences must be also analysed in

order to obtain a complete overview of the sensor behaviour and to try facing them to improve the sensor performance.

The optimization of the sensor dimensions may potentially introduce more sensors into the devices. For this purpose, we used COMSOL Multiphysics 4.2a to optimize the design.
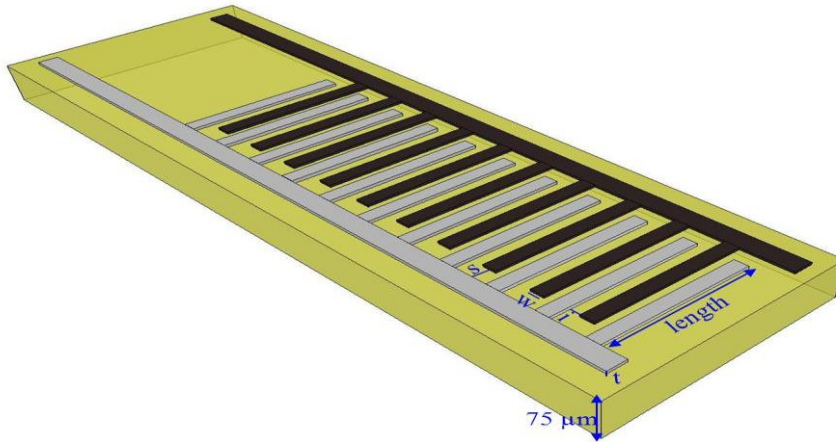
Figure 12. Layout of the designed IDE sensor (w = width, s = distance, i = interspacing, t = thickness).

Several parametric analyses were performed varying the fundamental geometrical parameters of the IDE such as the number of fingers, the gap width between two consecutive fingers and their dimensions (width, length and thickness of each finger). In order to optimize the area, we fixed the finger width to the minimum diameter landed drop (in our case 50 µm) and the gap between fingers also to 50 µm. This gap could be reduced below the drop diameter value to increase the capacitance value but this reduction will lead to a strong possibility of short-circuit between electrodes due to printing errors. The parametrical simulations showed that the thickness of the fingers hardly affects the capacitance value in this structure. In this work, we have also tested structures with one and two printed layers. As shown below, their thicknesses are under 1 µm in both cases implying extremely long simulation times because of meshing issues. Due to this fact, we set the thickness of the IDE to 5 µm for all the simulations to drastically reduce the computational time. Then, we extrapolated the value of the capacitance for the thickness of

1 layer and 2 layers according to Figure 13 where the slope of the curve is 0.019 pF/µm.
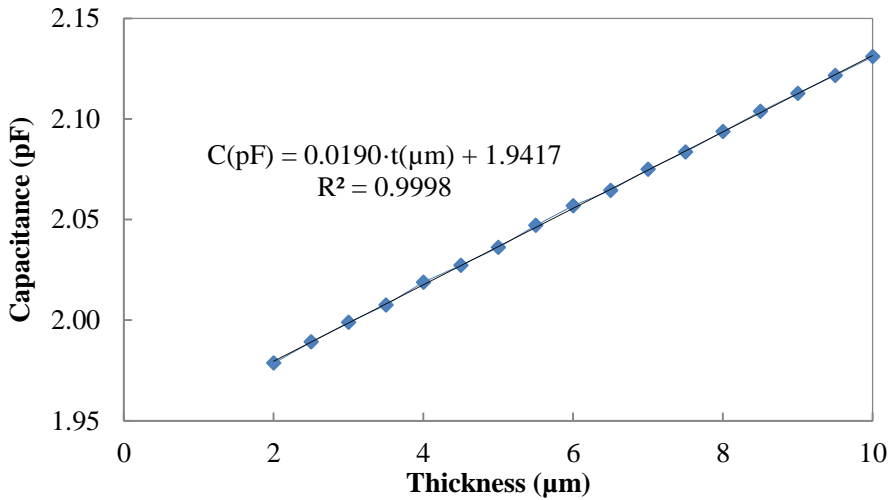
Figure 13. Numerical capacitance vs. Thickness of electrodes.

According to previous considerations, we manufactured the sensor following the specifications from Table 2 for a targeted nominal capacitance (for one printed layer) of 2 pF since they presented the best compromise between capacitance and area. Finally, the capacitance predicted by COMSOL Multiphysics 4.2a for this structure was 1.949 pF with only one printed layer in a dry atmosphere.

Table 2. Physical dimensions of the capacitive interdigitated structure.

Parameter	Value	Description
Length	1.6 mm	Length of each finger (y-axis)
Width	50 µm	Width of each finger (x-axis)
Thickness	420/900 nm	Thickness of electrodes (1/2 layers) (z-axis)
Number	32	Total number of fingers of the larger electrode
Interspacing	50 µm	Distance between consecutive fingers (y-axis)
Distance	50 µm	Distance between fingers of one electrode and the backbone of the other electrode (x-axis)

The designed IDE area was 11.65 mm^2 (L = 1.85 mm x W = 6.3 mm) composed of 63 fingers (32 fingers for one electrode and 31 for the other

one) with 50 µm width and inter-spacing (see Figure 12). This area is significantly smaller than other comparable printed humidity sensors presented in the literature (Molina-Lopez et al. 2012, Weremczuk et al. 2012, Starke et al. 2011, Oprea et al. 2008). In order to easily test the capacitor, we added two long terminals to couple the sensor to the measurement set-up.

Obviously, the greater the structure, the bigger the capacitance obtained. Our interest in such a small structure was not only to reduce cost in terms of materials and time of fabrication but also to integrate more different sensors into the same area.

2.2.2 Fabrication process

The DMP-2831™ Dimatix printer (Fujifilm Dimatix Inc, Santa Clara, USA) was used for inkjet printing. The selected materials were an ink of silver nanoparticles (U5603 SunTronic Technology, San Diego, USA) on a polyimide substrate (Kapton® HN with 75 µm of thickness, Dupont[TM]). Table 3 shows the main properties of the used ink and substrate, respectively.

Table 3. Substrate and Ink properties.

Conductive ink	Experimental resistivity ($\mu\Omega\cdot cm$)	Solid content (Ag)	Solvent	Curing Temperature (ºC)
SunTronic U5603	23 ± 2	20%	Ethanol, ethanediol	150-300
Substrate	**Chemical composition**	**Dielectric constant**	**Dissipation factor**	**Glass transition (ºC)**
Kapton HN	Polyimide	3.5 (1kHz)	0.0020 (1kHz)	360-410

The first step before printing was to prepare the substrate to ensure the best quality and to avoid failed printings with a cleaning process. First, we immersed the substrate in acetone for 2 min to remove dust on the surface, then we submerged it in propanol about 2 min to remove the acetone. After that, we washed the sample with purified water to eliminate the propanol and finally a drying step at 120ºC during 5 min.

This treatment was done to remove all traces of particles that could affect the printing process. The substrate temperature was fixed at 40ºC while printing. A drop space of 25 μm was settled in the printer for 50 μm landed diameter drops followed by a sintering step at 120ºC for 60 min.

In order to know the thickness of the printed layer, the theoretical model given in Equations (5) to (11) has been used. The irregularity in the contribution of the outer part of the lines to the average thickness has to be taken into account only if the printed element is comparable in size with the diameter of one printed drop. Therefore, special care has to be taken to the amount of ink deposited along the width of the lines. The predictions of this model have been checked with the experimental data obtained from the interferometry study.

According to this model, the amount of used ink is 22.68 nl and 45.36 nl for one and two printed layers, respectively. With that printing and curing conditions, the resistivity of the conductive electrodes were 23 ± 2 μΩ·cm for both one and two printed layers (J.F. Salmeron 2013). The fabrication time is much lower than in the case of other sensors because no other sensing layer was needed (Molina-Lopez et al. 2012, Weremczuk et al. 2012, Starke et al. 2011). The fabrication process is also simplified because it only required printing one/two layer/s on one side of the substrate. A matrix of twenty eight capacitors –one half of them with one layer, the other half with two layers- has been fabricated in order to test the reproducibility of the process.

2.2.3 Characterization results

The physical characterization, the roughness of printed patterns as well as the thickness of the patterns has been done using a Wyko NT1100 Optical Profiling System (VEECO, Tucson, AZ, USA). The AC electrical characterization for the different fabricated capacitors has been performed by measuring their capacitance and dissipation factor, using the four-wire measurement technique with a precision Impedance Analyser 4294A and an impedance probe kit (4294A1) (Agilent Tech., Santa Clara, CA, USA). The excitation voltage applied in all measurements was $V_{DC} = 0$ and $V_{AC} = 500$mV. The frequency sweep of analysis was from 100 kHz to 10 MHz. We

have considered this frequency range for its compatibility with a wide variety of readout electronic circuits in real applications.

As it has been mentioned above, one of the end sides of the backbones has been enlarged to facilitate its connection to any analyser. A SMA (SubMiniature version A) male connector has been glued to these ends points using silver-filled epoxy EPO-TEK® H20E (Epoxy Technology, Inc., Billerica, USA) (see Figure 14).
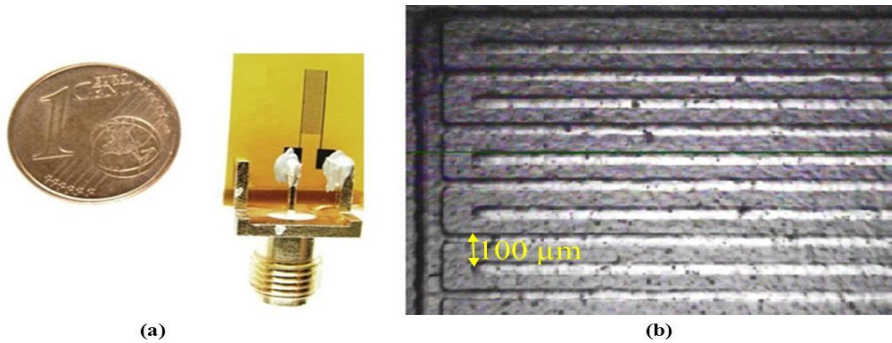
Figure 14. (a) Image of the inkjetted capacitor and, (b) capture image with the Dimatix printer fiducial camera showing the 50 µm-gaps of the printed fingers.

It was necessary to calibrate up to the SMA connectors including the mentioned extensions of the backbones to rigorously characterize. For this purpose, we measured several commercial capacitances placed in the same configuration, as shown in Figure 14a, with the 16034G SMD Test Fixture (Agilent Tech., Santa Clara, CA, USA). After processing all data, the total added parasitic capacitance was 2.70 ± 0.02 pF in the whole spectrum of the impedance analyser.

We have manufactured fourteen samples with one printed layer and other fourteen samples with two layers. According to a previous developed physical model of layer thickness by inkjet printing (see Eq. (11)) (J.F. Salmeron 2013, Molina-Lopez et al. 2012) the estimated thicknesses are 430 nm and 860 nm, respectively. The real dimensions of the structures are given in Table 4.

Table 4. Comparison between numerical and experimental physical dimensions of one and two printed layers IDE capacitors.

Parameter	Model 1 layer	Experimental 1 layer	Model 2 layer	Experimental 2 layer
Finger length (mm)	1.60	1.63 ± 0.01	1.60	1.68 ± 0.01
Finger width (µm)	50.0	57 ± 5	50.0	57 ± 5
Gap between fingers (µm)	50.0	46 ± 4	50.0	50 ± 4
Thickness (nm)	430	420 ± 50	860	900 ± 50
Roughness, R_q (nm)	-	530 ± 50	-	420 ± 50
Roughness, R_a (nm)	-	410 ± 50	-	320 ± 40

As can be observed in Figure 15, we used a profiling system to study the real physical characteristics of the printed sensors. Table III also shows the differences between the estimated dimensions and the measured ones for sensors of one and two printed layers. Uncertainties were calculated as the standard deviation of the experimental data.

R_q is the root mean square (RMS) and R_a the arithmetic average of the absolute values, both of the surface roughness heights. In general, modelled dimensions are very close to experimental ones, showing the greatest difference in the finger width. This can be explained by the spread of the ink drop when it is deposited on the substrate (Derby 2010).
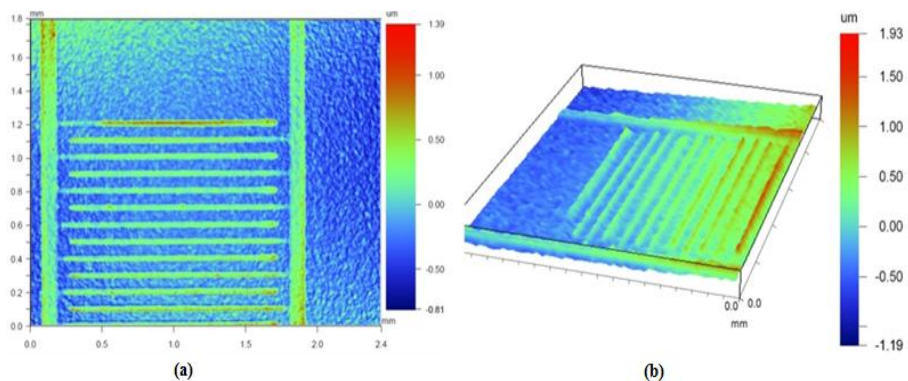
Figure 15. Profiling system captions. (a) 2D, (b) 3D analysis.

There is a very good agreement between the measured and the simulated values of the capacitances of the replicated IDE capacitors; this confirms that the proposed extrapolation procedure works properly for the given electrode thicknesses. The measurements were taken in ambient conditions (30% RH and 25ºC) at 1 kHz. The employed frequency was not too high to hinder polarization. During these tests, a preliminary (the total number of fabricated samples was 28) manufacturing yield of 90% was found, that is, one sample out of ten was totally or partially broken. This yield was calculated from low frequency capacitance measurements of several replicas of IDE capacitors.

As expected by the numerical simulation (see Figure 13), capacitors with two printed layers showed only a 0.036 pF bigger capacitance than those with one layer, due to the low influence of the finger thickness on this electrical magnitude. Moreover, the standard deviation is reduced in almost 3 times in case of two printed layers because more similar structures are obtained with the second layer. This improvement is due to the fact that the second layer covers the irregularities of the first printed layer, smoothing the structure surface.

Table 5. Statistics of the different replicas.

	Numerical Capacitance (pF) (COMSOL) [1]	Experimental Capacitance (pF) [2]
1 layer	1.973	2.053 ± 0.002
2 layers	1.982	2.0890 ± 0.0006

[1] Simulated value at 30% RH. [2] Measured value at room ambient conditions at 1 kHz.

According to the simulated capacitance, the measured values are about 5% higher in both cases (Table 5). The discrepancy between these results might be caused because the real dimensions of the sensor are not exactly the same as the simulated ones. As described by Derby et al. (Derby 2010), printing electronics techniques present undesirable effects. Those effects lead to an inaccuracy in the printed structure. For example, drops tend to spread out when they are deposited on many substrates. This behaviour results in wider fingers and narrower inter-spacing as shown in Table 4. In addition to this, the frequency dependence is not taken into account in the simulations. As this sensor is quite small, any dimensional difference can affect the results. Therefore, these results confirm that the approximation taken in the

numerical simulations for the thickness can be done without inducing substantial errors.

2.2.4 Results as humidity sensor and discussion

After the physical characterization, hereafter the sensor capacitance has been analysed as a function of humidity and temperature in a wide frequency range. Let's remember that a humidity response with minimal thermal drift is our goal for the developed IDE capacitor.

A. Humidity and Temperature Responses

The stationary humidity and temperature responses of these sensors have been measured in a climatic chamber VCL 4006 (Vötsch Industrietechnik GmbH, Germany). The humidity range varied from 10% RH to 98% RH in a temperature range of + 10 °C to + 95 °C. The humidity deviation in time was ± 1% to ± 3%, whereas the temperature deviation in time was ± 0.3 °C to ± 0.5 °C. Due to the slow response of the mentioned climatic chamber, the dynamic response has been measured in a customized humidity measurements set-up (9 x 3 cm^2), which automatically controls wet and dry airflow inside a small gas cell at room temperature. Two LCR-meters (HP 4284L and Agilent E4980A, Agilent Tech., Santa Clara, CA, USA) have been used to measure the corresponding capacitance values at a frequency of 100 kHz every 5 s. Capacitance and time measurements of the printed sensors have been controlled and recorded using the software Labview 2012. RH and temperature measurements have also been registered by a commercial sensor (SHT15, Sensirion AG, Switzerland) in order to verify the data given by the chambers' displays. In all cases, the IDE capacitors have been placed in the middle of the climatic chambers allowing the atmosphere interaction in both faces of the sensors, printed and non-printed.

For five IDE capacitors with one printed layer, we have measured the capacitance as a function of the relative humidity and temperature in the frequency range from 100 kHz to 10 MHz. Furthermore, the measurements have been carried out in both directions for both humidity and temperature sweeps, that is to say, increasing and decreasing the relative humidity at fixed temperature for obtaining the sensor hysteresis in RH and vice versa for

temperature. The capacitance response to the relative humidity was characterized taking into account the measurement frequency and the temperature dependences. Regarding all these experimental data, we analysed the ratio of humidity sensitivity and thermal drift to find the frequency range where humidity can be accurately measured without compensation of thermal effects.

Figure 16 and Figure 17 show the measured capacitance of the sensor for different values of RH at 40 ºC and 30 ºC, respectively. As can be observed, the sensor presents very similar response in frequency for each of the tested RH. Weremczuk *et al.* (Weremczuk et al. 2012) found comparable capacitance curves for an IDE structure with a deposited layer of Nafion as sensing material. The displacement between curves due to RH variations is constant up to 70%. From 80% RH, the displacement between lines slightly increases; this tendency can be explained by the condensation of water on the sensor surface at high humidity levels which could connect the electrodes and modify the global impedance (Sahm et al. 2007). For our results, the general decreasing trend with the frequency can be explained by the electrical permittivity decrease found in the Kapton HN substrate (Dupont[TM] Kapton® polyimide film datasheet).
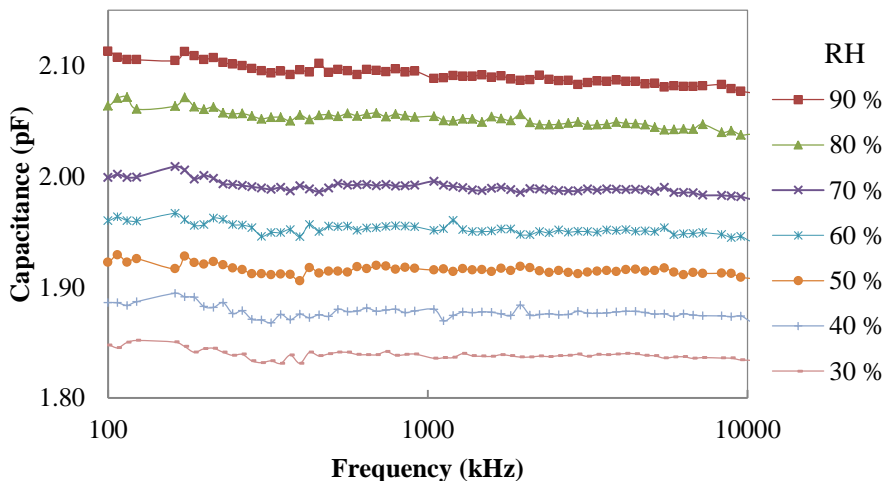
Figure 16. Capacitance for RH as a function of frequency at 40ºC.
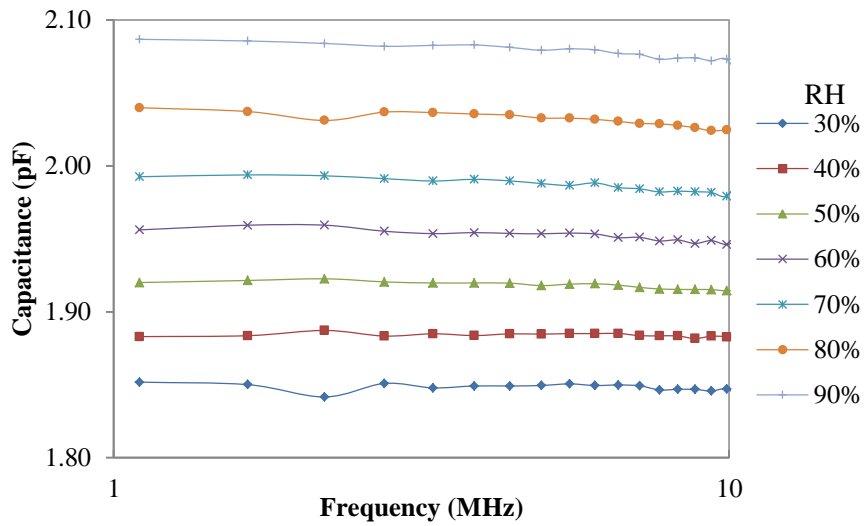
Figure 17. Capacitance for RH as a function of frequency at 30ºC.

As mentioned, the temperature is the most important interfering factor in the response of the developed capacitive sensors. To test this dependence, Figure 18 displays the capacitance as a function of frequency for several temperatures at 60% RH. These curves are practically overlapped up to 40°C, and then a displacement is observed. The range of frequencies where the least difference between lines happens is from 1 MHz to 10 MHz.
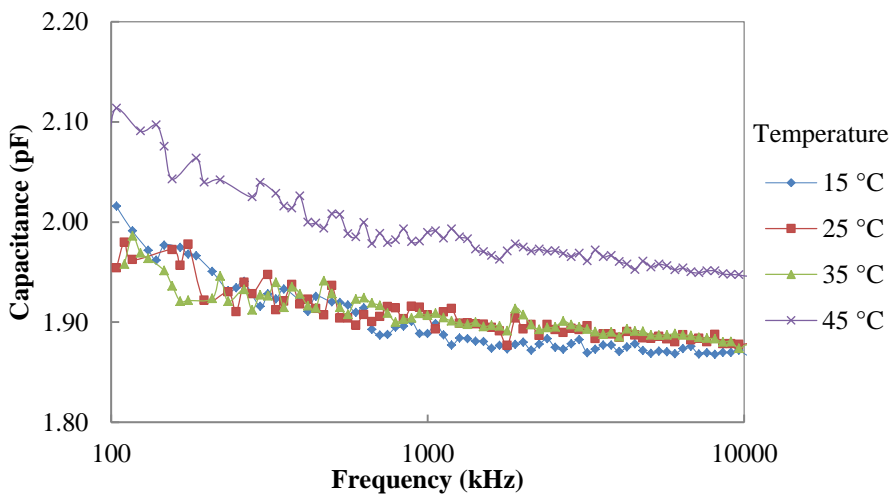
Figure 18. Capacitance for several temperatures as a function of frequency at 50% RH.

To obtain a better insight of the whole sensor response, we have defined the partial sensitivities of the capacitance to the relative humidity, S_{RH} (f), and the temperature, S_T (f) as a function of the measurement frequency, f, as:

$$S_{RH}(f) \equiv \frac{\partial C_{T=cte}\,(RH)}{\partial\,RH} \qquad\qquad (\,14\,)$$

$$S_{RH}(f) \equiv \frac{\partial C_{T=cte}\,(RH)}{\partial\,RH} \qquad\qquad (\,15\,)$$

Both sensitivities are shown in Figure 19. Regarding humidity sensitivity, it decreases from around (4.5 ± 0.2) fF/%RH and tends to (4.0 ± 0.2) fF/%RH at the highest analysed frequencies. This tendency is a direct consequence of Figure 16 where the separation between consecutive experimental curves decreases at higher frequencies. This range of sensitivities, about 2200 ppm/%RH, is a typical value in comparable previous works (Molina-Lopez et al. 2012, Oprea et al. 2008, Altenberend et al. 2012). With respect to the temperature behaviour of the sensor in the whole spectrum, the thermal dependence decreases at higher frequencies, from about (-0.4 ± 0.2) fF/°C at 100 kHz to less than (-0.2 ± 0.2) fF/°C at 1 MHz. The errors in sensitivities have been estimated by linear propagation of experimental errors in the calculated linear regression.
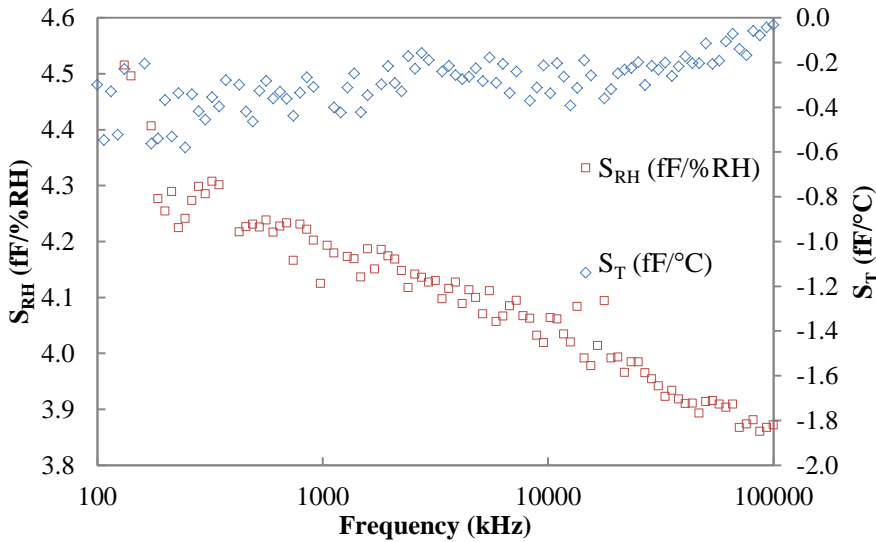
Figure 19. Relative Humidity and Thermal sensitivities as a function of frequency.

Comparing thermal and humidity sensitivities (Figure 19), this sensor shows a humidity sensitivity between 11 and 22 times higher than the thermal drift in the analysed frequency range. Considering the central frequency of the analysed span, 1 MHz, we have measured a sensitivity ratio of 21. This means that our sensor would show a maximum error of 2% in RH without thermal compensation, within a temperature range of 40ºC. This inaccuracy could be acceptable in many low-cost applications such as those related to RFID tags with sensing capabilities.

B. Calibration curves

Now, the calibration curves with the relative humidity and its hysteresis is presented. The response of the sensor to changes in the relative humidity is directly extracted from the curves obtained with the impedance analyser. In Figure 20 we show a graph of these curves at the chosen frequency to compare and contrast the response of the sensor to variations in RH at different temperatures.
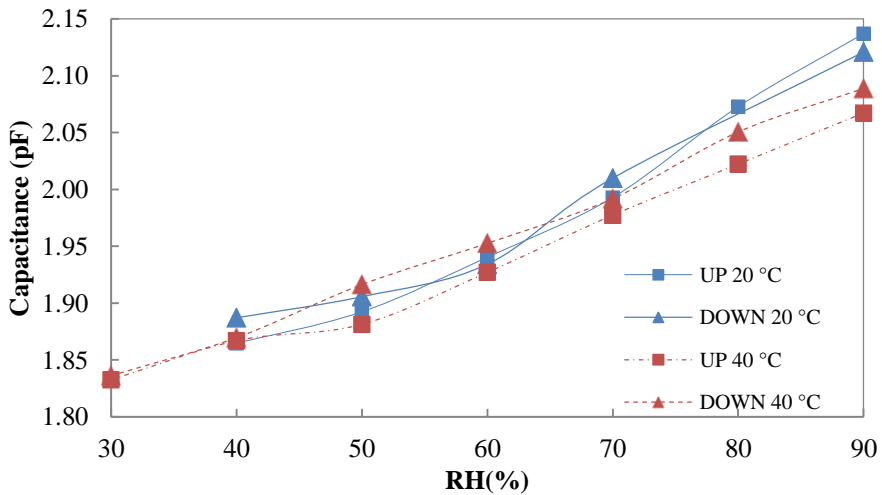
Figure 20. Capacitance vs. Relative humidity at 1 MHz.

We have calculated the calibration curves of the experimental data shown in Figure 20. Equations (16) and (17) show these calibration curves. The coefficient of linearity is bigger than 0.98 in all cases.

$$C(pF) = 0.0041 \cdot RH(\%) + 1.693.\ R^2 =\ 0.983.\ Increasing\ RH \qquad (16)$$

$$C(pF) = 0.0043 \cdot RH(\%) + 1.702.\ R^2 =\ 0.996.\ Decreasing\ RH \qquad (17)$$

The maximum relative error due to the hysteresis between eq. 14 and 15 and experimental data is less than 2% up to 70% RH and below 4% at higher RH values.

An important design aspect of sensors is the hysteresis of the device. The maximum shift between curves with increasing RH steps (represented as "UP" in Figure 20) and with decreasing RH steps (representing as "DOWN" in Figure 20) is less than 7 fF at 1 MHz up to 70% RH and less than 10 fF from 80% RH. Therefore, the maximum absolute error associated to the hysteresis is around 2% RH.

C. Response time

Another important property of any sensor is how fast the sensor output (the capacitance, in our case) changes when there is a variation in the input, which in our case is the relative humidity.
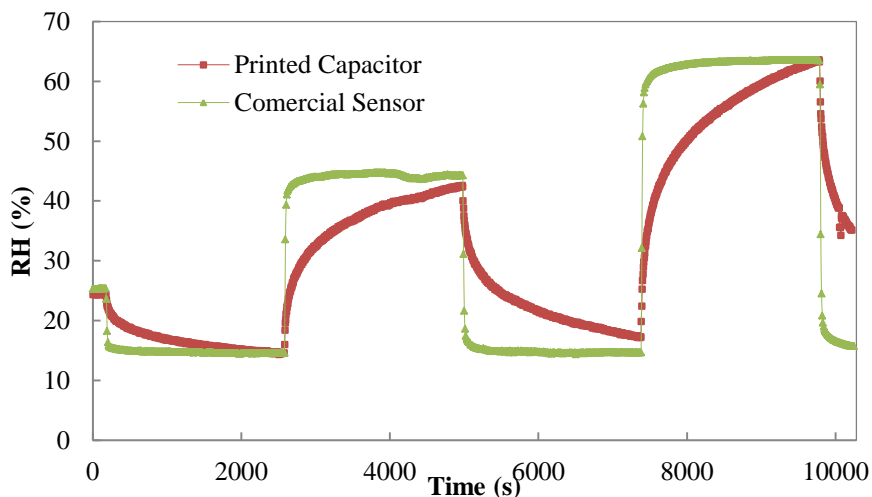
Figure 21. Transient response of the IDE capacitor.

The dynamic response of the sensor is depicted in Figure 21 and shows a high stability along different measurement cycles and over time. The output of the printed sensor is presented together with that of a commercial sensor

and their results are comparable. Defining the response time as t = τ, it would correspond to the 63% of the maximum value of capacitance (reached at equilibrium) for every increasing step of RH presented in Figure 21. Although the sensor does not reach the steady state in these cycles, their behaviours can be adjusted by exponential curves; we estimated the response time from the adjusted curves. This time is equal to 356 ± 3 s. Additionally, the response time for desorption, τ', can be defined as the time associated to the 37% of the maximum value of capacitance for every decreasing step of RH; this value is 367 ± 4 s. These long response times can be explained in terms of different diffusion rates in our solid substrate compared to the deposited layers in other IDE structures (Molina-Lopez et al. 2012, Weremczuk et al. 2012). The printed sensors can hardly compete in terms of response time with commercial CMOS-based humidity sensors (SHT15, Sensirion AG, Switzerland) with times smaller than 10 s. This lower performance in response time does not hinder the use of these printed humidity sensors due to the fact that humidity is an environmental property, which often changes gradually.

In any case, the response time is also directly related to the squared value of the thickness of the sensitive layer (Igreja and Dias 2006). Then, this time can be reduced by using a thinner substrate. Anyway, this sensor as it is presented here could be useful for environmental humidity monitoring, where changes are usually gradual and slow. Harrey et al. (Harrey et al. 2002) developed a parallel-plate capacitive sensors with a number of humidity sensitive polymers including polyimide (Kapton HN) and polyethersulphone (PES). Furthermore, they showed the improvement in time response by using thinner sensitive layers. In that study, the times achieved varied from 5 min to 10.5 min for Kapton HN depending on the thickness of the film.

D. Time Stability

The sensors have been measured once a week for more than 6 months and data show a small maximum variation of ± 9.3 fF of the average value. In order to estimate the aging drift, we did a stability test 5 months after its fabrication. After the fifth month, the humidity sensor was tested for 10 days at fixed relative humidity (30%) and controlled temperature (30 °C) every 6

hours. The aging drift was less than 3% RH, which is within the time drift specification of the used climatic chamber.

2.3   Serpentine electrode structure

As we have studied in previous section, the most common sensing capacitive structures are the planar parallel plate and the interdigitated electrode (IDE). Nevertheless, some authors have analysed other constructions such as spiral electrodes and concentric rings in order to improve the performance of this design (Yang et al. 2011, Boltshauser et al. 1993). In this section, the focus is on the underlying electrode structure more than on novel materials to improve the sensor sensitivity. We have looked into the geometry of the structure to enhance the sensor performance as it was indicated in the review of Mamishev et al. (Mamishev et al. 2004).

Here, we present a novel periodic electrode structure as a combination of meandering and interdigitated electrodes in a serpentine-shaped geometry in a single structure. Therefore, we have denominated this structure serpentine electrode, SRE. Serpentine-like electrodes have previously been used as electrode guard of IDE structures (Mamishev et al. 2002), impedance sensor for conformal skin hydration monitoring (Huang et al. 2012) and a three phase electrode array for AC electroosmotic flow pumping, where the serpentine electrode creates a compact and symmetric design (Xie et al. 2010). Here, this novel serpentine electrode (SRE) structure and the well-known IDE structure has been compared in detail as generic capacitive transducers by numerical simulation, showing the bigger capacitance for the former with identical areas. From these simulations, the relevant geometrical dimensions which increase even more the SRE capacitance have been found. To verify the theoretical analysis, we have measured the response to relative humidity of printed SRE and IDE capacitive sensors on a flexible substrate. Capacitors have been printed with silver nanoparticles by inkjet printing on a polyimide thin film whose electrical permittivity changes with the moisture in the environment. Our results show the advantages of the SRE as a higher sensitive sensor compared with IDE structures made of the same materials and dimensions.

2.3.1 Design and simulation results

Dimensionally identical serpentine electrode (SRE) and interdigitated electrode (IDE) structures are represented in Figure 22a and b, respectively. As we will show throughout this document, this SRE structure will exhibit a bigger capacitance than the IDE one with the same geometrical dimensions. Therefore, having a bigger capacitance only due to its geometrical structure, SRE will have a higher sensitivity as a capacitive transducer.

To prove this, we have simulated deposited SRE and IDE capacitors on a substrate, always with the same dimensions, the same bottom substrate and the same top layer, calculating and comparing the DC capacitances of each structure. Given the complicated geometry of the serpentine capacitors, we have skipped the development of an analytical model and we have directly used the multiphysics numerical simulator COMSOL Multiphysics 4.2a (COMSOL Inc., Stockholm, Sweden).
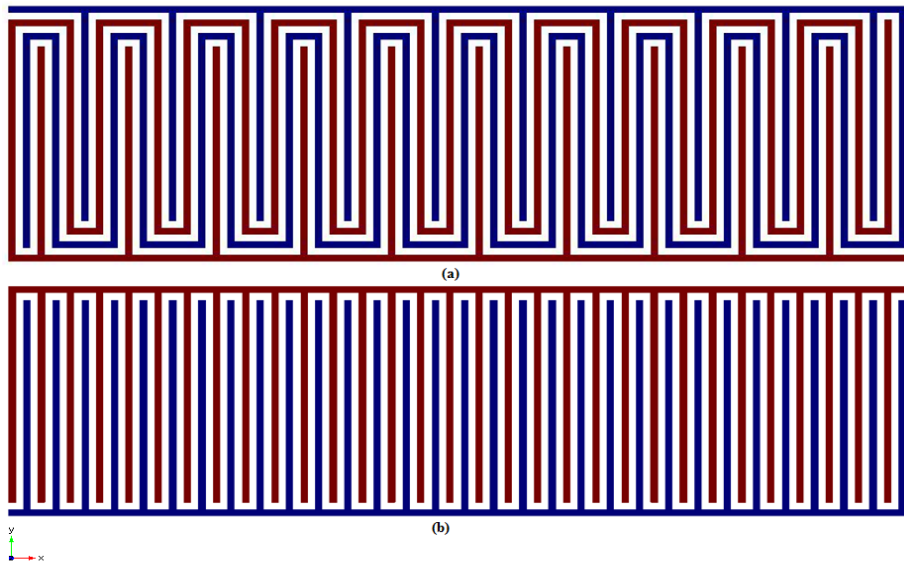
Figure 22. (a) Serpentine electrode (SRE) and (b) Interdigitated electrode (IDE) structures.

A three dimensional view of the simulated structure including the notation of its geometrical parameters is depicted in Figure 23. Multiple numerical simulations have been carried out to compare and contrast both structures, as described below. We have looked over which dimensions are relevant to the

capacitance differences of SRE with respect to IDE capacitors. The electrical properties of the substrate, top layer and the conductive electrodes have also been included in the simulator. In view of the very different vertical (submicron in some cases) and horizontal dimensions (millimetres), extremely long simulation times could be necessary.

To overcome this drawback, we have taken advantage of the negligible influence of the electrode thickness in the calculated capacitance for the analysed range of thicknesses (around and below 1 μm). Here, we have also applied an extrapolation method, presented in the previous section for the IDE structure. The thickness has been set to 5 μm for all the simulations to drastically reduce the computational time and after that, the real capacitance values have been inferred taking into account the thickness effect, where both slopes of extrapolation curves were 0.019 pF/μm for the SRE and the IDE capacitors.
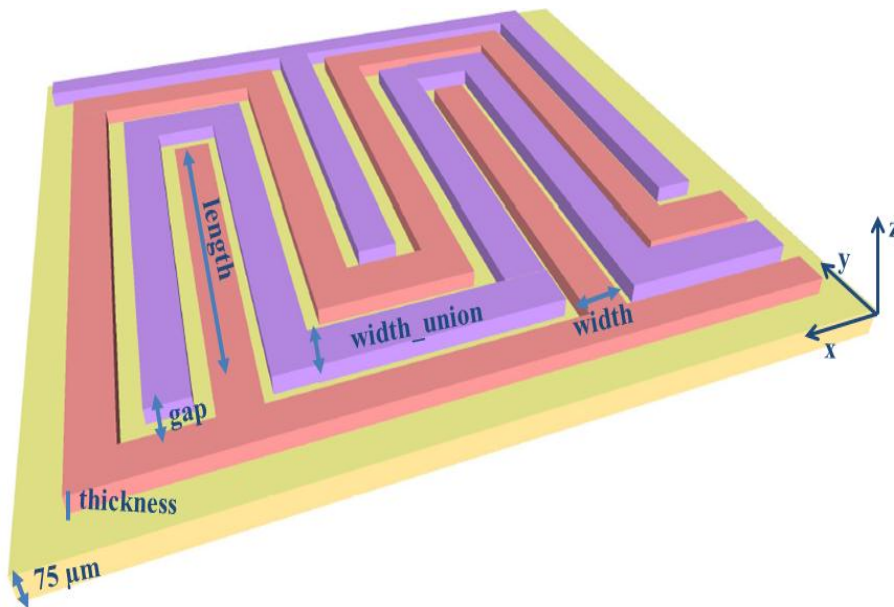
Figure 23. Layout of the designed SRE capacitor indicating the notation of the dimensions and the Cartesian axes.

We have performed different numerical simulations, comparing the calculated DC capacitances of SRE and IDE structures always with the same dimensions and materials. There are multiple geometrical factors that can be varied in these simulations but for the sake of clarity, we have focused on

some of them, keeping fixed the rest. As mentioned above and with the aim of saving area, we have set to the minimum safe dimensions of our fabrication process the different widths and gaps of the structures (see Figure 23). Therefore, we have used as simulation parameters the length, the number of electrodes and the sensitivity of the substrate and top layer to the relative humidity.

Table 6 summarizes these geometrical parameters for simulation. Let us remember that the measured capacitors have only been fabricated with fixed dimensions without varying any geometrical parameter. The first relevant result always showed in our simulations is a higher capacitance value in the SRE structure than the one obtained in the IDE. For example, simulating the fabricated capacitors with one printed layer, we have obtained numerical capacitances of 1.973 pF for IDE and 2.256 pF for SRE. This means an increase of 14.3%. From the point of view of their sensing capabilities, the fact that the geometrical factor of the capacitance is higher in SRE capacitors means that its sensitivity as sensor will be always higher with equal areas. Moreover, the capacitance and sensitivity increases will result in the same amount. Next, we have calculated the numerical capacitances with some variable parameters to optimize the performance of SRE capacitors.

Table 6. Physical dimensions of the simulated (Sim) and fabricated (Fab) capacitors.

Parameter	SRE	IDE	Description
Width	50 µm	50 µm	Width of each finger (*x*-axis)
Gap	50 µm	50 µm	Distance between consecutive fingers (*y*-axis)
width_union	50 µm	50 µm	Width of each union (*x*-axis)
Thickness	420/900 nm	420/900 nm	Thickness of electrodes (1/2 layers) (*z*-axis).
Number	Fab: 32 Sim: 32 to 130	Fab: 32 Sim: 32 to 130	Total number of fingers of the larger electrode
Length	Fab: 1.1 mm Sim: 1 to 1.8 mm	Fab: 1.6 mm Sim: 1 to 1.8 mm	Length of each finger (*y*-axis) without including unions

Regarding the influence of the substrate as sensing element, we calculated the DC capacitance for different substrates without any deposited layer on the electrodes (Figure 24). The results always showed a higher capacitance value for the serpentine structure than for IDE. Keeping fixed all the dimensional parameters, the enhancement in capacitance was always constant. In addition to these studies, the influence of a deposited layer was also analysed (Figure 24). As in the previous case, there was always an improvement in the capacitance of the serpentine electrodes and the ratio between capacitances was also fixed if the electrodes dimensions were fixed.
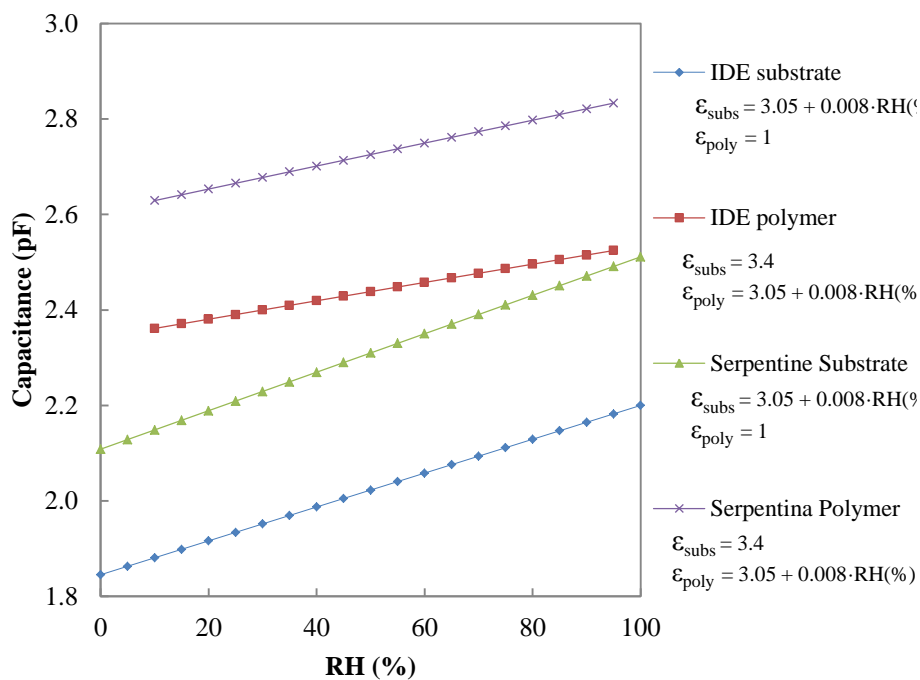
Figure 24. Capacitance variation with RH depending on the sensitive layer.

The influence of the finger length (from 1.5 to 1.8 mm) has been evaluated for IDE and SRE capacitors with 32 fingers (Figure 25). Both curves showed virtually the same slope (about 1.2 pF/0.1 mm) since the enlargement of the fingers has the same contribution to the capacitance in both structures, and therefore no improvement of the capacitance is obtained.
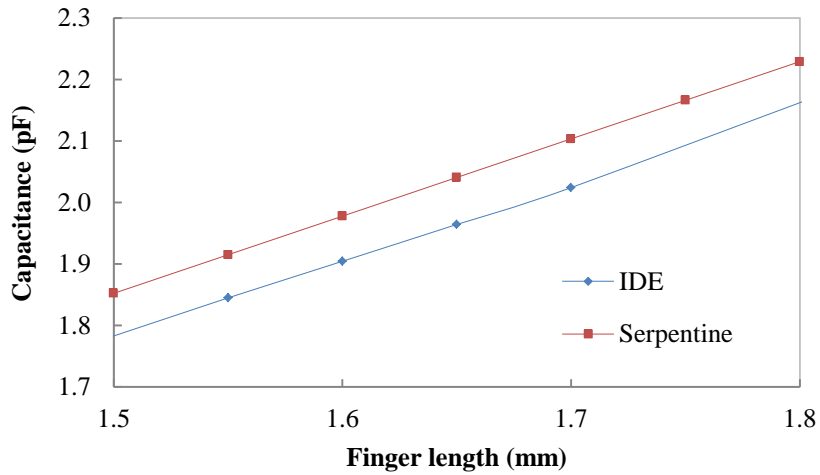
Figure 25. Capacitance vs. Finger length.

However, a different behaviour appears when we calculate the impact of the number of fingers on the capacitance (see Figure 26) with the fixed finger length given in Table 1. Now, the SRE capacitance slope (0.039 pF/finger) is higher than the IDE one (0.032 pF/finger). This improvement is due to the fact that increasing the number of fingers leads to an increase in the number of meanders. Through this result, we can conclude that the enhancement in capacitance of serpentine is caused by the only difference between both structures: the meandering of the fingers.

$$C(pF) = 0.0386 \cdot NF - 0.2062$$
$$R^2 = 0.9994$$

$$C(pF) = 0.0320 \cdot NF - 0.0420$$
$$R^2 = 0.9975$$
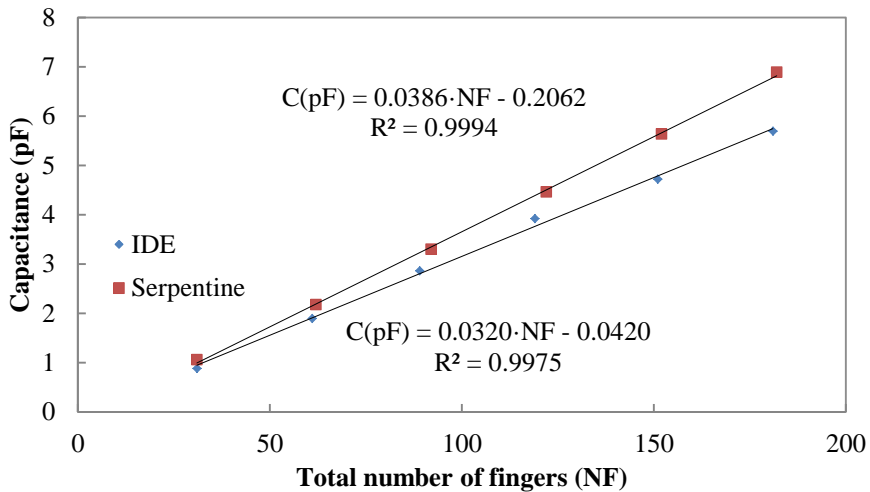
Figure 26. Numerical capacitance vs. number of fingers for SRE and IDE capacitors.

This meandering shape causes a higher electric displacement D in the SRE compared with the IDE structure, as is shown in Figure 27. The electric displacement field changes the charge stored between the sensor electrodes, and thus alters the inter-electrode capacitance. This can be used to infer the properties of the material under test, in this case, the humidity sensitive substrate. This result agrees with the study of the capacitance sensitivity as a function of the structure shape by Hu et al. (Hu and Yang 2010) where meandered shapes shows more sensitivity.
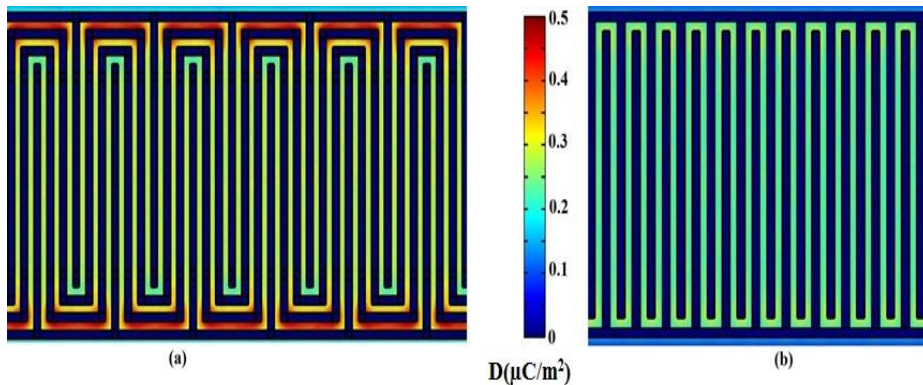
Figure 27. Comparison of the calculated Electric displacement field of the (a) SRE and (b) IDE structures simulated at the same electric conditions.

Other numerical simulations including the changes of the electrical permittivity with the humidity in the substrate and the top layer have shown that this higher capacitance value for the SRE compared with the IDE one is linked to the geometrical factor of the capacitance. No more capacitance improvement is obtained between SRE and IDE structures by the fact of having a substrate or top layer with electrical permittivity dependent of some analyte (in this case, humidity).

2.3.2 Fabrication process and characterization results

The fabrication process is the same than that used for the IDE structures described in section 2.2.2, with the only difference of the electrode layout. The DMP-2831™ Dimatix printer (Fujifilm Dimatix Inc, Santa Clara, USA) was used for inkjet printing of the electrodes. The selected materials were an ink with a solid content of 20% of silver nanoparticles dispersed in ethanol/ethanediol (U5603 SunTronic Technology, San Diego, USA) printed

on a polyimide substrate with 75 μm thickness (Kapton® HN, Dupont[TM], Wilmington, DE, USA). No sensing layer was deposited onto the electrodes, being the substrate the only element which changes with the relative humidity.

A total of thirty SRE and thirty IDE capacitors –one half of them with one printed layer, the other half with two layers- were fabricated in order to test the reproducibility of the process and to carry out the comparative study. For experimental comparison of both capacitive structures and in accordance to the previous section, a targeted nominal capacitance of 2 pF was chosen for one printed layer, as this value presented a suitable compromise between capacitance and area. The areas of both IDE and SRE structures were 11.65 mm^2 (L = 1.85 mm x W = 6.3 mm) composed of 62 fingers (31 fingers for each electrode) for IDE and SRE with 50 µm width, gap and with_union as minimum secure dimensions of our fabrication procedure (see Figure 23). In order to easily test the capacitors, we added two long terminals to couple the sensors to the measurement set-up. According to the model presented in the previous section (see equation (11)), the calculated amount of used ink were 22.68/45.36 nl and 23.46/46.92 nl (one/two printed layers) for interdigital and serpentine structures, respectively. With these printing and curing conditions, the average resistivity of the conductive electrodes were 23 ± 2 µΩ·cm for all electrodes and number of printed layers (J.F. Salmeron 2013).

The geometrical characterization of the fabricated capacitors has been done using a Wyko NT1100 Optical Profiling System (VEECO, Tucson, AZ, USA). The electrical characterization has been carried out by measuring their capacitances and dissipation factors, using the four-wire measurement technique with a Impedance Analyser 4294A and an impedance probe kit (4294A1) (Agilent Tech., Santa Clara, CA, USA). The excitation voltage applied in all measurements was V_{DC} = 0 and V_{AC} = 500 mV. The frequency sweep of analysis was from 100 kHz to 10 MHz. As we already did for the IDE sensors, one of the end sides of the backbones has been enlarged to facilitate its connection and a SMA (SubMiniature version A) male connector has been glued to these ends points using silver-filled epoxy EPO-TEK$^®$ H20E (Epoxy Technology, Inc., Billerica, USA) (see Figure 28). A complete compensation method has been implemented to eliminate the contribution of parasitic capacitances.
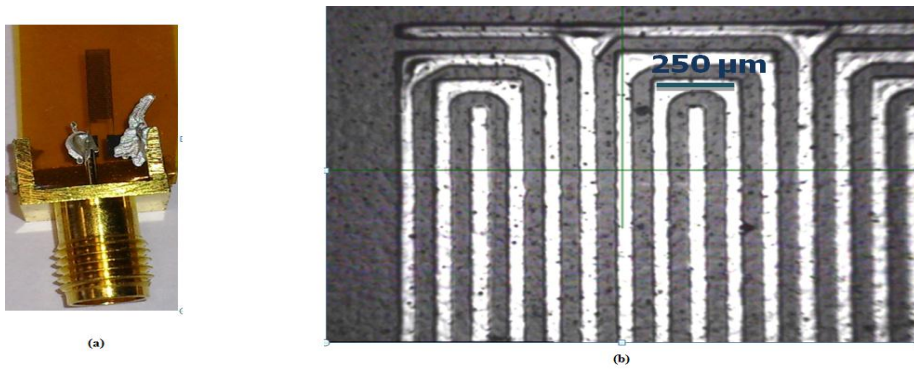
Figure 28 (a) Image of the inkjetted capacitor with the connector and, (b) capture image with the Dimatix printer fiducial camera showing the 50 μm gaps of the printed fingers.

To experimentally check the simulation results, thirty replicas of both IDE and SRE structures with identical areas of 11.65 mm^2 (L = 1.85 mm x W = 6.3 mm) were printed on Kapton HN and physically characterized (Figure 29). According to a previously developed physical model of layer thickness by inkjet printing (see equation (11)), the calculated thicknesses are 430 nm and 860 nm, respectively. The real dimensions of the structures are presented in Table 7, showing the differences between measured and predicted dimensions for sensors with one and two printed layers. Uncertainties were calculated as one standard deviation of the experimental data.

Table 7. Comparison between numerical and experimental physical dimensions of one and two printed layers serpentine capacitors.

Parameter	Model 1 layer	Experimental 1 layer	Model 2 layer	Experimental 2 layer
Finger length (mm)	1.10	1.19 ± 0.01	1.10	1.21 ± 0.01
Finger width (μm)	50.0	57 ± 5	50.0	61 ± 4
Gap between fingers (μm)	50.0	45 ± 3	50.0	42 ± 3
Thickness (nm)	430	380 ± 50	860	847 ± 50
Roughness, R_q (nm)	-	340 ± 60	-	266 ± 50
Roughness, R_a (nm)	-	250 ± 50	-	210 ± 40

R_q is the root mean square (RMS) and R_a the arithmetic average of the absolute values, both of the surface roughness heights. In general, real dimensions are alike to modelled ones, being the biggest discrepancy in the

finger width. The same dimensional parameter showed the biggest variation between experimental and modelled values in IDE capacitors (see Table 4). These concordant results can be explained by the spread of the ink drop when it is deposited on the substrate (J.F. Salmeron 2013).
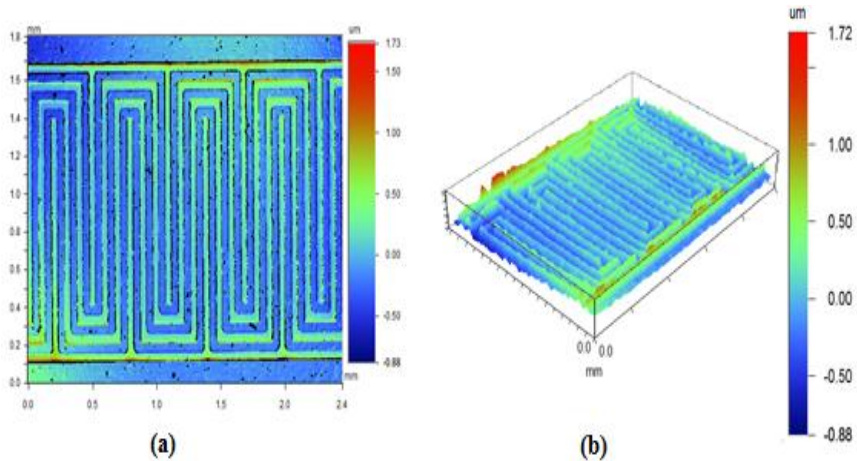
Figure 29. Profiling captions of SRE (a) 2D, (b) 3D.

The measured and the simulated values of the capacitances of the replicated serpentine capacitors are in very good agreement, as shown in Table 7. The measurements were carried out in room conditions (30% RH and 25 ℃) at 1 kHz to avoid polarization effects. During these tests, a preliminary manufacturing yield of 80% was found, that is, two samples out of ten were broken. In contrast to IDE capacitor, when there is any printing error, the serpentine structure is totally broken due to the higher complexity of this structure. This complexity also results in a lower fabrication yield than the IDE design (90%).

As predicted by the numerical simulation, capacitors with two printed layers presented a capacitance only a 0.029 pF bigger than a one layer capacitor, confirming the negligible effect of the electrode thickness on this electrical magnitude. A reduction in the standard deviation of two printed layers is observed due to fact that the second layer provides more regular geometries.

Table 8. Comparison of numerical and experimental capacitances of IDE and SRE capacitors.

	Numerical IDE Capacitance (pF) (COMSOL) [1]	Exp. IDE Capacitance (pF) [2]	Numerical SRE Capacitance (pF) (COMSOL) [1]	Exp. SRE Capacitance (pF) [2]
1 layer	1.973	2.053 ± 0.002	2.256	2.877 ± 0.003
2 layers	1.982	2.0890 ± 0.0006	2.265	2.906 ± 0.0007

[1] **Simulated value at 30% RH.** [2] **Measured value at room conditions at 1 kHz.**

The measured values are about 20% higher than the simulated ones in SRE capacitors. This discrepancy was found in the IDE characterization, but only of 5%. These differences arose because the real dimensions of the sensor are not exactly the same as the simulated ones. This mismatch is higher in SRE than the found in IDE because the serpentine design presents more contact area than the IDE. Then, any variation from the desired dimensions causes a higher deviation from the expected capacitance. As explained by Derbi et al. (Derby 2010), printing electronics techniques present undesirable effects resulting in an inaccuracy on the printed structure, such as wider fingers and narrower inter-spacing, as shown in Table 8.

As these sensors are substantially small, any dimensional variation can affect the expected results. Actually, we simulated both structures tuning the geometry to the found mean dimensions, and the difference between real and simulated capacitance was drastically reduced (less than 5% in SRE and less than 3% in IDE). These results also support the validity of our numerical simulations for this kind of structures and the extrapolation of the electrode thickness procedure to reduce the computation time.

2.3.3 Results as humidity sensor and discussion

In this section, the capacitance response to the relative humidity is characterized taking into account frequency and temperature dependences. Next, the aging effect and dynamic response are shown. All these characterization data are compared with the analogues of the IDE structure presented in the previous section.

For five serpentine capacitors with one printed layer, the capacitance has been measured from 100 kHz to 10 MHz as a function of the relative humidity and temperature. All the experiments have been carried out increasing and decreasing the relative humidity at a fixed temperature for obtaining the sensor hysteresis in RH and vice versa for temperature. Figure 30 and Figure 31 shows the measured capacitance of the sensor at different values of RH at 40ºC. As it can be seen, the response with the frequency is very similar for each of the tested RH. As happened in the IDE response, the displacement between curves due to RH variations is constant up to 70%. The distance between consecutive lines slightly increases for RH values higher than 70%; this behaviour can be justified by the condensation of water on the sensor surface at high values of RH.
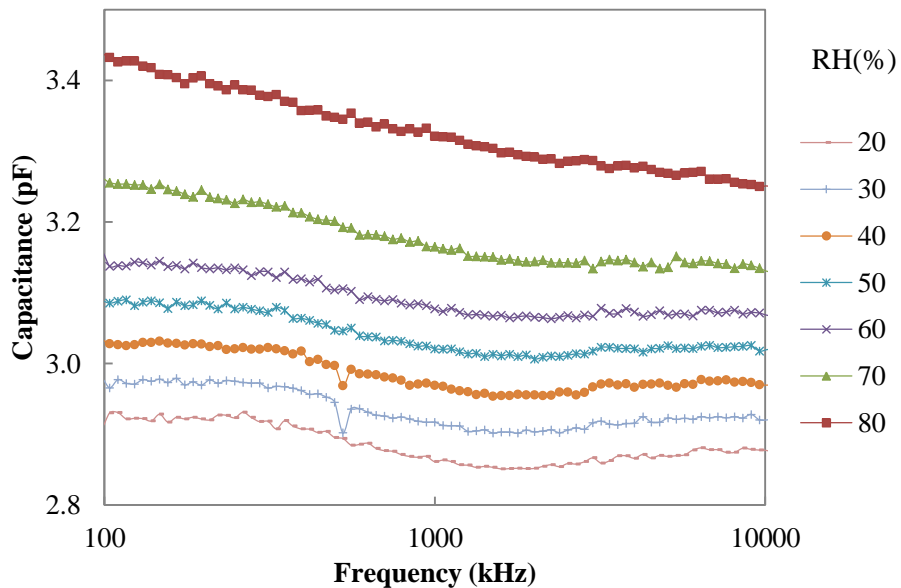
Figure 30. Experimental capacitance increasing RH as a function of frequency of SRE capacitors at 40ºC.
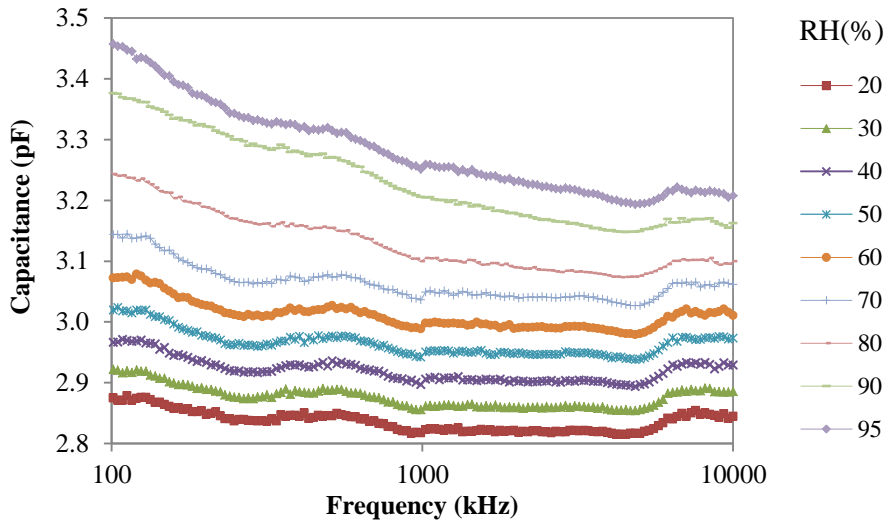
Figure 31. Experimental capacitance increasing RH as a function of frequency of SRE capacitors at 30ºC.

As indicated, one of most important interfering factor in the response of this kind of humidity capacitive sensors is the temperature. Figure 32 displays the measured capacitance as a function of RH for several temperatures at 1 MHz.

Figure 32. Experimental capacitance for several temperatures of SRE capacitors as a function of relative humidity at 1 MHz.

As happened in the IDE characterization, there is an overlap between these curves up to 40 °C, with the calibration curve that best fits these data given by Equation (18).

$$C(pF) = 0.0052RH(\%) + 2.6917, R^2 = 0.9923 \qquad (18)$$

To obtain a better insight of the whole sensor response, we have defined the partial sensitivities of the capacitance with the relative humidity, $S_{RH}(f)$, and the temperature, $S_T(f)$ as a function of the measurement frequency, f, as shown in (14) and (15).
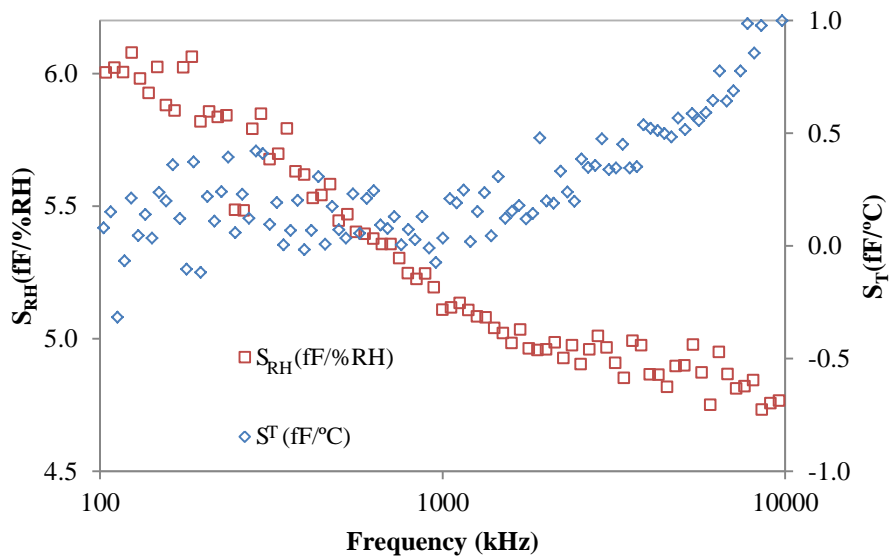
Figure 33. Experimental relative humidity and temperature sensitivities of SRE capacitors as a function of frequency.

With respect to the humidity sensitivity, it decreases from almost (6.2 ± 0.3) fF/%RH and tends to (4.7 ± 0.3) fF/%RH at the highest analysed frequencies (see Figure 33). Looking at Figure 30, the distance between consecutive lines is higher at lower frequencies and is tending to a constant value at higher frequencies. In our previous work for IDE sensors, we found a sensitivity of (4.5 ± 0.2) fF/%RH at 100 kHz and (4.2 ± 0.2) fF/%RH at 1 MHz, whereas the sensitivity of the serpentine is (6.1 ± 0.3) fF/%RH at 100 kHz and (5.2 ± 0.3) fF/%RH at 1 MHz. This result means a sensitivity enhancement of 1.4 times at 100 kHz and 1.2 times at 1 MHz. This range of sensitivities, 5100 ppm/%RH, is a typical value in comparable previous

works (Oprea et al. 2008, Altenberend et al. 2012, Molina-Lopez et al. 2012) but it has been obtained here with a printed sensor by only using the substrate as sensing material. Moreover, we have observed a very low thermal drift, tending to zero below 2 MHz in contrast to the IDE temperature behaviour (Figure 19). Therefore, measuring the capacitance between 100 kHz and 2 MHz a virtually temperature independent humidity sensor is achieved.

Now, we present the calibration curves with the relative humidity and its hysteresis at 1 MHz and 40ºC to directly compare them to the IDE ones (Figure 34). Equations (19) and (20) show the obtained mean straight lines after a linear regression of curves shown in Figure 34:

$$C(pF) = 0.0053 \cdot RH(\%) + 2.690. \ \mathrm{R}^2 = 0.9885. \ Increasing \ RH \qquad (19)$$

$$C(pF) = 0.0055 \cdot RH(\%) + 2.700. \ \mathrm{R}^2 = 0.9833. \ Decreasing \ RH \qquad (20)$$

The maximum relative error between Equations (19) and (20) and experimental data is less than 1.5% in all cases. The maximum shift between curves obtained by increasing RH (represented as "UP" in Figure 34) and those obtained by decreasing RH (represented as "DOWN" in Figure 34) is less than 10 fF in the whole range of RH. This value is comparable with the hysteresis found in the IDE capacitors.

Figure 34. Capacitance vs. Relative humidity of SRE capacitors at 1 MHz at 40ºC.

The dynamic response of the sensor presents a high stability along different measurement cycles and over time. Defining the response time as t = τ, it would correspond to the 63% of the maximum value of capacitance (reached at equilibrium) for every increasing step of RH. This time is equal to 350 ± 3 s. In regard to the response time for desorption, τ′, it can be defined as the time associated to the 37% of the maximum value of capacitance for every decreasing step of RH; this value is 365 ± 4 s. These times are virtually the same as those obtained with the IDE sensor. The response time is directly related to the square value of the thickness of the sensitive layer (Igreja and Dias 2006). Therefore, this time can be reduced by using a thinner substrate. This improvement in the time response was shown by Harrey et al. (Harrey et al. 2002) by using sensitive layers with different thicknesses. The times achieved varied from 10.5 min to 5 min for Kapton HN decreasing the thickness of the film.
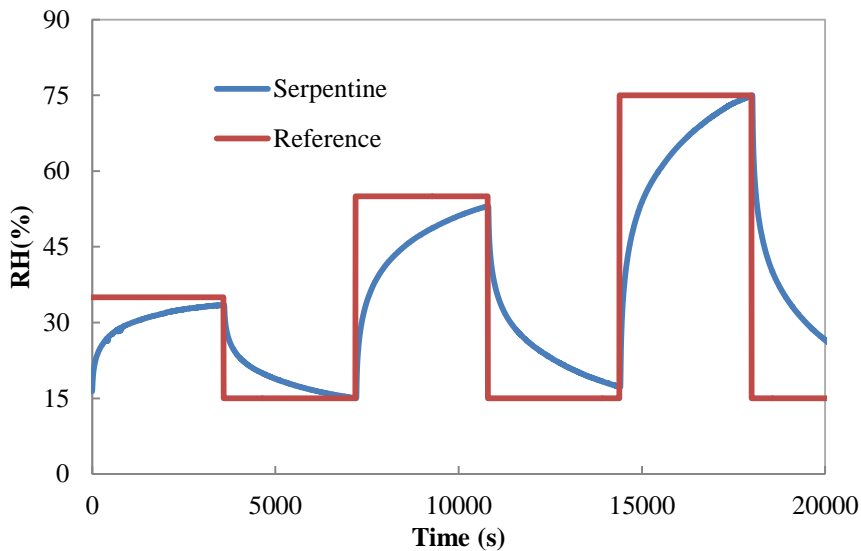
Figure 35. SRE time response.

To test the sensor time stability, the samples have been measured at ambient conditions once a week for more than 6 months and the variation between data is less than 10 fF. To have a better insight of the aging drift, we have performed a stability test 5 months after their fabrication. The humidity

sensor has been measured for 10 days at fixed relative humidity (30%) and controlled temperature (30 °C) every 6 hours. As in the case of IDE sensor, the error associated to the standard deviation shown in this test is less than 3% RH. This value is within the humidity deviation in time of the used climatic chamber.

2.4 Spiral Electrode Structure

Another studied structure has been the spiral electrodes. This structure has been previously reported by (Boltshauser et al. 1993, Wang et al. 1997). The advantage of this kind of structures is the fact that it can be fabricated on a substrate by deposition of a layer without including any step of micromaching. That allows the compatibility with any kind of technology.

Although they can be manufactured as suspended electrodes, the main application of them is as static electrodes where the change in the capacitance is induced by a change in a layer below or above these electrodes. In this case, the electrodes are placed as a coil inductor. The aim of this layout is to study its performance in order to try to improve the contact area between them and, therefore, a higher sensitivity will be obtained.

In this section, we will show the design, fabrication and characterization as humidity sensor of spiral capacitor following the same structure presented for IDE and SRE capacitors.

2.4.1 Design and simulation results

This sensor is based on coil electrodes, that is to say, two concentric squared coil electrodes as shown in Figure 36.
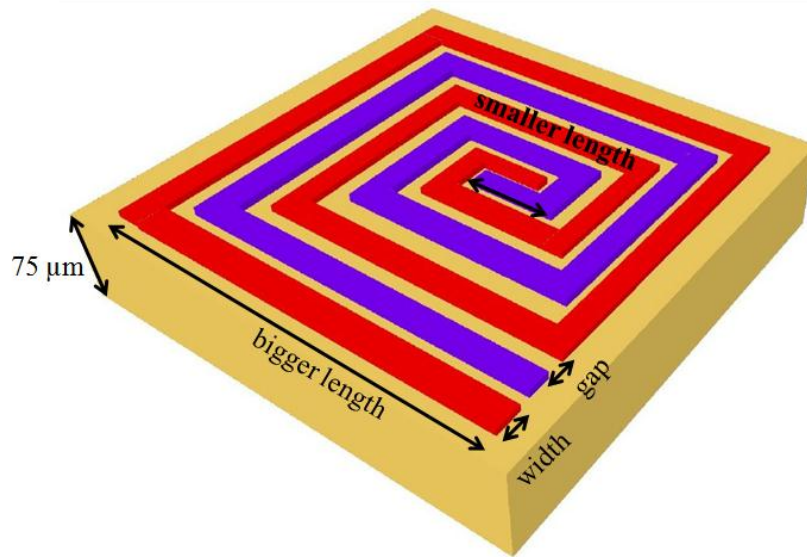
Figure 36. Layout of the designed spiral sensor.

The optimization of the sensor dimensions may potentially introduce more sensors into the devices. For this purpose, as we did with the IDE and SRE structures we used COMSOL Multiphysics 4.2a (COMSOL, Inc. USA) to optimize the design.
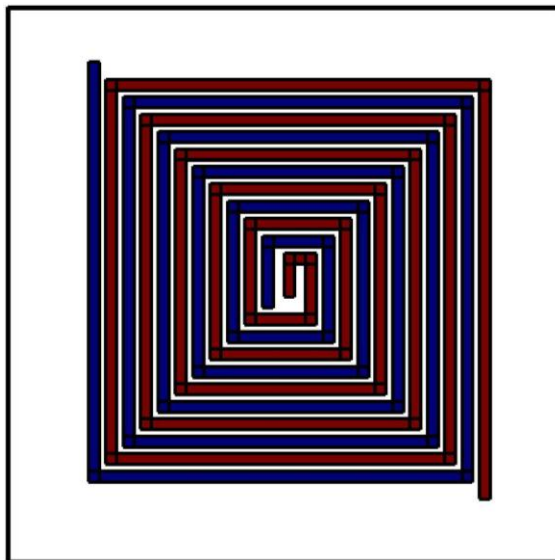
Figure 37. Schematics of the spiral electrodes.

Several parametric analyses were solved varying the fundamental geometrical parameters of the spiral electrode such as the number of fingers, the gap width between two fingers and their dimensions (width, length and thickness of each finger). As we did in the design of IDE and SRE sensors, we fixed the finger width to the minimum diameter landed drop (in our case 50 µm) and the gap between fingers also to 50 µm. This gap could be reduced below the drop diameter to increase the capacitance value but this reduction will lead to a strong possibility of short-circuit between electrodes due to printing errors. The parametrical simulations showed that the thickness of the fingers hardly affects the capacitance value in this structure. As shown below, their thicknesses are under 1 µm in both cases which implies extremely long simulation times because of meshing issues. Due to this fact, we set the thickness of the spiral electrodes to 5 µm for all the simulations to drastically reduce computational time. Then, we extrapolated the value of the capacitance for the chosen thickness (Figure 38) where the slope of curve is 0.0098 pF/ µm. This dependence is lower than in SRE and IDE; this may be caused by the fact that the screening in spiral electrodes is higher than in the other two electrode configurations.
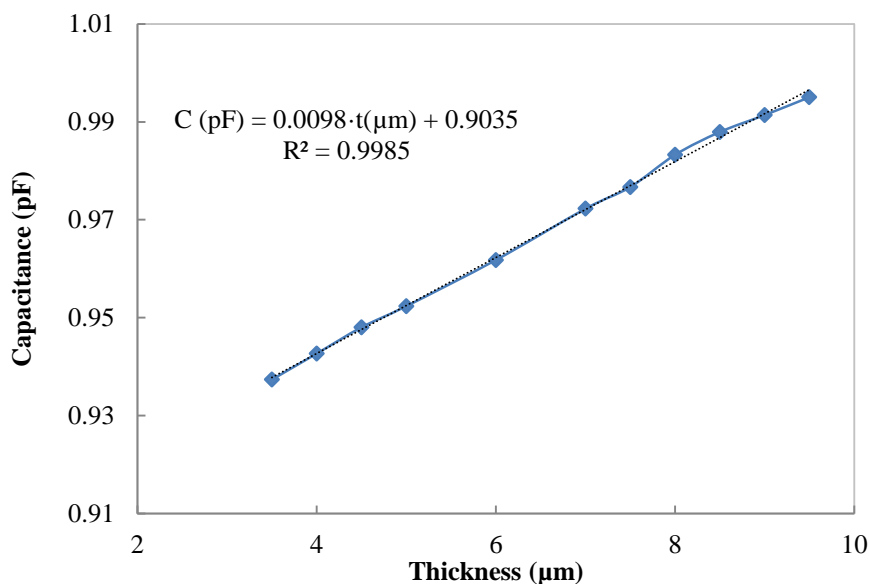
Figure 38. Numerical capacitance vs. Thickness of electrodes.

According to previous considerations, we manufactured the sensor following the specifications from Table 9 for a targeted nominal capacitance (for one printed layer) of 1 pF because they presented the best compromise between capacitance and area. Finally, the capacitance predicted by COMSOL Multiphysics 4.2a for this structure was 0.91 pF with only one printed layer in a dry atmosphere.

Table 9. Physical dimensions of the capacitive spiral structure.

Parameter	Value	Description
Length smallest	0.20 mm	Length of the smallest finger (y-axis)
Length biggest	2.35 mm	Length of the biggest finger (y-axis)
Width	50 μm	Width of each finger (x-axis)
Thickness	420 nm	Thickness of electrodes (1 layers) (z-axis)
Number	6	Total number of turns of each electrode
Interspacing	50 μm	Distance between consecutive fingers (y-axis)

The designed area was 5.52 mm^2 (L = 2.35 mm x W = 2.35 mm) composed of 6 turns for each electrode with 50 μm width and inter-spacing (see Figure 36). This structure area is virtually half of the others previously studied and it also results in half capacitance value.

Looking at the electrical displacement vector, D, (Figure 39), the highest values are concentrated on the edges of the coil electrodes, as happened in SRE displacement vector (Figure 27). The electric displacement field changes the charge stored between the sensor electrodes, and thus alters the inter-electrode capacitance. This can be used to infer the properties of the material under test, in this case, the humidity sensitive substrate. This result agrees with the study of the capacitance sensitivity as a function of the structure shape by Hu et al. (Hu and Yang 2010) where spiral electrodes showed a higher value.
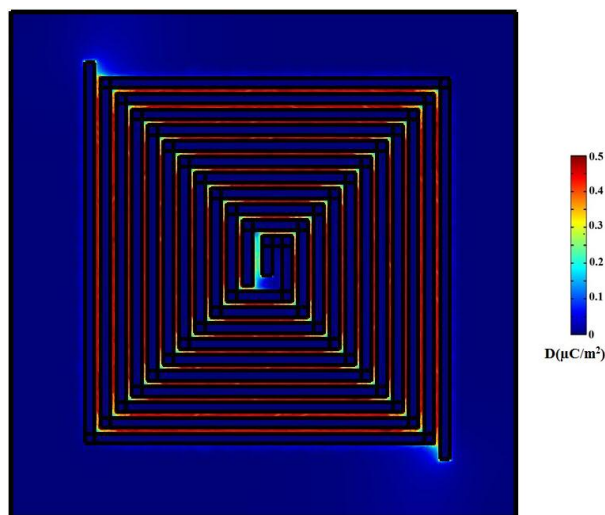
Figure 39. Displacement vector of Spiral electrodes.

2.4.2 Fabrication process and characterization results

The DMP-2831™ Dimatix printer (Fujifilm Dimatix Inc, Santa Clara, USA) was also used for inkjet printing of the electrodes. The ink and substrate materials and the fabrication process were the same than for the IDE and SRE structures, described in sections 2.2.2 and 2.3.2.

A total of twenty capacitors with one printed layer were fabricated in order to test the reproducibility of the process and to carry out the comparative study. A targeted nominal capacitance of at least 1 pF was chosen as this value presented a suitable compromise between capacitance and area. The area was 5.52 mm^2 (L = 2.35 mm x W = 2.35 mm) composed of 6 turns each electrode with 50 µm width and gap as minimum secure dimensions of our fabrication procedure (see Figure 23). In order to easily test the capacitors, we added two long terminals to couple the sensors to the measurement set-up. According to the model presented in the previous section (see equation (11)), the calculated amount of used ink were 10.96 nl. With these printing and curing conditions, the average resistivity of the conductive electrodes were 23 ± 2 µΩ·cm for all electrodes and number of printed layers (J.F. Salmeron 2013).

The physical characterization of the roughness of printed patterns and the thickness of the patterns has been carried out using a Dektak XT™ Stimulus

Surface Profiling System (Bruker Corporation, Conventry, UK). The electrical characterization has been carried out by measuring their capacitances and dissipation factors, using the four-wire measurement technique with a Impedance Analyser 4294A and an impedance probe kit (4294A1) (Agilent Tech., Santa Clara, CA, USA). The excitation voltage applied in all measurements was $V_{DC} = 0$ and $V_{AC} = 500$ mV. The frequency sweep of analysis was from 100 kHz to 10 MHz. As we already did for the IDE and SRE sensors, one of the end sides of the backbones has been enlarged to facilitate its connection and a SMA (SubMiniature version A) male connector has been glued to these ends points using silver-filled epoxy EPO-TEK® H20E (Epoxy Technology, Inc., Billerica, USA) (see Figure 28). A complete compensation method has been implemented to eliminate the contribution of parasitic capacitances (see section 2.1.4).

The characterization was carried out following the same procedure and using the same instrumentation as shown in sections 2.2.3 and 2.3.2. The stationary humidity and temperature responses of these sensors have been measured in a climatic chamber VCL 4006 (Vötsch Industrietechnik GmbH, Reiskirchen, Germany).

2.35 mm

Figure 40. Image of the inkjetted capacitor with the connector.

To experimentally check the simulation results, thirty replicas of spiral structures with identical areas of 5.52 mm² (L = 2.35 mm x W = 2.35 mm) were printed on Kapton HN and physically characterized (Figure 41). According to a previously developed physical model of layer thickness by inkjet printing (see equation (11)), the calculated thickness is 430 nm,

respectively. The real dimensions of the structures are presented in Table 10, showing the differences between measured and predicted dimensions for sensors with one printed layer. Uncertainties were calculated as one standard deviation of the experimental data.

Table 10. Comparison between numerical and experimental physical dimensions of the spiral sensor.

Parameter	Model	Experimental
Length smallest	0.20 mm	0.19 ± 0.02 mm
Length biggest	2.35 mm	2.21 ± 0.03 mm
Width	50 µm	57 ± 3 µm
Thickness	430 nm	520 ± 57 nm
Interspacing	50 µm	52 ± 2 µm

In general, real dimensions are alike to modelled ones, being the biggest discrepancy in the turn thickness. This result can be explained due to printed silver obtained being porous and the model applied to estimate the thickness considered a perfect flat deposition. As it can be seen in Figure 41, this substrate presented a higher roughness.
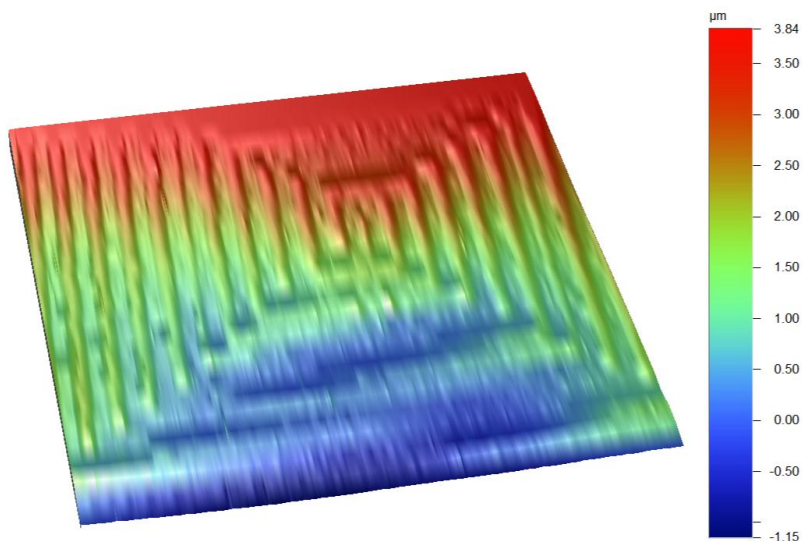

Figure 41. Profiling 3D caption of spiral sensor.

2.4.3 Results as humidity sensor and discussion

In this section, the capacitance response to the relative humidity is characterized taking into account frequency and temperature dependences. All these characterization data are compared with the analogues of the IDE and SRE structures presented in sections 2.2 and 2.3.

A. Humidity response

For five spiral capacitors with one printed layer, the capacitance has been measured from 100 kHz to 10 MHz as a function of the relative humidity and temperature. All the experiments have been carried out increasing and decreasing the relative humidity at a fixed temperature for obtaining the sensor hysteresis in RH and vice versa for temperature. Figure 42 shows the measured capacitance of the sensor at different values of RH at 40ºC. As it can be seen, the response with the frequency is very similar for each of the tested RH. As happened in the IDE and SRE response, the displacement between curves due to RH variations is constant up to 70%. The distance between consecutive lines slightly increases for RH values higher than 70%; this behaviour can be justified by the condensation of water on the sensor surface at high values of RH.
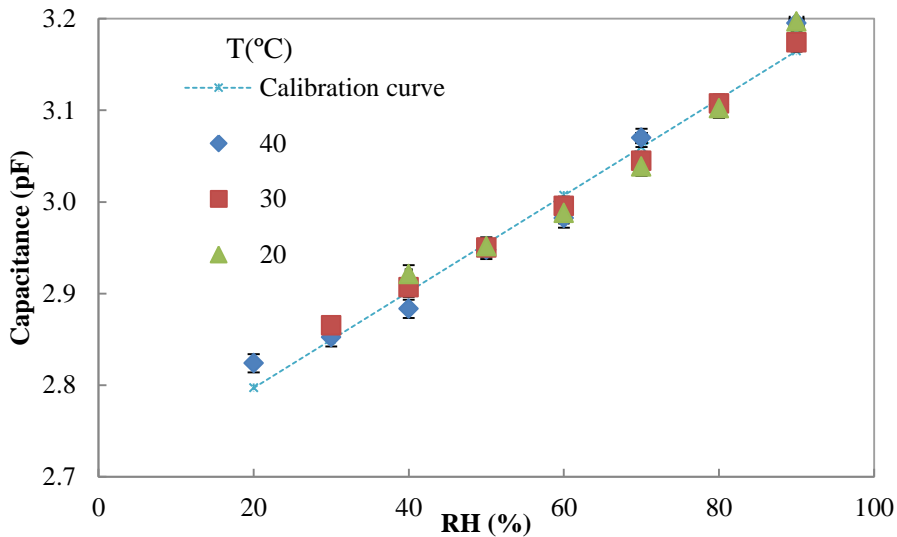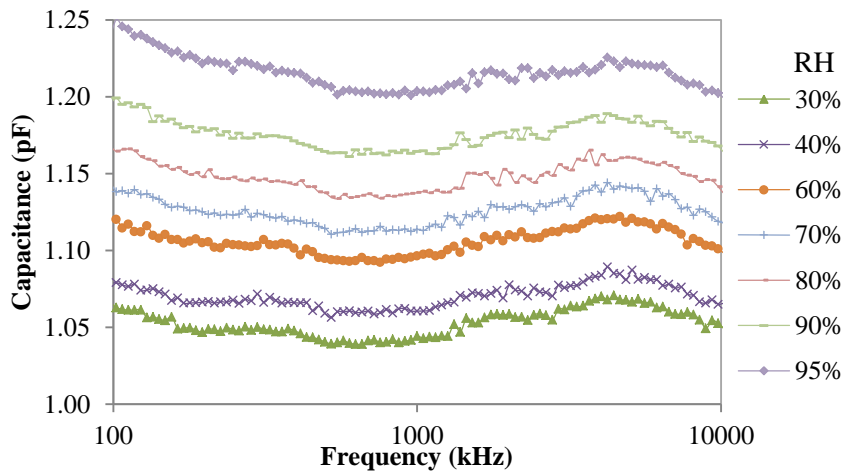

Figure 42. Experimental capacitance increasing RH as a function of frequency of spiral capacitors at 40ºC.

As indicated, one of most important interfering factor in the response of this kind of humidity capacitive sensors is the temperature. Figure 43 shows the experimental capacitance at constant humidity (55%) for different values of temperature as a function of frequency. As happened in IDE and SRE sensors, the thermal effect is very low, especially below 45 ºC and 3 MHz.
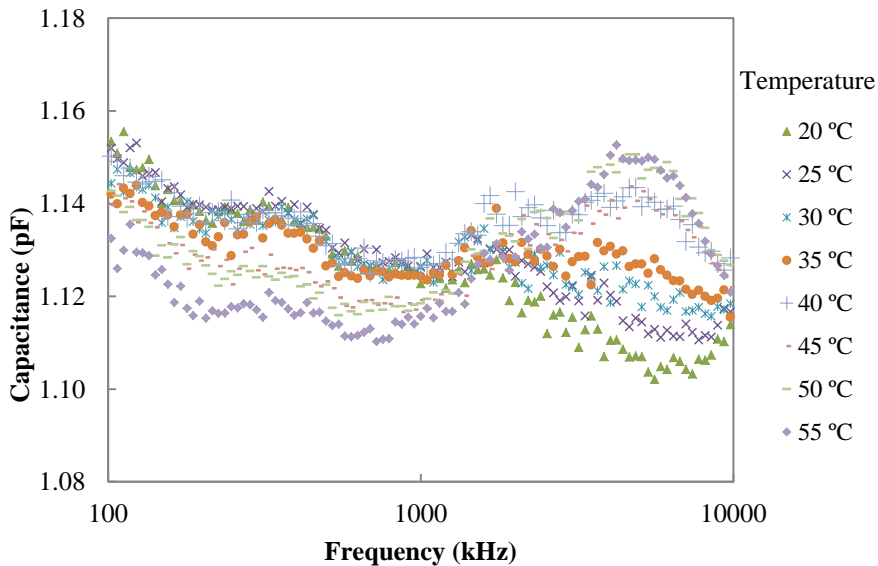
Figure 43. Experimental capacitance increasing T as a function of frequency of spiral capacitors at 55% RH.

With respect to the humidity sensitivity, it decreases from about 2.66 fF/%RH to 2.08 fF/%RH at the highest analysed frequencies (see Figure 45). Let's remember that the sensitivity for IDE decreases from around 4.5 fF/%RH to 4.2 fF/%RH whereas the sensitivity for SRE capacitors decreases from 6.2 fF/%RH to 4.7 fF/%RH. We cannot directly compare these values because the spiral electrodes resulted in half area, then we are going to consider the effect of two spiral capacitor connected in parallel (Figure 44). In this case, the total area would be 11.05 mm^2 and the modelled capacitance in dry atmosphere 1.86 pF. These values are comparable with the areas and capacitances of IDE and SRE sensors. Taking into account that the equivalent capacitance of two capacitors connected in parallel is equal to the sum of both values, then we can assume that the equivalent sensitivity is going to be also doubled.
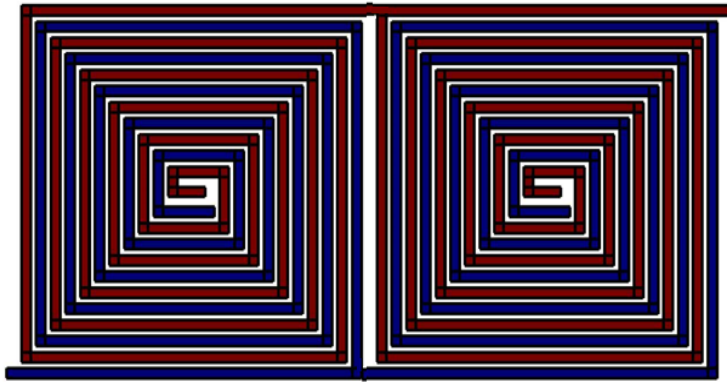
Figure 44. Double spiral capacitor connected in parallel.

Looking at Figure 42, the distance between consecutive lines is higher at lower frequencies and is tending to a constant value at higher frequencies. In previous sections, we found sensitivities of 4.2 fF/%RH for IDE and 5.2 fF/%RH for SRE at 1 MHz, the sensitivity for the parallel association of spiral electrodes is 4.62 fF/%RH at 1 MHz (Figure 45). This result suggests that the highest sensitivity is found in SRE capacitors, followed by spiral electrodes and IDE sensor shows the lowest sensitivity value.
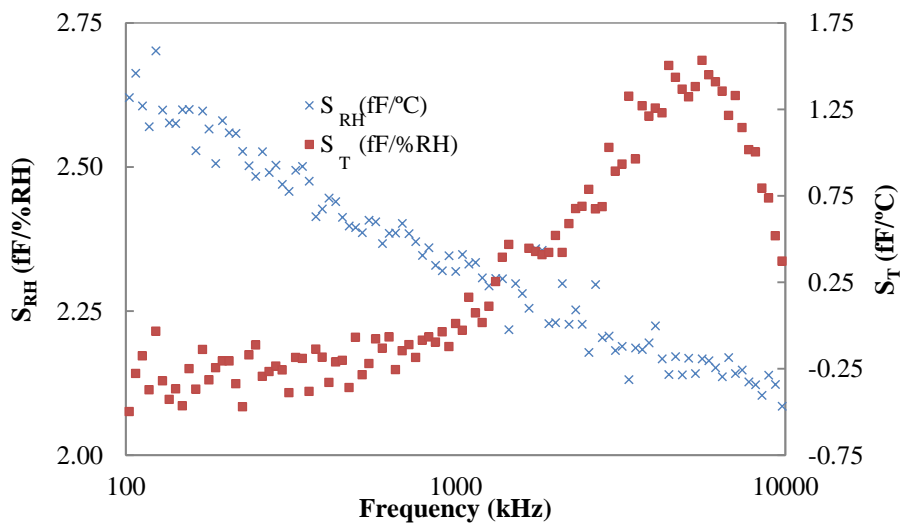
Figure 45. Experimental relative humidity and temperature sensitivities of spiral capacitors as a function of frequency.

Moreover, we have observed a very low thermal drift, tending to zero below 2 MHz whereas at higher frequencies the thermal drift is increased (similar to the SRE temperature behaviour, Figure 33). Therefore, measuring the capacitance between 100 kHz and 2 MHz, a virtually temperature independent humidity sensor is achieved.

For this design, we have not studied its dynamic response and either its time stability because the used material are the same as IDE and SRE capacitors and, therefore, these values should be virtually the same. As we have previously studied, the response time is directly related to the square value of the thickness of the sensitive layer (Igreja and Dias 2006); as we have used the same substrate, the time response should be around 350 s. The time stability is directly associated with the materials. Then, as all the material are exactly the same, we can assume that this sensor is going to have a long lifetime.

B. Calibration curves

Now, we present the calibration curves with the relative humidity and its hysteresis at 1 MHz and 40 ºC. Equations (21) and (22) show the obtained mean straight lines after a linear regression of curves shown in Figure 46:

$$C(pF) = 0.0020 \cdot RH(\%) + 0.9805. \ R^2 = \ 0.9922. \ Increasing \ RH \qquad (21)$$

$$C(pF) = 0.0021 \cdot RH(\%) + 1.0226 . \ R^2 = \ 0.9982. \ Decreasing \ RH \qquad (22)$$

The maximum relative error between Equations (21) and (22) and experimental data is less than 2% in all cases. The maximum shift between curves obtained by increasing RH (represented as "UP" in Figure 46) and those obtained by decreasing RH (represented as "DOWN" in Figure 46) is less than 25 fF in the whole range of RH. This value is comparable with the hysteresis found in the IDE and SRE capacitors.
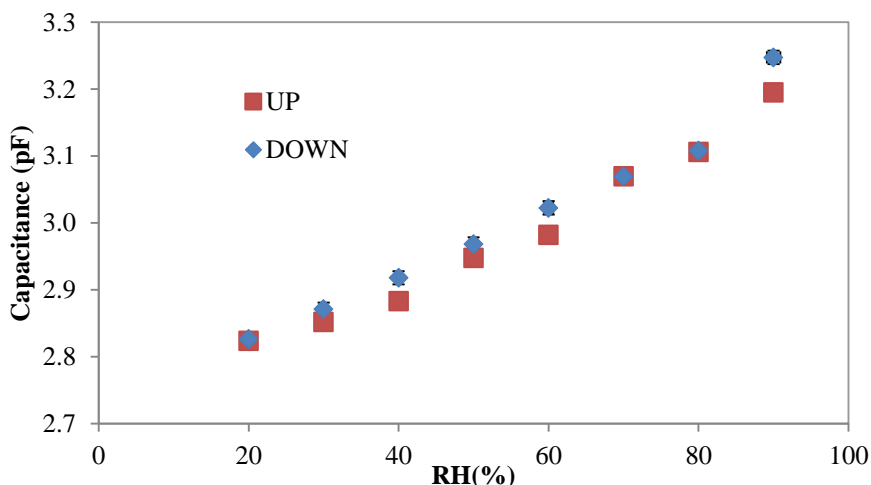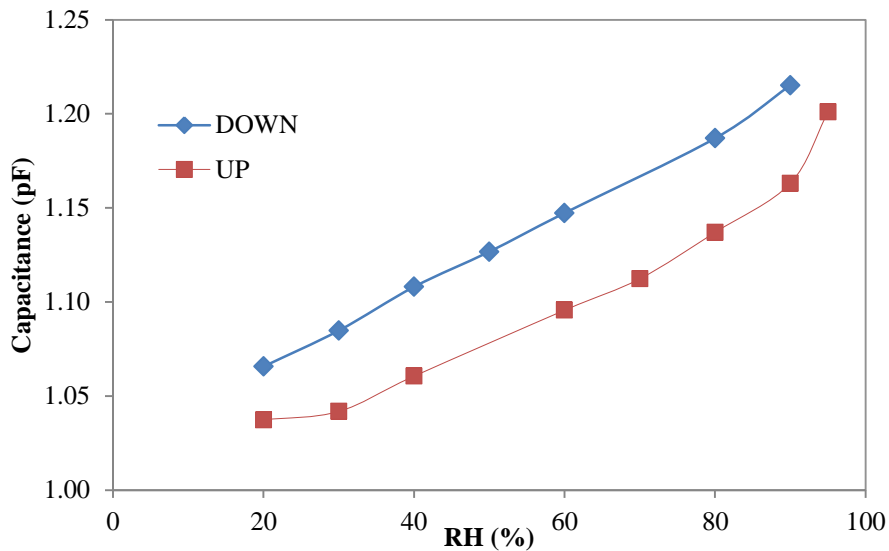
Figure 46. Capacitance vs. Relative humidity of spiral capacitors at 1 MHz at 40ºC.

2.5 Asymmetric enhanced surface interdigitated electrode capacitor with two electrodes out-of-plane

The last structure analysed in this chapter is a capacitor based on the IDE but with a multilayer structure. Obviously, the complexity of the fabrication process is increased but the enhancement of the sensitivity justifies this drawback. The sensitive element is a deposited polymer on the electrodes and around them. These interdigitated electrodes enhance the capacitance due to its asymmetrical construction and the location out-of plane of the electrodes.

Other strategies have been followed to improve the sensitivity of interdigitated electrodes (Molina-Lopez, Briand and de Rooij 2013a). Here, we are describing the design of this improved structure and some approaches to manufacture it. We will show the first results obtained.

2.5.1 Design

To better understand this capacitive sensor, we are going to summarize its main parts.

a. Bottom electrode. This electrode is composed by an interdigitated structure and a parallel plate (Figure 47).

b. Thin deposited polymer. A thin film of the sensitive polymer is deposited between the interdigitated electrodes. This layer is going to insulate the back and the top electrodes (Figure 48).

c. Top electrode. The other electrode is interdigitated-shape placed on top of the thin polymer without contact with the bottom electrode (Figure 49).

d. Thick deposited polymer. All the surroundings around both interdigitated electrodes are filled with the sensitive polymer. Therefore, the total contact area is increased since the sensitive compound is around the electrodes. Furthermore, the top electrode is not only laterally but also horizontally enclosed by the back electrode (Figure 50).
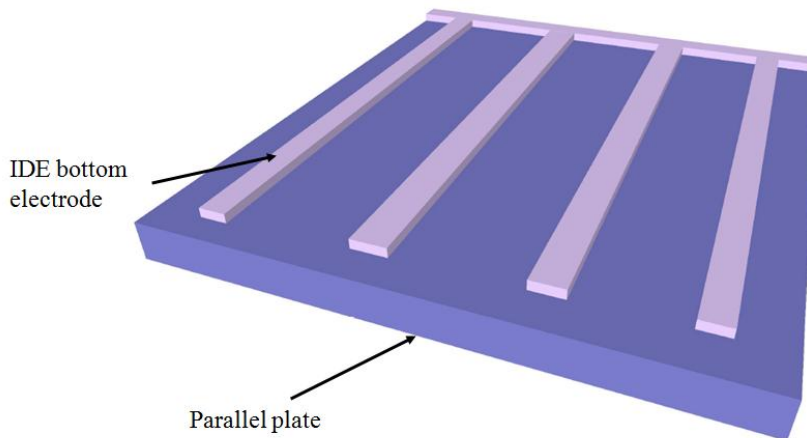
Figure 47. Bottom electrode composed by parallel plate and interdigitated electrode. The substrate is not represented.
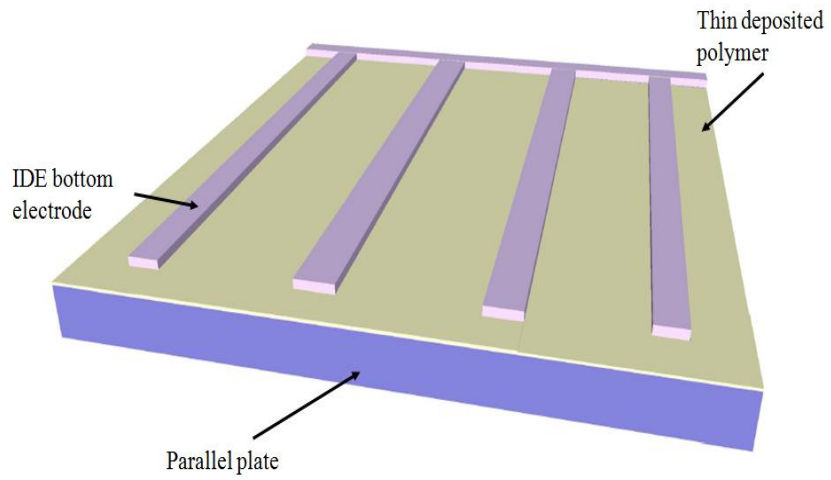
Figure 48. Bottom electrode with thin polymer deposited.
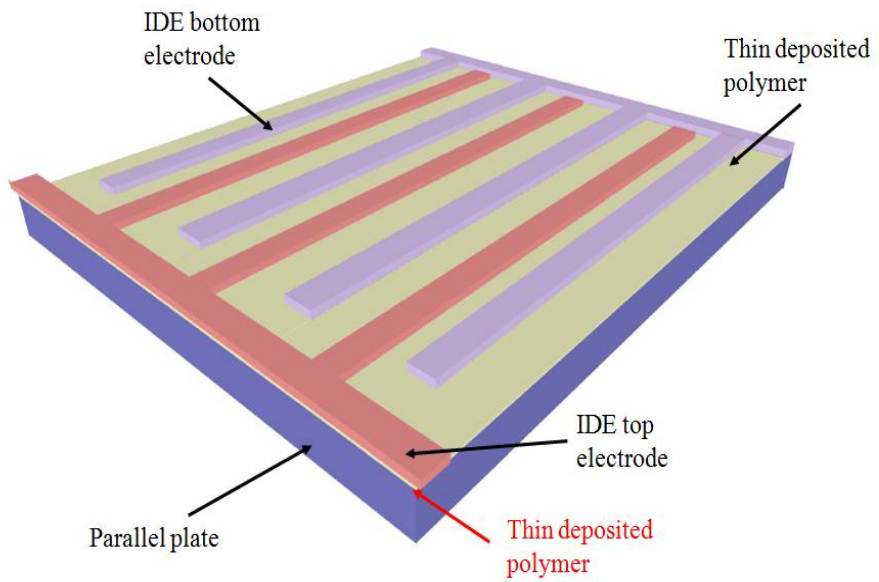
Figure 49. Top interdigitated electrode is defined on top of the thin polymer deposited.
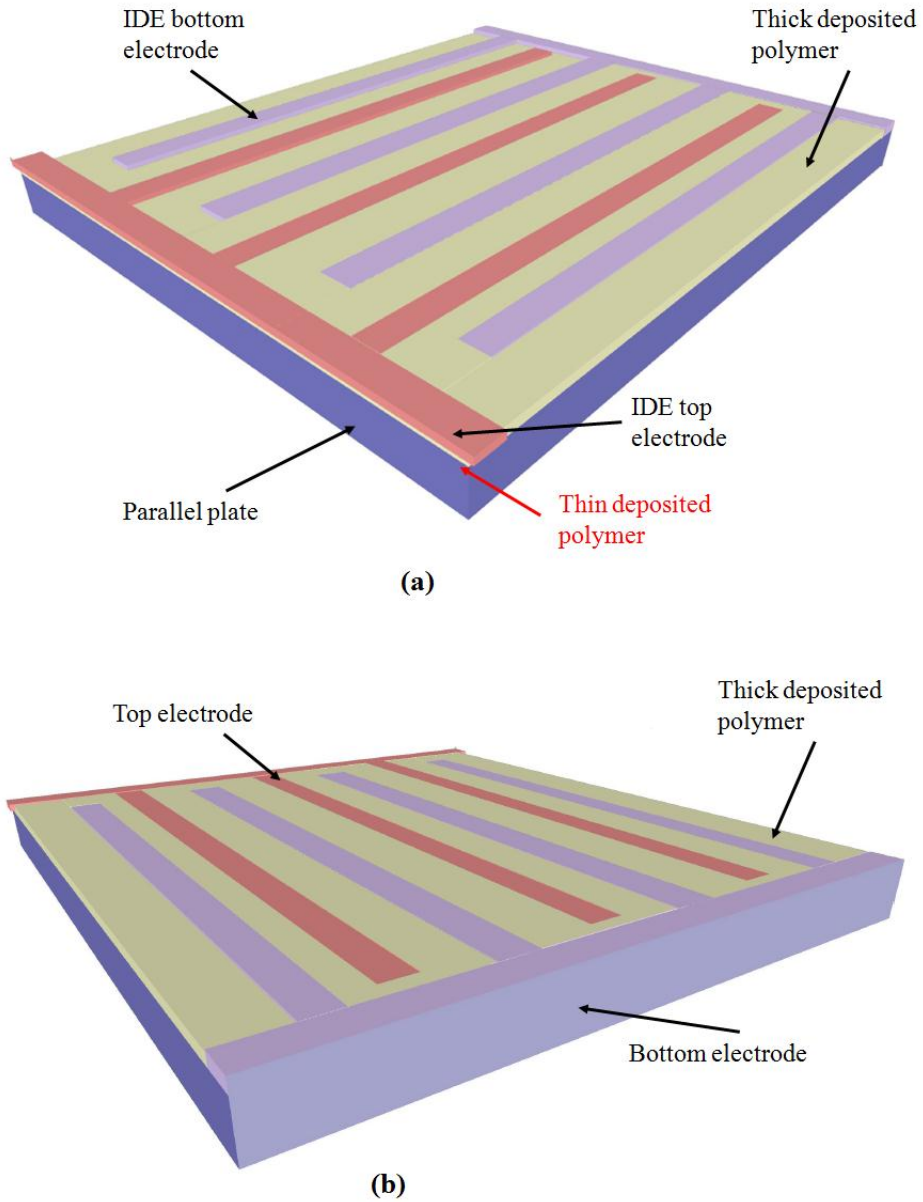
Figure 50. Final capacitive structure after depositing the thick layer of sensitive polymer. (a) Lateral view, where the isolation between top and bottom electrode through the thin polymer layer (b) Lateral view where the whole bottom electrode is appreciated.

Table 11. Dimensions of the sandwich sensor.

Parameter	Value	Description
Length	1.0 mm	Finger length
Width	50 μm	Finger width
yGap	50 μm	Gap between consecutive finger in x-axis
xGap	5 μm	Gap between electrodes in y-axis
Thickness	5 μm	Electrode thickness
Number	10	Number of fingers of each electrode
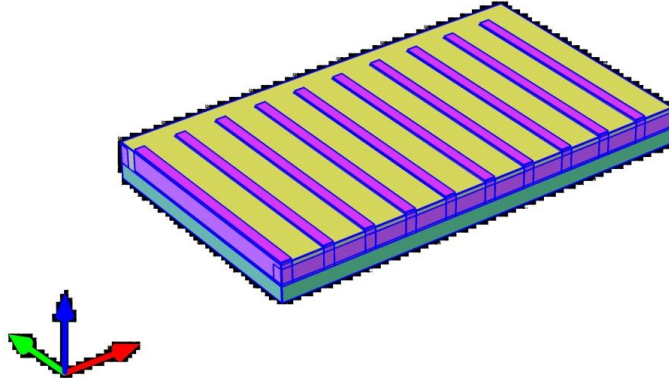
Figure 51. 3D Model of sandwich capacitive sensor. The polymer is represented in yellow. The electrodes are in purple and the substrate in green.

The capacitance obtained with parameters shown in Table 11 is 3.45 pF with a total area of 2.2 mm^2. During the simulation process, we found a high dependence between the finger thickness and the capacitance. This result is easily comprehensible because this structure contains a sensitive polymer around all electrodes axes and therefore, the thicker the electrodes defined, the greater the capacitance obtained. For example, the capacitance obtained with 20 μm finger thickness is 12 pF.

2.5.2 Fabrication process and characterization results

The interdigitated electrodes and polymer have been manufactured with a Serfix III screen printing machine (Seglevint SL, Barcelona, Spain). The screen used to manufacture the patterns had a mesh density of 120 Nylon thread per centimetre (T/cm) in an aluminium rectangular structure of 50 cm width and 35 cm length to fabricate them with only a single-layer screen printed. The selected conductive material was a conductive silver ink CRSN

2569 (Sun Chemical Corporation, Parsippany, USA). For the preparation of the humidity sensitive layer, cellulose acetate butyrate (CAB) 13.5 wt% acetyl and 37% butyryl content from Sigma–Aldrich (Madrid, Spain) was dissolved over several days in hexyl acetate 99% from Sigma–Aldrich (Madrid, Spain). This polymer has been already used to developed printed humidity sensors (Molina-Lopez et al. 2012).

The selected substrate to develop this structure also was the Kapton polyimide, with 75 µm thickness (Kapton® HN, Dupont[TM], Wilmington, DE, USA).

The physical characterization of the roughness of printed patterns and the thickness of the patterns has been carried out using a Dektak XT™ Stimulus Surface Profiling System (Bruker Corporation, Conventry, UK).

Several approaches can be followed to fabricate this device. First, we can choose a non-sensitive substrate not to interfere the data or a sensitive substrate to enhance the whole device sensitivity. Another possibility is to use a metallic substrate reducing the number of fabrication steps.

Regarding the definition of the top electrode, we can directly print the top electrode with the proper mask or transfer the electrodes which have been previously printed in another substrate. Another decision to take is the thickness of the thick polymer deposition; this layer can cover both electrodes, only the bottom electrode or both electrodes can be superficially uncovered.

Figure 52 presents the first experiment developed, where we printed a thin CAB layer on a polyimide substrate and after that a silver layer was printed on top of the CAB film. Figure 53 and Figure 54 show details of the different profiles. CAB thickness is about 0.52 µm whereas the average of silver thickness is 8.7 µm.
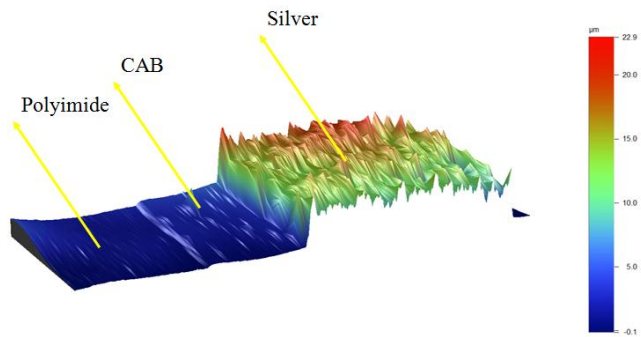
Figure 52. 3D profile of silver layer printed on CAB polymer deposited onto polyimide substrate.
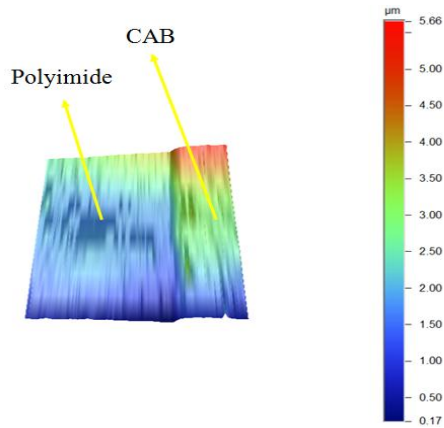
Figure 53. 3D profile of CAB polymer on polyimide substrate.
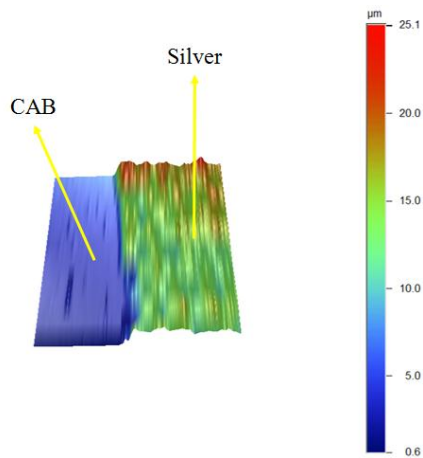
Figure 54. 3D profile of silver layer on CAB film.

2.6   Conclusions

In this chapter, we have designed, modelled, manufactured by printing techniques, and characterized small and low-cost humidity sensors that can be easily and quickly fabricated and integrated into RFID tags. The first three prototypes have been obtained by inkjet printing and the difference between them is the electrode shape. First an interdigitated sensor is presented, then a serpentine one and finally a sensor with spiral electrodes.

The sensing element of these sensors is the substrate whose electrical permittivity is directly related to the relative humidity in the environment. Furthermore, the fabrication process is reduced not only because no extra sensing layer is needed, but also because only one printed layer is required to define the capacitors. The materials used are Kapton HN sensing substrate and SunTronic U5603 ink in all sensors.

The interdigitated sensor only requires less than 12 mm^2 of substrate and about 23 nl silver ink for one printed layer. Experimental data are in good agreement with results extracted from COMSOL Multiphysics 4.2a, validating the extrapolation procedure for very thin printed layers. The proposed sensor shows a stable humidity response from 100 kHz to 10 MHz; its sensitivity is (4.5 ± 0.2) fF/%RH at 100 kHz and (4.2 ± 0.2) fF/%RH at 1 MHz. Furthermore, a very low thermal drift has been obtained in a wide frequency range. The capacitance shows a thermal coefficient of around (-0.2 ± 0.2) fF/ºC at 1 MHz whereas this coefficient has a value of (-0.4 ± 0.2) fF/ºC at a frequency of 100 kHz. The relative humidity sensitivity is more than 11 times greater than thermal drift at 100 kHz and 21 times at 1 MHz. This result means that the compensation of temperature can be avoided if the frequency of work is properly chosen. The time response of the sensor is about 6 min but this value could be improved by reducing the thickness of the substrate. Finally, the sensor response has hardly changed as a consequence of aging effect. This manufacturing process not only requires a small amount of materials but also a short time of fabrication with a high rate of success.

Regarding the serpentine structure, we have looked over its capabilities as capacitive sensor by the comparison with the well-known interdigitated electrode capacitor. Numerical simulations of the capacitance of both

structures have been carried out to calculate the differences between them due exclusively to their geometrical characteristics at constant area. In these conditions, we have shown the capacitance improvement for the serpentine capacitors which is enhanced with the number of fingers. This improvement has resulted in 14% with structures of 32 fingers and 21% for 180 fingers. The rest of dimensional parameters and substrate or top layer characteristics have not added any further difference between both structures. We have validated the numerical results by the experimental characterization of capacitive sensors made of serpentine and interdigitated electrodes. Humidity capacitive sensors have been manufactured, resulting in a fabrication yield of 80%. Experimental results verified the capacitive differences between both structures with the same area. We have found a sensitivity of (5.2 ± 0.2) fF/%RH for serpentine electrode capacitors, whereas for IDE the sensitivity was (4.2 ± 0.2) fF/%RH at 1 MHz with a total area of 11.65 mm^2 for both structures. Moreover, we have achieved a serpentine capacitive sensor for monitoring humidity with a temperature-independent behaviour at frequencies between 100 kHz and 2 MHz. Serpentine capacitors showed linear calibration curves and a hysteresis comparable with the interdigitated structure. Time constants of about 6 minutes were measured for transients of moisture absorption and desorption. As this novel serpentine electrode structure presents a bigger geometrical capacitance factor compared with the interdigitated capacitor, in our opinion, it will be a promising base structure for multiple applications in the field of signal transduction.

Concerning spiral electrodes, we have followed the same procedure as in case of interdigitated and serpentine electrodes. The area of this sensor was only 5.52 mm^2 with a capacitance value of about 1 pF at ambient conditions. We cannot directly compare these values because the spiral electrodes resulted in half area, then we have considered the effect of two spiral capacitors connected in parallel. In this case, the total area would be 11.05 mm^2 and the modelled capacitance in dry atmosphere 1.86 pF. These values are comparable with the areas and capacitances of IDE and SRE sensors.

Taking into account that the equivalent capacitance of two capacitors connected in parallel is equal to the sum of both values, then we can assume that the equivalent sensitivity value is going to be also the double. The sensitivity for the parallel association of spiral electrodes is 4.62 fF/%RH at 1

MHz. This result suggests that the highest sensitivity is found in SRE capacitors, followed by spiral electrodes and IDE sensor shows the lowest sensitivity value. We found similar temperature behaviour to serpentine electrodes. The thermal drift is very low, tending to be zero below 2 MHz whereas the thermal drift is increased at higher frequencies.

Table 12 summarized the main features of the three types of electrodes studied to facilitate the comparison.

Table 12. Comparison between the electrodes designs. For comparison reasons, spiral electrodes features correspond to a parallel association of two capacitors. *We expect similar values because the same material has been used.

Parameter	IDE capacitor	SRE capacitor	Spiral capacitor
Area (mm^2)	11.65	11.65	11.05
Simulated capacitance (pF)	1.973	2.256	1.86
Experimental capacitance (pF)	2.053 ± 0.002	2.877 ± 0.003	1.107 ± 0.002
Sensitive range 100 kHz – 1 MHz (fF/%RH)	4.5 – 4.2	6.2 - 4.7	6.2 - 4.7
Thermal drift range 100 kHz – 1 MHz (fF/ºC)	-0.2 – -0.4	0 - 1	0 – 1
Sensitivity at 1 MHz (fF%RH)	4.2 ± 0.2	5.2 ± 0.2	4.6 ± 0.4
Thermal drift at 1 MHz (fF%ºC)	-0.2 ± 0.2	~ 0	~ 0
Time response (s)	356 ± 3	350 ± 2	--*
Desorption time (s)	367 ± 4	365 ± 4	--*
Time stability after 5 months	< 3% RH	3% RH	--*

Finally, an asymmetric enhanced surface interdigitated electrodes capacitor with two electrodes out-of-plane was presented. The modelled capacitance was 3.45 pF with a total area of 2.2 mm^2.

This structure contains sensitive polymer around all electrodes axes and, therefore, there is dependence between electrodes thickness and the capacitance obtained. For example, the capacitance obtained with 20 µm finger thickness is 12 pF. Several approaches can be followed to fabricate this device. First, we can choose a non-sensitive substrate not to interfere the data or a sensitive substrate to enhance the whole device sensitivity. Another possibility is to use a metallic to substrate reducing the number of fabrication steps.

Regarding the definition of the top electrode, we can directly print the top electrode with the proper mask or transfer the electrodes that have been previously printed in another substrate. Another decision to take is the thickness of the thick polymer deposition; this layer can cover both electrodes, only the bottom electrode or both electrodes can be superficially uncovered.

3.   Printed resistive sensors

Another transduction effect is the change in the resistance that is related to the difficulty or ease of a specific material to the flow of current. Resistive sensors are among the most common in instrumentation. The simplest resistive sensor is the potentiometer. Other resistive sensors include strain gages and thermistors. Resistive sensors are often combined with Wheatstone bridges (Fraden 2010). The theoretical background for all these sensors is the theory of resistivity. The resistance can be altered either by geometric parameters (A, L) or material resistivity (ρ) in the resistive element, as shown in (23).

$$R = \rho\,\frac{L}{A} \qquad\qquad\qquad (\,23\,)$$

The resistivity is a measure of how strongly a material opposes the flow of electric current. A low resistivity indicates a material that readily allows the movement of electric charge. The resistance of a material depends on four factors:

·   Composition
·   Length
·   Temperature
·   Cross Sectional Area

To change the resistance of a material, the value of one of the above factors must be modified. When length (L) is modified the variation in resistance is direct. The change in the cross sectional area (A) has an inverse effect on the modification in resistance, whereas changes in composition or temperature do not vary the material resistivity in such a simple way (Dally, Riley and McConnell 1993).

Chemiresistors are small, simple, sensitive detectors with low power requirements capable of sensing chemical vapours in air, soil, or water. The working principle of a chemiresistor is based on a thin electrically conductive polymer film that swells in the presence of chemicals in vapor phase. The chemical concentration is related to swelling degree measured through a change in the electrical resistance across the film (Ho et al. 2001).

Chemiresistors have no moving parts and only require simple DC circuitry to read electrical resistance.

In this chapter, we will first present a double sensor with two sensing capabilities. This structure integrates a capacitive sensor, like one of those analyzed in chapter 2, and a resistive one. In order to show its capabilities, this double sensor has been tested as capacitive humidity sensor in combination with a resistive toluene detector. Then, we will show a detailed study of different parameters that can interfere in the resistive polymeric film sensitive to toluene. For this reason, we have looked at the influence of the polymer composition, the screen mesh density used to print the composite and the shape of the electrodes. Finally, the best solution will be shown.

3.1   Double sensor

Chemical sensors constitute one of the largest groups of sensors (Hierlemann et al. 2003). Different transduction mechanisms have been used to develop this kind of sensors, such as resistive and capacitive sensors. Chemoresistive sensors rely on the change in the conductivity due to the chemisorption of gas molecules at the sensitive layer surface (Janata 2009), whereas chemocapacitive sensors are based on variations of the dielectric constant of the sensitive layer in presence of the analyte studied (Gründler 2007).

Many chemical sensors are limited in terms of analyte discrimination or sensor selectivity (Hierlemann and Gutierrez-Osuna 2008). Different approaches have been followed to face this drawback, for example, using higher-order sensing systems that result in sensor arrays covered with different sensitive films (Hagleitner et al. 2001, Chang and Yuan 2009) or configuring proper pattern recognition algorithms (Hossein-Babaei, Hosseini-Golgoo and Amini 2009). Another alternative is measuring different properties of a sensitive layer, known as multifunctional sensors (Covington et al. 2003, Su, Beardslee and Brand 2013). In this respect, a combined Seebeck and resistive sensor was presented by Ionescu (Ionescu 1998) for SnO_2 detection, a resistive and capacitive sensor was developed by Vasquez-Quintero et al. (Quintero et al. 2013) in order to measure temperature and humidity, respectively. A pressure and temperature sensor

was introduced by Butler (Butler and Milkovic 1981) by capacitive and resistive mechanisms, respectively.

The majority of the chemical sensors have been manufactured by semiconductor device technologies (Janata 1985), such as deposition of material layers, patterning by photolithography and etching to produce the required shapes (R. Ghodssi 2011). Advances in printed electronics sensors on polymeric substrates have been recently reported by several authors (Mayr et al. 2009, Su, Lee and Chou 2009, Cho et al. 2008, Skotadis et al. 2013). The interest in this technology is the large-area manufacturing, low-cost materials, flexibility and biodegradability (Briand et al. 2011a).

Regarding printed capacitive sensors, several moisture detectors have been described. Different fabrication processes have been used to develop this kind of sensors, such as gravure, screen printing and inkjet-printing; and different strategies have been applied to include the sensing capability in the capacitor. The most common approach has been to deposit the sensing layer over the capacitor (Molina-Lopez et al. 2012, Weremczuk et al. 2012, Starke et al. 2011). Some frequently used polymers are cellulose acetate butyrate (CAB), polymethylmethacrylate (PMMA) and polyvinylchoride (PVC), among others. Another possibility is to use the flexible substrate as the sensing element. In this case, polyimide (Virtanen et al. 2011a) and photographic paper (Briand et al. 2011b) have already been described, saving fabrication steps compared with the former approach. These capacitive sensors have a high thermal drift as one of the main challenges to be overcome in order to obtain an accurate humidity measurement but we found a low-thermal drift in humidity capacitive sensors fabricated on polyimide (see chapter 2).

With respect to printed resistive sensors, different temperature detectors have been reported (Quintero et al. 2013, Dziedzic et al. 1997) as well as gas sensors (Lonergan et al. 1996, Oprea et al. 2009a, Crowley et al. 2010). Lorwongtragool et al. (Lorwongtragool et al. 2012) developed chemiresistive vapor sensors whose electrical resistance changes in presence of selected VOCs, using silver interdigitated electrodes, multi-walled carbon nanotubes (MWCNTs) and poly (styrene-co-maleic acid) partial isobutyl/methyl mixed ester (PSE). A MEMS-based benzene gas sensor was presented by Ke et al.

(Ke et al. 2009) where the sensitive element was a thin-film WO3 layer. The most common used structure in both capacitive and resistive modes is the interdigitated electrodes (Molina-Lopez et al. 2012, Igreja and Dias 2006, Courbat et al. 2011, Lorwongtragool et al. 2012) due to its high contact area rate and ease of manufacturing (Mamishev et al. 2004) but other designs have been also adopted (Kim, Kim and Yoo 2010, Djuric et al. 2011).

Here, we present a sensor structure for simultaneously determination of relative humidity and toluene concentration in a non-interacting manner. The proposed design is based on four meandered electrodes printed on polyimide substrate. Two of these electrodes the device is covered with are made of a graphite-polystyrene composite to sense toluene concentration by resistance changes in the deposited film. The other half is directly used as capacitive humidity sensor by changes in the electrical permittivity of the substrate. To verify its response, we have measured both capacitance and resistance changes as a function of relative humidity (RH) and toluene concentration. Temperature drifts have also been analysed as a possible interfering magnitude.

3.1.1 Sensor design

The devices analysed in this study are planar meandered capacitor and resistor which allow a direct interaction between the sensor and the surrounding environment. Although there are other geometries that offer higher nominal capacitance per surface area (Molina-Lopez et al. 2012) than the one displayed in Figure 55, we chose this design because it allows us to increase the functionality of the platform by including in the same area a resistive sensor with the same footprint. The usual approach for providing humidity or gas sensitivity is to deposit a sensing layer on this structure with some humidity-dependent electrical property (Weremczuk et al. 2012, Molina-Lopez et al. 2012) but another possibility is to directly use the substrate as sensing element (Virtanen et al. 2011a, Rivadeneyra et al. 2014). We have combined both strategies in a single device; therefore we have two different sensors in virtually the same area.

In order to functionalize this double or mixed sensor, the two sensed magnitudes are humidity and toluene concentration. The relative humidity is

measured through changes in the electrical permittivity of the substrate, so that, the capacitance of these electrodes changes with the humidity. The toluene concentration is derived from changes in the resistivity of a deposited composite onto the other electrodes of this sensor; therefore, this part of the sensor is resistive whereas the other part is capacitive.

A three dimensional view of the simulated structure including the notation of its geometrical parameters is depicted in Figure 55. This combined sensor consists of four meandered electrodes or fingers depicted in different colours (see Figure 55), and four terminals. The two top electrodes with the deposited composite form the resistive sensor for toluene determination. Whereas the two bottom electrodes constitute the capacitive sensor with the substrate as sensitive layer. As shown in Figure 1, each part (resistive or capacitive) of this structure has two terminals for external connection.

This sensor structure allows the introduction of optimization of more sensing capabilities into the devices, saving manufacturing materials and area. For this purpose, we used COMSOL Multiphysics 4.2a (www.comsol.com, COMSOL, Inc. USA) to optimize the design by partial differential equations with the finite element method. This software has previously been used to deeply study similar structures (Mohd Syaifudin et al. 2012, Oikonomou et al. 2012).

Several parametric analyses were performed varying the fundamental geometrical parameters of the meander structure such as the number of fingers, the gap width between consecutive fingers from different sensors and their dimensions (width, length and thickness of each finger). In order to optimize the area, we fixed the finger width to the minimum secured diameter landed drop by inkjet printing (in our case 50 µm) and the gap between fingers from the same sensor also to 50 µm. This gap could be reduced below the drop diameter value but this reduction will lead to a strong possibility of short-circuit between electrodes due to printing errors.
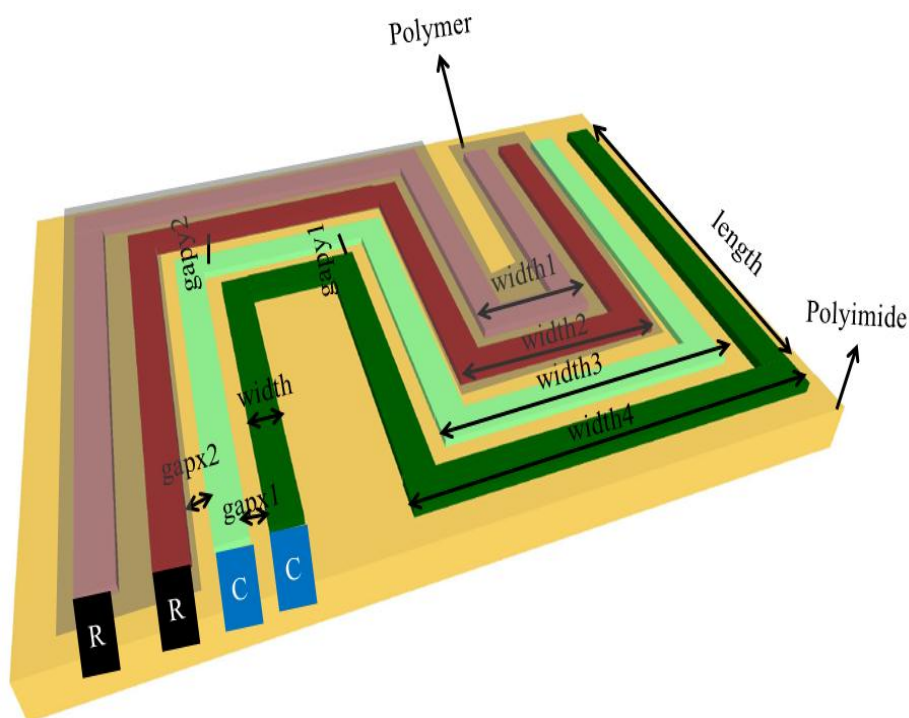
Figure 55. Layout of the designed capacitive-resistive sensor indicating the notation of the dimensions. R corresponds to resistive terminals, C form capacitive sensor.

As the composite deposition was done by screen printing, the gap between fingers between the resistive and the capacitive elements was set to the minimum secure length that allowed us to align without printing on the capacitor electrodes but this gap could also be reduced with other screen printing technologies providing a more compact design. As shown in our previous works detailed in chapter 2, the thickness of the fingers hardly affects the capacitance value in this kind of structures; therefore thickness electrodes were defined with just one layer. According to these previous considerations, we manufactured the sensor following the specifications from Table 13 for a targeted nominal capacitance (for one printed layer) of 3 pF since they presented the best compromise between capacitance and area. The resistance found for these electrodes without deposited composite was about 510 MΩ.

Table 13. Physical dimensions of the double capacitive-resistive sensor.

Parameter	Value	Description
Width	50 µm	Width of each finger (*x*-axis)
Length	1.80 mm	Length of each finger (*y*-axis) without including unions
Gap1y	50 µm	Distance between consecutive fingers of the same sensor element (*y*-axis)
Gap2y	150 µm	Distance between consecutive fingers of different sensors elements (*y*-axis)
Gap1x	50 µm	Distance between consecutive fingers of the same sensor element (*x*-axis)
Gap2x	150 µm	Distance between consecutive fingers of different sensor elements (*x*-axis)
Width1	250 µm	Width of sub-interior union (*x*-axis)
Witdth2	500 µm	Width of sub-interior union (*x*-axis)
Width3	700 µm	Width of sub-exterior union (x -axis)
Width4	900 µm	Width of exterior union (x -axis)
Number	45	Total number of fingers of each electrode of each sensor
Thickness1	420 nm	Electrodes thickness (1 layers) (*z*-axis)
Thickness2	7 µm	Composite thickness (1 layers) (*z*-axis)

The designed sensor structure area was 89.0 mm^2 (L = 4.00 mm x W = 22.25 mm) composed of 180 fingers (45 fingers for each electrode) with 50 µm width (see Figure 55). In order to easily test the device, we added four long terminals to couple the sensor to the measurement set-up. This sensor device presents capacitive and resistive transduction mechanisms on the same meandered finger structure and provides a very compact and repetitive way to design environmental sensors with a minimum fabrication steps involved.

3.1.2 Fabrication process

All the patterns were printed on a polyimide substrate with 75 µm thickness (Kapton® HN, Dupont[TM], Wilmington, DE, USA). With regard to the humidity sensors, we have followed the same working principle as shown in chapter 2, no sensing layer was deposited onto the electrodes, being the

substrate the only element which changes with the relative humidity. This polyimide is a well-known and broadly used material (Virtanen et al. 2010, Harrey et al. 2002, Rivadeneyra et al. 2014) whose electrical permittivity, ε_r shows a high sensitivity to the relative humidity according to Equation (11) of Chapter 2.

The composite sensitive to toluene was a mixture of 50% graphite and 50% polystyrene (Lonergan et al. 1996). The composite was deposited by only one layer by screen printing. The products used to prepare the sensitive composite were ethyl acetate 99% (Fluka, Switzerland), cyclohexanone (Sigma Aldrich, Spain), polystyrene average MW (molecular weight) ca. 280000 GPC grade (Sigma Aldrich, Spain), graphite powder 1 micron. (Sigma Aldrich, Spain). The polystyrene was dissolved in ethylacetate under stirring for 20 h. After that, we added the graphite and the cocktails were agitated in an ultrasonic bath for 15 min. Then, cyclohexanone was added to each cocktail in order to adjust the viscosity and avoid polystyrene solidification during printing process. Once the patterns were printed with these inks, they were dried at ambient conditions.

The fabrication of the electrodes was done with a DMP-2831™ Dimatix printer (Fujifilm Dimatix Inc, Santa Clara, USA). The selected material was an ink with a solid content of 20% of silver nanoparticles dispersed in ethanol/ethanediol (U5603 SunTronic Technology, San Diego, USA). The composite was deposited with a Serfix III screen printing machine (Seglevint SL, Barcelona, Spain). The screen used to manufacture the patterns by screen printing had a mesh density of 120 Nylon thread per centimetre (T/cm) in an aluminium rectangular structure of 50 cm width and 35 cm length to fabricate them with only a single-layer screen printing.

In the fabrication process of this sensor, the first step before printing was to prepare the substrate to ensure good printability, following the same procedure presented in section 2.2.2. During the inkjet printing, the substrate temperature was fixed at 40ºC while printing with the DMP-2831. A drop space of 25 μm was settled in the printer for 50 μm landed diameter drops followed by a sintering step at 120ºC for 60 min. In both printing techniques, the sintering took place in two different stages; a ramping of the temperature

from room temperature to 160ºC at 3ºC/minute, followed by an hour at constant 180 ºC temperature.

3.1.3 Characterization

The physical characterization of the patterns has been carried out using a Dektak XT™ Stimulus Surface Profiling System (Bruker Corporation, Conventry, UK). The electrical characterization has been carried out by measuring their capacitances and dissipation factors (capacitance measurements) and impedance module and phase (resistance measurements), using the four-wire measurement technique with a Impedance Analyser 4294A and an impedance probe kit (4294A1) (Agilent Tech., Santa Clara, CA, USA). The excitation voltage applied in all measurements was $V_{DC} = 0$ and $V_{AC} = 500$ mV. The frequency sweep of analysis was from 100 kHz to 5 MHz. Both end sides of the backbones have been enlarged to facilitate its connection and a SMA (SubMiniature version A) male connector has been glued to these ends points using silver-filled epoxy EPO-TEK® H20E (Epoxy Technology, Inc., Billerica, USA). A complete compensation method has been implemented to eliminate the contribution of parasitic capacitances (detailed in section 2.1.4).

The stationary humidity and temperature responses of these sensors have been measured in a climatic chamber VCL 4006 (Vötsch Industrietechnik GmbH, Reiskirchen, Germany). The humidity range varied from 10% RH to 98% RH in a temperature range of + 10 °C to + 95 °C. The humidity deviation in time was ± 1% to ± 3% and the temperature deviation in time was ± 0.3 °C to ± 0.5 °C.

The response to toluene concentration was measured with a controlled evaporator mixer (Bronkhorst HI-TEC, the Netherlands) (Wohler et al. 2011) and a multimeter 34410A (Agilent Tech., USA) to measure the corresponding capacitance values at a frequency of 100 kHz and DC resistance every 2 s.
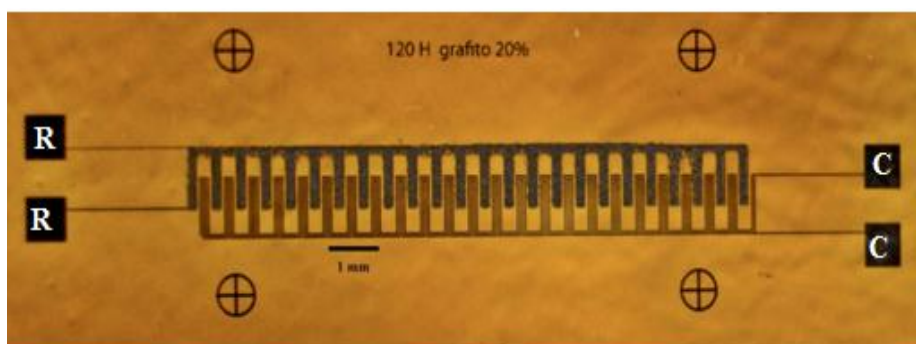
Figure 56. Image of the double sensor.

The vapour generation system consists of a liquid flow controller where the toluene was introduced, a mass flow controller (MFC) for carrier gas, in this case nitrogen. The temperature controlled mixing was set at 111 ºC in order to vaporize the toluene. The pressure of both flows was set at 2 bar and the nitrogen flow was fixed to 40%. Then, we varied toluene concentration from 2.5 % (the minimum stable value) to 60 %.

3.1.4 Results and discussion

In this section, we first present the physical characterization of the printed double sensors shown in Figure 56. After that, the capacitance is characterized taking into account the measurement frequency and the temperature dependences as a function of the relative humidity and toluene concentration. Finally, the resistance is studied as a function of relative humidity, temperature and toluene content.

A. Physical characterization

Twenty replicas of the double sensor in an area of 89 mm^2 (L = 4.00 mm x W = 22.25 mm) were printed on Kapton HN and physically characterized (Figure 56). According to the model presented in previous works (Salmerón et al. 2014, Molina-Lopez et al. 2012), the layer thickness by inkjet printing for just one printed layer is 430 nm for interdigital and serpentine structures, respectively. With these printing and curing conditions, the average resistivity of the inkjetted conductive electrodes was 23 ± 2 µΩ·cm (Salmerón et al. 2014).

The real dimensions of the structures are presented in Table 14, showing the differences between measured and predicted dimensions for these structures. Uncertainties were calculated as one standard deviation of the experimental data.

Table 14. Comparison between numerical and experimental physical dimensions of the double sensor.

Parameter	Model	Experimental
Width	50 µm	57 ± 2 µm
Length	1.80 mm	1.83 ± 0.24 mm
Gap1y	50 µm	57 ± 3 µm
Gap2y	150 µm	162 ± 2 µm
Gap1x	50 µm	56 ± 2 µm
Gap2x	150 µm	163 ± 3 µm
Witdth0	150 µm	166 ± 2 µm
Width1	250 µm	251± 4 µm
Witdth2	500 µm	514 ± 3 µm
Width3	700 µm	708 ± 2 µm
Width4	900 µm	904 ± 4 µm
Thickness1	420 nm	470 ± 50 nm
Thickness2	7 µm	5 ± 2 µm

In general, real dimensions are alike to modelled ones, being the biggest discrepancy in the widths. These concordant results can be explained by the spread of the ink drop when it is deposited on the substrate (Salmerón et al. 2014, Rivadeneyra et al. 2014). The thickness of the sensitive composite differs significantly from predicted value but it also shows a high roughness value. This might be caused by the mesh density. In order to define thin patterns, we had to use a thinner mesh that obstructs more the particles path to the substrate.
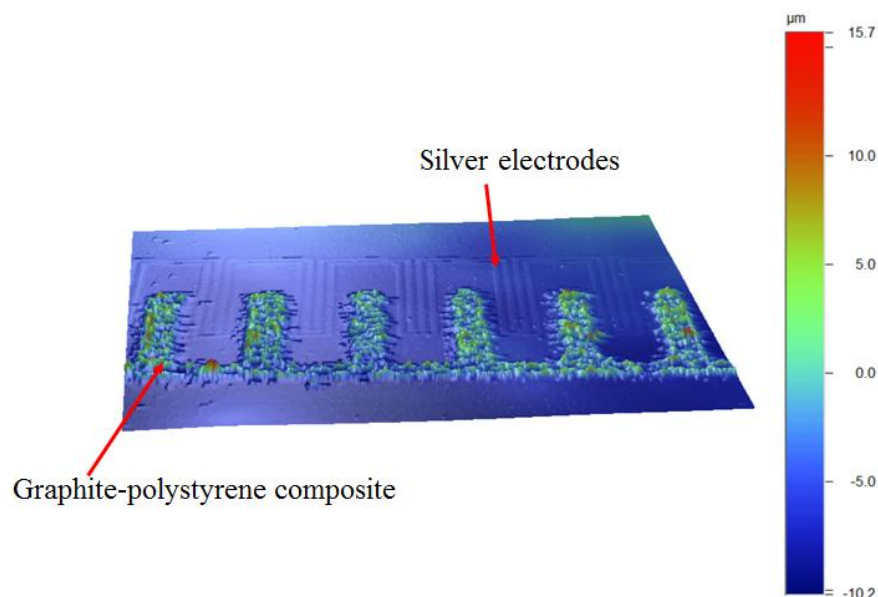
Figure 57. Profiling 3D caption of double sensor.

B. Capacitive part

After the physical characterization, hereafter the sensor capacitance and resistance has been analysed as a function of humidity and temperature in a wide frequency range. For five sensor devices, we have measured the capacitance and resistance as a function of the relative humidity and temperature in the frequency range from 100 kHz to 10 MHz. Furthermore, the measurements have been carried out in both directions for both humidity and temperature sweeps, that is to say, increasing and decreasing the relative humidity at fixed temperature for obtaining the sensor hysteresis in RH and vice versa for temperature.

Figure 57 shows the measured capacitance of the sensor for different values of RH at constant temperature. As can be observed, the sensor presents very similar response in frequency for each of the tested RH. In our previous works shown in chapter 2, we found comparable capacitance curves for an interdigitated electrode capacitor and a serpentine electrode capacitor where the sensing material was directly the polyimide substrate in both cases.

Temperature is the most important interfering factor in the response of capacitive humidity sensors (Oprea et al. 2009a). To test this dependence, we

studied the capacitance as a function of frequency for several temperatures at a constant RH value. These curves are practically overlapped up to 2 MHz, and then a displacement is observed but it is lower than 16 fF. The range of frequencies where the least difference between lines happens is from 1.2 MHz to 2.3 MHz. Similar results have been found in previous studied following the same philosophy, detailed in chapter 2.
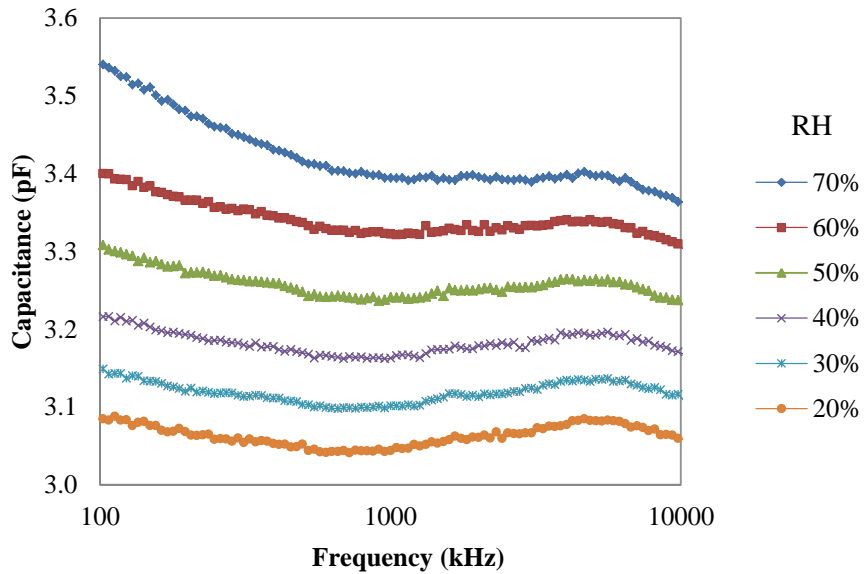
Figure 58. Capacitive sensor as a function of frequency for different RH values at 40ºC.

We have calculated the calibration curves of the experimental data shown in Figure 58. Equation (24) shows this calibration curve at 1 MHz. The coefficient of linearity is bigger than 0.98.

$$C(pF) = 0.0049 \cdot RH(\%) + 2.9481 \ \ R^2 = \ 0.9818 \qquad (24)$$

The maximum relative error between eq. (24) and experimental data is less than 20 fF.

Regarding the change of the capacitive part of this mix sensor, we found a deviation of only 1% between the measurements at ambient condition and at saturated toluene atmosphere for 24 hours. Therefore, we can conclude there is no significant change in the capacitance due to changes in toluene concentration.
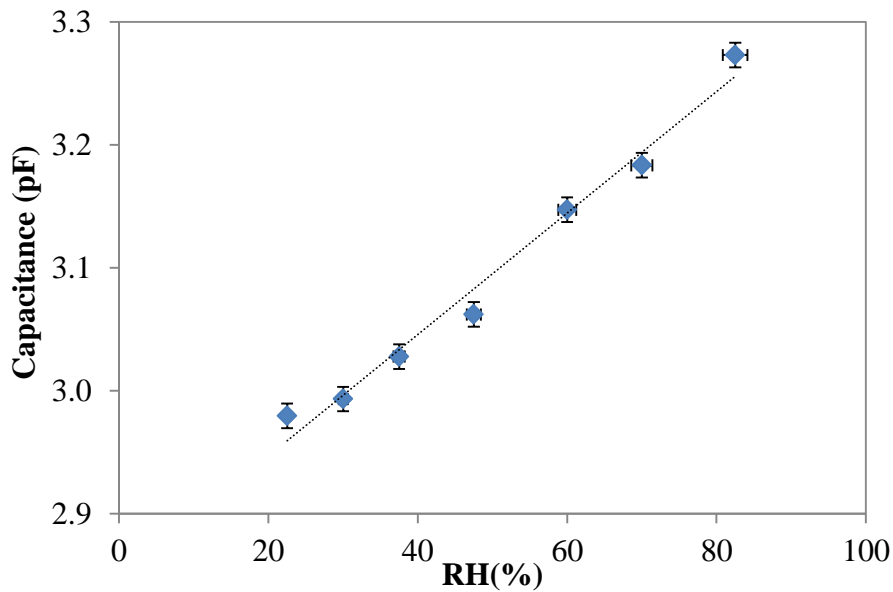
Figure 59. Capacitance vs. Relative humidity at 1 MHz.

C. Resistive part

We performed several RH sweeps and we noticed that the impedance value decreased the first time from about 344 Ω to 288 Ω at ambient conditions and then, the sweeps were stable. After this first exposure to RH, the resistance varies around 10 Ω in the whole RH and temperature sweeps developed. As expected, the resistance was invariable with frequency. We have calculated the calibration curves of the experimental data. Equation (25) shows this calibration curve at 1 MHz. The coefficient of linearity is bigger than 0.98.

$$R(\Omega) = 0.0991 \cdot RH(\%) + 281.76 \ R^2 = \ 0.9865 \qquad (25)$$

The maximum relative error between eq. (25) and experimental data is less than 0.5 Ω. This dependence can be compensated with the humidity value extracted from the capacitive part of this double sensor.
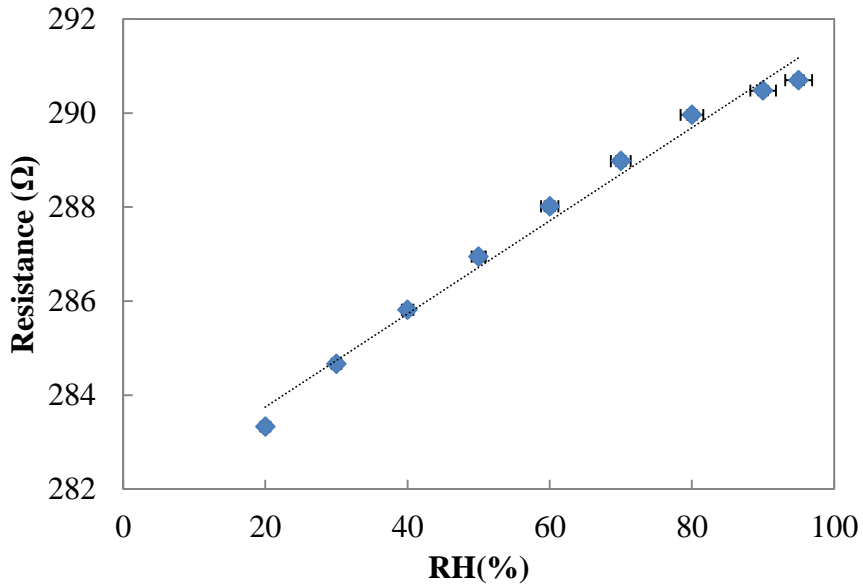
Figure 60. Resistance vs. Relative humidity at 100 kHz at 40ºC.

In terms of thermal dependence, we have looked at the calibration curves of the experimental data shown in Figure 61. Equation (26) shows this calibration curve at 100 kHz. The coefficient of linearity is bigger than 0.97.

$$R(\Omega) = 0.0872 \cdot T(°C) + 280.34 \;\; R^2 = \; 0.9720 \qquad\qquad (26)$$

The maximum relative error between eq. (26) and experimental data is less than 0.25 Ω.

The thermal dependence of this resistance will require thermal compensation to erase its effect. There are many different options to face this problem, for example, we could include a thermoresistor in the design or if we include this sensor in a radiofrequency identification (RFID) tag, there are some chips (i.e. SL900A) that directly integrate a temperature sensor.
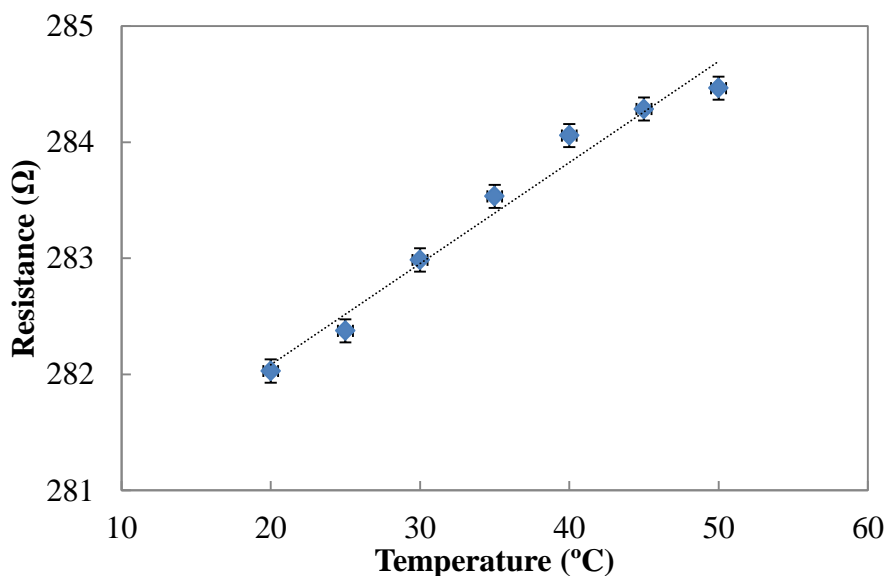
Figure 61. Resistance vs. temperature at 1 MHz at 40 %.

After the relative humidity and temperature characterization, the sensor resistance has been analysed as a function of toluene concentration at ambient conditions. For five double sensors, we have measured the DC resistance as a function of toluene concentration and capacitance at 100 kHz. Furthermore, the measurements have been carried out in both directions for increasing and decreasing toluene concentrations.

Figure 62 presents the relative variation in resistance as a function of toluene concentration. The data were recorded every 3 min and the value show in the graph is the mean value of 5 different samples. The curve that best fits the experimental data is presented below.

$$R(\Omega) = 5 \cdot 10^{-8} \cdot [T_{ppm}]^2 \ + \ 0.0003 \cdot [T_{ppm}] \ + \ 291.88 \ \ R^2 = \ 0.9985 \qquad (\,27\,)$$

The correlation coefficient is higher than 0.99, showing a very good agreement between eq. (27) and the resistive part of the double sensor.
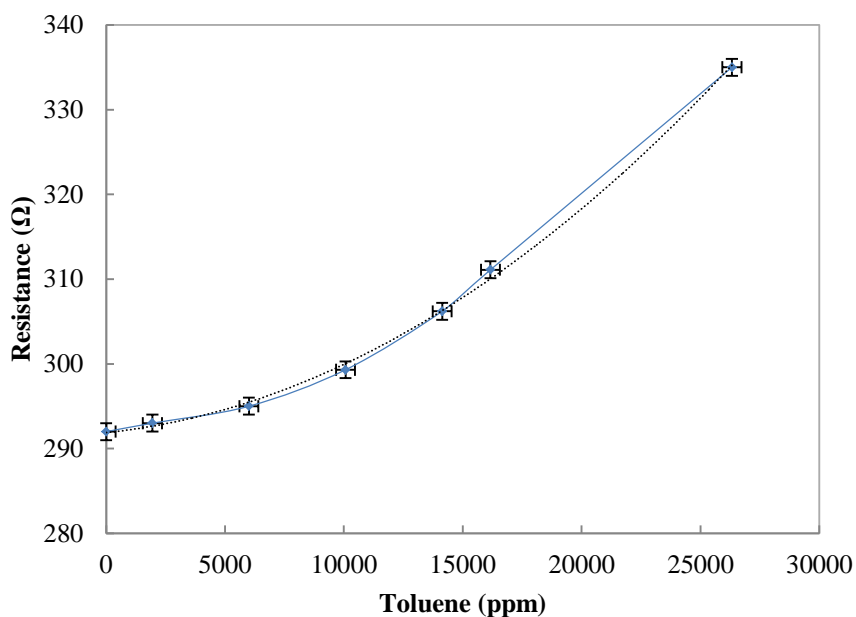
Figure 62. Relative resistance change upon exposure of toluene.

As we have mentioned above, the time between resistance measurements was only 3 min. We chose this time interval between measurements to know if there was a significant and reproducible change in resistance in short time. We left the sensor a saturate toluene atmosphere for 24 hours and the resistance triplicated its value in absence of toluene. More research should be done to better know the composite sensitivity.

3.2   Full-printed chemiresistor with ppb-level toluene detection capabilities

After developing the double sensor, we carried out the characterization of the graphite based composite to optimize its response to toluene. We found that the resistance at saturated toluene atmosphere triplicated its nominal value. For this reason, we tested the change in resistance in water dissolution and we found a promising variation.

Here, we present a deep study of the influence of different controllable parameters in the fabrication of printed resistance to sense toluene concentration in very low concentrations (parts per billion, ppb). First, we

look at the impact of mesh density of the screen on the reproducibility of the manufacturing process and the nominal value of resistance. After that, we show the response to toluene concentration for different composite compositions. Finally, the influence of the bottom electrodes is also analysed.

3.2.1 Fabrication process

The fabrication of the electrodes was done with a DMP-2831™ Dimatix printer (Fujifilm Dimatix Inc, Santa Clara, USA). The selected material was an ink with a solid content of 20% of silver nanoparticles dispersed in ethanol/ethanediol (U5603 SunTronic Technology, San Diego, USA).

The composite sensitive to toluene was a mixture of graphite powder and polystyrene. We tested 4 different inks varying the content of graphite from 20% to 50%. The products used to prepare the sensitive composite were ethyl acetate 99% (Fluka, Switzerland), cyclohexanone (Sigma Aldrich, Spain), polystyrene average MW ca 280000 GPC grade (Sigma Aldrich, Spain), graphite powder 1 micron. (Sigma Aldrich, Spain).

Table 15. Cocktail composition.

%W Ps / %W graphite	Polystyrene (g)	Graphite (g)
20/80	4.8	1.2
30/70	4.2	1.8
40/60	3.6	2.4
50/50	3.0	3.0

The polystyrene amounts in Table 15 were dissolved in ethylacetate under stirring for 20 h. After that, we added the graphite and the cocktails were agitated in an ultrasonic bath for 15 min. Then, cyclohexanone was added to each cocktail in order to adjust the viscosity and avoid polystyrene solidification during the printing process. Once the patterns were printed with these inks, they were dried at ambient conditions.

All these composites were deposited with a Serfix III screen printing machine (Seglevint SL, Barcelona, Spain) on top of the ink jetted electrodes. The screens used to manufacture the patterns by screen printing had a mesh density of 43 and 120 Nylon thread per centimetre (T/cm), respectively, and

patterns have been printed with only a single-layer. All the patterns were printed on a polyimide substrate with 75 µm thickness (Kapton® HN, Dupont^{TM}, Wilmington, DE, USA).

3.2.2 Characterization

The physical characterization of the patterns has been carried out using a Dektak XT™ Stimulus Surface Profiling System (Bruker Corporation, Conventry, UK). The electrical characterization has been carried out by measuring their impedances, using the four-wire measurement technique with a Impedance Analyser 4294A and an impedance probe kit (4294A1) (Agilent Tech., Santa Clara, CA, USA).

In order to measure the response to variations in toluene concentration, we immersed the sensors in a toluene dissolution in water and the DC resistance were measured with a multimeter 34410A (Agilent Tech., USA) every 2 s using four-point probe technique. The toluene dissolution of 5 mg/l (5 ppm) was prepared by adding 5.8 µl of toluene to 1 litre of water in glass bottle. The mixture was under stirring for 48 h to assure its dissolution.

3.2.3 Results and discussion

A. Screen mesh density

The analysis performed here was with two meandered electrodes. Figure 63 presents the physical dimensions of these printed resistors. Basically, we defined half of the double sensor shown in section 3.1 to study how different parameters affect to the resistance but in order to avoid alignment difficulties, we covered completely the electrodes.

As we have explained in the previous section, we have tested 4 inks with different graphite content and printed them using two different screen mesh densities. Table 16 presents the mean value and standard deviation of the different inks with different screen mesh densities. Inks with lower graphite content provide higher resistance values but also poorer reproducibility. Regarding the mesh density influence, a bigger mesh gives better reproducibility in a more variety of graphite content but it also results in lower pattern definition.
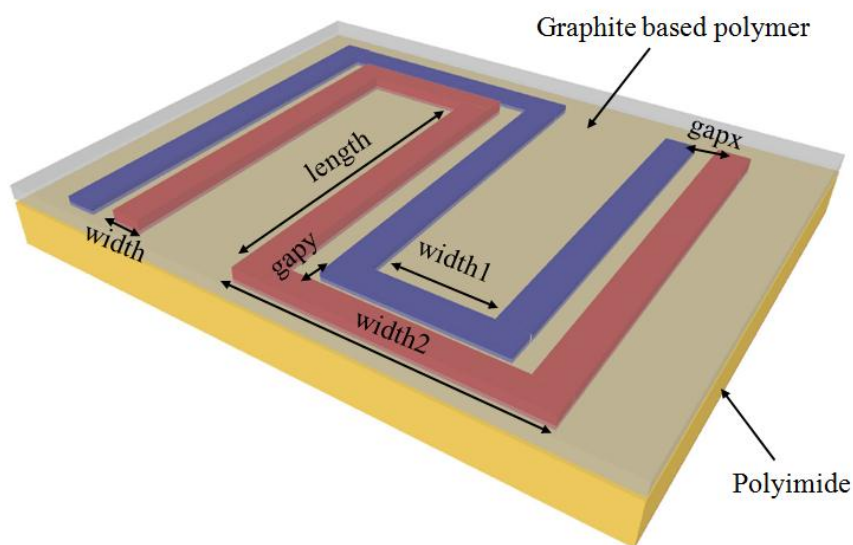
Figure 63. Model of the fabricated resistors to study the influence of the screen mesh density.

In terms of reproducibility, we could conclude that the ink with the highest graphite content works quite well with both screen mesh densities. In case of using 43 T/cm mesh density, we can obtain a reliable printed pattern. Notice that patterns printed with 120 T/cm always result in higher resistance than patterns printed with 43 T/cm, which might be caused by the fact that a higher mesh density obstructs the transference of graphite to the substrate.

Table 16. Mean value and standard deviation of resistances printed with different inks and screen mesh densities.

Mesh (T/cm)	Graphite content			
	20%	30%	40%	50%
43	1500 ± 400	440 ± 50	230 ± 17	148 ± 8
120	1700 ± 800	1200 ± 1000	500 ± 180	263 ± 17

B. Graphite composition

In this section, we have studied the time response of those combinations of ink and screen mesh density that showed better reproducibility (see Table 16), using the same electrodes as shown in Figure 63. All resistances were

monitored in 3 different scenarios: air, water and solution of 150 ppb of toluene in water. The sensors were measured about 20 min in each scenario.

Figure 64 presents the time response of the resistance with 40% graphite content printed with 43 T/cm mesh density. Figure 65 and Figure 66 show the time response of the sensor printed with the ink based on 50% graphite with a mesh density of 43 T/cm and 120 T/cm, respectively. At it can be seen, there is a fast and higher response to toluene than the behaviour in only water in all samples. Curves obtained with higher resistance values (Figure 64 and Figure 66) show a more saturated response than the resistance with lower nominal value (Figure 65). There is also a relationship between the response to water: the lower nominal value corresponds to a higher graphite content and presents lower sensitivity to water than the other patterns.
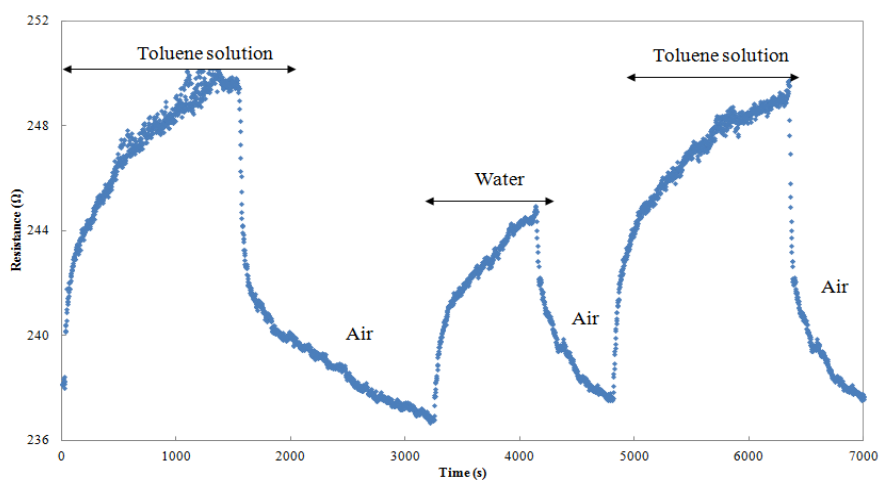
Figure 64. Time response to water and solution with 150 ppb of toluene for a resistance with 40% graphite content and screen mesh density of 43 T/cm.
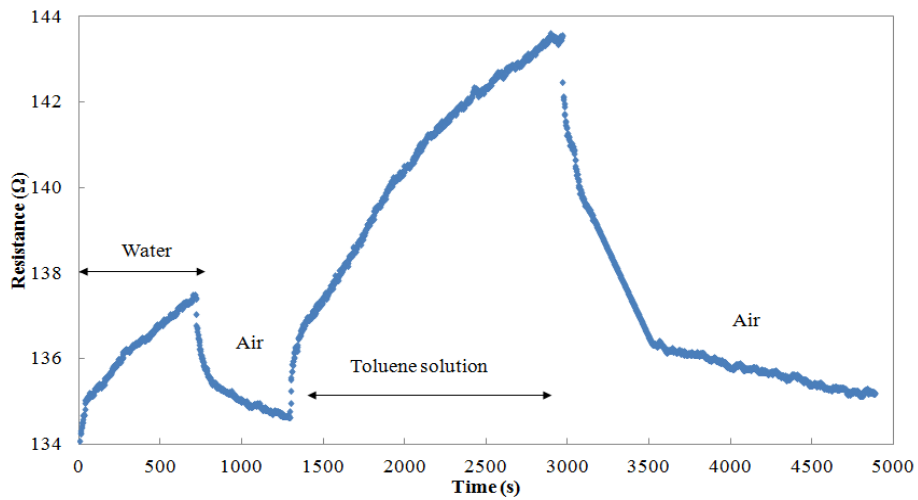
Figure 65. Time response to water and solution with 150 ppb of toluene for a resistance with 50% graphite content and screen mesh density of 43 T/cm.
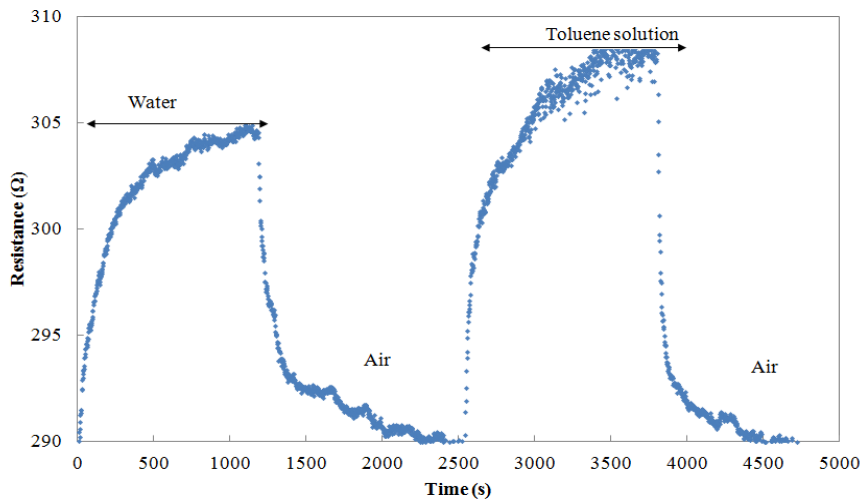
Figure 66. Time response to water and solution with 150 ppb of toluene for a resistance with 50% graphite content and screen mesh density of 120 T/cm.

C. Electrode layout

The electrodes considered in this study are interdigitated (see Figure 12 in chapter 2) and serpentine (see Figure 23 in chapter 2), all fitting in the same

area. Table 17 shows the mean values and standard deviations of the resistance at ambient conditions of the different electrode configurations. IDE and SRE are printed in the same area and both resistance values present a low standard deviation. SRE structure results in 12.7% more resistance than IDE configuration.

Table 17. Mean value and standard deviation of resistances printed with different electrodes configurations.

Parameter	IDE	SER
Mean (Ω)	148 ± 10	167 ± 5
Area (mm^2)	11.63	11.63

We also tested the double sensor presented in section 3.1 (see Figure 55) in order to know its response in toluene water dissolution. Figure 67 shows the normalized resistance as a function of time at 150 ppb. The normalization has been done by the stable resistance value achieved in water.

After that, we studied the response as a function of toluene concentration at fixed time. We recorded data every 1 min and 3 min (Figure 68). As expected, the more time the sensor is immersed, the higher its response is. The main result is the fact that the sensor responded below 70 ppb.
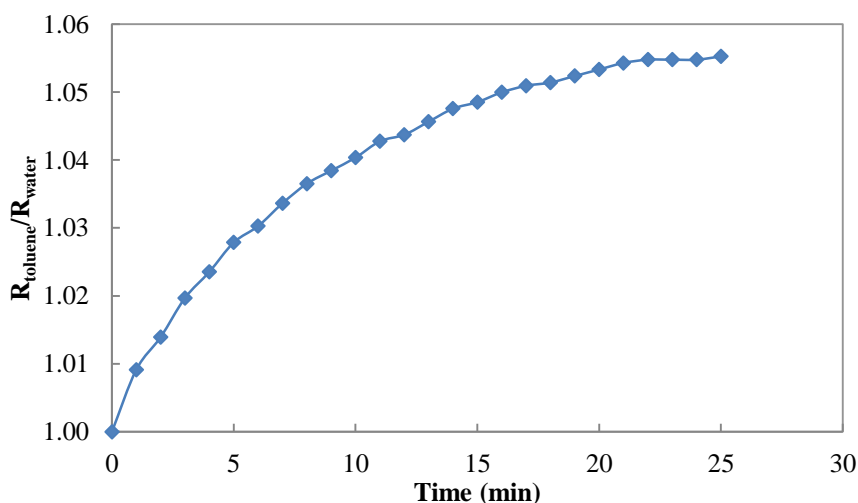
Figure 67. Normalized resistance of the double sensor resistive part in toluene water dissolution at 150 ppb.
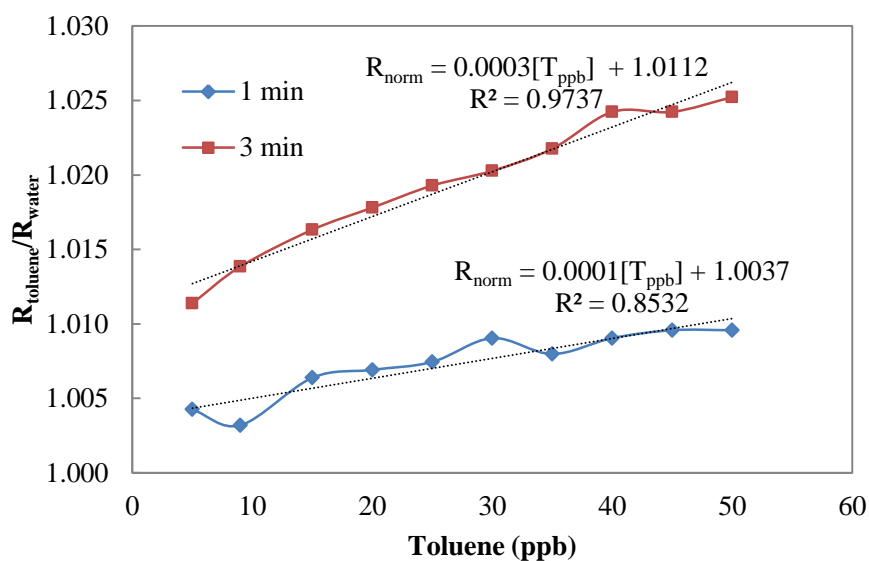
Figure 68. Normalized resistance of the double sensor resistive part in toluene water dissolution, recorded at different times.

Finally, we tested this device in water dissolution with methanol and toluene (Figure 69). Measurements were taken after 3 min in dissolution. Comparing with Figure 67, if we increased the toluene concentration the response is much faster than at low concentrations.

The response to methanol dissolved in water was also measured but there were virtually no change with the response to water after 20 min immersed.
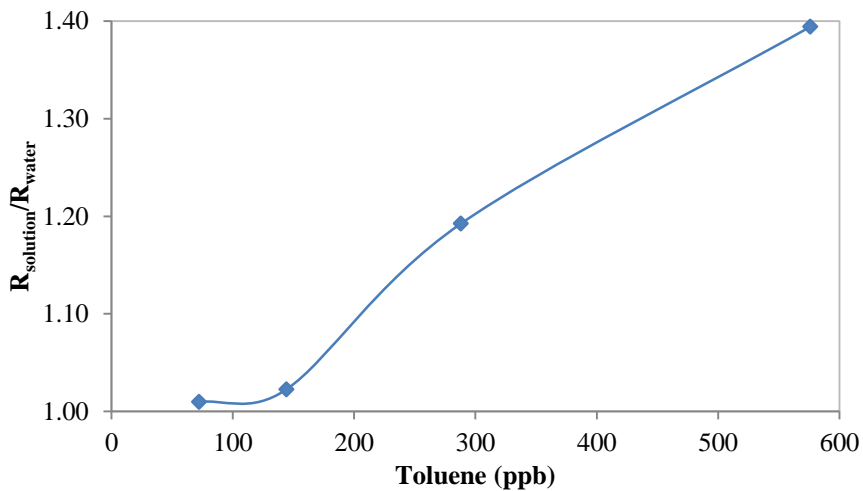
Figure 69. Normalized resistance of the double sensor resistive part in methanol-toluene water dissolution.

3.3   Conclusions

First, we have presented a double sensor for capacitance and resistance measurements. The proposed design is based on four meandered electrodes printed on polyimide substrate. Although there are other geometries that offer higher nominal capacitance per surface area than the one presented here, we chose this design because it allows us to increase the functionality of the platform by including in the same area a resistive sensor with the same footprint. The usual approach for providing humidity or gas sensitivity is to deposit a sensing layer on this structure with some humidity/gas-dependent electrical property but another possibility is to directly use the substrate as sensing element. We have combined both strategies in a single device; therefore we have two different sensors in virtually the same space.

In order to functionalize this double or mixed sensor, the two sensed magnitudes are humidity and toluene concentration. The relative humidity is measured through changes in the electrical permittivity of the substrate (polyimide), so that the capacitance of these electrodes changes with the humidity. The toluene concentration is derived from changes in the resistivity of a deposited composite based on graphite onto the other electrodes of this sensor; therefore, this part of the sensor is resistive whereas the other part is

capacitive. We have characterized both sensitive parts as a function of relative humidity, temperature and toluene concentration. Regarding capacitive part, we found a sensitivity of 5 fF/%RH at 1 MHz. This value is comparable with the found sensitivities in chapter 2 but more area is required to define the capacitor in this case. Thermal dependence was negligible, as happened in structures detailed in chapter 2. In addition, the change in capacitance at atmosphere saturated in toluene was about 1% from the capacitance value at ambient conditions. With respect to the resistive part, we found dependences of 0.05 Ω/%RH and 0.1 Ω/°C. The RH dependence can be compensated with the humidity value extracted from the capacitive part of this double sensor. The thermal dependence of this resistance will require thermal compensation to erase its effect. There are many different options to face this problem, for example, we could include a thermoresistor in the design or, in case of introducing this sensor in a radiofrequency identification (RFID) tag; there are some chips (i.e. SL900A) that directly integrate a temperature sensor. If we measure every 3 min, the sensitivity to toluene is 0.3 mΩ/ppm of toluene, but we found that the resistance value was triplicated at an atmosphere saturated in toluene after 24 hours. So, it would be necessary to study in depth this sensitive composite to optimize its response. We have also found a promising change in resistance in water dissolution.

For this reason, we have presented a deep study of the influence of different controllable parameters in the fabrication of printed resistance to sense toluene concentration in very low concentrations (parts per billion, ppb).

First, we look at the impact of mesh density of the screen on the reproducibility of the manufacturing process and the nominal value of resistance. In terms of reproducibility, we could conclude that the ink with the highest graphite content works quite well with both screen mesh densities. In case of using 43 T/cm mesh density, we can obtain a reliable printed pattern. Notice that patterns printed with 120 T/cm always result in higher resistance than patterns printed with 43 T/cm which might be caused by the fact that a higher mesh density obstructs the transference of graphite to the substrate.

After that, we have shown the response to toluene concentration for different composite compositions at fixed toluene concentration. There is a fast and

higher response to toluene than the behaviour in only water in all samples. Curves obtained with higher resistance values show a more saturated response than the resistance with lower nominal value. There is also a relationship between the response to water: the lower nominal value corresponds to a higher graphite content and presents lower sensitivity to water than the other patterns.

Finally, the influence of the bottom electrodes has also been analysed. We fabricated IDE and SRE in the same area and totally covered with the same composite composition and using the same mesh density. Both resistance values present a low standard deviation. SRE structure results in 12.7% more resistance than IDE configuration.

4.   Suspended structures

Suspended platforms are useful to form microstructures such as accelerometers, pressure sensors, actuators, fluidic devices, biochemical devices, and miniature machines. Microelectromechanical systems (MEMS) are one example of a system that can incorporate a suspended platform. MEMS technology offers the opportunity to produce mechanical, electromechanical, and electrochemical devices with the same unprecedented levels of miniaturization and functionality as modern very large scale integrated technology. For instance, MEMS can integrate micromechanical elements and electronic elements on a common substrate material such as a silicon wafer. On another front, micromechanical elements can be fabricated using micromachining techniques that deposit layers of materials to form mechanical and electromechanical devices or that selectively etch one or more layers of material to form mechanical and electromechanical devices (Horsley 2002)

Suspended structures can be used to define:

1.   Internal cavities
2.   Bridges
3.   Cantilevers Beams

Anyway, their uses are virtually the same but the differences are in the performance and complexity of fabrication. A summary of some typical applications of cantilever beams is written by Lang et al. (Lang et al. 1999). A scanning force microscope (SFM) basically consists of a cantilever with a sharp tip on his free end to study a sample surface (Binnig, Quate and Gerber 1986). When a thin layer of metal is evaporated onto one side of the cantilever, a bimaterial actuator is formed. Due to the difference in the thermal expansion coefficients of the two materials, cantilever bending occurs with changing temperature. Exothermic and endothermic phase transitions can be detected in a small amount of material attached to such a cantilever (Berger et al. 1996). Photothermal spectroscopy can be performed by using a bimaterial cantilever upon light irradiation (Galaxy 1994). Furthermore, a bimaterial cantilever has been found to show oscillatory behaviour (Gimzewski et al. 1994). A gold-coated cantilever has been found

to produce a change in surface stress (Berger et al. 1997). The mass change by evaporation from a sample mounted on the apex of a cantilever can be determined by measuring the resonance frequency shift of the cantilever. This oscillation technique can also be used to characterize environmental conditions by tracking the resonance frequency of a cantilever coated with a sensor layer. By attaching a sample to the apex of an oscillating cantilever, mass changes of the sample can be observed as a function of temperature (Berger et al. 1998). This structure can be also used as an energy harvester, that is, the mechanical strain produced by its oscillation can be converted into electric current or voltage by using a piezoelectric material.

In this chapter, we will show different structures with a suspended part designed in different technologies and for different purposes. First, printed cantilevers are presented, showing different strategies to fabricate them and their characterization. Then, two different kinds of devices that use MEMS technology are deeply studied: a silicon energy harvester, designed with the aim of broadening its quality factor, and a capacitive microphone. These last structures have not been fabricated yet but a deep modelling study has been carried out. The fabrication techniques are very different in the three cases, and details are thus provided in the corresponding section, as well as the obtained results.

4.1   Printed cantilever by printed sacrificial layer

The interest in printed electronics is growing due to the versatility that it provides to electronics systems. There are diverse advantages in these technologies such as flexible substrates, low-cost materials, degradability and biocompatibility. Most efforts have focused in printed sensors and thin film transistors (TFT) but there are still some aspects that should be improved in terms of performance.

Suspended structures are a fabrication feature not totally resolved by printed techniques. The significance of this kind of constructions is the wide range of applications that it can cover, from switches to harvesters and sensors. The main problem to achieve them by printing is the sacrificial layer. This layer is not permanent and is eventually released at some point of the fabrication process. The fact of using a sacrificial layer is either to help to define cavities

below another layer or to protect the layer underneath during the fabrication process. This layer has to be smooth enough to deposit on it a consistent layer and an easy and non-destructive method of removal must exist.

Several approaches have been followed to face this challenge. Lam et al.(Lam, Li and Schmidt 2009) presented a poly(methyl methacrylate) (PMMA) sacrificial layer to develop a cantilever by screen printing. The releasing method was based in chloroform baths and dried N_2 gun. Park et al. (Park et al. 2012, Park et al. 2011) also used PMMA solution as sacrificial layer to develop an ink-jetted switch. In this case, the PMMA was removed by an acetone bath. Castille et al. (Castille, Dufour and Lucat 2010) used a carbonate-based sacrificial layer which was released by immersing the device in a H_3PO_4 aqueous solution. Nathalie Serra et al. (Serra 2012, Serra et al. 2011) employed a solution based on trimethylolethane (TME) to develop bridges and cantilevers by screen printing. This layer is removed by thermal treatment, reducing the abrasive method of a bath. The problem of this sublimated layer is the limited temperature to cure inks and the need of using another structural layer to avoid reactions between the sacrificial layer and the electrical layer that can change the sublimation temperature. In general terms, the main problems of these fabrication methods are the printability of the sacrificial layer as well as its thermal and mechanical stability.

Regarding the substrates, different materials have already been tested. Fuller et al. (Fuller, Wilhelm and Jacobson 2002) used glass to develop cantilevers by inkjet printing. Park et al. (Park et al. 2012) chose a silicon substrate to fabricate their devices. Wei et al. (Wei et al. 2013a, Wei et al. 2013b, Wei et al. 2012a, Wei et al. 2012b, Wei et al. 2012c) fabricated cantilevers on cotton by screen printing to develop force sensors. Alumina substrate has been chosen to manufacture suspended structures for several authors (Serra 2012, Serra et al. 2011, Lakhmi et al. 2010, Lakhmi et al. 2013, Lucat et al. 2008). Very few examples have been developed on flexible substrate since the fabrication is more challenging. There are some examples of microelectromechamical switches developed on polyimide substrate (Nakano et al. 2008, Yokota et al. 2008) or electrostatic microactuators made of a flexible sheet (Ataka et al. 2013).

In this section, we will describe different approaches to fabricate full printed cantilevers by using a sacrificial layer. Particularly, we want to manufacture a printed cantilever on plastic foil by printing techniques to work as an accelerometer to test its performance. After modelling an accelerometer based on a cantilever structure, different techniques and materials have been tested to manufacture it based on a surface micromachining process. In this respect, we have tested 4 different materials as sacrificial layers: poly(methyl methacrylate) (PMMA), photoresist, copper and trimethylolethane (TME). Three different silver inks, conductive epoxy, copper and graphene ink have been assessed as structural materials. Two substrates have been evaluated: polyethylene terephthalate (PET) and polyimide. The techniques used to develop this research have been flexography, inkjet printing and screen printing.

4.1.1 Material and methods

4.1.1.1. *Printing Technology and characterization*

Here, we are going to describe the printed techniques used for manufacturing this suspended structure. Basically, we used a roto printer Testacolor 171 (Norbert Schläfli, Switzerland) which incorporates three different printing techniques: gravure, flexography and screen printing. We just used the last two procedures. In addition to this, a flat screen printer (Novacentrics, USA) was also used for tests.

In order to make easier the cleaning process for test purposes, two masks for the flat screen printer were ordered. These masks are made of Polyester using two different mesh sizes depending on the printing material. Figure 70 shows the schematics of these masks. The sacrificial layer is shown in pink; the cantilever is drawn in red. In this case only PET substrate with no pre-treatment has been tested. We also used the Dimatix printer for inkjet printing tests.

To correctly print the different layers, the viscosity of the solutions must be carefully controlled. A viscometer Brookfield LVDV-II+PRO (Brookfield Engineering Laboratories, Inc., USA) has been used to adjust the viscosity of the prepared solutions. The study of the roughness and thickness obtained in

each step of the process has been carried out with a White Light Interferometer NT100 DMEMS (WYKO) (VEECO, Tucson, AZ, USA). The magnification objectives were 5x0.5x in VSI mode for all WYKO measurements. In order to measure the gap between the substrate and the suspended part, we have been used a Scanning Electron Microscope (SEM) (ESEM XL 30 FEG, Philips, UK) working at 2.0 kV.
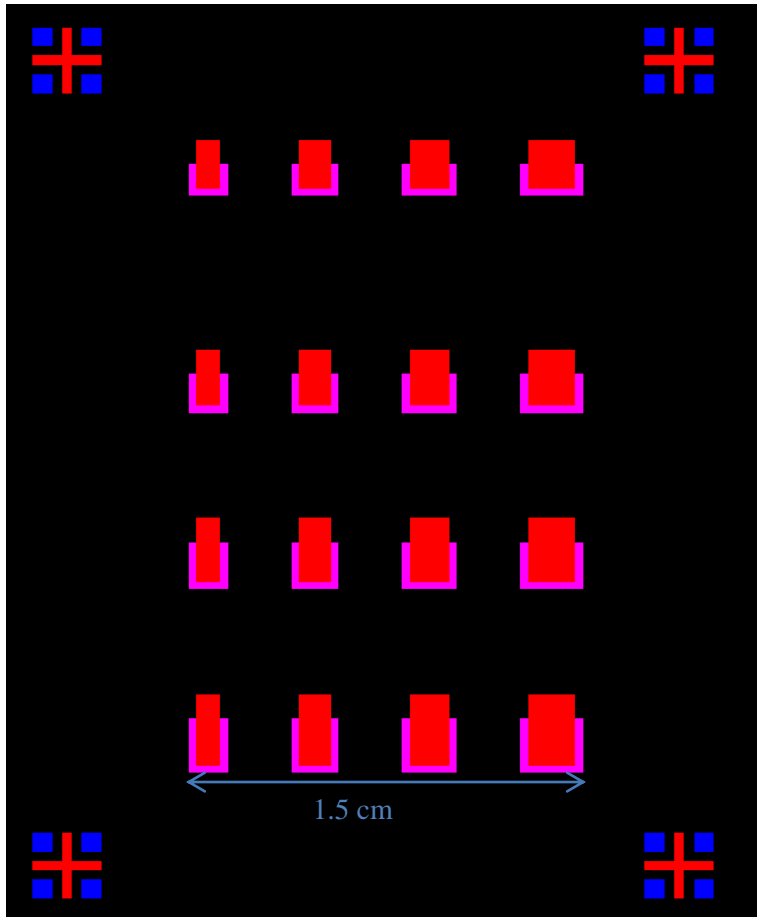
Figure 70. Flat screen printing masks.

4.1.1.2. Substrates

Two different substrates were used in the experiments: commercial polyimide (Upilex®, UBE Industries Ltd, Japan) of 50 µm thickness and 125- µm PET film (Melinex® ST506 from DuPont^{TM}, USA).

4.1.1.3. Sacrificial layers

We are going to summarize the different solutions tested as sacrificial layers and to comment the solution preparation.

PMMA

Poly(methyl methacrylate) (PMMA) is a transparent thermoplastic. A proper viscosity is required to be able to print it. There are two main approaches to get this target:

- Dissolution of solid PMMA (Sigma-Aldrich 182230) in one of these solvents (acetone, benzene, chloroform, MEK, THF, chlorobenzene, chloroform, xylene, cyclohexanone, methylene chloride, formic acid).
- Polymerization of MMA

Then, PMMA can be easily removed by using a solvent like acetone. This polymer has been already tested as sacrificial layer (Pabst et al. 2011).

i)   Dissolution in chlorobenzene

Following the first approach, we chose chlorobenzene (ClB) (Sigma-Aldrich 23570) because it is the least dangerous for human health. Several mixtures were prepared to find the best concentration in terms of printability and viscosity. After preparing the mixing, it is necessary to keep it in the fridge.

We prepared two groups of solutions during different days and measured their viscosity using the viscometer Brookfield LV DV-II+PRO.

As can be seen in Figure 71, there is no coherence between data. In order to detect the cause of this disagreement, we repeated the measurements of these mixtures for two other days. Figure 71 shows all the measured values. There is almost no significant change in temperature to induce these variations. There are two main reasons to explain these differences: It is really important to mix well before measuring the viscosity and it has to be considered that ClB evaporates very fast at ambient conditions and it is almost impossible to avoid this effect (then the viscosity is going to be surely higher when time goes by).
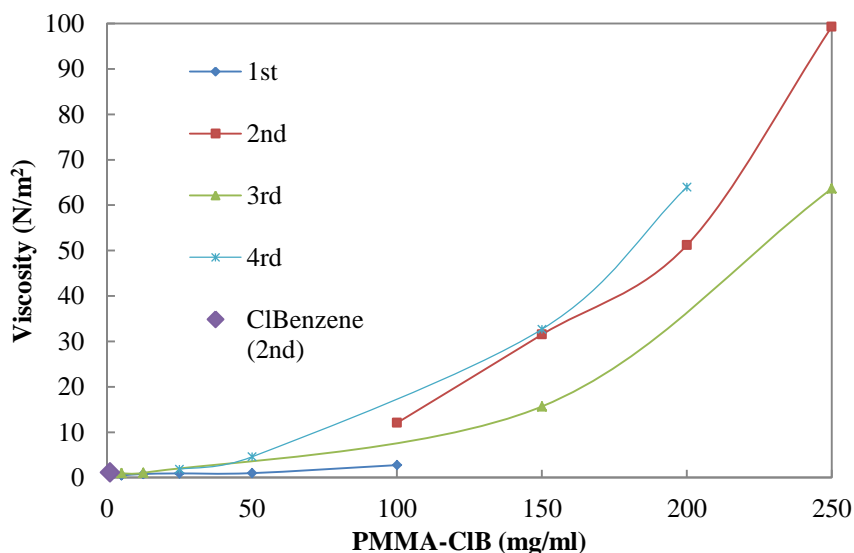
Figure 71. Viscosity measured different days, 1ˢᵗ corresponds to the oldest one.

Apart from previous concentrations, we also prepared solutions at 300 mg/ml, 350 mg/ml and 350 mg/ml.

ii)   Polymerization of MMA

The mixture for the preparation of poly(methyl methacrylate) is:

- 1 mL MMA (Sigma-Aldrich M55909). Methyl methacrylate ($CH_2=C(CH_3)COOCH_3$). It is a methyl ester of methacrylic acid (MAA); it is a monomer produced on a large scale for the production of poly(methyl methacrylate) (PMMA)
- 0.2 g AIBN (Sigma-Aldrich 441090). Azobisisobutyronitrile ($[(CH_3)_2C(CN)]_2N_2$). Used as a radical initiator producing radical species under mild conditions and promote radical reactions
- 0.4 mL EGDMA (Sigma-Aldrich 335681). Ethylene glycol dimethylacrylate used in free radical copolymer crosslinking reactions
- 16 mL toluene
- 4 mL ethanol
- 2 mg ethylcellulose (Sigma-Aldrich 538256)

A typical composition is:

- 98%MMA
- 2%AIBN
- <5% EDGMA

The preparation process is described as follows:

1. Mix solvents: 80/20% toluene/ethanol containing less than 10% ethylcellulose. Heating (below 100 ºC) and stirring until a homogenous mixture is observed.
2. Add MMA. Stirring without heating until a homogenous mixture is observed.
3. Add EGDMA. Stirring without heating until a homogenous mixture is observed.
4. Add AIBN. Advice: Add organic colorant to better recognition. Stirring without heating until a homogenous mixture is observed.

After that, the mixture must be kept in cold ambient.

After printing, it is necessary to dry it during 1 hour at 80 °C.

TME

Trimethylolethane (TME) is a versatile polyol with significant quality features. It has three hydroxyl groups of primary alcohol type used in different polyol applications.

We found some different ways to prepare a paste using TME (Sigma-Aldrich T87807):

- TMP/TME. (Trimethylolpropane) Solvents: Cyclohexanol (CH) (Sigma-Aldrich 105899), water and propyleneglycol (PG) (Sigma-Aldrich 82280) (Serra 2012, Serra et al. 2011, Serra et al. 2009).
- NPG/TME. (Neopentyl glycol or 2,2-Dimethyl-1,3-propanediol) (Sigma-Aldrich 538256). Solvents: CH and water (Serra 2012, Serra et al. 2011, Serra et al. 2009).
- DMHD/TME (2,5-Dimethyl-2,5-hexanediol). Solvents: CH and water (Serra 2012, Serra et al. 2011, Serra et al. 2009).
- TME. Solvents: CH and PG (Wei et al. 2012c, Wei et al. 2012b, Wei et al. 2013b, Wei et al. 2013a, Wei et al. 2012a).

We started using NPG/TME and TME:

Table 18. TME solution.

TME	CH	PG
4.25 g	3.875 g	0.5 g

As PG is just supposed to stabilize the boiling point, we also used TME just with CH and water (the same concentrations as Table 18, but water instead of PG).

The substrate is PET 125 µm without plasma treatment in all these experiments and no pre-treatment. After preparing the solutions, they must be at ambient temperature.

Regardless of the chosen mixture, all the components are added together and stirring and heating (below 90 °C) are necessary (using a hot plate). Normally, a long time is required to properly mix all the components.

The temperature has been normally set around 60 ºC (depending on the used hot plate, the temperature can be more or less accurate) and left the mixture at this temperature for more than 7 hours. The time depends on the amount of prepared mixture and the size of TME blocks.

Note: TME films cannot be analyzed by WYKO because there is no reflection of the incident light: all the light is absorbed by the sample.

Copper

We tested the copper ink (Metalon ICI-021) that can be easily removed with water.

Photoresist

The sacrificial layer is based on shipley photoresist (Shipley MICROPOSIT S1813). This layer can be removed by acetone bath.

Table 19 summarizes all materials and its variants used as sacrificial layer.

Table 19. Material tested as sacrificial layer.

Material	Types
PMMA	Dissolution of solid PMMA with chlorobenzene
	Polymerization of methyl methacrylate (MMA)
TME	Neopentyl glycol + Ciclohexanol + Water+ TME
	Ciclohexanol + Water+ TME
	Ciclohexanol + Propylene glycol+ TME
Copper	Metalon ICI-021
Photoresit	Shipley MICROPOSIT S1813

4.1.1.4. Structural materials

Table 20 summarizes all materials and its variants used as structural layer.

Table 20. Material tested as structural layer.

Material	Types
Silver	Dupont, Suntronic U5603 for inkjet printing
	InkTec Tec-Pr-020 for gravure
	Dupont 5064H for screen printing
Copper	Metalon ICI-021
Grapene	Vor-ink^{TM} X103
Conductive Epoxy	H20 Epo-Tex

4.1.2 Sensor design

To design a capacitive accelerometer it is necessary to model the variation of capacitance due to an applied force. There are different ways to simulate this effect in COMSOL Multiphysics 4.2a. In this study, we chose the electromechanics module which integrates both solid mechanics and electrostatics physics in just one node and avoids coupling different modules and directly implements the moving mesh (after deforming the geometry due to the applied forced, this module recalculates the mesh).

Through simulations, we were looking at a resonance frequency high enough to avoid fractures (above 1 kHz) and enough sensitivity to detect changes in the applied force (at least 0.1 pF/g). Then, the best compromise between dimensions and sensitivity (F/ms^{-2}) is shown in Table 21.

Table 21. Modelled cantilever.

Parameter	Value	Description
Length	0.8 mm	Length of the beam
Width	0.7 mm	Width of the beam. Electrodes are square of this size
t_electrodes	6.0 μm	Thickness of electrodes
Gap	4.25 μm	Thickness of the pillar/ Distance between beam and substrate
t_beam	6.0 μm	Thickness of the beam

Figure 72a illustrated a z-x view of the cantilever. Figure 72b shows the geometry modelled with the simulator.
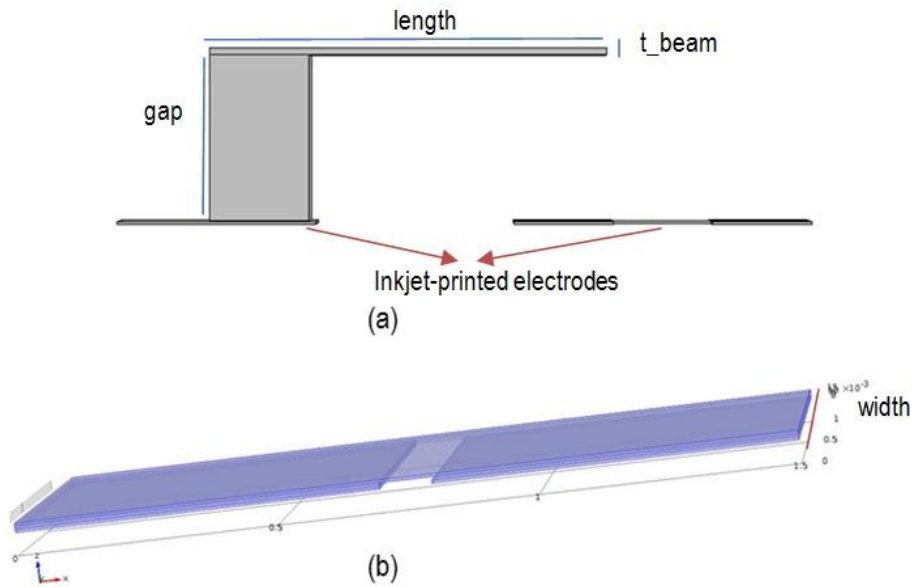
Figure 72. (a) Schematics of the cantilever. (b) Model in COMSOL Multiphysics.

The stationary analysis was done applying a force

$$F = Ng\rho$$

(28)

where g is the gravity constant, ρ is the structural material density and N is a rational number (N=1, 2, 3, etc.). We also include a damping factor equal to $\eta = 2\xi$, (fixing ξ to the worst case for metals $\xi_{metals} < 0.01$) (Cremer and Heckl 1988). This damping factor is just the intrinsic one but as we had no

experimental results we can only work with this value. We have done a parametrical analysis varying N from 0.25 to 1 and the found sensitivity is 104 fF/ ms^{-2} (Figure 73).
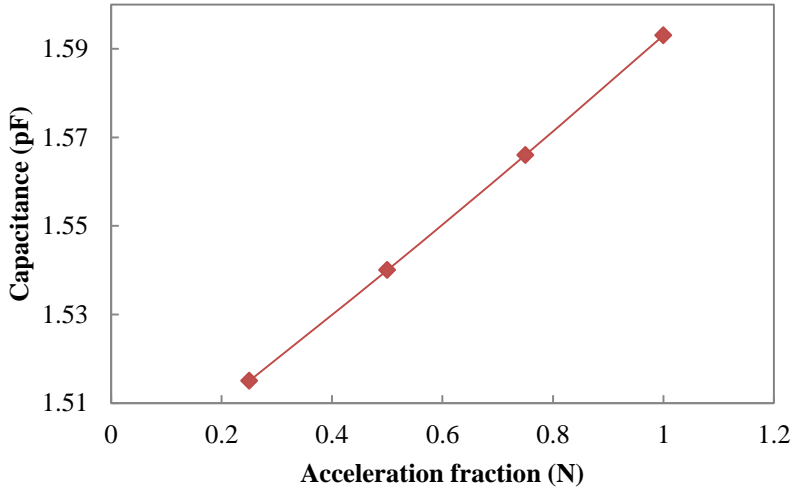
Figure 73. Capacitance vs. Force.

These results can be modelled following the equation:

$$C(pF) = 0.104N + 1.4885, \quad R^2 = 0.9997 \qquad (29)$$

To see the effect of the polarization of the struture, we also run a parameter analysis varying the applied force from 1 to 100 V and the change in the capacitance can be neglected compared to the change induced by the applied force.

As the geometry was changed from the previous analysis, we recalculated the resonance frequency for the chosen geometry. The found value is 4.5 kHz. This frequency is still high enough to work as an accelerometer.

4.1.3 Results and discussion

In this section, we are going to explain all the experiments that were carried out, including all the sacrificial layers tested and its compatibility with the different structural materials used.

4.1.3.1 Sacrificial layers

Dissolved PMMA

i)   *Flexography*

We tested the printability of these PMMA solutions on polyimide without any pre-treatment.

The results are not promising. As can be seen, there is not continuity in the samples and the adhesion is really poor. Apart from the mask, which is not the proper one for this ink, the ink dries extremely fast and the process do not seem compatible with this ink.
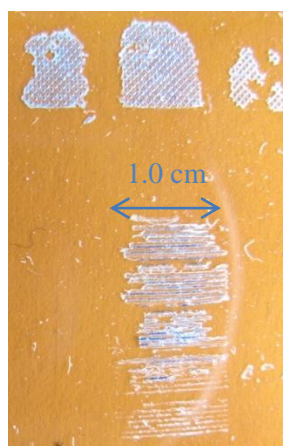
Figure 74. PMMA-ClB on PI substrate by flexo after drying 1 hour at 130 ºC.

ii)   *Screen printing*

We printed these PMMA solutions on polyimide (PI) and PET substrates without any pre-treatment.

Although samples are not good enough, they are better than flexography results. At first glance, the printability seems better in PI than PET. After analyzing them with White Light Interferometer NT100 DMEMS (WYKO), the coffering effect is greater in PI than PET, resulting in higher roughness (see Figure 75 and Figure 76). Then, we tested PET with plasma treatment and the continuity of the samples was improved.

Regretfully, the inks also dry too fast to have good ink transference and reproducibility.

The best results are obtained with PMMA/ClB concentrations between 200-300 mg/ml.
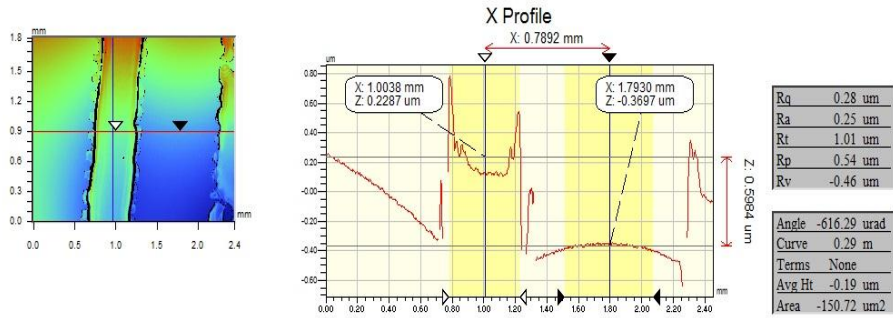
Figure 75. 200ml/mg PMMA-ClB on PI substrate by roto screen printing.
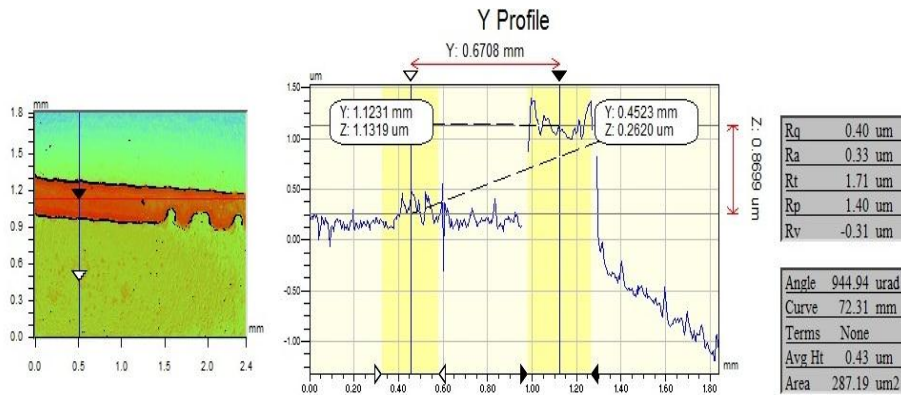
Figure 76. 200ml/mg PMMA-ClB on PET substrate by roto screen printing (without plasma treatment).

iii)   Planar screen printer

Surprisingly, the adhesion with this technique is pretty good. Since the printing process is faster than roto printing, the ink transfer is faster than the drying. Furthermore, the printing patterns are smaller than the roto printer mask, helping the success of this process. Here, I only tested 200 and 250 mg/ml PMMA/ClB concentrations.

Figure 77 shows a sample of this ink on PET. The thickness is about 1.6 µm although the expected value is around 5 µm. This thickness is much better than the one obtained by roto screen printing (about 0.9 µm) but this can be just a direct consequence of the used mask in each case.

The used roller in roto printing was not designed for this purpose in terms of mesh which directly affects the thickness, whereas the mask in flat screen was specially manufactured for this ink and the desired thickness. Regarding roughness, the measured value is about 0.77 µm that is suitable for our target.
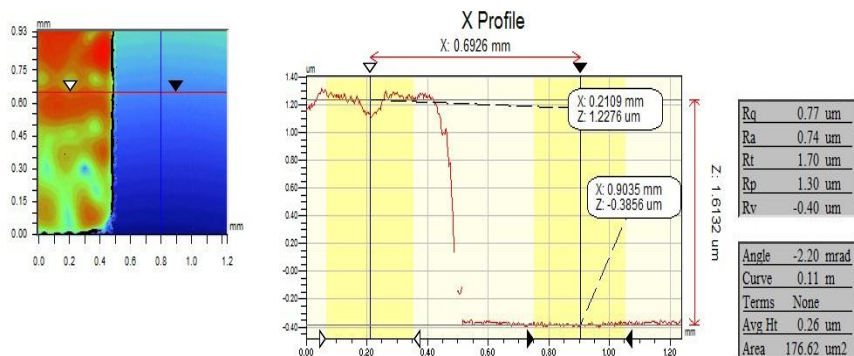
Figure 77. 250mg/ml PMMA-ClB on PET substrate by flat screen printing.

Polymerization of MMA

This ink can be only tested in the flat screen printed because it contains toluene and needs air extraction to work with and there is no good ventilation in the room where the roto printed is located. This ink has only been tested on PET substrate.

Results are similar to the ones shown with the solubilisation of PMMA, and then we just focused our experiments on PMMA-ClB solution to make further tests because the toxicity of toluene is higher than chlorobenzene.

TME

i)   *TME+NPG+CH+H$_2$O*

This type of solution was tested with roto screen printing and planar printer.

In both cases, the printability is not good enough. After drying at ambient conditions, the TME solutions are partially powder (Figure 78). This problem lies in the mixture of TME, NPG and CH. These components form a ternary mixture not well-known and depending extremely of the manufacturing conditions (temperature, sintering, and order of adding elements and so on) the mixture can result in failure or success.

2 cm

Figure 78. TME+NPG on PET substrate by flat screen printing.

ii)   *TME+CH+H$_2$O*

This type of solution was tested with planar printer. After drying at ambient conditions, the solid layer is not homogenous, less than the previous example.

iii)   *TME+CH+PG*

This type of solution was tested with planar printer. This mixture shows better results than the others, therefore, this is the one to be used for further tests (Figure 79).
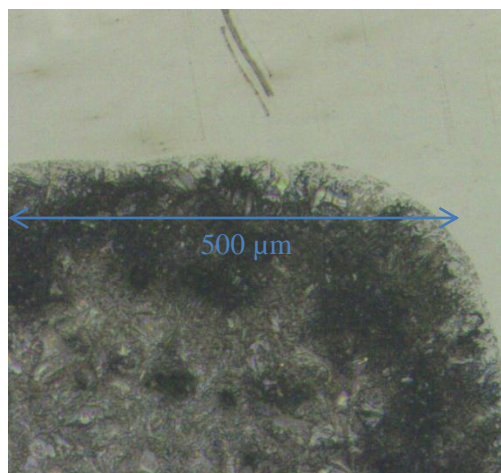
Figure 79. TME+CH+PG on PET substrate by flat screen printing.

The type of squeegee affects the homogeneity of the printed silver layer. In this case, better results have been obtained with the bigger squeeze.

Note: It is very important to control the drying temperature (below 80°C). We normally dried at 60 ºC during 5 minutes and then waited 1 hour at ambient temperature before printing on TME. We also tried to dry it only at ambient temperature and worked properly but this procedure needs more time before printing on it. We tried to measure the viscosity but it is extremely high for the viscometer.

Copper

The substrate is PET without plasma treatment. This type of solution was tested with planar printer. The copper was printed on a layer of screen printer silver (Figure 80).

The used copper ink is based in copper oxide, then after printing is necessary to reduced it to get copper.
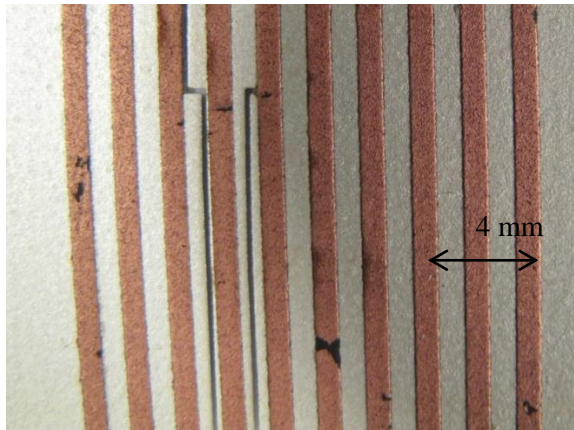
Figure 80. Copper oxide on screen silver ink by flat screen printing.

The main problem found here is that the solution needed to remove copper is based on chloride (Iron (III) chloride, Schneider). Silver reacts faster than copper with chlorine resulting in a non-conductive component.
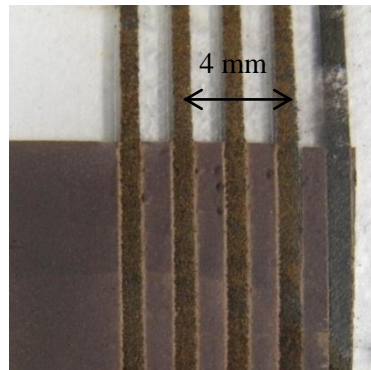
Figure 81. Reduced copper on screen silver ink by flat screen printing and treated with iron chloride solution.

One solution could be looked for another solution to remove copper or find another conductive material which is not affected by chloride but the remaining problem is that the reduction of copper oxide is not homogenous enough to be used as sacrificial layer.

Photoresist

The shipley photoresist is inkjet printed and the substrate PET is kept at 45 °C. The problem is the instability of this ink. If one nozzle is working well,

after cleaning process, it is barely impossible to get the same nozzle properly working.

4.1.3.2. Structural materials

Inkjet silver ink

This silver ink (Dupont, Suntronic U5603) was inkjet printed on PMMA and TME. PMMA is compatible with Suntronic, while TME is dissolved with it. This was only a preliminary test to know compatibilities. To do so, just one layer was printed. The thicknesses were not measured.

Copper

This ink was just printed with the flat screen printer on TME layers. The adhesion and printability are good. After sintering, copper was reduced with the Xenon lamp (PulseForge 3300, Novacentrix, Germany) and it was almost totally reduced. The problem is that copper react with TME mixture and cannot be totally removed (Figure 82). The thickness was not measured.
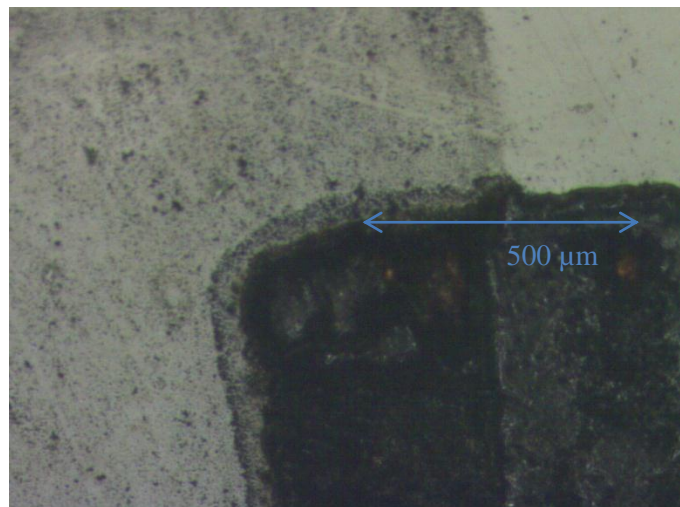
Figure 82. One copper layer on one TME+CH+PG layer after trying to remove the sacrificial layer heating at 130 °C.

Conductive Silver Epoxy

The epoxy (H20 Epo-Tex) was just printed with the flat screen printer on PMMA and TME layers. Here, only the samples with TME were analyzed. Although the roughness is quite high, there is a step of about 3.8 μm between the part not covered with epoxy and the covered one (Figure 83).
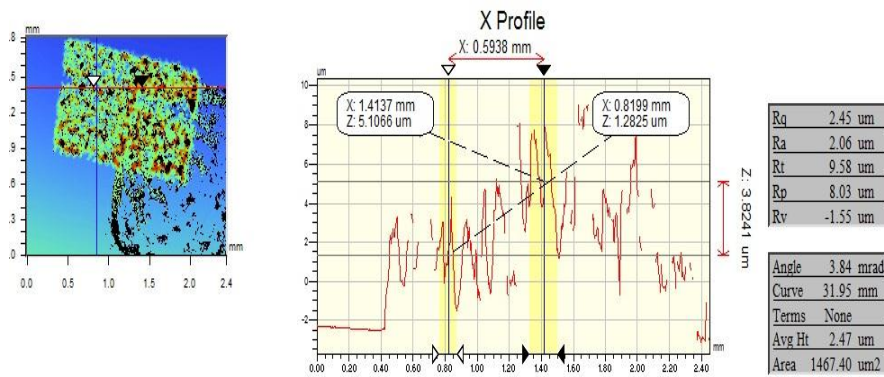
Figure 83. One conductive expoxy layer on two TME+CH+PG layers by flat screen printing. The TME layer is about 1.3 μm thick whereas the epoxy on TME is about 5.1 μm thick.

The printability is pretty good but conductive epoxy reacts with TME, disabling TME to be removed by heating (Figure 84).
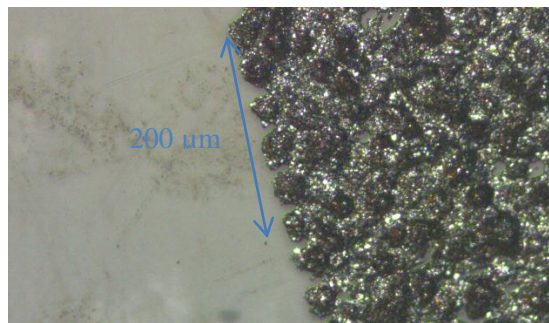
Figure 84. One conductive expoxy layer on two TME+CH+PG layers by flat screen printing after heating at 130°C for more than 12 hours. There is some powder that indicates the sacrificial layer is not totally removed. The TME layer is about 1.3 μm thick whereas the epoxy on TME is about 5.1 μm thick.

Graphene

This ink (Vor-ink^{TM} X103) was just printed with the planar printed on PMMA and TME layers. Both layers resist the ink. Concerning PMMA, it cannot be removed with acetone without removing graphene too (Figure 85 shows the result before trying to remove the PMMA-ClB solution); but this removal process seems to work with toluene.
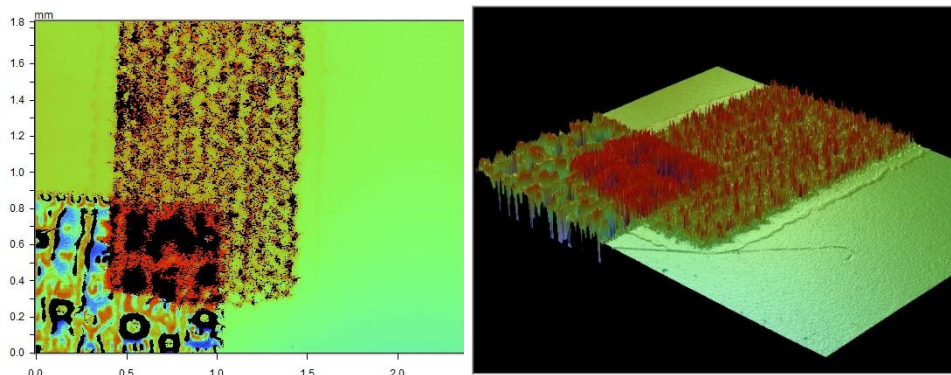
Figure 85. One graphene layer on one PMMA-ClB layer solution by flat screen printing. The PMMA layer is about 3.1 µm thick whereas the graphene on PMMA is about 4.9 µm thick.

Regarding the TME, graphene reacts with TME disabling it from being removed by heating (Figure 86).
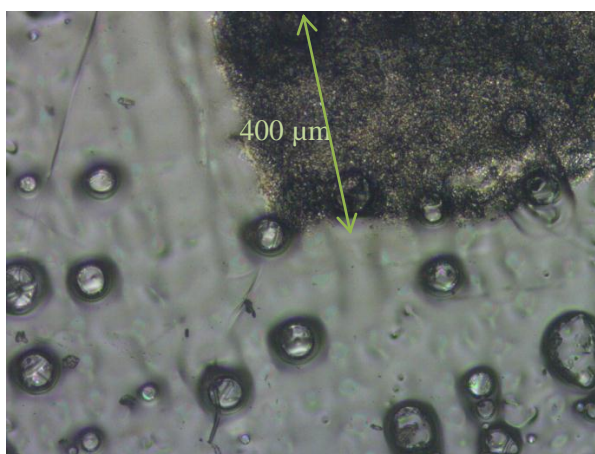
Figure 86. One graphene layer on one TME+CH+PG layer by flat screen printing after heating at 130 °C during 1 hour. No physical characterization was done after this step.

Gravure silver

This ink (InkTec Tec-Pr-020) was just printed with the flat screen printer on TME layers. Gravure nanoparticle silver ink reacts with TME avoiding TME to be removed by heating (Figure 87). Furthermore, the adhesion is not good.
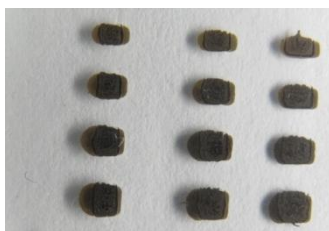
Figure 87. Gravure silver ink on TME+CH+PG after sintering and drying at 130 °C during 1 hour.

Note. Solvents of gravure silver ink: 2-ethyl-1-hexanol ($< 30\%$) and alpha-terpineol ($< 28\%$) and particulate silver of 40%.

Screen silver

This ink (Dupont 5064H) was just printed with the flat screen printer on PMMA and TME layers.

Regarding PMMA and silver compatibility, both layers can be appreciated in Figure 88. The effect of the type of squeeze to the homogeneity of the printed silver layer has been tested. In this case, better results have been obtained with the smaller squeeze.

The problem is that a plastic film is formed around the printed area, while removing the PMMA layer. Note. Solvents of screen silver ink: Ketone (20%) and dimethyl succinate (5%) and particulate silver 65%.
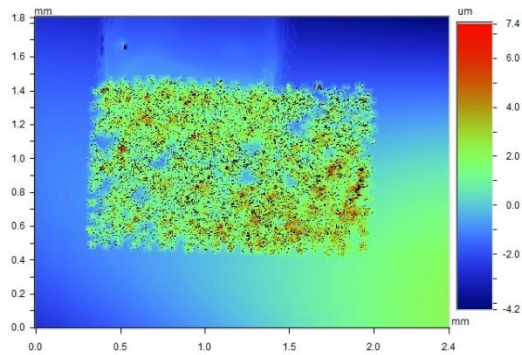
Figure 88. One screen silver ink layer on one PMMA-ClB (big squeegee) layer solution after sintering.

Finally, the best tested combination has been screen silver ink on TME+CH+PG mixture. Figure 89 shows a thick and well defined layer of silver (around 5 µm thickness and less than 1.5 µm roughness) before removing process of sacrificial layer. Comparing to other combinations, here there is no TME presence after thermal removing, at least, at first glance (Figure 90).

Figure 91 presents the printed structure after removing the sacrificial layer. Two different regions can be perfectly appreciated, one of 4.3 µm thickness (where TME was before) and another one of 2.1 µm thickness. Figure 92 shows a SEM image, where the border between both areas can be perfectly recognized.
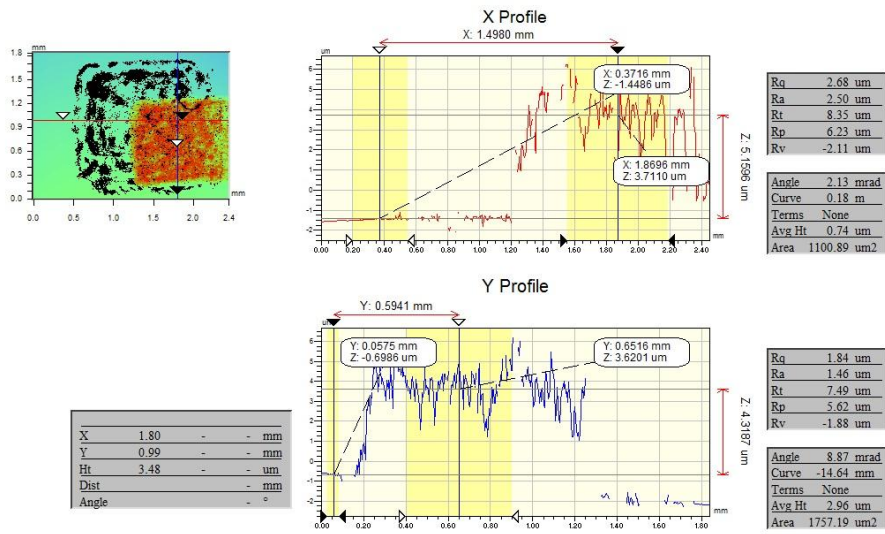
Figure 89. Screen silver ink on TME+CH+PG solution after IR sintering (NIR120 adphos). 2 layers of TME solution and 1 layer of silver ink. The total thickness where silver and TME are printed is between 4.3 μm and 5.2 μm.
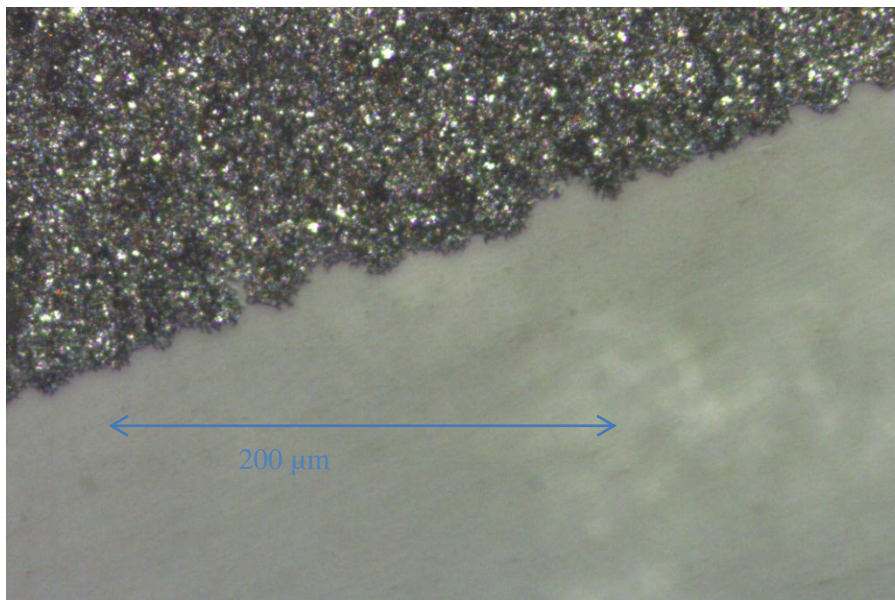
Figure 90. Screen silver layer after removing TME film at 130 °C during 1 hour. 2 layers of TME solution and 1 layer of silver ink. Physical characterization is shown in Figure 91.
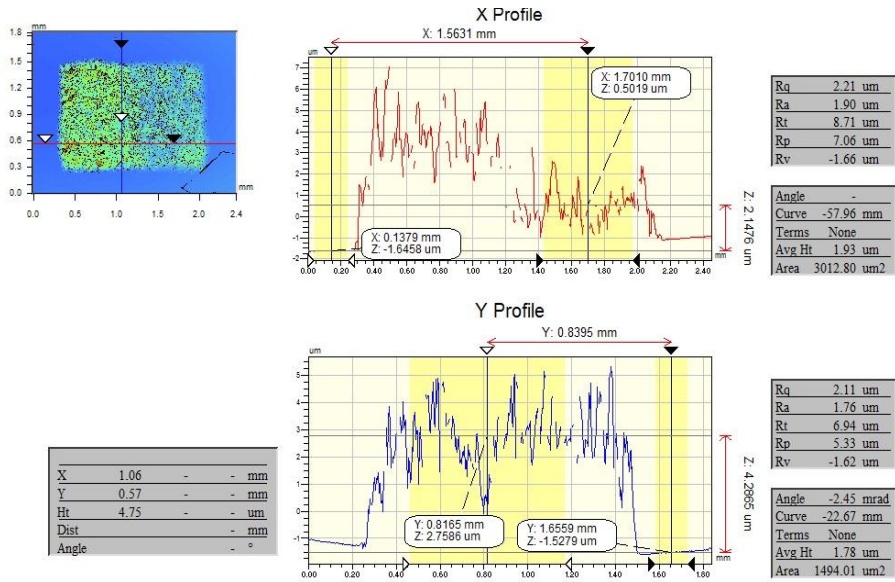
Figure 91. Screen silver ink on TME+CH+PG solution after sintering and drying. 2 layers of TME solution and 1 layer of silver ink. The smallest area (where no TME was printed) is about 2.1 µm. The biggest area (where TME was printed and sublimated) is about 4.3 µm.
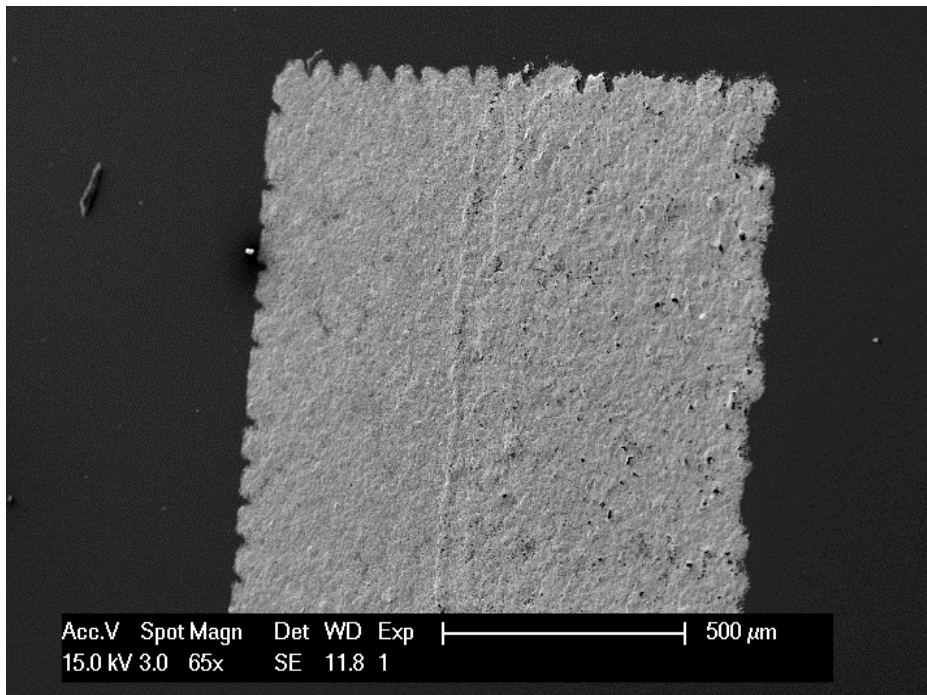
Figure 92. SEM image of sample shows in Figure 91.

4.1.3.3 Cantilever

Figure 93 shows the created interface of both layers (anchor and suspended layer). Figure 94 shows a lateral SEM image where a hole can be perfectly appreciated. In Figure 95, the height of the suspended areas is measured and agrees with the expected results according to Figure 91 and it is about 4 μm. The fabrication process can be summarized as follows:

1. Two flat screen printed layers of TME+CH+PG with the big squeegee on 125 μm PET foil (no pre-treatment was done). The printed layers were done in a row (no drying between them).
2. Drying at room temperature during 1 hour.
3. One flat screen printed layer of screen silver ink with the small squeegee.
4. Sintering with near IR lamp (two manual and sequential cycles. Power level of 90% and distance of 30mm).
5. Heating at 130 °C during 1 hour to remove the sacrificial layer.

On one hand, it is possible to thermally remove TME. This can be improved by introducing samples in the oven at temperature above 130 °C but not below, and then waiting enough time to allow all TME solution sublimatation.

On the other hand, hollow spaces can be obtained; this is the first step to actually build a cantilever. Using the flat screen printed is quite difficult to control the applied pressure, the distance between the screen and the substrate and the alignment of layers. As all these parameters can be controlled in the roto printer, we think the same process can success in manufacturing cantilevers.
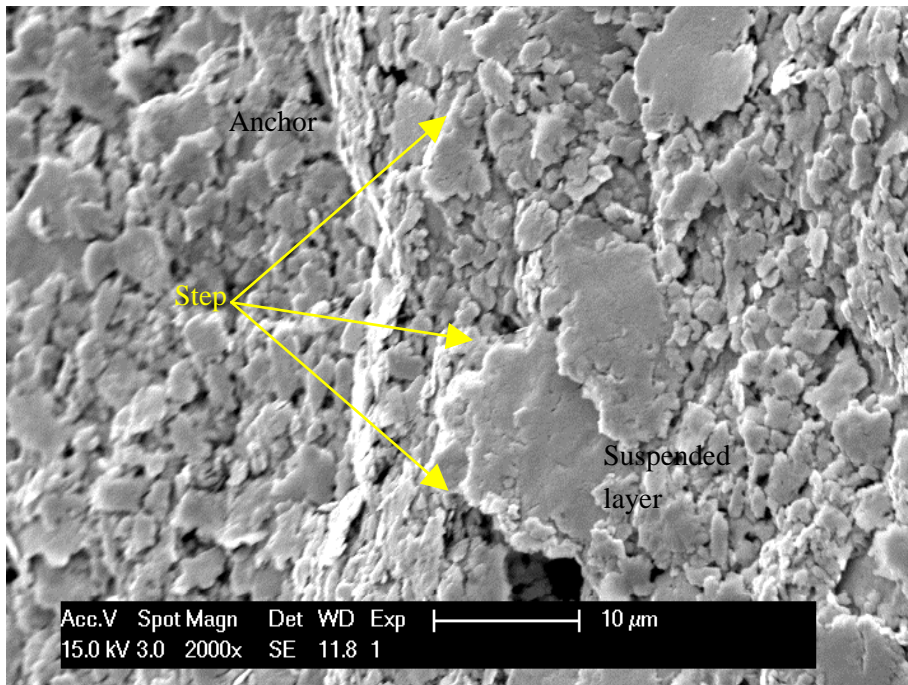
Figure 93. Silver screen layer after removing TME layer.
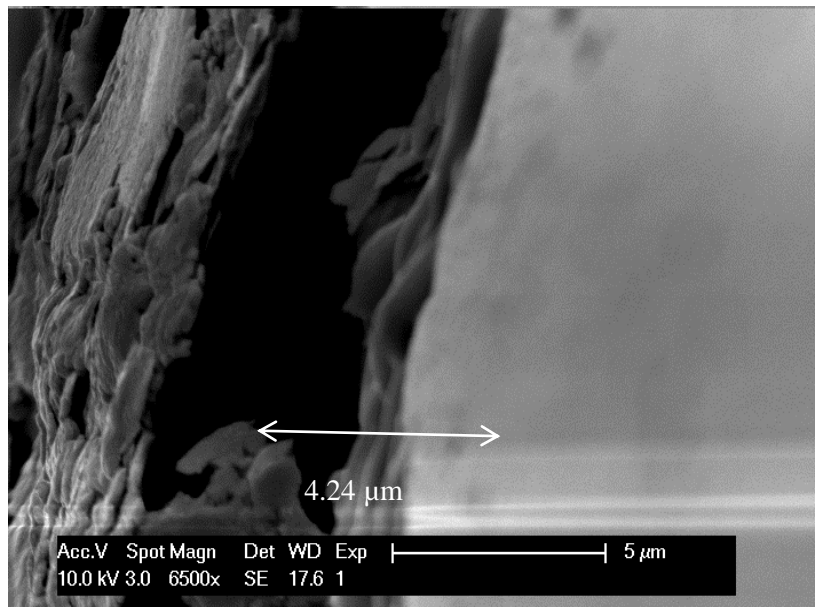
Figure 94. Lateral image of Silver screen layer after removing TME solution. Here, a partially suspended area is shown.
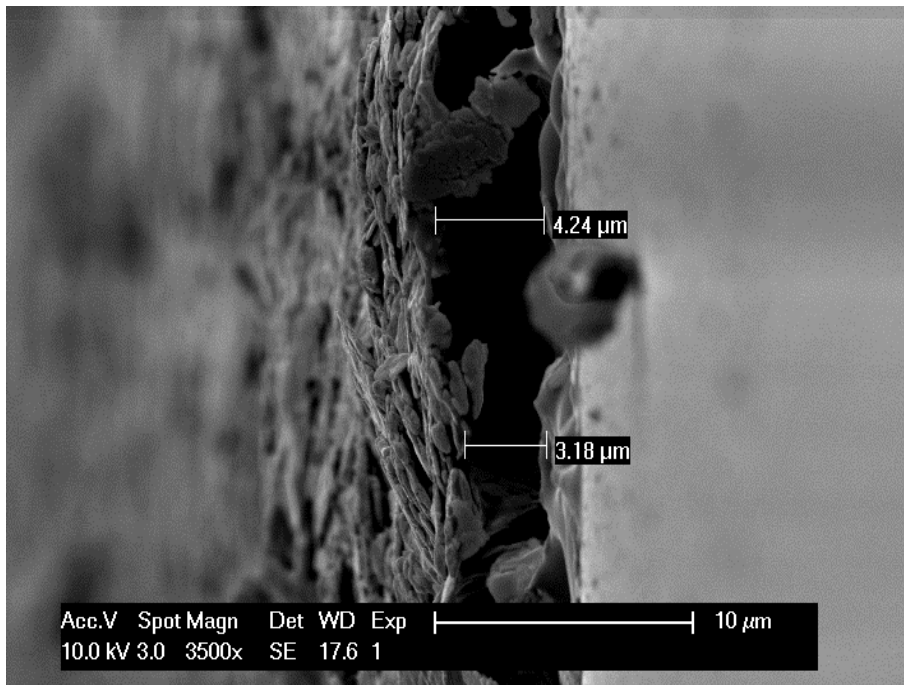
Figure 95. Lateral image of Silver screen layer after removing TME solution. Here, a partially suspended area is shown. This suspended region is 3-4 µm height that agrees with results shows in Figure 91.

In order to face the problems related to the flat screen printer, we developed the same process but using the roto screen printer. Two rollers were prepared with the same layouts presented in Figure 70. Thereby, we solved the alignments problems and also the pressure and the distance were controlled while printing.

The whole cantilever can be easily fabricated by adding one initial step: a thin inkjet-printed electrode below the active area (see Figure 96).
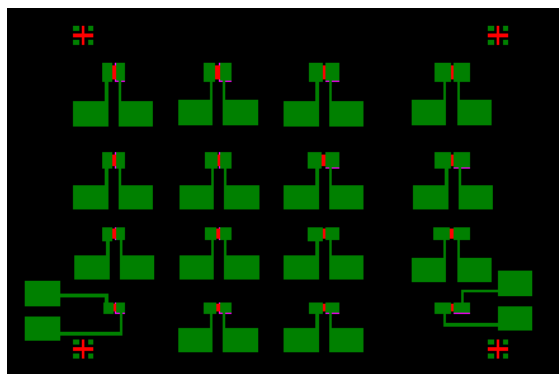
Figure 96. Bottom electrodes to functionalize the printed cantilever (in green).

First, the bottom electrodes were printed by inkjet printing with silver ink. It was necessary to dry and sinter them in the oven at 130 ºC during 1 hour. After several experiments, we found that the best combination was 2 layers of TME and at least 4 layers of silver ink. After printing the sacrificial layer, we had to wait at least for one hour at ambient conditions before printing the structural layer. Figure 97 shows the alignment between the sacrificial layer and the inkjetted electrodes.
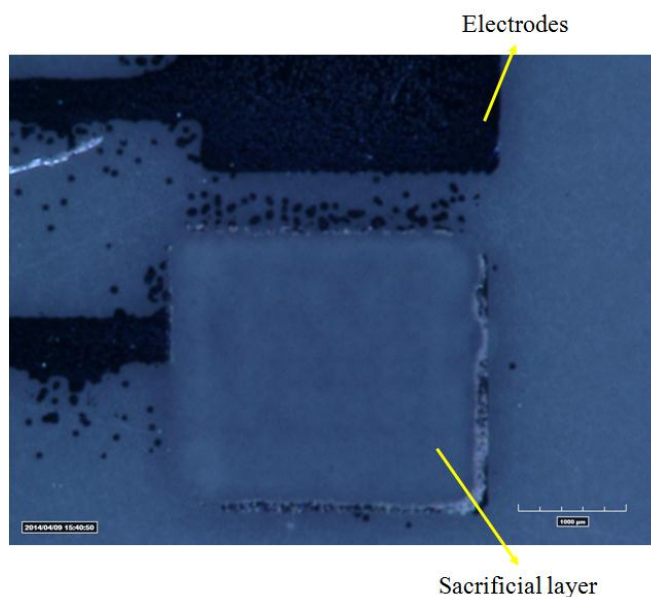
Figure 97. Microscope picture of the inkjetted electrodes with deposited sacrificial layer.
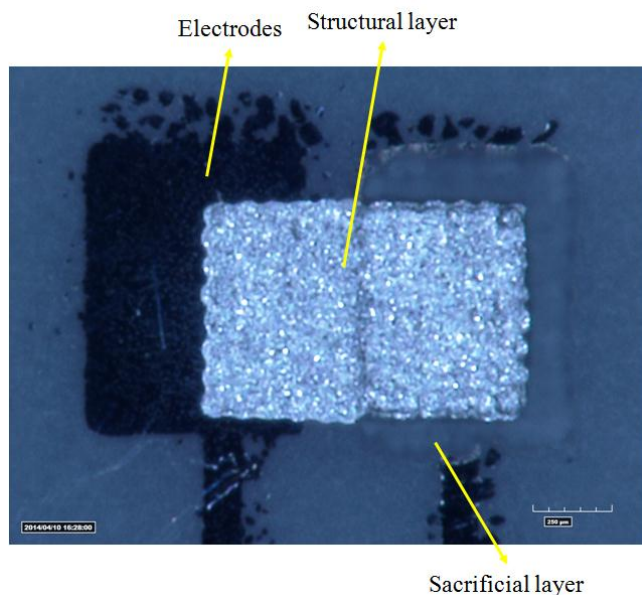
Figure 98. Microscope picture of the inkjetted electrodes with deposited sacrificial layer and structural layer without removal in the oven.
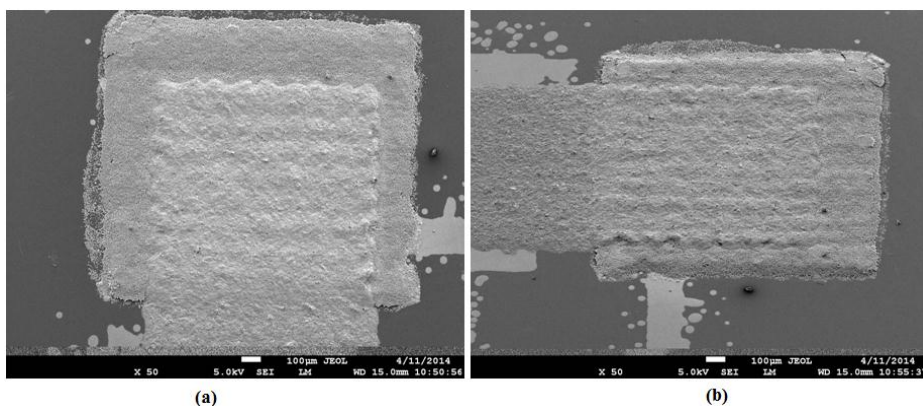
Figure 99. SEM image of the inkjetted electrodes with deposited sacrificial layer and structural layer without removal in the oven.

After printing the structural layer, we tried two different sintering processes: directly using the IR lamp; and first ink dry and then oven sintering. There were inappreciable differences between both procedures, so we decided to use the latter one. In this regard, we left the samples for at least 20 min at ambient conditions in order to be well dried and after that we introduced the samples in the oven for at least 1 hour at 130 ºC.

Figure 98 and Figure 99 present the structural material printed on top of electrodes and sacrificial layer and the result after 1 hour in the oven at 130 ºC is depicted in Figure 100 and Figure 101. Although some suspended part can be appreciated, there are still sacrificial layer traces in the structure. Figure 102 and Figure 103 present the results after 5 hours in the oven at the same temperature. There are still traces of the sacrificial layer but thinner than the results with only 1 hour of oven. Anyway, the structural silver layer seems too thin to support the removal of the sacrificial layer.
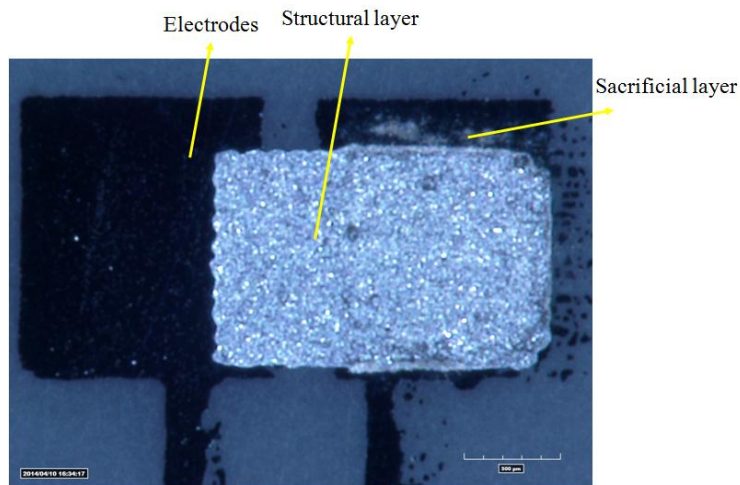
Figure 100. Microscope picture of the inkjetted electrodes with deposited sacrificial layer and structural layer after 1 hour at 130 ºC in the oven.
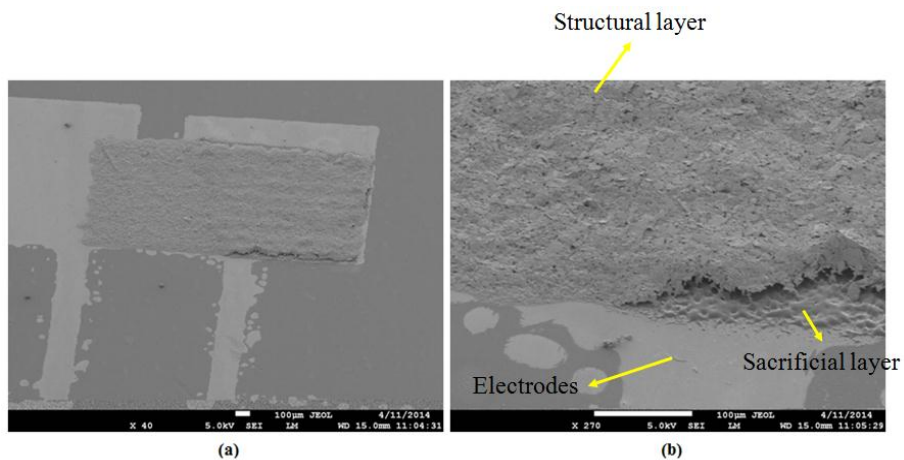
Figure 101. SEM image of the inkjetted electrodes with deposited sacrificial layer and structural layer after 1 hour at 130 ºC in the oven.
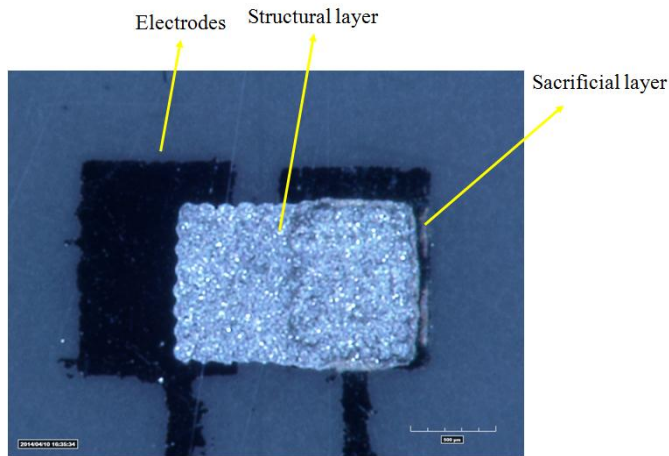
Figure 102. Microscope picture of the inkjetted electrodes with deposited sacrificial layer and structural layer after 5 hours at 130 ºC in the oven.
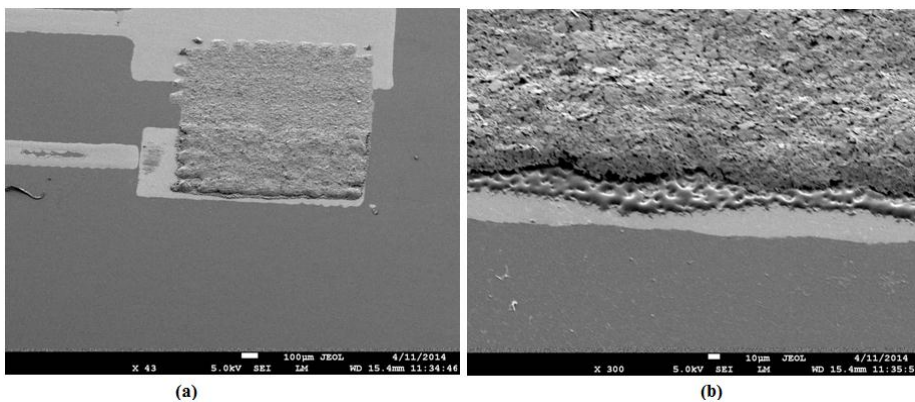
Figure 103. SEM image of the inkjetted electrodes with deposited sacrificial layer and structural layer after 5 hours at 130 ºC in the oven.

4.2   Printed cantilever following bonding philosophy

Here we present the design, fabrication and characterization of a full printed cantilever on foil substrate. The structural material of this cantilever is silver ink and the sacrificial layer is a PMMA film. One difference of this device to others that use the same sacrificial material is the direct use of a commercial film but the main difference remains in the collocation of this layer, instead of being between the substrate and the beam, it is placed on top of the beam. In addition to this, the substrate is a plastic foil which provides less stability

to the manufacturing process of the cantilever but gives more flexibility to this device.

4.2.1 **Design**

Given the complicated geometry of the printed cantilever, we have skipped the development of an analytical model and we have directly used a multiphysics numerical simulator: COMSOL Multiphysics 4.2a (COMSOL Inc., Stockholm, Sweden). This software based on partial differential equations with the finite element method has previously been used to calculate displacements and resonance frequencies in similar structures (Rivadeneyra et al. 2012, Emam 2008).

We have studied not only the mechanical response of the device but also its electrical behavior. We have used this simulation tool to model the resonance frequency of this device, the deflection when a force is exerted and the capacitance when this force is being applied using the electromechanics module in 3D which couples structural mechanics and electromagnetism. The boundary conditions and solvers were chosen according to the parameter studied. The substrate properties given by the manufacturer and the printed and cured conductive silver ink according to our characterization were included in the numerical simulator (Salmerón et al. 2014). Several parametrical analyses were carried out in order to obtain a sensitivity comparable with other previous studies (Serra et al. 2011), about 0.1 pF/g, and a resonance frequency high enough to avoid fractures while the structure is oscillating, above 1 kHz. The chosen dimensions are shown in Table 22.

Table 22. Dimensions of the designed suspended structure.

Parameter	Value	Description
Length (mm)	5.0	Length of the beam
Width (mm)	2.5	Width of the beam
Gap (µm)	150	Distance between the back electrode and the beam
Thickness (µm)	15	Thickness of the beam

Figure 72a illustrated a z-x view of the cantilever. Figure 72b shows the geometry modelled with the simulator.

4.2.2 Fabrication process

The cantilever was printed on Polyethylene terephthalate (PET) substrate of 75 µm thickness (ES301061 Goodfellow Cambridge Ltd., Huntingdon, UK) with a Serfix III screen printing machine (Seglevint SL, Barcelona, Spain). The screen used to manufacture the patterns by screen printing had a mesh density of 43 Nylon thread per centimetre (T/cm) in an aluminium rectangular structure of 50 cm width and 35 cm length. We chose this mesh density in order to reduce the number of printing layers to achieve the desire thickness (Salmerón et al. 2014). The DMP-2831™ Dimatix printer (Fujifilm Dimatix Inc, Santa Clara, USA) was used to print the electrodes. We decided to define them by inkjet printing because we only needed a thin layer to functionalize the cantilever. The structural materials were the conductive silver ink CRSN 2569 (Sun Chemical Corporation, Parsippany, USA) and epoxy EPO-TEK H20E (Epoxy Technology, Inc., Billerica, USA). The electrodes were made of silver nanoparticles (U5603 SunTronic Technology, San Diego, USA). The sacrificial layer is a Poly(methyl methacrylate) (PMMA) film (ME301200 Goodfellow Cambridge Ltd., Huntingdon, UK) of 50 µm thickness. The direct use of a commercial film assures a smooth surface and avoids problems related to its deposition. Furthermore, the thickness of this film is not critical to the manufacturing process.

The miniaturization of the structures is directly related to the mesh density of the screen. In our case, the cantilevers could be done half size without increasing the complexity and success of the process.

The process flow contains 6 steps as summarized below (Figure 104):

1. The beam is fabricated using the silver CRSN 2569 ink by screen printing on a PMMA film.
2. The pillar is also built by screen printing and aligned with the beam.
3. Concurrently, a layer of silver U5603 ink is printed on PET substrate by inkjet printing. A sintering of 1 hour at 160ºC is required.
4. On top of the pillar is deposited by screen printing a layer of adhesive epoxy.
5. Then, both PMMA and PET films are carefully aligned and pasted thanks to the adhesive epoxy. A sintering of 30 min at 80ºC is needed to harden the adhesive.

6. The final step is to remove the sacrificial layer. For this purpose, the device is submerged in acetone at 60ºC during 2 min. The acetone only dissolves the PMMA.
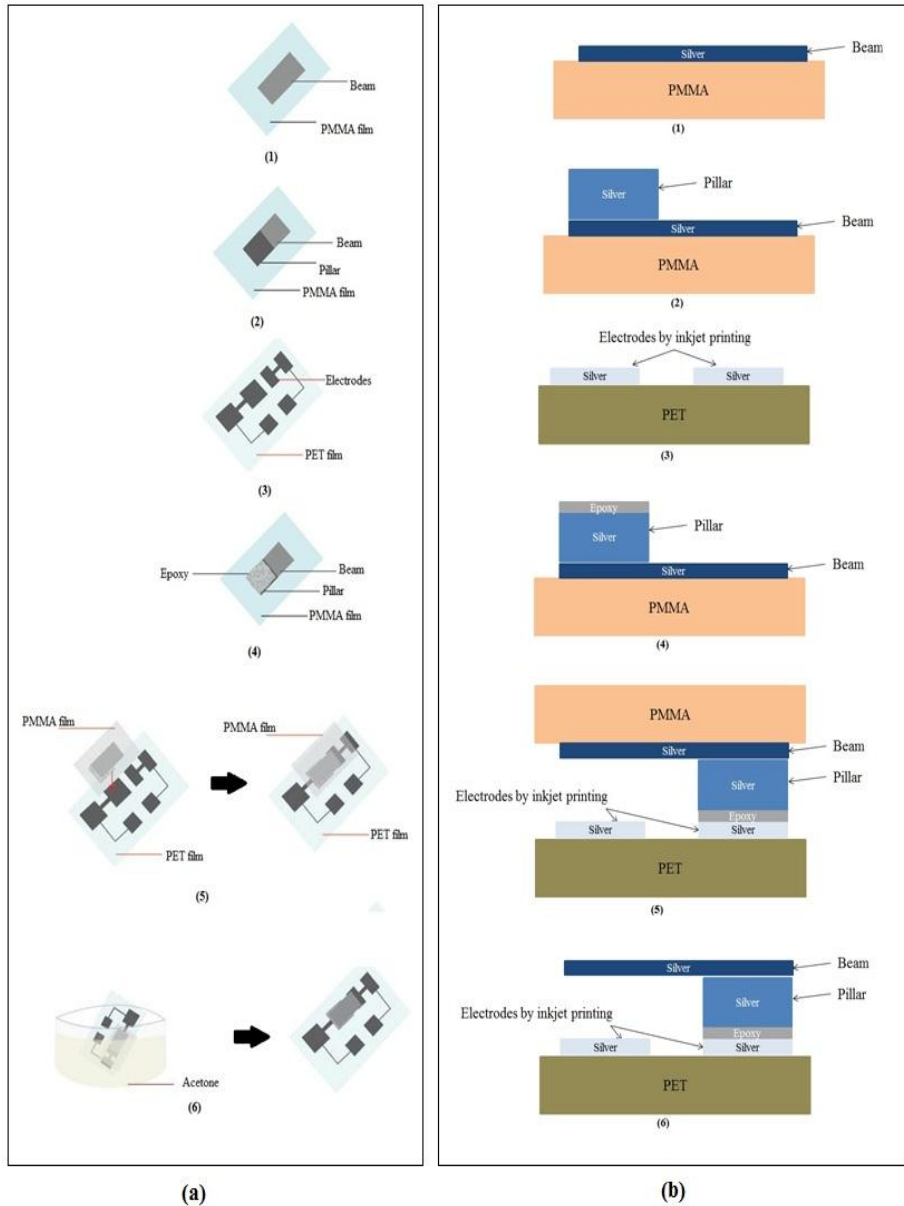
Figure 104. Fabrication flow (a) Top view, (b) Lateral view.

4.2.3 Characterization

The physical characterization, the roughness of printed patterns and the thickness of the patterns has been carried out using a Dektak XT™ Stimulus Surface Profiling System (Bruker Corporation, Conventry, UK). The AC electrical characterization for the different fabricated cantilevers has been performed by measuring their capacitance and dissipation factor, using the four-wire measurement technique with a precision Impedance Analyser 4294A and an impedance probe kit (4294A1) (Agilent Tech., Santa Clara, CA, USA). The calibration method has been described in section 2.1.4 (Rivadeneyra et al. 2014). The data acquisition and analysis have been automated using Labview software (National Instruments Corporation, Texas, USA).
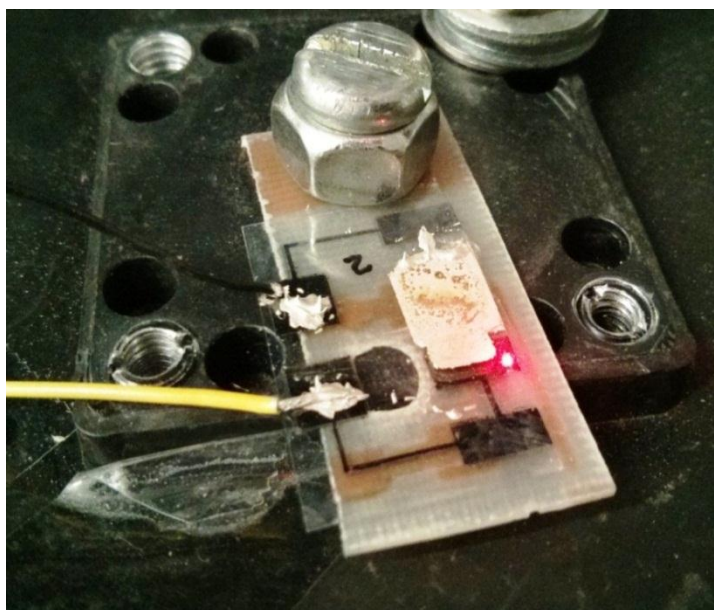
Figure 105. Image of the screen printed cantilever.

The displacement of the cantilevers have been investigated with an electrodynamics shaker (Brüel & Kjaer type 4811), an exciter control (Brüel & Kjaer type 1050) and (Brüel & Kjaer type 2712), by applying an oscillation at varying frequency and acceleration as mechanical input. A laser Doppler vibrometer (LDV) from Polytec is used to measure the peak-to-peak displacement during the excitation. This set-up has been previously used by

Ruan et al. (Ruan et al. 2013) to test piezoelectric cantilevers as harvesters while they are vibrating at a desired frequency. Figure 105 depicts the fabricated suspended structure placed in the set-up for deflection and capacitance measurements.

4.2.4 Results and discussion with PMMA as sacrificial substrate

In this section, we present the results of the physical and electrical characterization of five cantilevers. First, the physical characterization was carried out, showing the reproducibility of this fabrication process. Then, the resistance to different frequencies was studied. Finally, the deflection and capacitance were measured and compared with the simulations.

A. Physical characterization

After the fabrication, we characterized the dimensions, thickness, gap and roughness of our devices. As it can be observed in Figure 106, we used a profiling system to study the real physical characteristics of the printed sensors. Table 23 shows the differences between measured and predicted dimensions for these devices. Uncertainties were calculated as one standard deviation of the experimental data.

Table 23. Comparison between numerical and experimental physical dimensions of the cantilever beams.

Parameter	Model	Experimental
Length (mm)	5.0	4.98 ± 0.05
Width (mm)	2.5	2.59 ± 0.05
Gap (µm)	120	149.17 ± 2.19
Thickness (µm)	15	16.3 ± 0.1

In general, real dimensions are alike to modelled ones, being the biggest discrepancy in the gap of the cantilever. This may have been caused because the removal of the sacrificial layer is a critical step. If the sample is immersed more time than the required, the epoxy layer starts to react and induces a deformation in the beam. Then, the obtained cantilever is not totally parallel to the back electrode, but there is an angle that represents a bigger gap than

the one expected. Furthermore, we obtained an 80% manufacturing yield; the failure rate might also be related to the substrate removal. If the immersion time is not well controlled, the cantilever can be more easily broken.
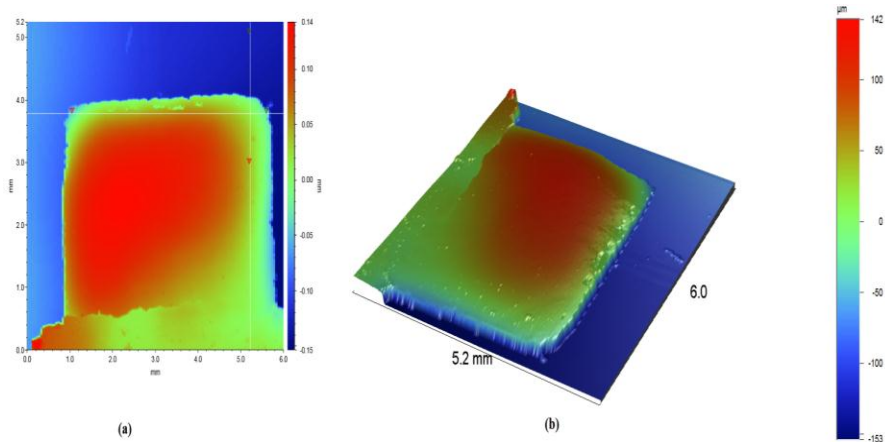
Figure 106. Profiling system captions (a) 2D, (b) 3D.

As we have already mentioned, the PMMA film tested was 50 μm thick, but the thickness of this layer is not critical. The thickness of the pillar and the beam is directly controlled by the chosen density mesh for the screen printing steps shown in Figure 104.

B. Frequency

First, the deflection of the cantilever was measured at 10 Hz, 25 Hz and 50 Hz. After that, the device was put down a frequency range from 10 Hz to 1 kHz at 1 g acceleration without crashing. After this experiment, we measured again the capacitance and deflection without appreciating any alteration. The simulations found the resonance frequency of this device at 1.6 kHz. The measurements showed that the resonance frequency is at least above 1 kHz.

C. Displacement

The displacement at the free end of the cantilever was measured at different frequencies for a wide range of accelerations. We performed several experiments, varying the frequency and the applied acceleration. We set the frequencies to 10, 25 and 50 Hz. The range of acceleration varied from 0.1 to 5 g, depending on the frequency. Figure 107 shows the peak to peak

displacement of the cantilever at 10 Hz. Displacements below 0.3 g were not possible to measure because the signal noise was comparable with the detected signal.
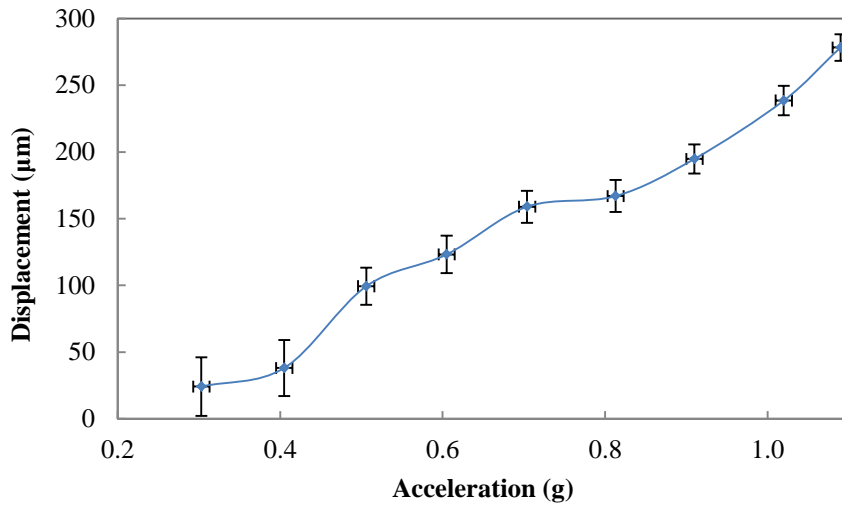
Figure 107. Peak to peak displacement vs. applied acceleration at 10 Hz.
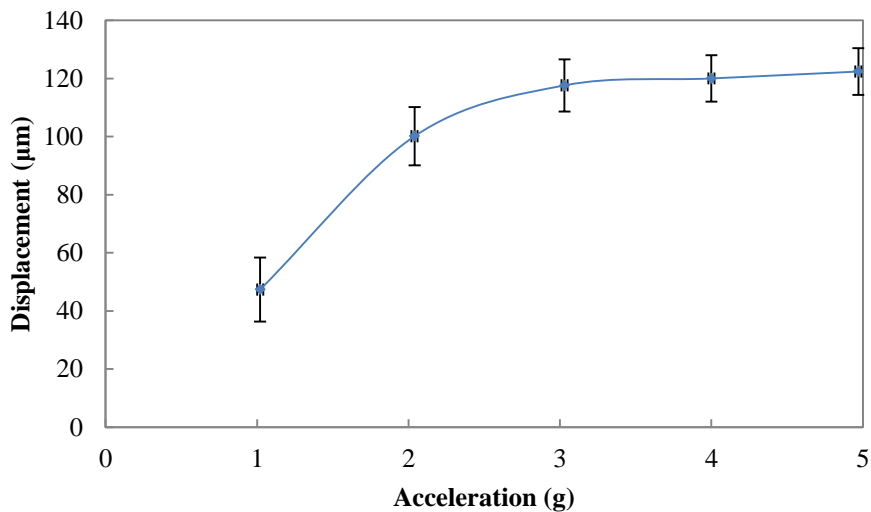
Figure 108. Peak to peak displacement vs. acceleration at 25 Hz.

The maximum applied acceleration at 10 Hz with this system was 1.2 g. In order to know the response for higher acceleration, we set the frequency of

oscillation at 25 Hz. At this frequency, the system can achieve acceleration up to 5 g (Figure 108). The curve obtained at 10 Hz presents a quite linear response (R² = 0.9769), whereas the behaviour at 25 Hz shows a saturated response above 3 g. A saturated value would be expected also at 10 Hz, but this result was not achieved since the set-up cannot provide higher acceleration values at this frequency.

The simulations and experimental results are presented in Figure 109. In this case, only the deflections are shown. There is a quite good agreement between modelled and experimental data above 0.5 g. The mismatch between experimental and model values below 0.5 g might be caused by the high noise in signals obtained at these accelerations. The slope obtained with the simulations is 132 μm/g whereas the one obtained with real data is 149 ± 12 μm/g. The errors for data above 0.5 g have been calculated as the standard deviation of measurements from different cantilevers. The big error bars for data below 0.5 g represent the high fluctuations of the measurements in this range instead.
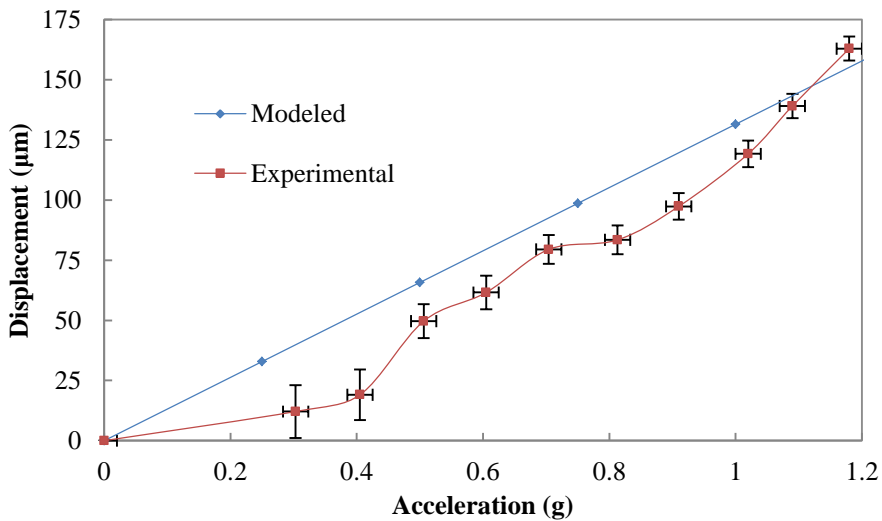
Figure 109. Simulated and Experimental deflections at 10 Hz.

The dependency between the frequency of work and the displacement of the cantilever beam is shown in Figure 110. For this purpose, we measured the displacement at different frequencies for an applied acceleration of 1g. There is an exponential response with a decay constant of -0.091 μm/Hz. Due to the

strong decay with frequency, we could not measure above 50 Hz with accuracy.
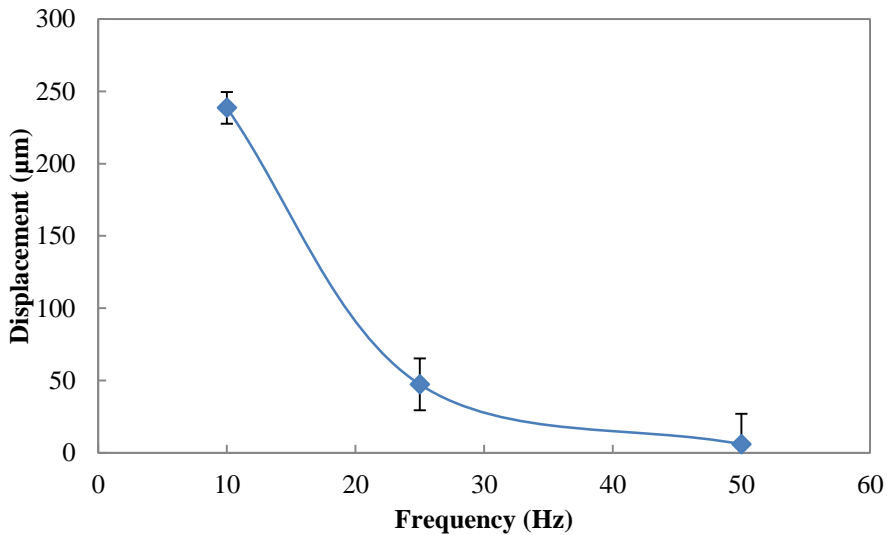
Figure 110.Peak to peak displacement vs. frequency at 1g.

D. Capacitance

In order to test the cantilever as accelerometer, we measured the change in capacitance induced by the applied acceleration. Capacitance measurements were taken using the 4294A impedance analyser. An array of 201 points containing capacitance values at 100 kHz were read-out out from the impedance analyser. According to the instrument manual, the faster data acquisition time is 5.6 ms to fill the buffer with the 201 measurements. We have synchronized the beginning of the measurements and vibrations through the external trigger mode. In order to ensure the measurements of capacitance versus acceleration, the frequency of work of the shaking setup was set to 10 Hz, the minimum allowed frequency for this set-up.

Figure 111 shows two different captions from the measurements taken with the impedance analyzer. There is a parasitic shunt capacitance of 2.5 pF. The first caption corresponds to the measurement set-up noise (Figure 111a). As expected, these peak to peak changes are around 3-4 fF without acceleration, whereas these variations are about 80-90 fF applying 0.3 g.
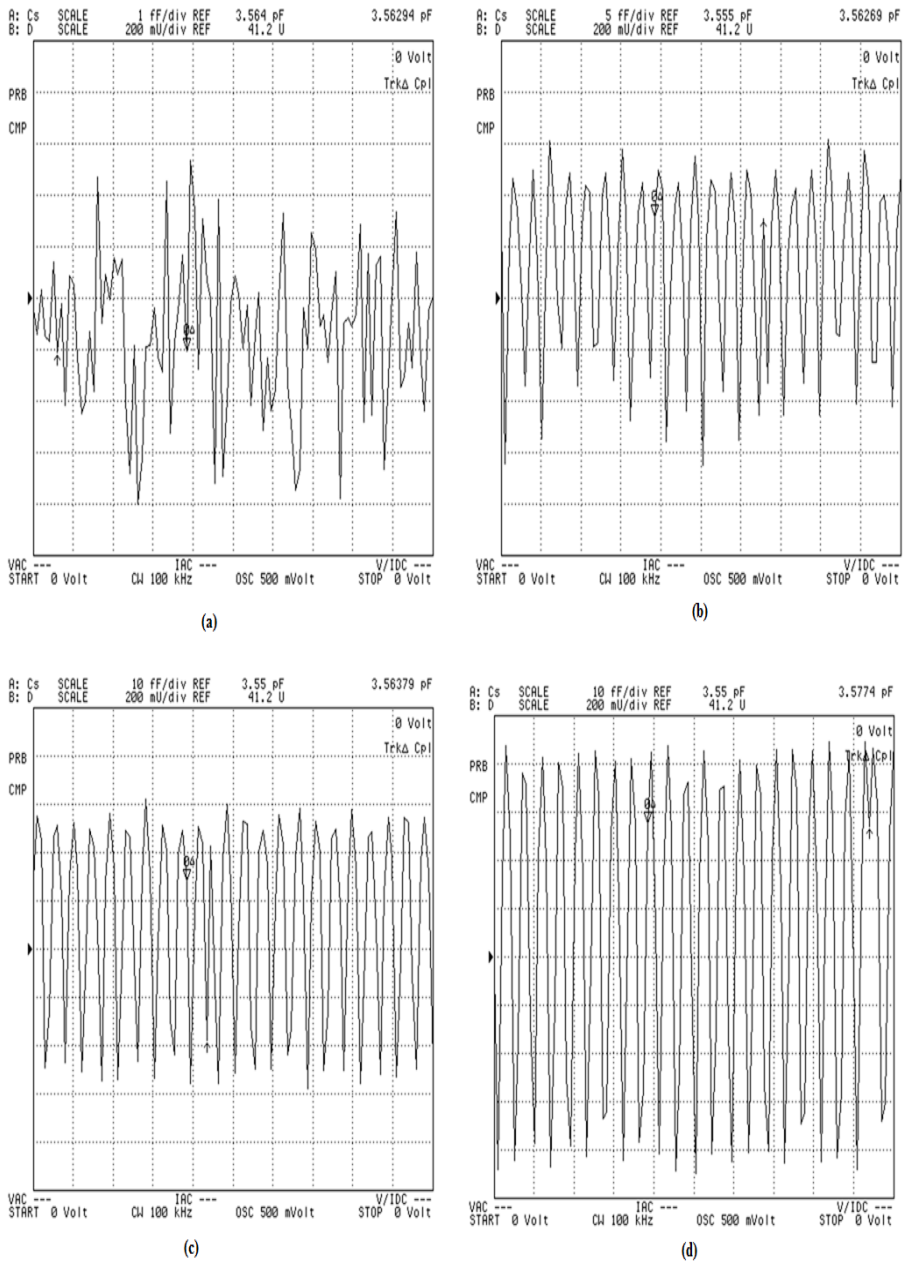
Figure 111. Capacitance in time (a) without acceleration (scale 1fF/div); (b) with acceleration of 0.1 g (scale 5fF/div); (c) with acceleration of 0.2 g (scale 10fF/div); (d) with acceleration of 0.3 g (scale 10fF/div).

The experimental set-up worked well at low acceleration values but the probe attachment to the shaker returned values with a noisy response at higher

accelerations. Due to this restriction, we were not able to measure changes in capacitance above 0.4 g. For this reason, we have simulated the change in capacitance with the deflection obtained experimentally shown in Figure 109. These capacitance variations are depicted in Figure 112. We have defined the change in the measured capacitance as the difference between the percentile 85 and 15 of the recorded data. As can be seen, the predicted capacitance taking into account the measured deflections coincides with the measured capacitance with the impedance analyzer in the whole range of accelerations. There is a mismatch between these data less than 20 fF. This agreement could indicate that the experimental variation of capacitance would fit the simulated change in capacitance for higher values of accelerations.

Looking at the simulated capacitance in the theoretical model, the expected change in capacitance is higher than the one obtained with the experimental displacement but both curves show a similar shape. The higher the displacement induced, the bigger the capacitance measured. The behavior of the relationship between the capacitance and the distance between electrodes of this capacitive cantilever is different from that of a parallel plate capacitor due to the difference in the distance between electrodes along the cantilever length.
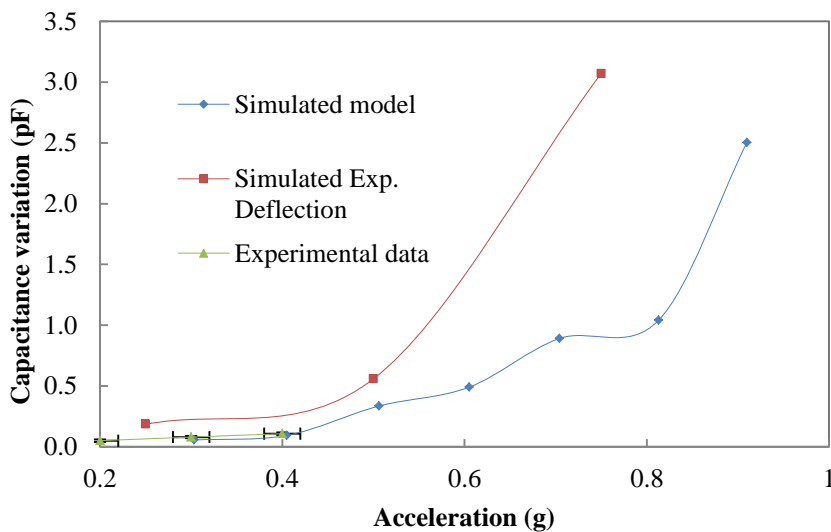
Figure 112. Variation in capacitance vs. applied acceleration at 10 Hz.

4.2.5 Results and discussion with PVA as sacrificial substrate

One not-resolved aspect of the suspended structure described in section 4.2.4 is the removal of the substrate layer. Although this process eases the fabrication of printed cantilever on plastic substrates, the solvent used to remove the sacrificial layer also reacts with structural materials, so that the cantilever flatness can be affected and, even worse, the cantilever can be broken if the time that it is submerged is not well controlled.

Here, we present an improvement of this fabrication process and the characterization of the full printed cantilever on plastic foil substrate. As described in section 4.2.4, this fabrication process differs from others on the use of a commercial film as sacrificial material but the main difference remains in the role of this layer: it is used as a substrate for printing the beam and the pillar, and then this structure is flipped in order to bond it to the electrodes. These electrodes have been previously printed on another substrate, after that the sacrificial substrate is removed. The innovation presented here is a technique similar to the wafer unibond procedure developed to obtain Silicon-On-Insulator wafers in microelectronic technology (Aspar 1996). In this procedure, there is no degradation of any layer during the removal of the sacrificial layer because it is a layer of transference. In addition to this, the substrate is a plastic foil which provides more flexibility to the final device but less stability to the manufacturing process of the suspended structure. To design this structure, we have followed the same model we developed in section 4.2.4 to directly compare results. The dimensions are shown in Table 22. In order to test the fabrication process, we also printed the same modelled cantilever but reducing the gap between the substrate and the suspended structure (about 40 μm).

The manufacturing procedure is basically the same as presented in section 4.2.4 but we have substituted the substrate layer for PVA (polyvinyl acetate) and the solvent to remove it is now water. In this sense, we have achieved no interaction between the structural and electrical material (silver) and sacrificial substrate solvent (water).

A total of 20 replicas have been fabricated following this procedure and only 2 of them were broken. This result shows a preliminary 90% rate of

manufacturing success and an increase of 10% compared with the previous strategy based on sacrificial substrate in section 4.2.4. The viability and enhancement in manufacturing yield of this novel fabrication process has been verified for printed suspended structures.

This procedure can be compared with the bonding process in SOI technology, where an additional oxidized substrate is used to partially transfer a silicon layer on top of it, followed by chemical etching of most of the original wafer. A process based on wafer bonding process was reported by Dubourg et al. (Dubourg et al. 2011) to develop microcantilevers on silicon wafer by shadow masking. These authors use omnicoat as the sacrificial layer material while the cantilever is made of PMMA. Here, we transfer the cantilever to the substrate thanks to the PVA layer. Following this manufacturing process, not only the problems related to the sacrificial layer are avoided but also the complexity of the fabrication process is reduced. First and foremost, we avoid the problems related to chemical reactions between the solvents to remove the sacrificial layer and the structural materials. In our previous procedure, we immersed the structure in an acetone bath but we had to take care of the duration of this immersion because if it was longer than 2 min, the acetone started to react with the silver layers. Figure 113 depicts the fabricated suspended structure placed in the set-up for deflection and capacitance measurements.
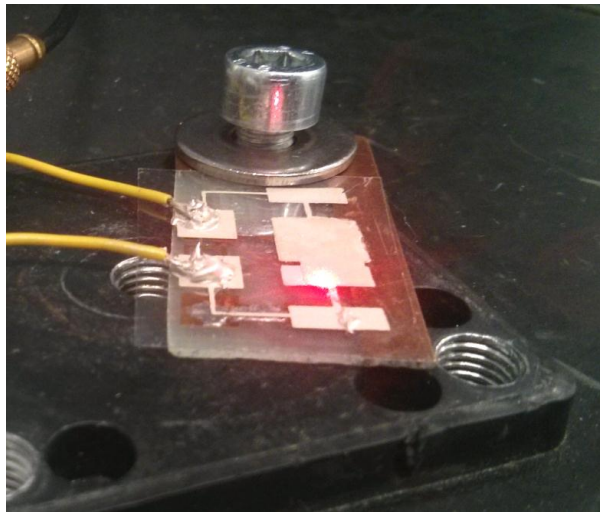
Figure 113. Image of the screen printed cantilever by transference layer.

A. Physical characterization

After the fabrication, we characterized the dimensions of our devices (Figure 114).

In general, real dimensions and the modelled ones are similar, with the highest difference being found in the cantilever gap. But this difference (< 5%) is lower than the one obtained with the method based on PMMA (~ 10%). Moreover, this cantilever presents a more homogenous surface than the one fabricated on PMMA.

This flatter surface is achieved due to the no alteration of silver layers by the water bath to remove the PVA layer. Here, we can also observe a not totally parallel beam to the back electrode, but there is an angle that represents a gap bigger than expected. This angle is only appreciated at the end of the free end of the beam.

(a)   (b)
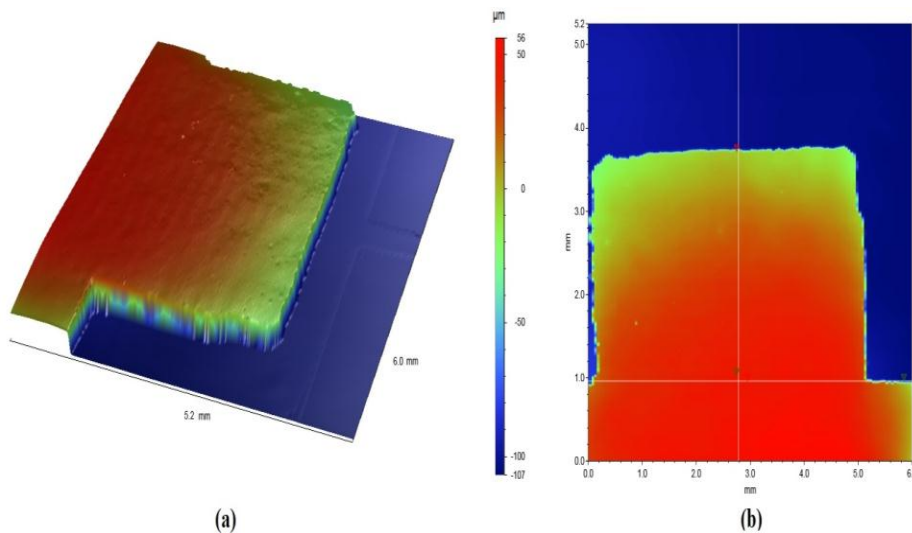
Figure 114. Profiling system captions of model with thicker pillar (a) 2D, (b) 3D.
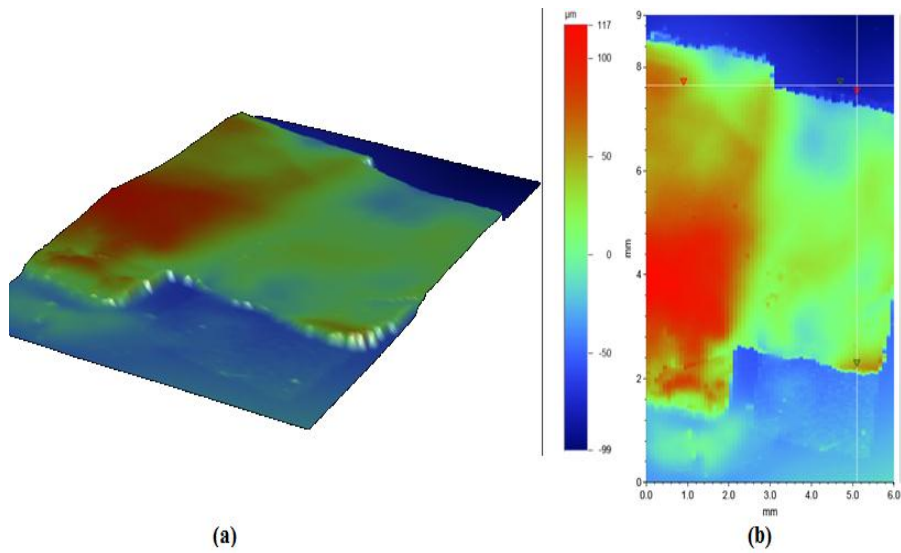
Figure 115. Profiling system captions of model with thinner pillar (a) 2D, (b) 3D.

Table 24 shows the differences between measured with a profiling system and modelled dimensions for these devices. We have also included in Table 24 the dimensions obtained with the fabrication process described in the previous section (section 4.2.4) for comparison purposes. Uncertainties were calculated as one standard deviation of the experimental data. Let's remember that the gap has been defined from the substrate to the bottom of the beam (see Figure 104).

Table 24. Comparison between numerical and experimental physical dimensions of the cantilever beams with PMMA layer and PVA layer.

Parameter	Model	Experimental procedure PMMA	Experimental procedure PVA
Length (mm)	5.0	4.98 ± 0.05	4.97 ± 0.05
Width (mm)	2.5	2.59 ± 0.05	2.56 ± 0.06
Gap (μm)	120	131.70 ± 2.19	125.70 ± 1.48
Thickness (μm)	15	17.3 ± 0.1	16.8 ± 0.1

Table 25. Comparison between numerical and experimental physical dimensions of the cantilever beams with thicker pillar (model A) and thinner pillar (model B).

Parameter	Model A	Experimental Model A	Model B	Experimental Model B
Length (mm)	5.0	4.97 ± 0.05	5.0	4.92 ± 0.08
Width (mm)	2.5	2.56 ± 0.06	2.5	2.62 ± 0.09
Gap (μm)	120	125.70 ± 1.48	35	42.00 ± 2.56
Thickness (μm)	15	16.8 ± 0.1	15	16.5 ± 0.2

As we have already mentioned, the PVA film tested was 50 μm thick, but the thickness of this layer is not critical. The thickness of the pillar and the beam is directly controlled by the chosen density mesh for the screen printing steps shown in Figure 104.

B. Frequency

We found the same frequency behaviour of this printed structure than the one shown by the printed cantilever with PMMA as sacrificial substrate.

C. Displacement

The deflection at the free end of the cantilever was measured as a function of acceleration at different frequencies. Several experiments were carried out varying the applied acceleration and the frequency of work. We set the frequencies from 10 Hz to 50 Hz. The range of acceleration varied from 0.1 to 5.5 g, depending on the frequency.

Figure 116 shows the deflection of the cantilever at 10 Hz. Deflections below 0.3 g were not possible to measure because the signal noise was comparable to the detected signal. The maximum applied acceleration at 10 Hz with this system was 1.25 g (see Figure 116).

In order to know the response for higher acceleration, we set the frequency of oscillation at 25 Hz. At this frequency, the system can achieve acceleration up to 5.5 g (Figure 117). The curve obtained at 10 Hz presents a quite linear

response (R^2 = 0.9569), whereas the behaviour at 25 Hz shows a saturated response above 4 g.

The slope obtained with the simulations is 132 μm/g whereas the one obtained with real data is 137 ± 10 μm/g (Figure 116). The slope obtained with this cantilever is more similar to the modelled one than the slope obtained by PMMA as sacrificial substrate. The errors have been calculated as the standard deviation of measurements from different cantilevers.

The dependency between the frequency of work and the deflection of the cantilever beam has also been studied (Figure 118). For this purpose, we measured the displacement at different frequencies for an applied acceleration of 1g. There is an exponential response with a decay constant of -0.169 μm/Hz. Due to this strong decay with frequency, we could not measure displacements above 50 Hz with enough accuracy to discriminate values.
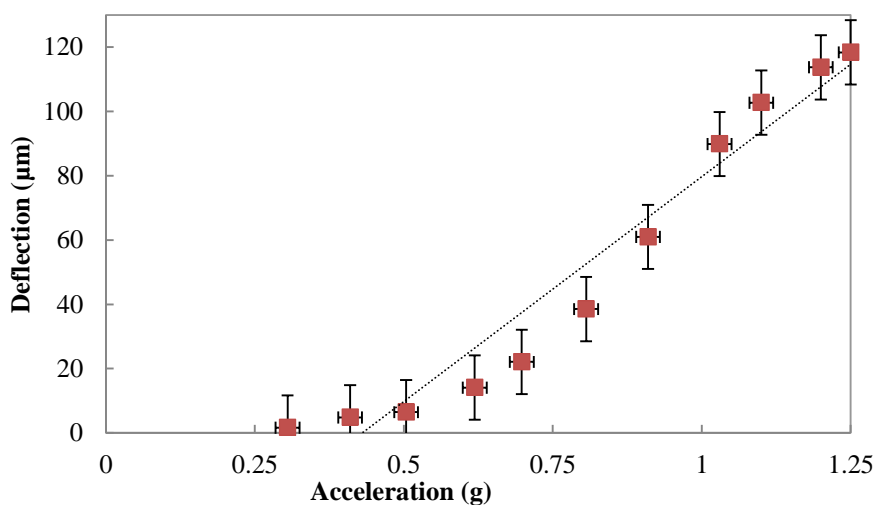
Figure 116. Cantilever with thicker deflection as a function of acceleration at 10 Hz.
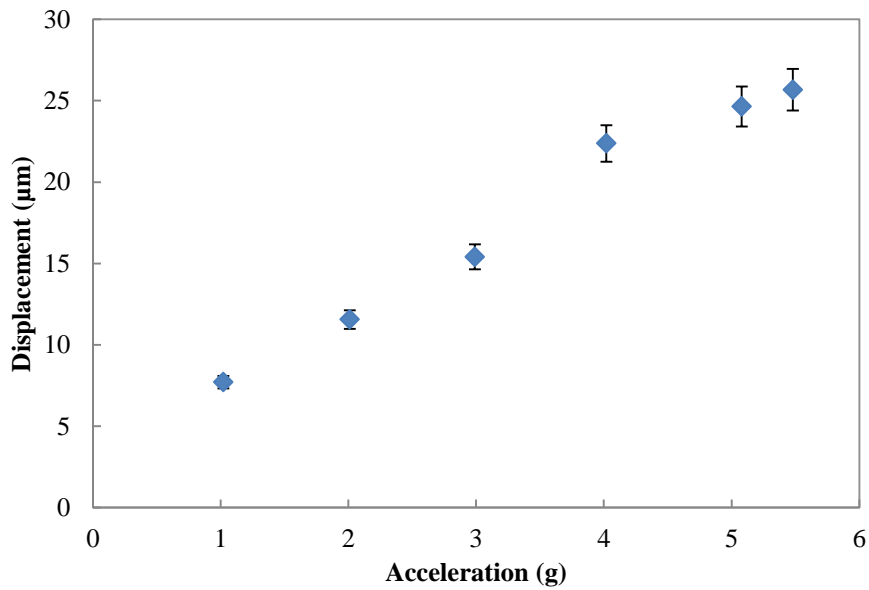
Figure 117. Cantilever with thicker pillar deflection as a function of acceleration at 10 Hz.
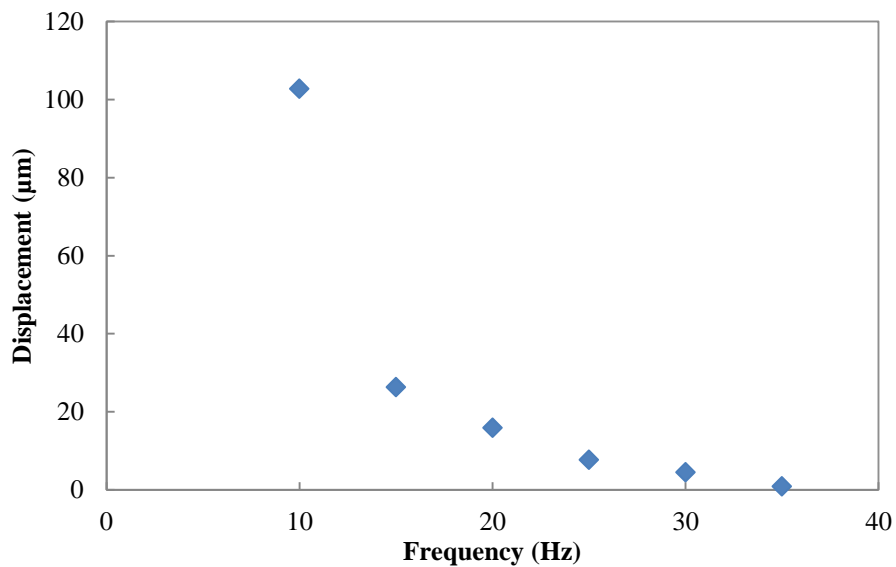
Figure 118. Cantilever with thicker deflection as a function of frequency at 1 g acceleration.

As we mentioned in the design section, we developed the same cantilever with a shorter gap between the suspended structure and the substrate.

Figure 119 displays the deflection of both cantilevers at 10 Hz. The short cantilever shows a slope of 37 um/g until 1 g where its response is saturated. Both curves present similar displacements at low acceleration values but around 0.6 g the short cantilever evolves slower than the big one.

This behaviour can be explained by the damping effect which is more appreciable when the gap between the cantilever and the substrate is reduced. The effect of damping is a decreased deflection (Choi et al. 2006, Zhang, Peng and Zou 2012).
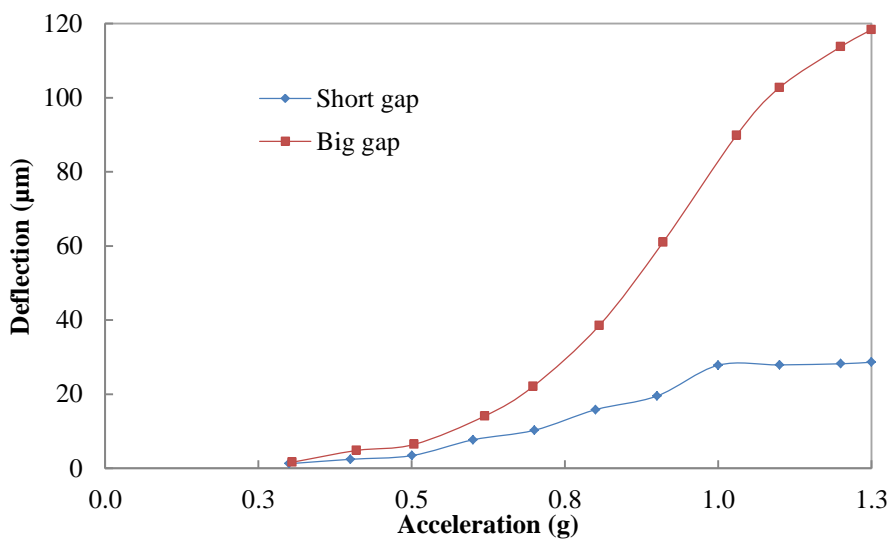
Figure 119. Cantilevers deflections as a function of applied acceleration at 10 Hz.

D. Capacitance

We measured the change in capacitance induced by the applied acceleration in order to test this device as accelerometer. An array of 201 points containing capacitance values at 100 kHz were read-out from the impedance analyser. The beginning of the measurements and vibrations were synchronized through the external trigger mode. In order to ensure the measurements of capacitance versus acceleration, the frequency of work of the shaking setup was set to 10 Hz, the minimum allowed frequency for this set-up.

Figure 120 shows two different display captures from the measurements taken with the impedance analyzer. There is a parasitic capacitance in

parallel with the device of 2.7 pF. As can be observed, the peak to peak changes are around 14 fF without acceleration and show a noisy behaviour, whereas these variations are about 70-80 fF applying a force of 0.3 g, showing a clear periodic response.
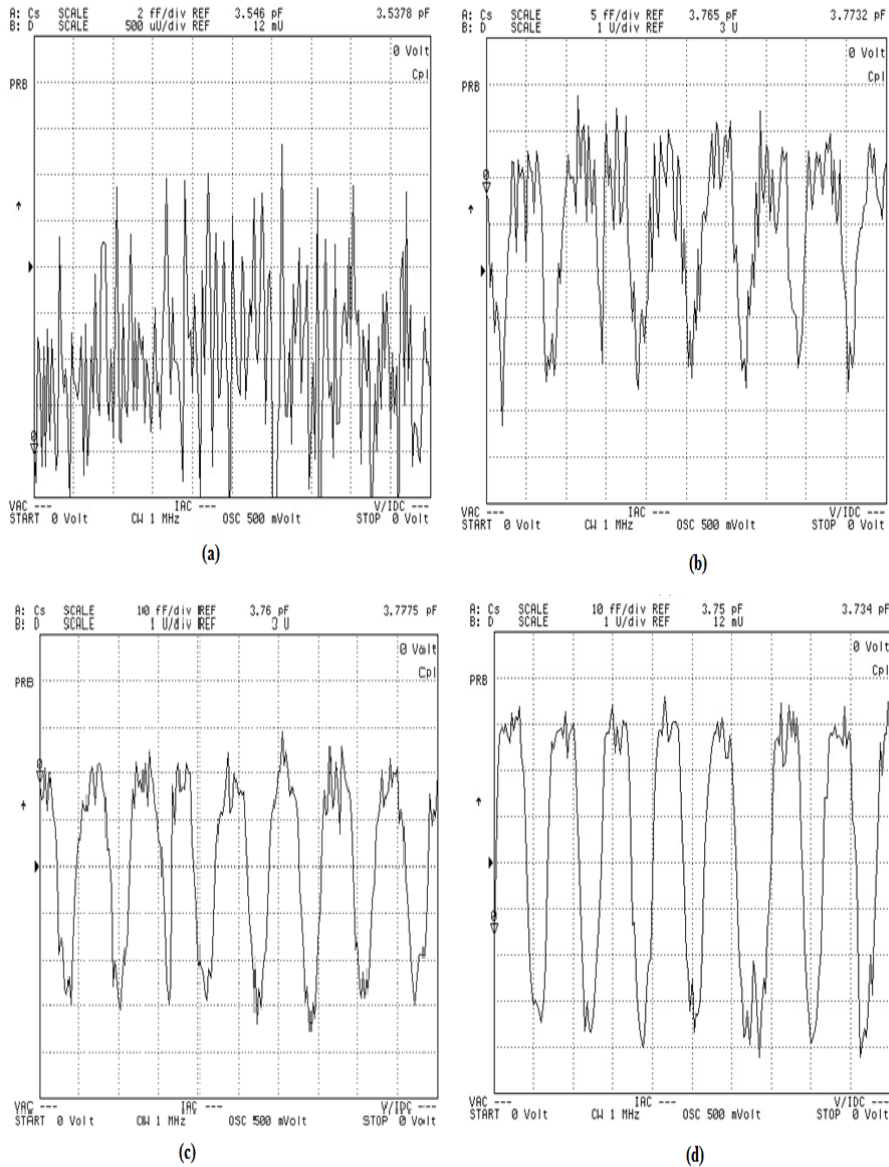
Figure 120. Capacitance of the thicker cantilever in time (a) without acceleration (scale 1 fF/div); (b) with acceleration of 0.1 g (scale 5 fF/div); (c) with acceleration of 0.2 g (scale 10 fF/div); (d) with acceleration of 0.3 g (scale 10 fF/div).

Due to constrain in the experimental set-up, we were not able to measure changes in capacitance above 0.4g. For this reason, we simulated the change in capacitance with the deflection obtained experimentally and the experimental one, shown in Figure 116. All these capacitance variations are depicted in Figure 121. We have defined the change in the measured capacitance as the difference between the 85th and 15th percentile of the recorded data. As can be seen, the predicted capacitance taking into account the measured deflections coincides with the capacitance measured with the impedance analyser in the whole range of accelerations. The mismatch between these data is less than 20 fF. This agreement could indicate that the experimental variation of capacitance would fit the simulated change in capacitance for higher values of accelerations.

Looking at the modelled capacitance, the expected change in capacitance is higher than the one obtained with the experimental displacement but both curves show a similar behaviour. The higher the displacement induced, the bigger the capacitance measured. The simulated capacitance with the experimental deflections with this fabrication process shows a more stable curve than the one obtained with the manufacturing process as sacrificial substrate.
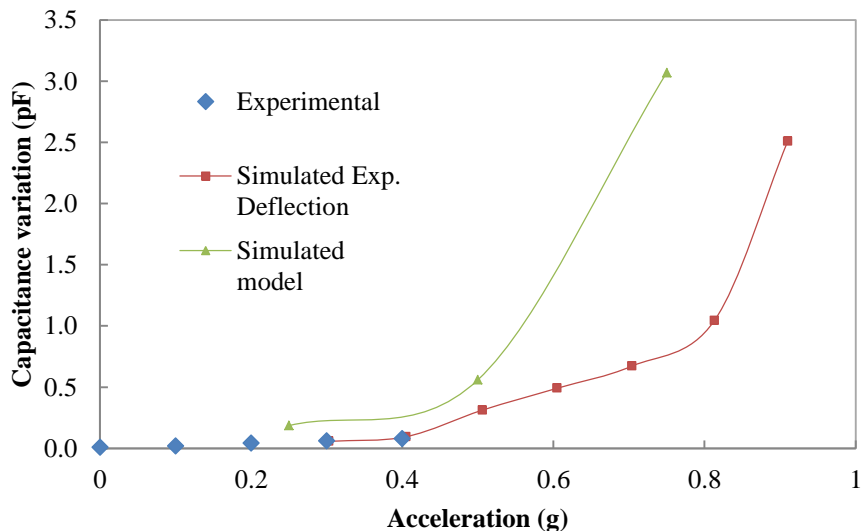
Figure 121. Variation in capacitance vs. applied acceleration at 10 Hz in cantilever with thicker gap.

4.3   Suspended structures in MEMS technology

4.3.1 Simulation tools

4.3.1.1. COMSOL Multiphysics

COMSOL Multiphysics is a powerful finite element (FEM), partial differential equation (PDE) tool. This software is organized in modules; each one solves different physical and chemical problems, from acoustics and electromagnetics to heat transfer or chemical engineering. These modules can be easily combined to study more complex problems. In addition, this tool can import and export computer-aided design (CAD) models, facilitating the geometry definition. Furthermore, this software can be controlled by Matlab in order to carry on more elaborated analysis. Another feature of this tool is the capability of solving 2D and 3D problems.

4.3.1.2. MEMS+

MEMS+ is a different kind of finite element analysis (FEA), based on a MEMS-specific library of high-order, parametric finite elements (Coventor, Inc. USA). This software provides a first approach to the electrical and mechanical behaviour of the studied structure. In addition to this, this software is directly integrated in Cadence environment, facilitating the design of the extra circuitry for the studied device.

4.3.1.3. Cadence virtuoso

This IC tool allows the implementation of all the different steps involved in IC design. There are different packages to develop the circuits' stages. Roughly speaking, the design starts by the entry of design concepts where the many interdependencies can be abstracted and visualized to understand and determine their effects on circuit performance. Then, the design captured in the schematic must be transformed into a digital blueprint that represents how the chip will actually be manufactured. Cadence offers a correct-by-construction physical implementation solution following the design rules from the foundry as well as the custom designer's own experience. Then, connections between devices must be done. After routing, designers must look at the parasitics in the design to analyse their effects and in case of

conflict re-design. Cadence offers a solution for parasitic extraction and analysis of all the parasitic effects in a design, and then designers can correct them as soon as possible.

4.3.2 Cantilever for energy harvesting

The field of energy harvesting has grown significantly over the past decade due to the need to produce portable and wireless electronics with extended lifespan. Ambient vibrations are a ubiquitous source of energy in the environment, especially where solar or thermal forms of energy might not be available or have a very low quality. Vibrational piezoelectric harvesting devices convert ambient vibration energy into electric energy. Here the focus is on low frequency (< 300 Hz) vibrations as many industrial and commercial devices operate at low frequency. MEMS (Micro-Electromechanical Systems) energy harvesters are interesting to investigate because of their potential to achieve low-volume, low-weight harvesters that can be fully integrated with other components such as sensors. MEMS piezoelectric energy harvesting devices are an attractive solution to this problem because of the extensive research in the MEMS fabrication techniques and the high energy conversion of piezoelectric materials (Anton and Sodano 2007). The Q factor is a particularly important factor for energy harvesting, a broad Q factor would allow for a system to harvest energy from a wide range of frequencies. However, broadening the Q-factor also causes it to decrease and a high Q factor will produce more power. Broadening the Q factor is of interest to many researches working with vibration energy harvesters, Choi et al. (Choi et al. 2011) used the flow of liquid within the device to demonstrate how this could be achieved.

The dominant frequency peaks from majority of sources surveyed lie between 20 and 60 Hz (such as a compressor or a controller). There is another set of frequencies lying between 120 and 140 Hz (i.e. a water pump). Some sources also contain peaks around 350 Hz, such as a pipe. The accelerations of the ambient vibrations were all below 0.7 $g \cdot Hz^{-1/2}$, with most accelerations on the order of 10^{-2} and 10^{-1} $g \cdot Hz^{-1/2}$ (Miller et al. 2011).

The most common thin piezoelectric materials are zinc oxide (ZnO), aluminium nitride (AlN) and lead zirconate titanate (PZT). They each present

different mechanical and electrical properties, as well as transduction capabilities as shown in Table 26. However these properties are highly dependent on the fabrication process. In comparison to PZT, AlN and ZnO offer small piezoelectric coefficients and coupling factors and even lower dielectric constants, giving a two order of magnitude lower output capacitance. Nevertheless, PZT contains lead, and has a high annealing temperature ($> 600°C$) barring it from all CMOS facilities whereas AlN is fully compatible with CMOS technology. ZnO can be CMOS compatible, but when used as a piezoelectric material it requires specific equipment and uses zinc salt solution which is not CMOS compatible but is integrated more easily with conventional processing than PZT (Horowitz et al. 2007).

Table 26. Typical material properties of most common piezoelectric materials. d31 and d33 are the piezoelectric coefficient in bending and compression mode, respectively. ε33r is the relative dielectric constant. E corresponds to Young's modulus and ρ represents the mass density.

Material	d_{31} (pC/N)	d_{33} (pC/N)	$\varepsilon_{33,r}$	E (GPa)	ρ (kg/m^3)
PZT	-130	290	1300	96	7.70
AlN	2.0	3.4	10.5	330	3.26
ZnO	-4.7	12	12.7	210	5.60

The aim of this section is to model by numerical simulation different structures to tune them into the frequency of interest. Accurate modelling of cantilever devices can be used to design more efficient piezoelectric energy harvesting devices. This can be achieved for whatever specifications are necessary i.e. broad Q, specific resonant frequency etc. An accurate model can be used to test new configurations and determine the optimum shape for the environment. The complexity of this problem is to be able to extract energy from a very thin layer of piezoelectric material. Here, a discussion of some of the energy harvesting cantilever designs modelled using COMSOL Multiphysics is implemented. (Emam 2008, O'Keeffe et al. 2013).

4.3.2.1 Numerical simulation: validation and modelled structure

To verify the validity of results obtained from COMSOL Multiphysics 4.2a, experimental measurements of cantilever beams of AlN have been tested. Table 27 contains the dimensions of the fabricated devices by Tyndall National Institute (Cork, Ireland). These devices were then modelled and the

results compared with the fabricated devices. This investigation determined the accuracy of the models and to aid in future optimisation. However, the models discussed here take the HH18 as the standard for comparison. The dimensions of the HH18 are beam width of 500 µm, beam length 5 mm, mass width 5 mm, mass length 1 mm. These dimensions remain the same in the latter models except where expressly stated.

Table 27. Dimensions of fabricated cantilever beams.

Beam #	Beam width (um)	Beam length (um)	Mass length (um)	Mass width (um)
HH17	500	5000	1000	3000
HH18	500	5000	1000	5000
HH19	500	3500	1000	1000
WB_5	500	2500	2500	2500

As it is seen in Table 28, the difference in the resonant frequencies changes from one device to the next and this is likely due to the elimination of the active layers. The structures consist of 5 layers on the beam and 7 layers on the mass of the structure. The piezoelectric element is aluminium nitride (AIN) and the metal layers are titanium (Ti) and aluminium (AI). The beam is 50 µm silicon (Si), 1 µm silicon dioxide (SiO_2), 200 nm Ti, 500 nm AIN and 1 µm AI. The mass consists of the layers of the beam and a 1 µm SiO_2 layer and 425 µm Si layer below the beam layers.

In order to reduce the complexity of the models, we respected the dimensions of the beams but we only defined Si as constitutive material because its thickness is considerably much larger than the other layers. Therefore, the modelled cantilevers consist of a beam of thickness of 27.6 µm of Si and a mass of 453.6 µm of Si. This simplification eliminates the complexity required when modelling thin layers and did allow for accurate modelling once this was considered. The maximum error between fabricated devices and simulated ones is less than 10%. This comparison shows that COMSOL Multiphysics is in agreement with theoretical numeric models and it can be used to simulate our devices prior to fabrication.

Table 28. Measured Vs. Modelled Resonant Frequency.

Device	Modelled Resonant Frequency (Hz)	Measured Resonant Frequency (Hz)
HH18	284.57	315.00
HH17	409.46	409.80
HH19	1012.86	1120.00
WB5	927.69	1024.50

In this section, the Solid Mechanics interface module of COMSOL Multiphysics has been used to run simulations (Multiphysics 2008). The beam and mass width and length, as well as the layer thickness, are parameterised.

The present work is basically a modelling problem where the main aim is to optimize simulations to conclude the best strategies to broaden the Q factor and reduce resonance frequency. In order to reach this objective, the mesh has been optimized to reduce computational time, using "mapped mesh" node. Sometimes the geometry for a problem can be very thin in one direction. Since the COMSOL Multiphysics free meshing by default creates triangles/tetrahedrals that are as isotropic as possible (non-flat), a large number of elements will be created in a thin layer. Also, large differences in scale may cause the mesh generator to fail in creating the mesh.

One way of getting an economical mesh is to create a surface mesh on a boundary and then sweep it from source boundaries to destination boundaries. Sweeping has the advantage that you are in control of the number of element layers and their distribution. Another advantage is that the number of mesh elements often is decreased. If the 3D domain consists of two boundaries which can be used as source and destination, you can sweep a free or mapped mesh from one boundary to the other. For each domain, the mapping algorithm defines a regular grid on a logical unit square and then maps it onto the real geometry using transfinite interpolation (Multiphysics 2012).

4.3.2.2 Structures of piezoelectric devices

Figure 122 shows one of the configurations which was examined using COMSOL Multiphysics. Here the effect of the reduction of beam mass from the centre of the beam at the anchor end is examined (Figure 123 and Figure 124). Thereby, a gap in the anchor has been defined and its impact on the resonant frequency has been studied varying its length and width. This reduces the resonant frequency but also decreases the effective area for energy harvesting. Increasing the width of the hole has a much greater effect than the length. Changing either the length or the width brings the 2nd resonant mode closer to the first, however the separation of the two modes are significantly far apart, which means that this design is not optimal for broadening the Q factor.
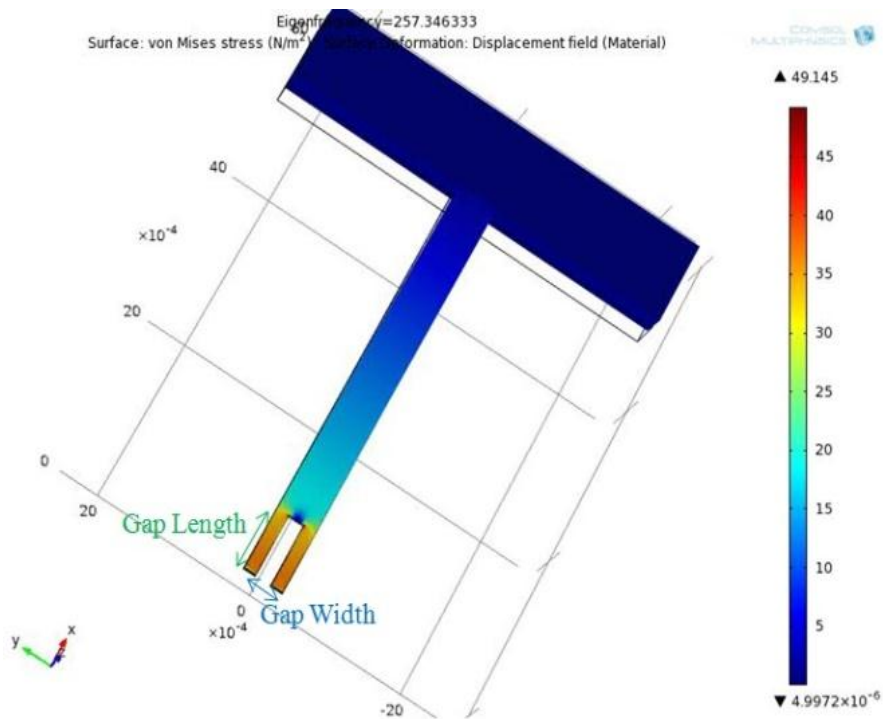
Figure 122. HH18 with Gap. Standard gap dimensions: width = 52.6 mm, depth = 170 mm, length= 500 mm.
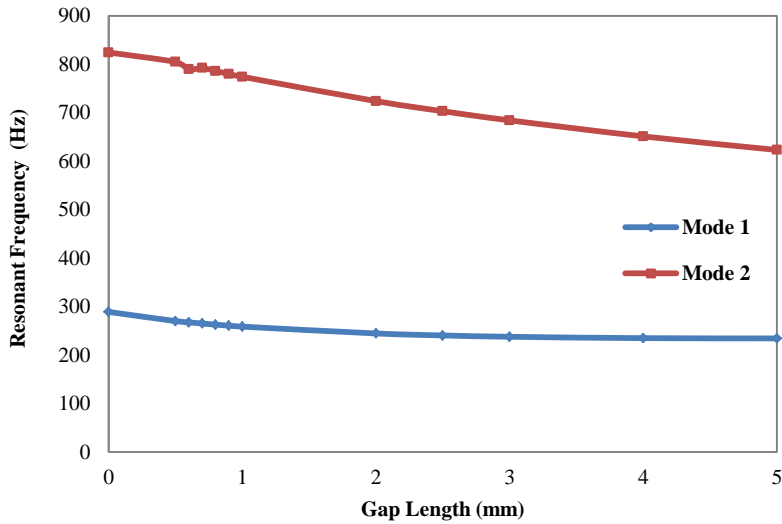
Figure 123. Resonant frequency vs. Gap length.
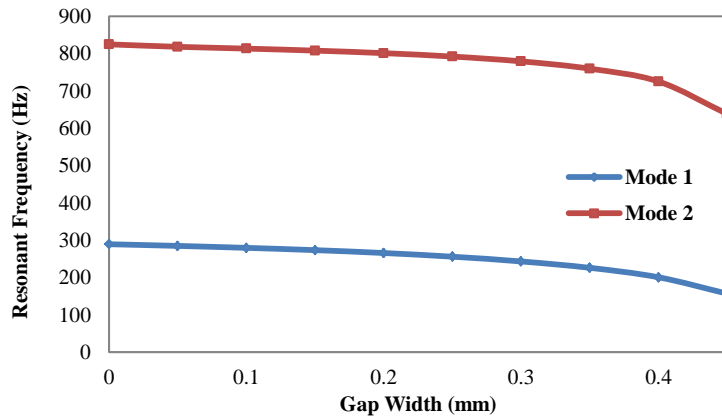
Figure 124. Resonant frequency vs. Gap width.

The values obtained for the frequency can also be compared to a beam with a spring at the anchor end such as that shown in Figure 125. Here it is seen that the resonant frequency in the first mode is significantly decreased from that of a traditional beam and it also brings the resonant frequency of the 2nd mode closer to the first but again the effect is not significant enough to be of use (Table 29). These energy harvesting devices have a very narrow Q factor, around 1Hz, and so the 2nd mode would need to be within 1Hz of the first to broaden the Q of the device.
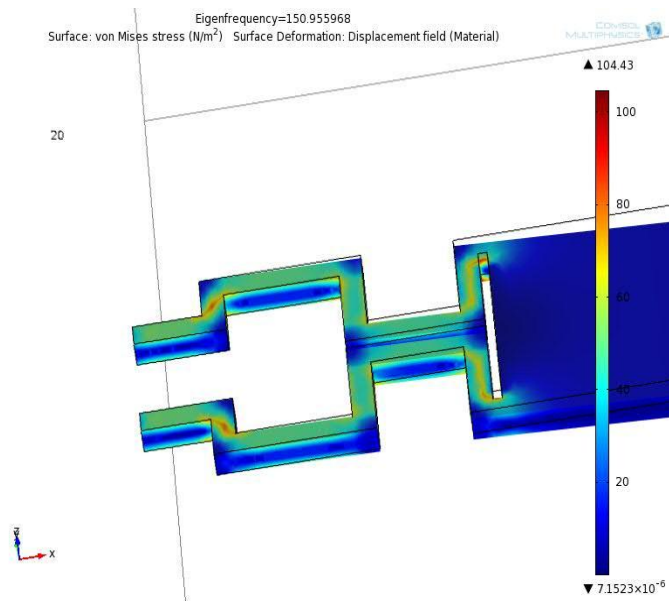
Figure 125. Spring at beam anchor end.

Table 29. Resonance frequency of spring at beam anchor end.

	Height (μm)	Width of supports (μm)	Frequency (Hz)
Ref	0	500x1	289.14
Gap	770	50x2	181.73
Spring	770	50x2	150.96

Figure 126 and Figure 127 show the difference between a beam with peaks along its length vs. a straight beam and a crinkled beam vs. a straight beam, respectively. The peaked/triangle beam increases the stiffness of the beam and so the resonant frequency is increased (Table 30).
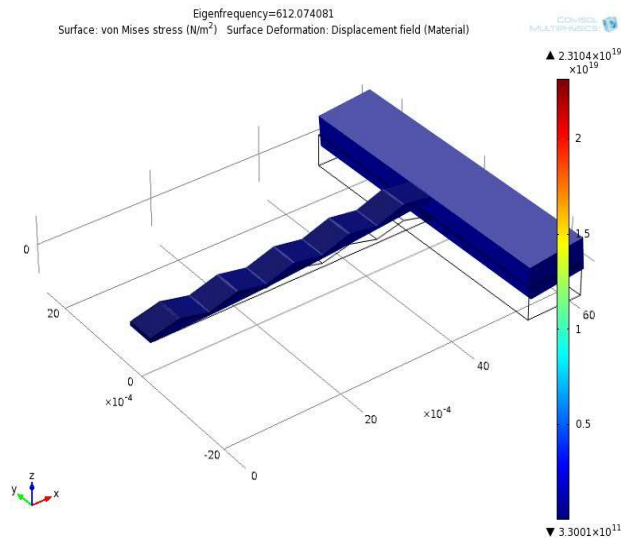
Figure 126. Triangular Beam.

Table 30. Resonant frequency of a triangular beam.

Max added height (µm)	Extra height at max (%)	Resonant Frequency (Hz)
0	0	289.14
52.6	100	484.07
84.3	150	560.62
105.2	200	612.07
210.4	400	811.49
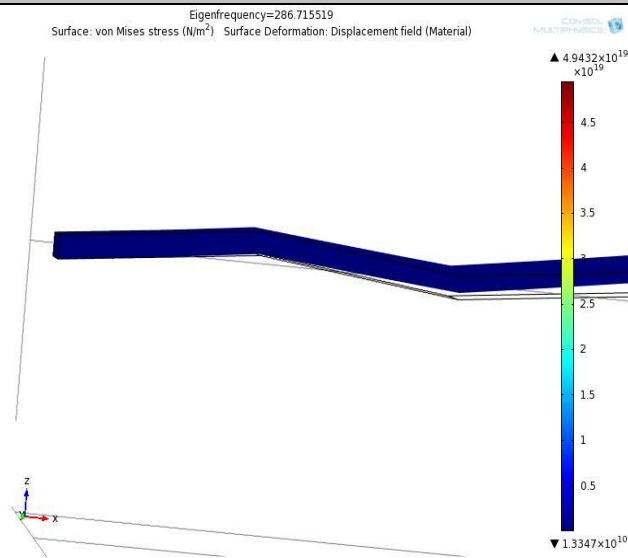
Figure 127. Crinkle Beam.

Table 31. Crinkled beams and its resonance frequencies. Height is defined from 0.

	Height (µm)	Length (µm)	Frequency (Hz)
Ref		5.000	289.14
Ref. length		5.425	258.55
Top	263.00	5.425	250.38
Bottom	210.40		
Top	157.80	5.109	279.36
Bottom	105.20		
Top	136.90	5.071	282.92
Bottom	84.30		
Top	105.20	5.028	286.72
Bottom	52.60		

The crinkled beam decreases the resonant frequency but this is due to the increase in length of the beam and is equivalent to increase a straight beam by the same amount (Table 31). It would also be very hard to fabricate either of these beams as the piezoelectric layer and metal layers are grown on the Si and it is better to have a flat surface for even distribution. There is a 3rd variant of this design which takes the peaks from the back of the device so that only the silicon is reduced, and the active layers are deposited on a flat surface. This would be a much more practical design for fabrication. This design also decreases the resonant frequency of the devices by reducing the stiffness but not the area of the active layers so the harvestable power is not reduced.

Figure 129 shows a beam divided in 5 columns and 20 rows to create a map of slots along the beam to study how location of a slot, 0.1x0.5x0.050 mm^3, in the backside of the beam affects the resonance frequency. In order to ease these long simulations; we have developed a Matlab interface (Figure 128) which automates the sweeps varying not only the number of slots but also the location and their thickness. All simulation data are properly stored and can be also directly represented.
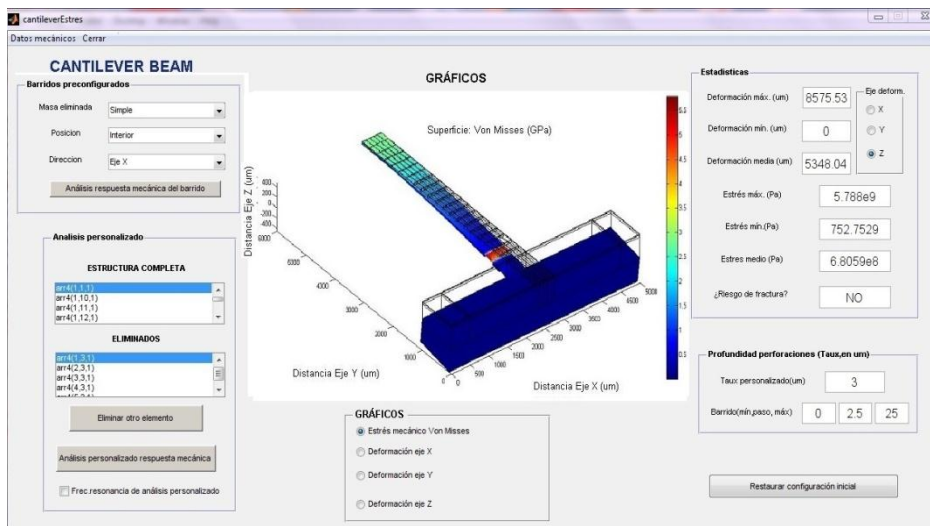
Figure 128. Matlab interface to run complex parametric sweeps.

Figure 130 and Figure 131 show how 1st and 2nd modes of resonance frequency are shifted depending on where the slot is located.
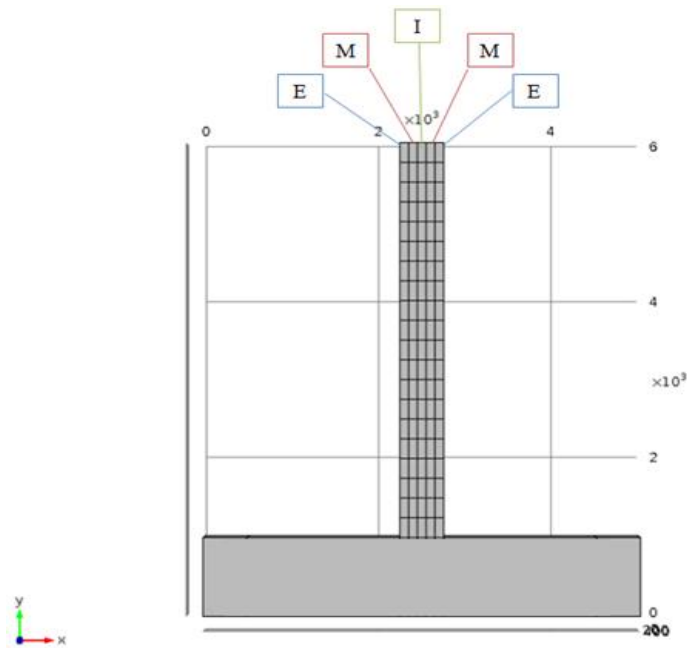
Figure 129. Schematic of location where slots were located.
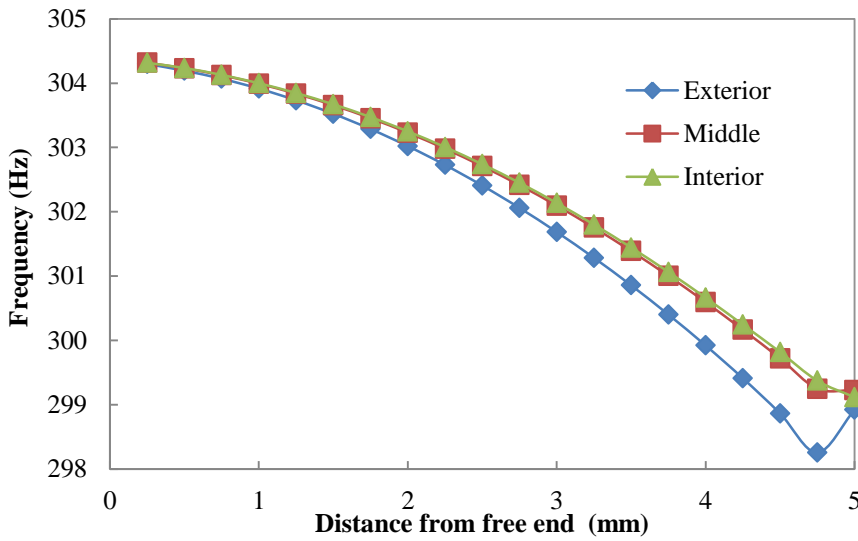
Figure 130. 1st mode including one slot.
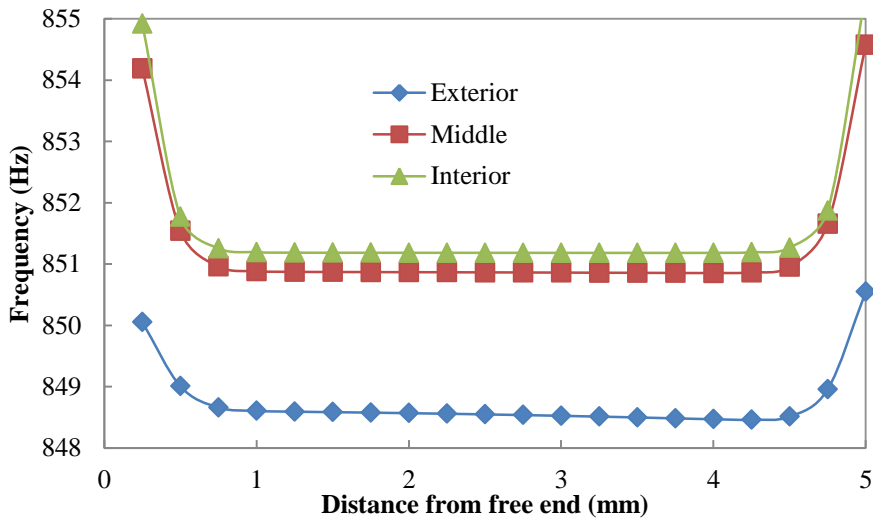
Figure 131. 2nd Mode including one slot.

There is a completely different behaviour in these modes. The first mode (odd mode) presents a fairly linear dependence between where the slot is located along the length of the beam whereas the influence of the position along the width on frequency shift is very low. The closer to the fixed end the slot is, the greater the frequency shift. The farther the mass distribution, the smaller the impact on the resonance frequency, therefore, the closer the

slot to the fixed end, the lower the resonance frequency with respect to the expected value without a slot on it. Regarding the second mode (even mode), the behaviour is not monotonous, showing less difference from the reference value. On contrast to first mode response, when the slot is located on the edge of the beam, the decrease in frequency is greater. This is due to the fact that the structure has more asymmetry for the torsional mode. Regarding the Q factor, there is no representative influence in it because the eliminated amount of mass is fairly small compare to the whole mass of the structure.

We looked at the effect of size of the slot. Figure 132 and Figure 133 show the first and second resonance frequency varying the number of slots in a row from 1 to 4 starting from the exterior column (see Figure 129). Obviously, the change in resonance frequency is more significant when the slot is bigger due to the difference in mass increased.
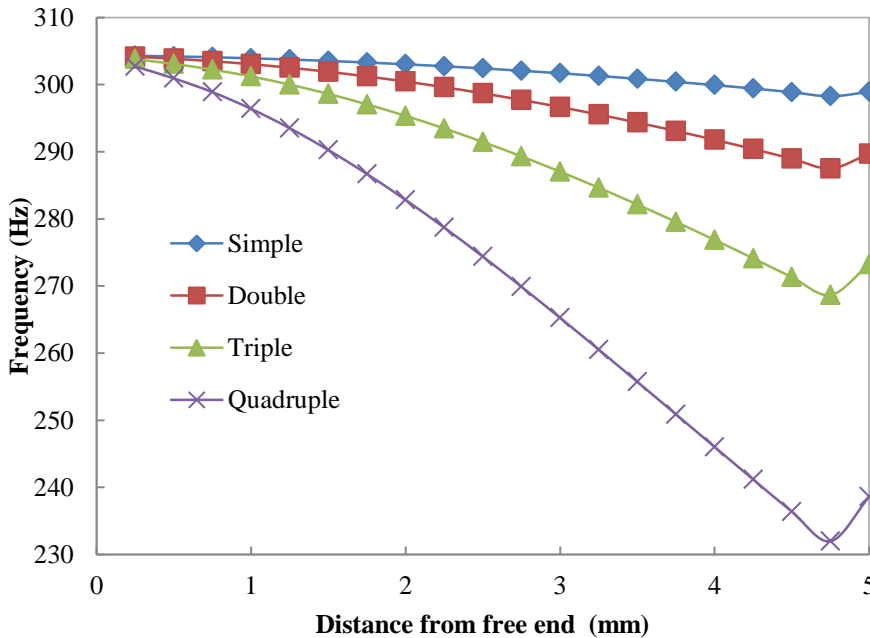
Figure 132. 1st mode varying the number of slots per row.
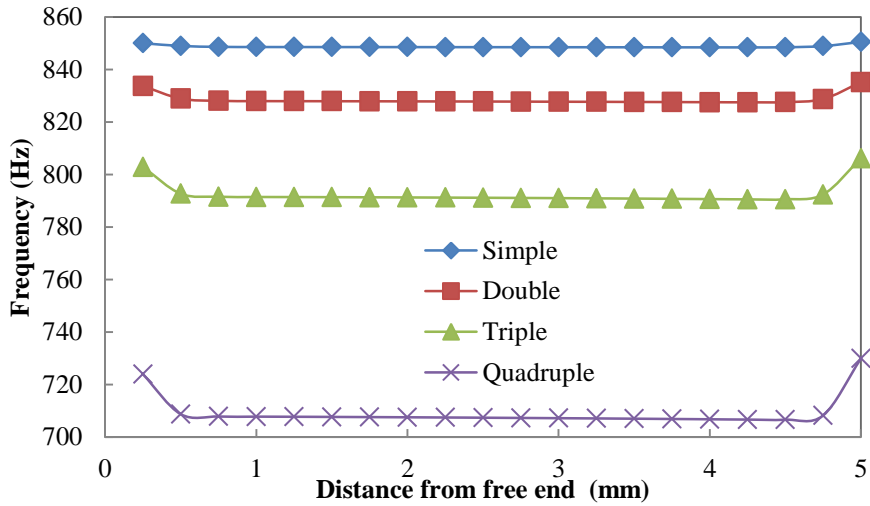
Figure 133. 2nd mode varying the number of slots per row.

Table 32 presents the volume removed as a function of the number of slots in the cantilever. Figure 134 illustrates this change in frequency as a function of slots volume at different positions along the beam. The closer the slots to the free end are placed, the lower the variation in frequency is appreciated. This dependence can be modelled as a second order function.

Table 32. Volume removed depending on the number of slots.

Number of slots	Simple	Double	Triple	Quadruple
Volume (mm^2)	0.0025	0.0050	0.0075	0.0100

Actually, if we remove a complete row, the 1st mode decreases up to about 40 Hz and the 2nd mode to about 60 Hz at the free end. That could be a perfect combination to bring closer the two first resonance frequencies and broader the Q factor. The problem is that if these slots are so deep that the manufacturing feasibility is null, then the structure would be broken. For this reason, we have studied the impact of the slot thickness on the resonance frequency when we have removed a whole row.
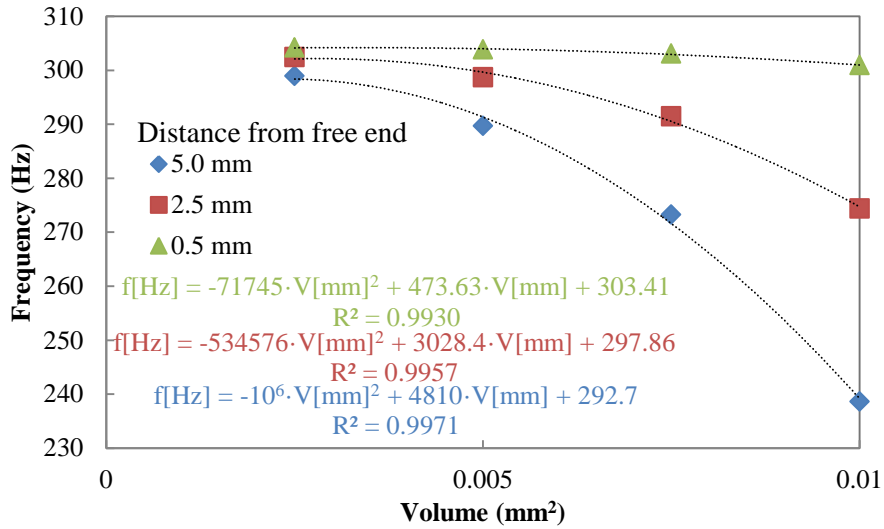
Figure 134. Resonance frequency as a function of the slot volume at difference distances from the free end.

Figure 135 and Figure 136 present the first and second mode as a function of the distance from the free end for different slots thicknesses. Undoubtedly, the influence of the slots increases when their size increases too. That is to say, the bigger the slots in the beam, the greater the variation in the resonance frequency, again, due to a higher mass difference.
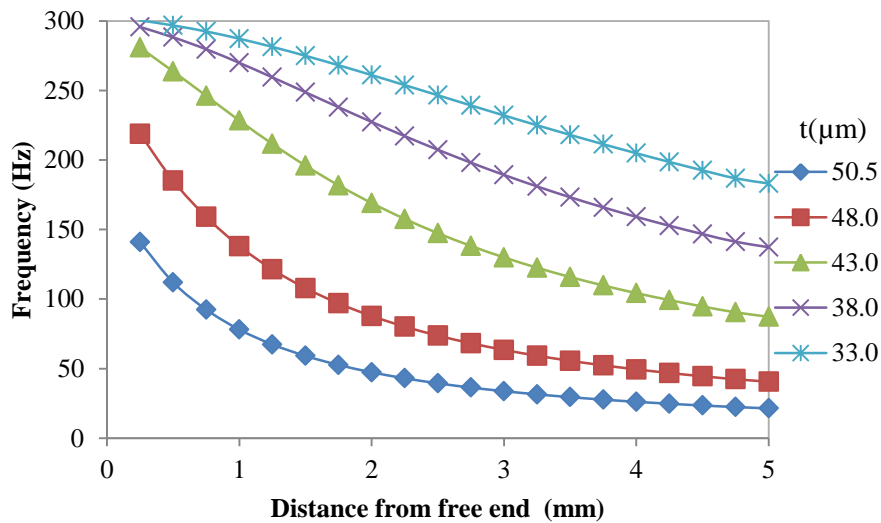
Figure 135. 1st mode varying the slot thickness.
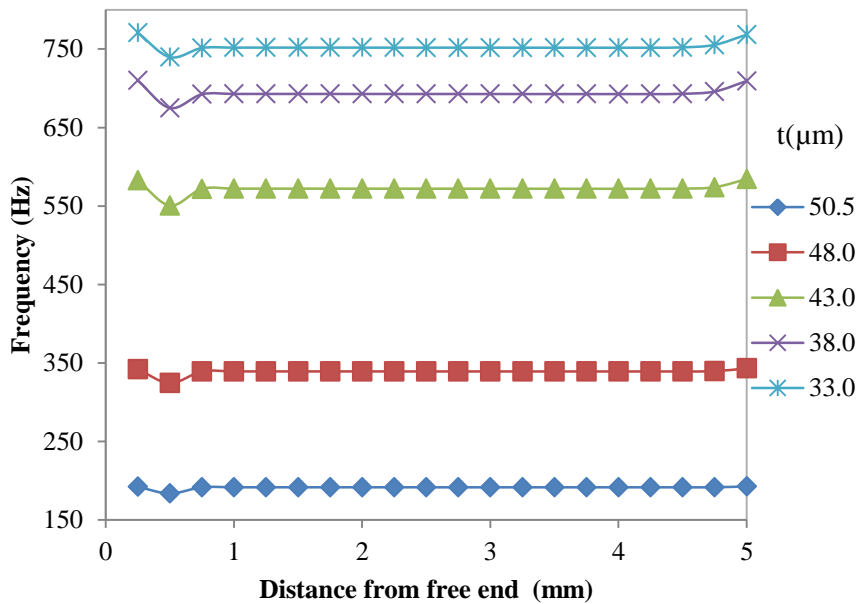
Figure 136. 2nd mode varying the slots thickness.

In order to know the compromise between slots thickness and manufacturing success, we have looked at the stress generated in the beam when a force has been applied. The stress is concentrated at the fixed end in the reference beam (without slots); however in this case the maximum stress value is located at the row with slots.

Figure 137 presents the maximum stress as a function of the distance from the free end where slots are defined for different slots thickness. Figure 138 illustrates the maximum stress as a function of slot thickness for different slot positions along the beam. The stress can be modelled as an exponential function. Figure 139 presents the maximum displacement of the beam in z-axis as a function of the location of the beams for different slot thickness. Table 33 presents the equivalency between the thickness of the slots and the total amount of volume removed. Table 33 presents the volume retired as a function of the slot thickness.
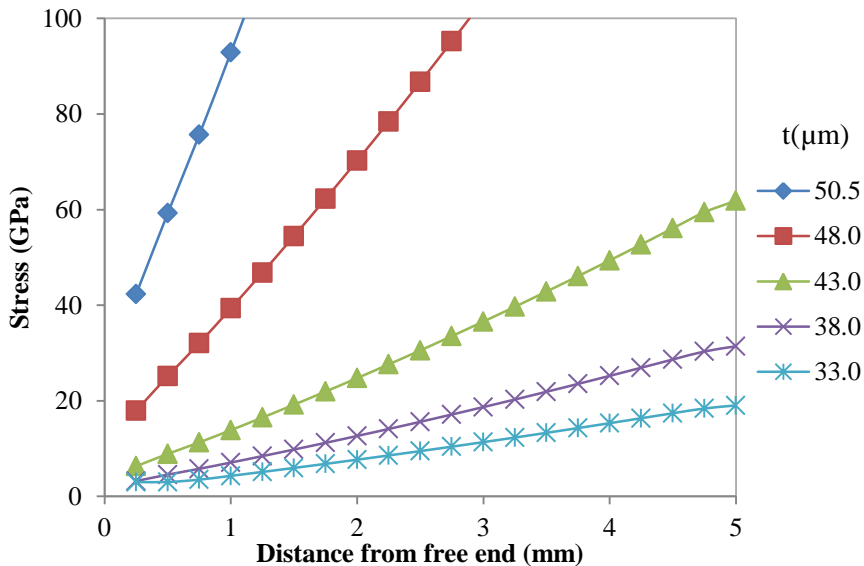
Figure 137. Stress as a function of the location of the slots in the beam varying the slot thickness.

Let's remember that 1st and 2nd mode are separated about 545 Hz. A good criterion to know the manufacturing success is looking at the yield stress of the structural material. In this case, the main fabrication material is silicon, whose yield stress varies from 5 GPa to 9 GPa. Taking into account the worst case (5 GPa), we could only manufacture beams with slots less than 1 mm from the free end and with a maximum thickness of 38 μm. In these conditions, the closest distance between the first two resonance frequencies would be 386.73 Hz for 38 μm-thick slots at 0.5 mm from the free end. For the best case (9 GHz), we could fabricate beams with slots less than 2.25 mm from the free end and with a maximum thickness of 43 μm. Being now the first mode and the second mode located at about 288 Hz and 675 Hz, respectively. In these conditions, the closest distance between the first two resonance frequencies would be 286.96 Hz for 43 μm-thick slots at 0.5 mm from the free end. The first mode decreases at about 185 Hz and the second mode at about 550 Hz.
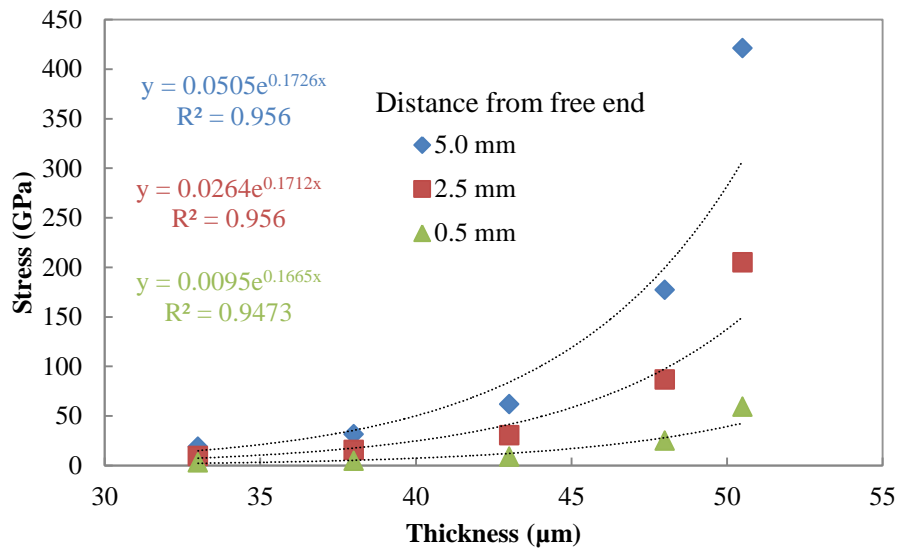
Figure 138. Stress as a function of the slot thickness at difference positions of the slots in the beam.
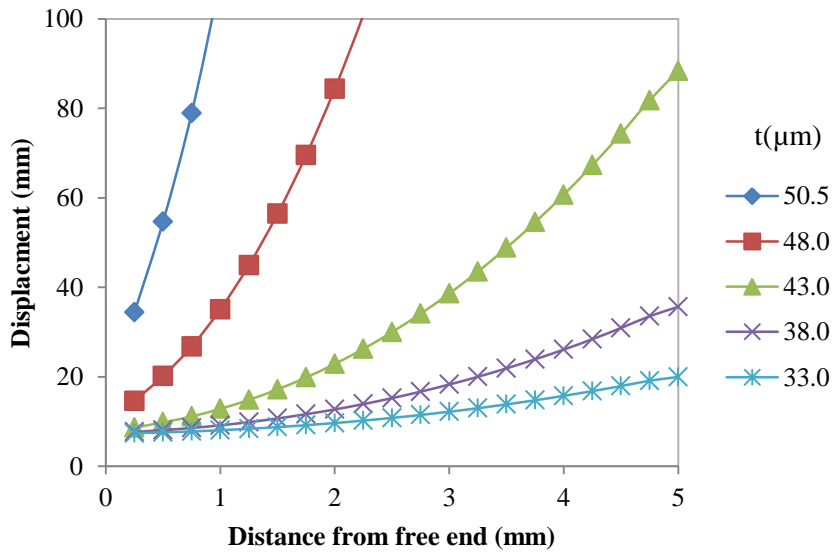
Figure 139. Displacement in z-axis as a function of the location of the slots in the beam varying the slot thickness.

Table 33. Volume removed depending on slot thickness.

	2.5	5	10	15	20
Volume (mm^2)	0.002525	0.0024	0.00215	0.0019	0.00165

4.3.3 Capacitive microphone

Finally in this chapter, we present our numerical simulation of a suspended capacitive microphone. This design is based on the proposal of Yang et al. (Yang 2010). Here, we have studied by numerical simulation how the dimensional parameters affect the sensitivity of this capacitor. The main application of this specific structure is as a microphone. The different between this novel structure and the mostly used is the lack of an internal cavity, simplifying the manufacturing process and giving more sensitive area than the traditional one.

Figure 140 shows a cross section of the traditional structure for microphones. The main elements of this design are the following:

- Diaphragm: Plate where the acoustic wave applies the mechanical pressure to the structure.
- Air Gap: The dielectric material between the two plates of the capacitor. This internal cavity is obtained by using a sacrificial layer. The variations in the acoustic pressure level directly affect the thickness of this inner space.
- Backplate: Plate with perforations which allows the air input/output when the acoustic wave impacts.
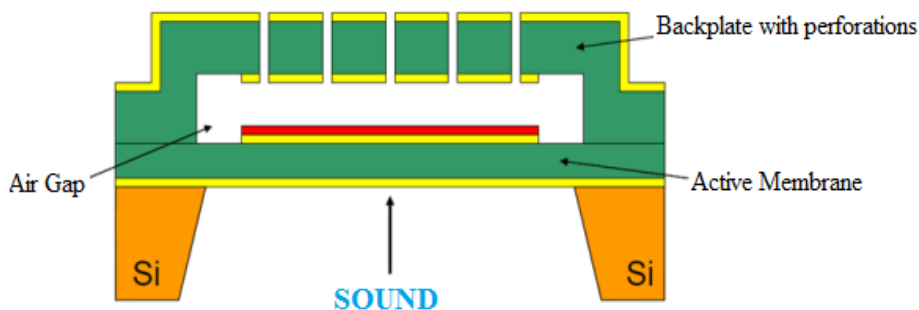
Figure 140. Traditional microphone structure.

The first MEMS microphone was presented by Hohm and Gehard-Multhaupt in 1984 (Hohm and Gerhard-Multhaupt 1984). This device was based on silicon technology and its diaphragm was fabricated with electret material. Scheeper et al. (Scheeper et al. 1992) developed one which has been becoming a classical structure and has been fairly exploited.

There are many examples in the literature of this structure. Bergqvist et al. (Bergqvist and Gobet 1994) fabricated a condenser microphone using metal electrodeposition on a sacrificial photoresist layer. The electroplate technology has been used to implement a copper microstructure of 15 mm thickness suspended and perforated which formed the back electrode of this microphone. The wide diaphragm of polycrystalline silicon (1.8 mm x 1.8 mm) was fabricated with anisotropic etching on the wafer. The manufactured prototypes had a sensitivity of 1.4 mV/Pa with a bias point of 28 V and a bandwidth of 14 kHz.

Another example was developed by Ning et al. (Ning, Mitchell and Tait 1996). In this case, the backplate and diaphragm were fabricated on silicon by plasma-enhanced chemical vapor deposition (PECVD) of silicon nitrure. The sacrificial layer was amorphous silicon and it was removed by dry etching. The dry etching avoids the problems of wet etching to keep together the diaphragm and the backplate caused by capillarity forces. This microphone had an open circuit capacitance of 9.5 pF and a sensitivity of 7 mV/Pa with a bias point of 6 V in a frequency range 10 Hz to 10 kHz.

Pedersen et al. (Pederson, Olthuis and Bergveld 1998) presented a polyimide microphone on silicon. Its sensitivity was 10 mV/pa and the Equivalent Noise Level (ENL) 27 dBA without bias voltage and 1.9 V of supply voltage. A more recent example was proposed by Ganjia et al. (Ganji and Majlis 2009). In this case, the moving diaphragm was placed on the back electrode, including lots of perforations to facilitate the air flow between the electrode and diaphragm and decreasing the acoustic decay in the microphone. As sacrificial layer and insulation layer, Spin-On-Glass (SOG) was used. The diaphragm was 3 mm thick and an area of 0.5 mm x 0.5 mm, allowing 1 mm of air. Comparing with similar work, this microphone showed several advantages, such as the following: perforations were done in the diaphragm and, therefore, it is not necessary to etch the back side and the dimensions are

reduced. Moreover, the fabrication process required less layers and masks, reducing manufacturing costs.

As already mentioned, a totally different structure for capacitive microphones was presented by Yang et al. (Yang 2010). This design is simpler and requires few masks during its manufacturing (Figure 141). The main advantage of this capacitive microphone is its compatibility with CMOS technology.
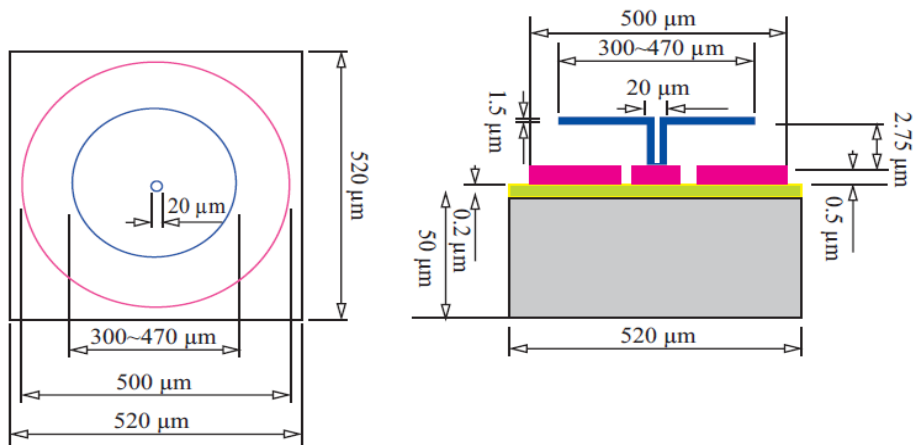
Figure 141. Capacitive microphone presented by Yang et al. (Yang 2010).

4.3.3.1 Simulation procedure

A. MEMS+

Firstly, we modelled with MEMS+ both designs (Figure 140 and Figure 141), in order to verify the better properties of this capacitive microphone. This software provides a first approach to the electrical and mechanical behaviour of the studied structure. In addition to this, this software is directly integrated in Cadence environment, facilitating the design of the extra circuitry for the studied device. Both structures have been implemented in PolyMUMPs technology to directly compare and contrast their characteristics. This technology is a standard technology (Koester et al. 2003).

B. Coventor

In order to know the mechanical behaviour of these microphones, the sensor has been polarized with a DC voltage source in one of its electrodes (Figure 142). The output of this circuit has been the other free electrode. The electrical excitation of the device is the pressure pin. This pin was defined in MEMS+, indicating which part of the sensor is affected by the acoustic pressure. The scale factor between applied voltage and applied pressure is 1 V : 1 Pa. We have studied the DC response of this circuit.

The capacitance pin is created in MEMS+ when an electrode and a moving part are connected and, therefore, allows measuring this capacitance. Thanks to this, we could compute in Cadence the voltage in this pin and directly extrapolate the capacitance with the following equality: 1V corresponds to 1 F. Obviously, this is not a real pin of the circuit, but it only provides a simple and direct way to measure the capacitance.
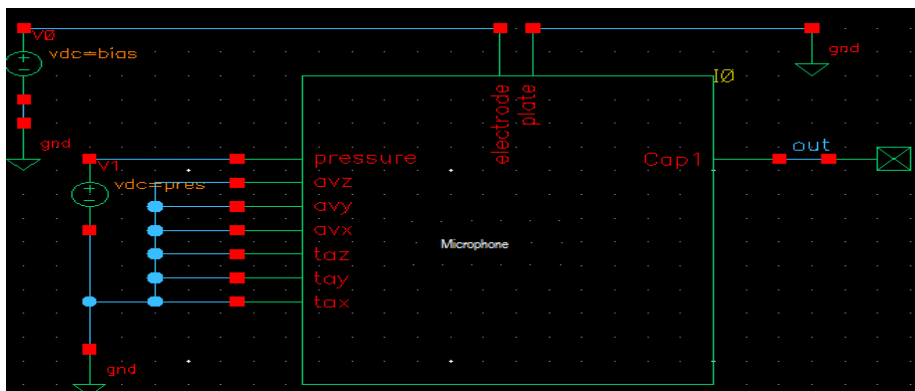
Figure 142. Schematics for the DC analysis.

The second circuit has studied the mechanical behaviour of these capacitive structures. In this case, an AC analysis has been performance (Figure 143). If the microphones act as expected, as a capacitance, the output of this circuit will correspond to a first order high pass filter.
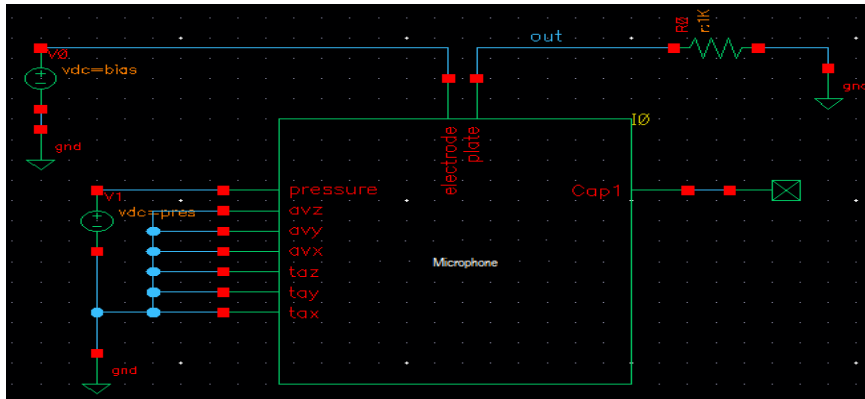
Figure 143. Schematics for AC analysis.

The cut-off frequency of this kind of filters is given by

$$f_c = \frac{1}{2\pi RC}$$

(30)

Extracting this frequency from the simulations, the capacitance can be easily calculated as

$$C = \frac{1}{2\pi R f_c}$$

(31)

The distance between the diaphragm and backplate can be approximated by the equation of a parallel plate capacitor

$$d = \frac{\varepsilon \cdot Area}{2\pi R f_c}$$

(32)

where ε is the electrical permittivity of the dielectric in the diaphragm, in this case the air.

C. COMSOL Multiphysics

The selected package to model and simulate these devices is COMSOL Multiphysics version 4.2a. It is a powerful interactive environment for solving problems based on partial differential equations. This software is a well-known tool for MEMS applications (Shivok 2007).

The geometrical model for the Yang´s structure is shown in Figure 144. Models for describing condenser microphones have classically been of the equivalent network type (Leach 2003). Analytical models exists for simpler

geometries but there are also highly advanced analytical models for more complex geometries (Lavergne et al. 2010). In the present model, a static analysis of the DC charging and deformation of the diaphragm is included and a time-harmonic finite element (FE) analysis of the dynamics of the diaphragm coupled to thermoacoustics is performed. The small-signal electric model for the system is solved as a lumped model coupled to the FE model.
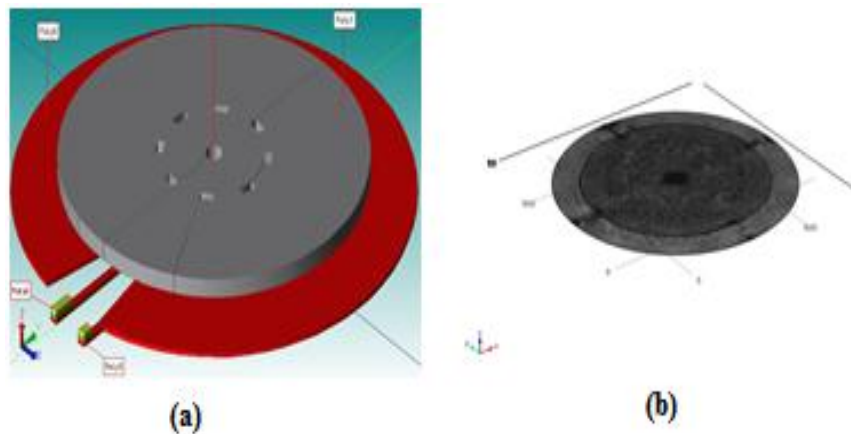
Figure 144. Geometry (a) and Mesh (b) of the studied microphone (not done to scale).

In this analysis, different physics have been used:

1. Themoacoustics
2. Electrostatics
3. Solid Mechanics
4. Electrical Circuit
5. Moving Mesh
6. Partial differential equation (PDE)
7. Global ordinary differential equations (ODE) and differential algebraic equations (DAE)

In order to reduce computational time, the model was simplified ignoring perforations in the diaphragm. These perforations are placed in order to produce special sensitivity characteristics of the microphone.

There are many examples of MEMS microphones in the literature. However, many of the silicon-device building processes were custom processes and therefore costs reflected those specialized processes.

The key to lowering the cost of devices is to try to use one of the existing standard processes. PolyMUMPs stands for Polysilicon Multi-User MEMS Processes and consists of three-layer polysilicon surface and bulk micromachining process, with two sacrificial layers and one metal layer (Koester et al. 2003). This microphone was designed with PolyMUMPs design kit, using two different layers of polysilicon to define its diaphragm and blackpate.

As we have already explained, the most widespread transduction method is capacitive based on the variation of capacitance owing to the displacement of the membrane due to variations in acoustic pressure. The diaphragm is deformed due to electrostatic forces from charging the capacitor and also because of the pressure variation from external incoming uniform acoustic signal.

The diaphragm is backed by a thin air gap of thickness H_m and a back electrode. It is essential to include thermal and viscous losses in the model due to the gap being so small. The diaphragm and back electrode build a capacitor which is polarized by an external DC voltage source. The air gap acts as a damping layer for the diaphragm vibrations. There is a voltage change induced by the variation of the distance between the diaphragm and the back electrode and is coupled to the capacitor and to an external very large resistive load.

The capacitance C of a parallel plate capacitor, with a fixed air gap h and area A is given by

$$C = \frac{\varepsilon_0 \varepsilon_r A}{h} = \frac{\varepsilon_0 \varepsilon_r A}{H_m + U_{0,av} + U_{av}} \qquad (33)$$

where H_m is the sum of the initial distance, U_0,av reflects the quiescent average deformation from equilibrium due to electrostatic forces of the pre-polarization condenser microphone and U_{av} represents an average deformation around the initial static gap distance (H_m+U_{av}) (Griffiths and College 1999).

4.3.3.2. Results and discussion

A. MEMS+

The following figures (Figure 145 and Figure 146) show both models in MEMS+ where the different layers have been labelled for better understanding. As this tool implements behavioural models, the designs do not include all the details, such as perforations.
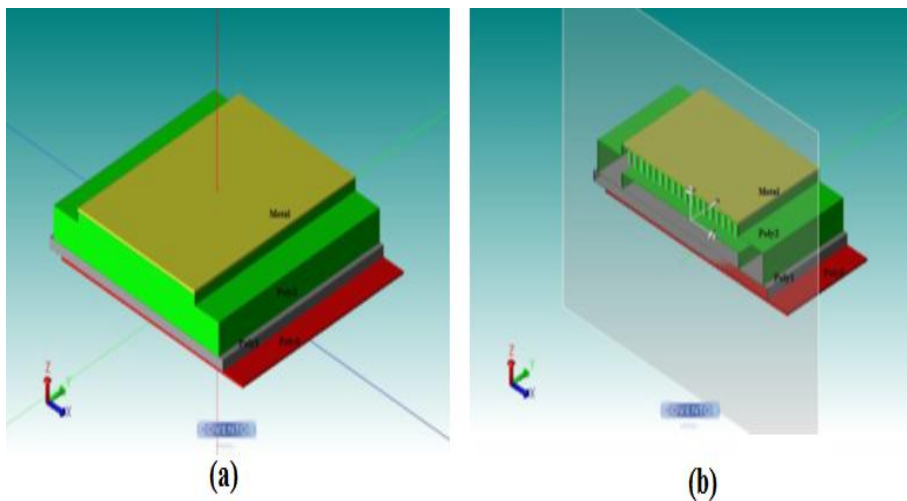
Figure 145. Capture of traditional microphone model in MEMS+ (a) global view, (b) cross sectional view.
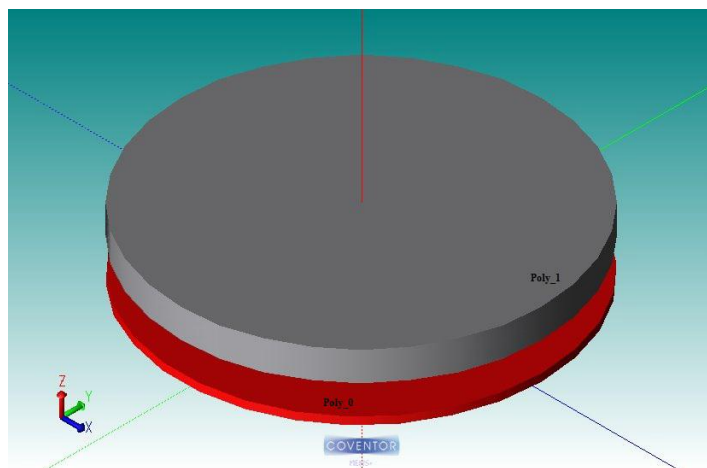
Figure 146. Capture of capacitive microphone model in MEMS+.

Both models were introduced in Cadence virtuoso and included in two different circuits to be able to study the response of each microphone.

B. Coventor

In order to be able to compare results, we have tried to define diaphragms which cover similar areas. Figure 147 and Figure 148 show the DC response of the microphones. As can be observed, the traditionally used microphone presented a much poorer response than this mushroom shaped. Figure 149 presents the frequency response of the novel design. We performed several analyses varying the radio of the microphone. As we can see, there is a slight shift in the resonance frequency, a lower frequency for the higher radius.
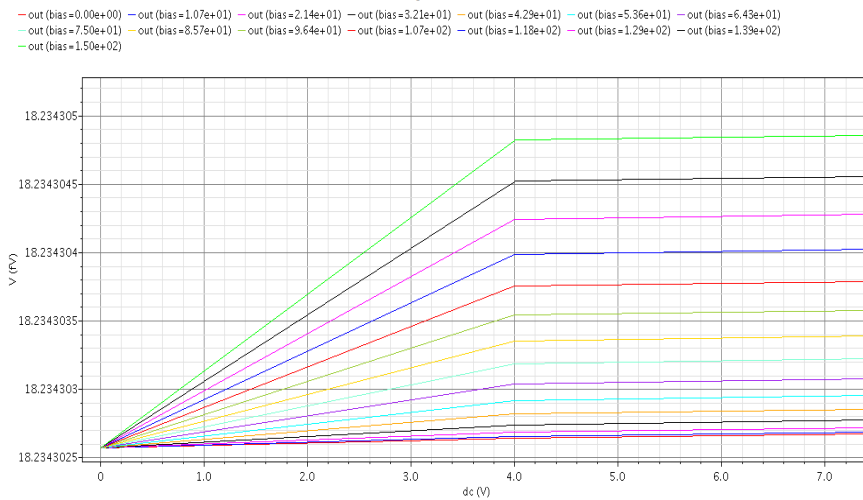
Figure 147. Results of the DC analysis of the traditional microphone for different bias voltages.
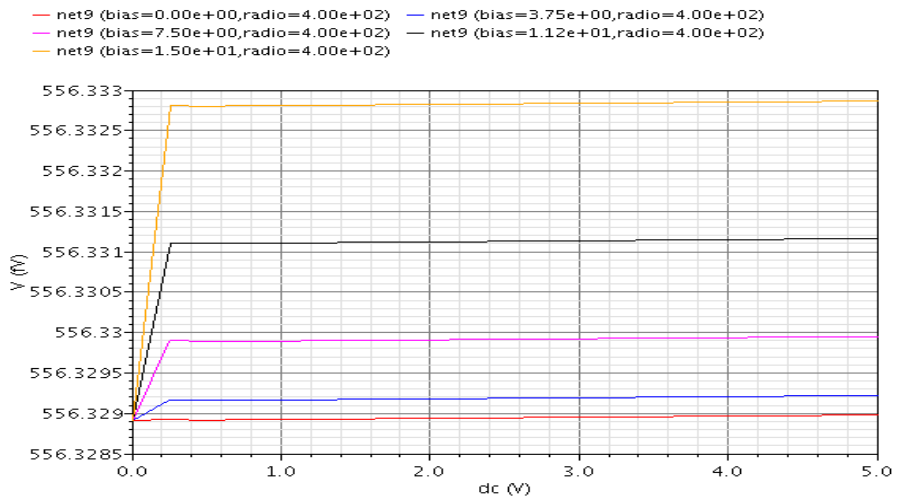
Figure 148. Results of the DC analysis of the Yang microphone for different bias voltages.
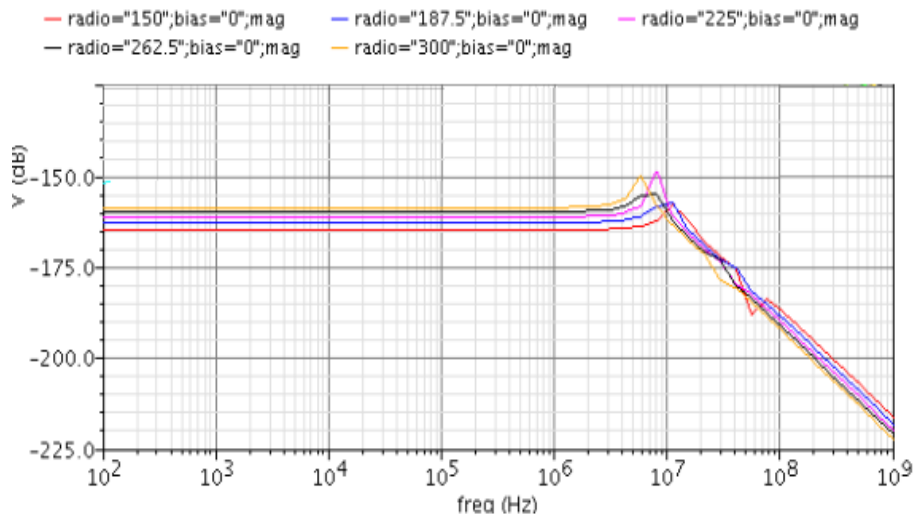
Figure 149. Yang microphone for different radio dimensions at different bias voltages.

We have proved that the Yang´s mushroom capacitor showed a better performance than the traditional microphone. Next, a detailed analysis of a MEMS microphone using PolyMUMPs is presented in this paper. The influence of its geometry on its characteristics has been studied.

C. COMSOL Multiphysics

The studied microphone is a circular central-post structure similar to a mushroom shape. The classical structure was not simulated with this tool beacause its performance compared with Yang's model was quite poor. The capacitance of this microphone has been studied for different values of diameter, thickness, and distance between the diaphragm and backplate.

Table 34. Dimensions of the reference microphone.

Parameter	Symbol	Value	Unit
Diaphragm Diameter	D_m	370	µm
Diaphragm Thickness	t_m	1.60	µm
Diaphragm Height	H_m	2.75	µm
Support Diameter	D_s	20	µm
Backplate Diameter	D_b	500	µm
Backplate Thickness	t_b	2.00	µm
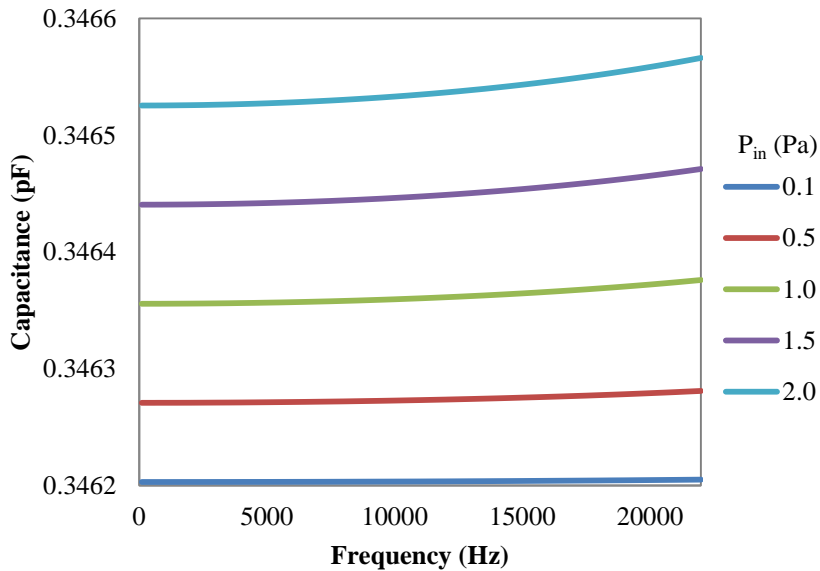
Figure 150. Frequency Response of reference Yang microphone.

Figure 150 shows frequency response of the reference microphone (Table 34) at different values of pressure in the audible range of frequencies. There is a slight difference of capacitance and it can be modelled as a second order function.

$$C(pF) = 4 \cdot 10^{-12} f(Hz)^2 - 8 \cdot 10^{-11} f(Hz) + 0.3464$$
$$R^2 = 0.9998$$
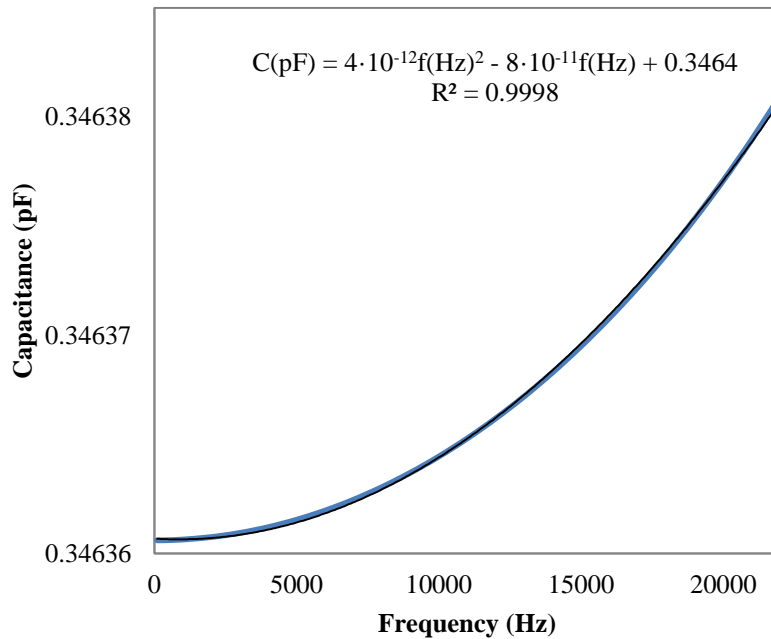
Figure 151. Frequency Response for 1 Pa of reference Yang microphone.

Figure 151 represents the frequency response of the reference Yang microphone for 1 Pa of pressure in order to better appreciate the frequency behaviour.

Figure 152 represents the capacitance as a function of the diameter of the diaphragm. This relationship can be modelled by a straight line, the larger the diameter, the higher the capacitance.

$$C(pF) = 0.0020 \cdot D_m(\mu m) + 0.4028$$
$$R^2 = 0.9980$$
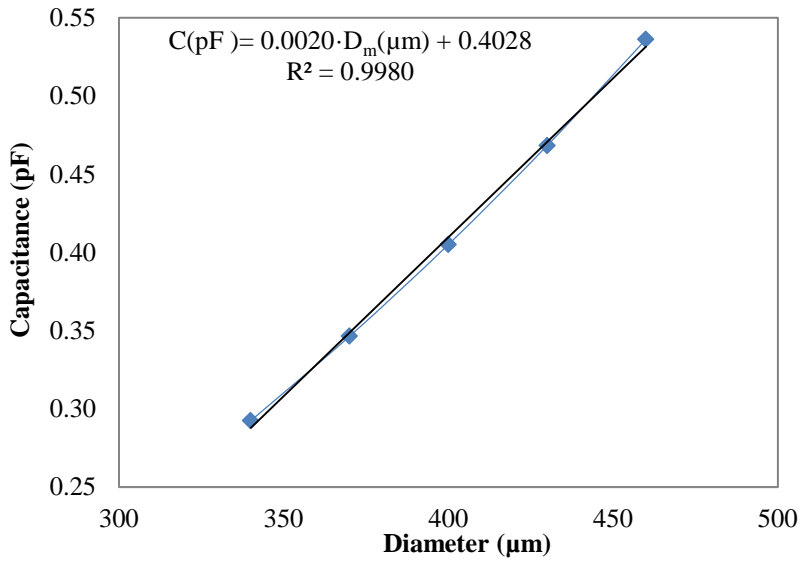
Figure 152. Capacitance vs. Diaphragm Diameter at 1 kHz for 1 Pa.

$$C(pF) = -0.1298 \cdot H_m(\mu m) + 0.7094$$
$$R^2 = 0.9882$$
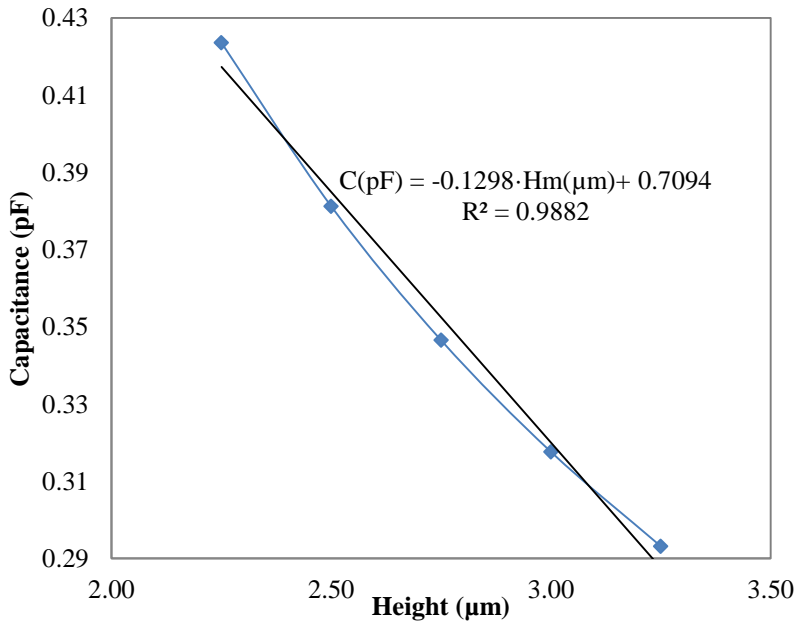
Figure 153. Capacitance vs. Height at 1 kHz for 1 Pa.

Figure 153 represents the variation of capacitance for different values of the height of the diaphragm. In this case, the lower the height, the greater the

capacitance. This behaviour is due to the reduction of the reference height and, therefore, the initial capacitance is higher (see equation (33)).

Figure 154 represents the frequency response of capacitance as a function of the diaphragm thickness. The narrower the diaphragm, the higher the sensitivity.

On the other hand, Figure 155 represents the capacitance as a function of the diaphragm thickness. The variation of capacitance due to its thickness dependence can be modelled as a polynomial curve of 2nd order.
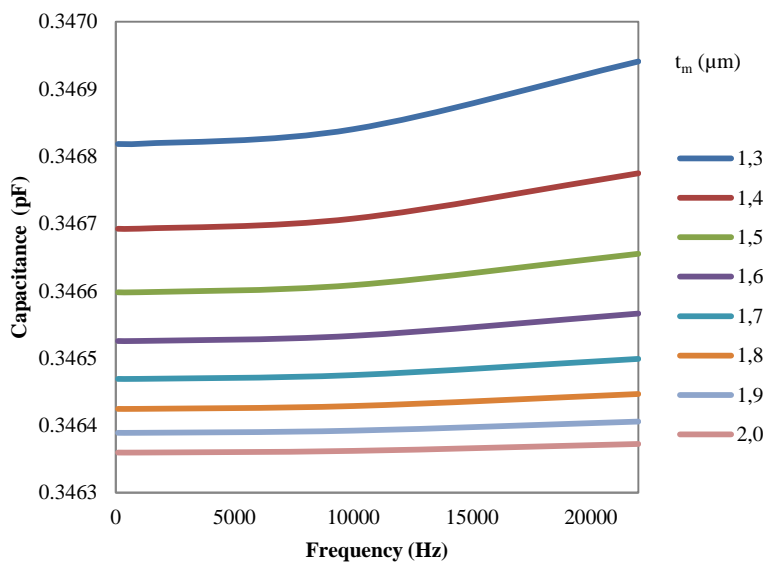
Figure 154. Frequency response of Capacitance vs. Thickness.
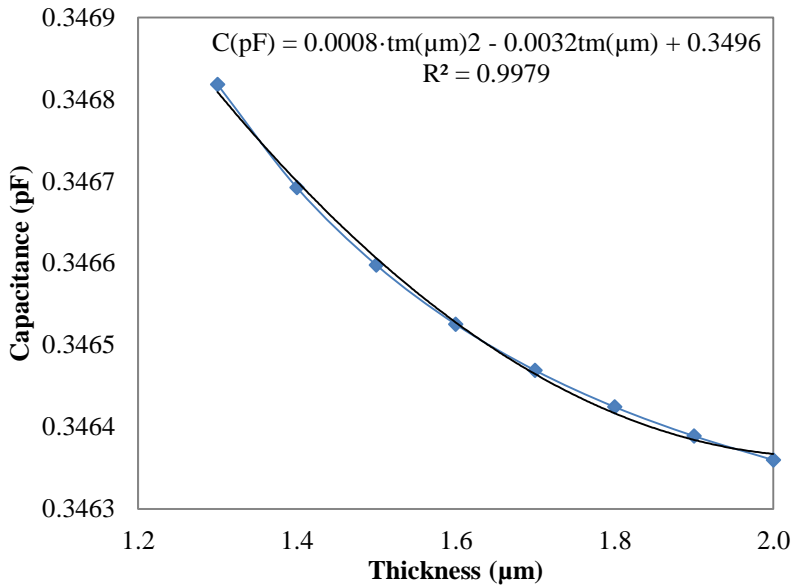
Figure 155. Capacitance vs. Thickness at 1 kHz for 1 Pa.

In this part, a study of capacitance response with variations on the microphone geometry was conducted. First of all, it has been shown that COMSOL Multiphysics can achieve accurate results when compared to theoretical models. This is an excellent advantage since the results of the simulation can provide not only verification concerning the validity of the physical assumptions made in defining the model but also simulations can be used to determine the design parameters that will optimize the device performance thus minimizing the time, effort, and expense required to construct and test an actual device.

The effect of various variations to the microphone was studied. The results show that capacitance is affected through changes on its geometry and the results can be used to determine the correct dimensions for fabricating devices. The higher values of capacitance are reached with higher values of diameter of the membrane, lower values of height of the membrane and narrower values of its thickness.

4.4   Conclusions

In this chapter, we have analysed different suspended structures both in printing and MEMS technologies. First, we have presented two different fabrication approaches to develop printed suspended structures. Then, two kinds of structures in MEMS technology have been studied.

For the suspended structures realized with printing technology, a full-printed cantilever beam by sacrificial layer was developed first. Then, we fabricated full-printed cantilever based on sacrificial substrate. In this later case, we have tested two different materials as sacrificial substrate.

Regarding the first approach, the fabrication of the cantilever has not been successfully achieved but there are some promising results. The justification of using a printed sacrificial layer is to achieve a very thin gap between the cantilever and the substrate. This small gap (~10 μm) provides higher nominal capacitance and higher sensitivity when any displacement happens. In addition to this, this kind of structure could be used easily integrated as switches.

The best found candidate as sacrificial layer is a mixture of TME, CH and PG, whereas the best conductive material to fabricate the cantilever is based on screen silver ink. This screen silver ink can be printed with quite good results on TME+CH+PG solution without reacting with it. Furthermore, the TME mixture can be removed after silver sintering. Another possible solution to those inks which reacts with TME avoiding its sublimation is inserting a structural layer, such as ethylcellulose between the sacrificial layer and the electrodes. We have not been able to test this solution because this solution adds another alignment step, and the flat screen printer does not have any accurate procedure to align.

Other alternatives to follow can be:

1. Further test using PMMA as sacrificial layer.
2. Formulate TME solution using DMHD composition.

The future research should be focused on improving the printed layers by using roto screen printing, finding the best manufacturing conditions that allow the reproducibility of this process.

Concerning sacrificial substrate, we have presented a novel manufacturing process to develop printed cantilevers on a foil substrate. The structural material of this cantilever is silver ink. This process reduces the number of steps, saving time. Furthermore, the sacrificial layer used here provides a flat area to easily print on it, reducing the roughness of the cantilever bean and, therefore, increasing the probability of avoiding fractures. The main difference between this procedure and the conventional ones is the fact that the sacrificial layer is now placed on top of the suspended structure instead of below it. This particularity plays down the importance of the sacrificial layer to the fabrication process since there is even no influence of the thickness of the sacrificial layer on the process. Moreover, the substrate is not a rigid surface but a plastic foil which provides more flexibility to this device. Finally, we have characterized these printed cantilevers as accelerometers to test the efficiency of this novel fabrication process. For this purpose, we have measured the deflections of these cantilevers as a function of the applied acceleration at different frequencies of oscillation. We have also measured the change in capacitance whilst the cantilever is shaking at some values of acceleration. In addition, we found that experimental data and simulations are in a good agreement.

As we have already mentioned, two different films have been tested as sacrificial layer: PMMA and PVA. The first prototype was developed with PMMA film. Although its response to applied acceleration as well as capacitance was successfully measured, we detected some imperfections in the homogeneity of the beams. These alterations in the beam might be caused during the removal of PMMA because it is submerged in an acetone bath and acetone reacts also with the silver structural layer. Then, we tested PVA film which can be removed with a water bath. We obtained a flatter beam profile and, therefore, a better reproducibility as well as a high manufacturing yield.

After that, we have studied a piezoelectric cantilever design to work as energy harvester suitable for being fabricated with MEMS technology. For this purpose, we have looked at its resonance frequency with changes in the beam geometry. It has been shown that COMSOL Multiphysics modelling of purely Si beams could achieve accurate results when compared to fabricated devices with multi-layered structures. This modelling simplification reduces the computational time to test the mechanical

properties of this harvester. The results show that resonant frequencies are affected through changes on the beam and the results can be used to determine the correct dimensions for fabricating devices of specific resonant frequencies. The effect on the Q factor was not so significant and further studies are required. The same models can be directly updated to include the piezoelectric element in order to model the electrical properties. The best compromise between manufacturing yield and closer first two modes of the resonance frequencies has been found when a row of slots has been defined at 0.5 mm from the free end with a thickness of 43 µm for good quality silicon and 38 µm for poor quality silicon.

Finally, we have modelled the capacitance response of a design for a MEMS microphone with variations in its geometry. The shape of this microphone is similar to a mushroom, being the suspended plate the diaphragm sensitive to the acoustic waves. Thanks to the results of the simulation, we can provide not only verification concerning the validity of the physical assumptions made in defining the model but also simulations can be used to help determine the design parameters that will optimize the device performance thus minimizing the time, effort, and expense required to construct and test an actual device.

The results show that capacitance is affected through changes on its geometry and the results can be used to determine the correct dimensions for fabricating devices. The higher values of capacitance are reached with higher values of membrane diameter, lower values of membrane height and narrower values of its thickness. We have not been able to fabricate this microphone, but it would be interesting to do in order to compare and contrast our model with experimental results. It would be interesting to try and fabricate this device by printing techniques following the process based on PVA sacrificial substrate.

5.   Multisensor systems for environmental monitoring

As we have remarked in the introduction, sensors are essential to many different applications, from health care to home security. But sensor do not work alone, they need to be integrated on a more complex system that extract the signal sensor, process it and transfer this value to another system or user that can interpret it.

Depending on the sensor and the concrete application, the complexity of the final system can extremely change but there are always some parts included in every sensorial electronic system:

1. Sensor. This part includes the sensing element and the transducer element, that is, the sensitive part and the element that converts this change into an electrical signal.
2. Signal processing. This block contains all the circuitry needed to adapt the sensor signal to the rest of the system. It can include filters, amplifiers, analog-digital converters and so on.
3. Signal Transmission. This information must be transmitted to other systems. For this reason, data bus, universal serial bus (USB) interface, RF link, among others, can be introduced.
4. Data visualization and/or storing. These data are displayed in a screen or stored in memories to be accessed by users in real time or historical archive, respectively.

In this chapter we will show different strategies to integrate humidity sensors (both developed by us and commercially available) in electronics systems to provide a complete functionality. First, a multisensory probe will be shown. This probe measures humidity, temperature and oxygen concentration in soils. For this purpose a commercial humidity-temperature sensor was selected together with an optical sensor previously developed in this research group. Then, a passive RFID tag will be presented. It provides two different parameters: humidity from a printed sensor and temperature. In order to extract these values, a RFID user interface is needed. Both parameters are read with high precision. The final prototype is another RFID humidity tag,

also with a printed humidity sensor, that can be read which any RFID reader but it just provides a threshold value; this prototype can be used as a humidity resonance sensor as well where the resonance frequency is shifted when the relative humidity changes.

5.1   Multisensor   probe   to   monitor   humidity, temperature and oxygen concentration in soils

In a previous work developed in this research group, an oxygen sensor was developed with the aim of measuring the oxygen content (Capitan-Vallvey et al. 2007, Martinez-Olmos et al. 2011, Martínez-Olmos et al. 2013, Palma et al. 2007b, Palma et al. 2007a, de Vargas-Sansalvador et al. 2011). This sensor is based on the luminescence quenching of a sensitive membrane by the presence of gaseous oxygen. The most common strategy in this type of sensors is to deposit a polymeric membrane permeable to oxygen, such as silicone or poly(methyl methacrylate) containing the luminescent compound and to include a light source (i.e. LED or laser diode) to excite the sensitive film, a photodetector to measure the emitted radiation and a fibre optic to transmit the light (Amao 2003). The sensitive material is placed between the light source and the photodetector. Many authors have prepared the sensitive polymer on a substrate where the forming material is along with the reagent. This can be achieved by immersion techniques, paint, spray or casting (Andrzejewski, Klimant and Podbielska 2002, Hauser, Liang and Muller 1995) after the flat substrate is covered and located between the light beam and the detector.

Another optical design with a higher degree of integration uses a fibre optic with the membrane included in the polymer which has been carefully adjusted at the distal ended and placed appropriately with the light source by gluing, fusion-assembly or mechanical connection (Peterson, Fitzgerald and Buckhold 1984). A greater efficiency in the collecting of light is obtained by light concentrators with coplanar guides. In this case, the luminescence is excited from one side of the light guide and efficiently guided to the photodiode (Lippitsch et al. 1988). The main problems in these solutions are the fibre curvature and the membrane photodegradation due to the need of

light sources with enough intensity to compensate the decay of the luminescence intensity in combination with the thin film used to get a fast response (Colvin Jr 1996). Moreover, it is important to study the system complexity and its cost as well as the requirement of addressing the light from LED to the optic fibre and optically filter the luminescence produced.

Some authors have developed compact configurations for the determination of oxygen. The first configuration includes the LED and the polymeric film with the sensitive membrane placed in the top part of an optical filter. This filter acts as a waveguide line and allows a fluoresce light to travel to the photodiode (Colvin Jr et al. 2001, Colvin Jr 1996, Colvin Jr 1999). After that, Bright el al. proposed the measurement of gaseous species (especially oxygen) by placing a sol-gel based film with a sensitive polymeric covered by a technique of aerosols deposition. This system includes a filter located between the LED and the detector. In addition, the film sensitive to oxygen is deposited in contact with the light source and needs an optical filter in the input of the photodetector (Watkins et al. 1998, Watkins et al. 2001). This configuration tries to simplify the circuitry associated with the oxygen sensor.

In the particular case of the oxygen sensor developed in our research group, the key point is to improve the efficiency in the collection of luminescence. This improvement has been achieved by directly covering the detection element with the oxygen photosensitive film. Thus, the only required substrate to deposit the membrane is directly the photodetector. This configuration provides faster response and lower energy consumption. Furthermore, the intensity of excitation signal can be reduced due to the optimal collection of light, and therefore, the sensor photodegradation is also reduced (Capitan-Vallvey et al. 2007).

The sensitive component is platinum octaethylporphyrin (PtOEP). This chemical was chosen for its suitable luminescence characteristics (Lee and Okura 1997) such as longer lifetime, visible absorption, Stokes displacement and compatibility with LED-photodiode configuration. The polymer used to encapsulate the membrane is polystyrene. Moreover, the singlet oxygen generated as consequence of luminescence quenching of PtOEP luminophore by oxygen is eliminated by including in membrane the, the heterocyclic

amine 1,4-diazabicyclo[2.2.2]octane (DABCO) as singlet oxygen scavenger (Palma et al. 2007b, Hartmann and Leiner 2001). This elimination increases the photostability of the membrane.

In this section, we will show the integration of this sensor together with a humidity and temperature sensor to monitor these three parameters in soils. A first prototype of this soil probe was previously developed in our research group (Martinez-Olmos et al. 2011), here we want to optimize this design.

Gas diffusion in porous media, such as soils and wastewater, can play an important role in moving vital compounds for the vegetation in the media. It is known that gas diffusion in soils affects a variety of exchange process, for example: denitrification, roots respiration, metabolism, methane formation, volatilization of organic chemicals and efficiency of wastewater remediation (Aachib, Mbonimpa and Aubertin 2004).

Plants roots are affected by different factors such as temperature (it has influence in roots permeability), aeration (it alters radical metabolism) and salinity (this property modifies water and nutrients absorption). When radical volume decreases, temperature range experimented by roots increases. This behaviour might be caused by oxygen depletion in the roots and the microflora (Roberts, Jackson and Smith 2006)

As we have already commented, we will monitor three important parameters in soils at typical root depth:

- Root temperature: Although temperature changes have less impact on plants than air or light temperature, variations in root temperature can affect significantly plant growing and nutrition (Urrestarazu and Gavilán 2004).
- Aeration: An adequate oxygen concentration at root zone is essential to a healthy plant growing. If oxygen level is too low, radical metabolism is inhibited, nutrients absorption is reduced or ceased and growing is slowed. If this condition is extended in time, plants can develop an iron deficiency (Urrestarazu and Gavilán 2004).
- Humidity. There is an inferior and superior water limits where plants cannot extract water or cannot take oxygen, respectively. It is

necessary that the water content is within these limits (Tibbitts 1979).

5.1.1 Materials and Methods

A. Reagents and materials

The sensor was prepared by deposition of the oxygen sensitive membrane on a photodetector of solid state by a coating technique. The disolutions to prepare the photodetector were obtained by disolving 0.5 mg of PtOEP (Porphyrin Products Inc., Logan, UT, US) and 12 mg of 1,4-diazabicyclo[2.2.2] octane (DABCO) in 1 ml solution of 5% w/v of polystyrene (PS, average MW 280000, Tg: 100 °C, GPC grade) in distilled tetrahydrofurane (THF) in a glass pot. All three supplied by Sigma–Aldrich Química S.A. (Madrid, Spain). The membrane was formed by deposition of layers of 5 µl of the cocktail on top of the active face of the photodetector using a micropipete.

B. Instruments and software

For the electrical characterization of the system, the following instrumentation was used: a mixed signal oscilloscope (MSO4101, Tektronix, Beaverton, OR, USA), an 8½-bit Digital Multimeter 3158A (Agilent Technologies, Santa Clara, CA, USA), a 15 MHz waveform generator 33120A (Agilent Technologies, Santa Clara, CA, USA), a DC power supply E3630A (Agilent Technologies, Santa Clara, CA, USA) and a balance DV215CD (Ohaus Co., Pine Brook, NJ, USA). A user interface made in Visual Basic© was used in a computer for calibration purposes. The standard mixtures for instrument calibration and characterization were prepared using N_2 as the inert gas by controlling the flow rates of the different high purity gases O_2 and N_2, entering a mixing chamber using a computer-controlled mass flow controller (Air Liquid Spain S.A., Madrid, Spain) operating at a total pressure of 760 Torr and a flow rate of 500 cm^3/min.

To produce different humidity conditions (from 14 to 100% RH), a CEM-system was used. This system consists of a mass flow controller for

measurement and control of the carrier gas flow (N_2), a mass flow meter for liquids (MiniCoriflow) with a range of 0.4–20 g/h of liquid (water in this case), and a CEM 3-way mixing valve and evaporator for control of the liquid source flow and mixing the liquid with the carrier gas flow resulting in total evaporation.

A thermostatic chamber, with a lateral hole for the connection to a computer and gas tubing entrance, made possible to maintain a controlled temperature between −50 °C and +50 °C with an accuracy of ±0.1 °C for thermal characterization of the tag.

5.1.2 Sensors

A. Oxygen sensor preparation

The sensor was prepared by deposition of the oxygen sensitive membrane on a photodetector of solid state by a coating technique. The dissolutions to prepare the photodetector were obtained by dissolving 0.5 mg PtOEP and 12 mg DABCO in 1 ml solution of 5% w/v of polystyrene (PS) dissolved in tetrahydrofurane (THF). The membrane was formed by deposition of layers of 5 μl of the cocktail on top of the active face of the photodetector using a micropipette by spin-coating technique. After each deposition, the device was dried in darkness. The final deposited volume was 15 μl. Once the cover was finished, the photodetector was dried in a dryer at saturated THF atmosphere for 24 hours at ambient conditions in darkness. After all, the photodetector showed its lens homogeneously covered by a transparent and pinkie film. The averaged thickness of this film was 23 μm with an approximated concentration of PtOEP of 14.4 mM. Figure 156 shows the final result of the photodetector covered by the membrane. In order to avoid the photodegradation, the photodetector was kept in darkness until its use (Schäferling et al. 2003).

Figure 156. Picture of the covered photodetector. The pinkie film sensitive to oxygen is shown in the active face of this device.

The film deposited on the photodetector contains the PtOEP film encapsulated in polystyrene and stabilized with amine heterocyclic DABCO. The indicator molecule/polymer in PtOEP/PS system is produced by the excitation of the metalloporphyrin in the Q band at 534 nm. This excitation produces luminescence emission at 647 nm which is quenched dynamically by oxygen. The oxygen content induces changes in both phosphoresce intensity and lifetime. The spectrum PtOEP properties are not affected by DABCO presence, only the decay time is slightly increased (104.4 µs at 0% O_2 and 13.7 µs at 100% O_2 for membranes with 25% DABCO) in comparison with membranes without DABCO (99.9 µs at 0% O_2 and 10.8 µs at 100% O_2 for membranes without DABCO). The addition of DABCO provides a substantial increase in stability with an average temporal derive of 0.02% in the oxygen concentration per day.

The sensitive film is optically excited with a green light emitting diode (LED) with the emission peak at 525 nm (110104, Marl International Ltd., Ulverston, UK). A current source thermally stable is included in order to improve the excitation stability. The direct contact between the sensitive film and the detection element achieves the optimal efficiency in luminescence capture. Furthermore, neither lens nor optical filters are required; therefore, the sensor system is compact and robust. The possible influence of light can be neglected because the sensory probe is protected; only gases can access the instrument.

The selected photodetector (IS486, Sharp, Japan) consists of a Schmitt trigger circuit whose binary output depends on the illuminance threshold, I_{th}: a high value is obtained when the incident light is above this threshold and a low value when the incident light is below this threshold. The photodetector

changes its output from high to low value when the emitted light decays below the threshold value. Typical values for a threshold of 15 lux are 100 ns of rise time and 50 ns of decay time. This digital pulse duration is digitally processed.

Figure 157 shows the elements configuration of this oxygen sensor. The distance between LED and covered photodetector is about 2.5 mm.
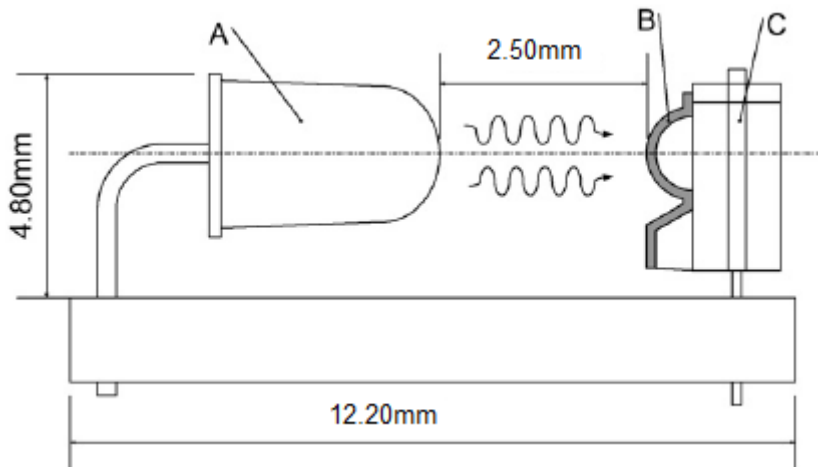
Figure 157. Oxygen sensor: (A) LED; (B) deposited film; (C) photodetector.

B. Signal processing of oxygen sensor

Figure 158 presents the signal processing. The information of oxygen content is in the internal variable N. The procedure is summarized below:

1. After LED excitation, the covered photodetector senses the decay of phosphorescence emission, I(t), from the sensitive film. The photodetector output (PO) remains in high while phosphorescence level is above the illuminance threshold (I_{th}). PO signal changes to low level, when the phosphorescence emission descends below the threshold. The phosphorescence emission depends on the analytical oxygen concentration; therefore, the time that PO signal remains in high level, t^N, is directly related with the oxygen content.
2. Next, it is necessary to accurately quantify t^N. For this purpose, this parameter is multiplied with a high frequency signal, in our case, the microcontroller signal clock (CLK).

3. Finally, this impulse train is codified by counting the number of periods in the interval t^N with a built-in microcontroller counter.

An input timer in the microcontroller counts the number of generated pulses, N. Finally, the oxygen concentration is extracted from a programmed calibration curve. This curve should include thermal compensation (see section 5.1.3.3). The signal processing is completed improving the signal-to-noise ratio. In this respect, several measurements are carried out and then average together. The microcontroller sends a control signal of 2 kHz and 50% Duty to the LED polarization circuit.
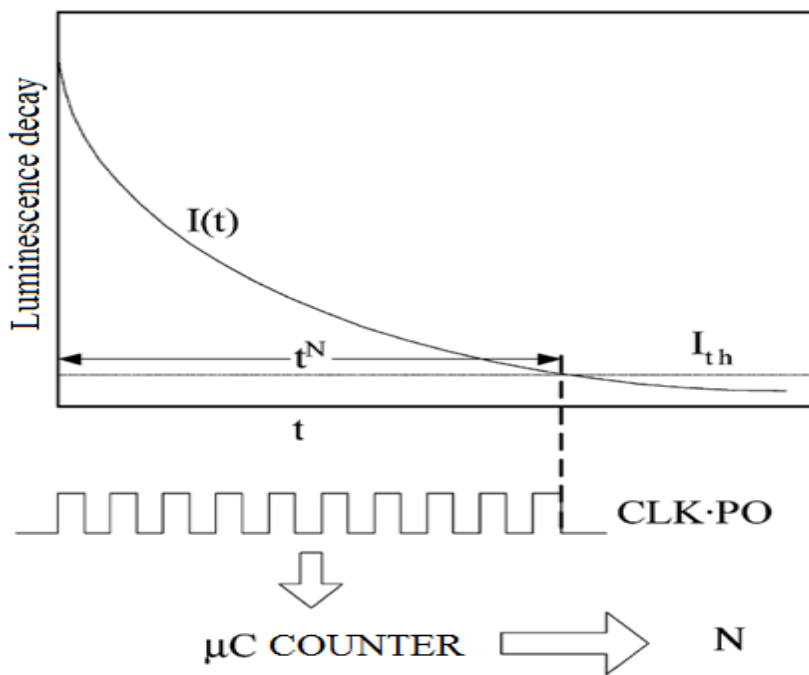
Figure 158. Signal processing schema. The luminescence decay, I(t), overlapped with photodetector illuminance threshold, Ith. The time where I(t) is higher than Ith is known as tN. This time is quantified using the high frequency signal CLK and finally it is codified by the microcontroller counter (µC COUNTER). The final result is the analytical parameter N.

C. Temperature and Humidity sensor

We chose the integrated humidity and temperature sensor STH15 (Sensirion, Switzerland). This device is superficial mounted and it includes not only the sensing part but also all the signal processing in a small encapsulation. The

digital output is perfectly calibrated with a measurement range of 0-100% in RH and -40 ºC to 123.8 ºC in temperature. The accuracy is ± 2% in RH and ± 0.3 ºC. The DC power supply must be between 2.4 V and 5.5 V, being 3.3 V the typical value. This device is low power consumption (typically 30 µW).

The transduction method for humidity is capacitive and the temperature measurement is through a band gap semiconductor sensor. CMOSens® technology provides high reliability and long term stability. The conditioned sensor output is connected to a 14 bits analog-digital converter and a serial interface. The calibration coefficients are internally stored so that the calibration is transparent for the user. Furthermore, the small size of this sensor and its low power consumption facilitate its integration in the multisensory probe. One of the requirements of this probe is the size: the smaller the probe, the faster response of the sensors because the probe can be placed in a smaller atmosphere whose environmental parameters would be quickly equilibrated with the soil atmosphere. This sensor presents a fast response (lower than 4 s).

5.1.3 System Design

The developed system consists of the following elements:

1. Microcontroller. This module controls the multisensory probe, data processing and system communication.
2. Conditioning circuit. This part translates the information extracted from the oxygen sensor into a parameter understandable by the microcontroller.
3. Communication. This unit transforms the serial communication of the microcontroller in an USB connection to easily extract data.
4. Battery. This module provides the required power to each block.
5. Multisensor probe. The probe includes an oxygen sensor, a temperature sensor and a relative humidity sensor.

5.1.3.1 Hardware

In this section, we just explain the blocks directly related to the probe, that is, the multisensor probe, the LED power source and the logic to transform the data from the oxygen sensor.

A. Multisensory probe

The printed circuit board (PCB) layout is a double face with superficial mounted devices; the final dimension is 12.96 mm x 17.02 mm. The connection wire is tinned copper braid covered by black polyvinyl chloride (PVC) wire of 0.25 mm (RS-4825493); the total length is about 1.5 m.

A   B   C
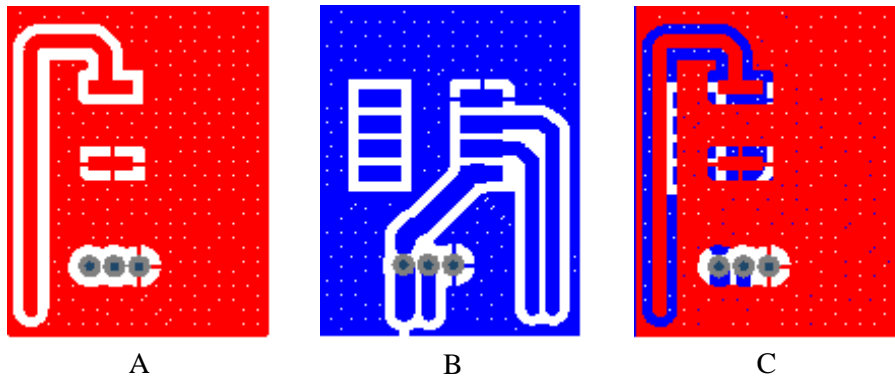
Figure 159. Probe layout: (A) top; (B) bottom; (C) overlapped.

Figure 160. Picture of the probe: (A) top; (B) bottom; (C) lateral.

Figure 161. Picture of the protection box and connection wire.

The protection box is made of Teflon (see Figure 162) because this material is impermeable to water, high resistant to adverse environmental conditions but, at the same time, it allows the gas exchange. This box is hermetically closed using silicone to glue the cover and the tape. The box diameter is 17.50 mm and its depth is 10 mm. The probe container volume is quite reduced facilitating the equilibrium between the probe atmosphere and the soil atmosphere; therefore, the probe response to changes is comparable with the time response in the surroundings.

A   B
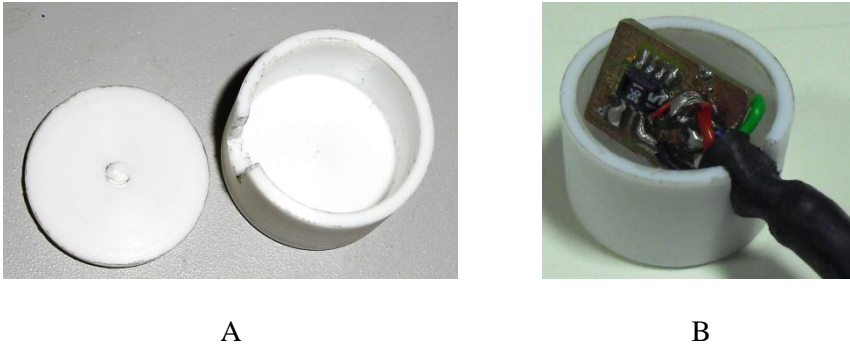
Figure 162. (A) Protection box. (B) Probe inside the protection box.

Comparing with the first prototype (19.29x37.07 mm), the dimensions has been reduced more than 4 times in terms of the probe.

B. LED power source

The LED power source used presents the schematics shown in Figure 163.

We used OPA357 (Texas Instruments Inc., USA) integrated circuit which has an enable pin (ENA). This pin was controlled by a pulse-width modulation (PWM) signal of 2 kHz to avoid the degradation of the sensitive film due to continuous LED luminescence. The output current is ±100 mA with a reference voltage (V_{ref}) of 1.23 V by using the LM385Z-1.2 (National Semiconductor, USA). We selected the resistance to obtain a LED current about 10 mA ($I_{LED} \approx 10$ mA).

$$I_{LED} = \frac{1,23}{R_2} \qquad\qquad (34)$$
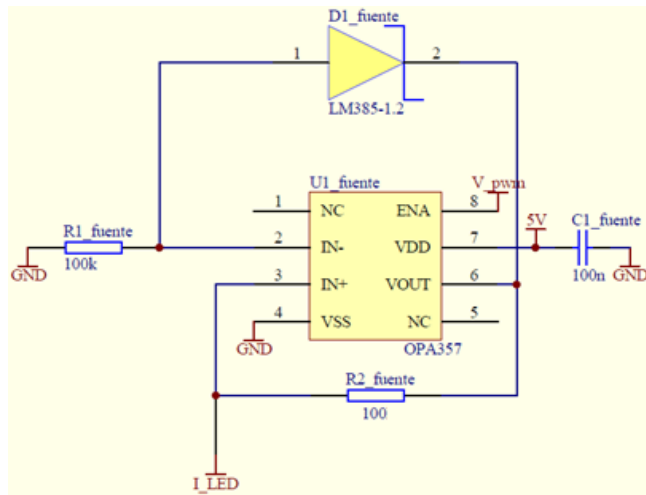
Figure 163. LED power source schematics.

C. Conditioning circuit

Figure 164 presents the schematics of the logical block. This block processes the photodetector signal to obtain the impulse train which represents the oxygen concentration.
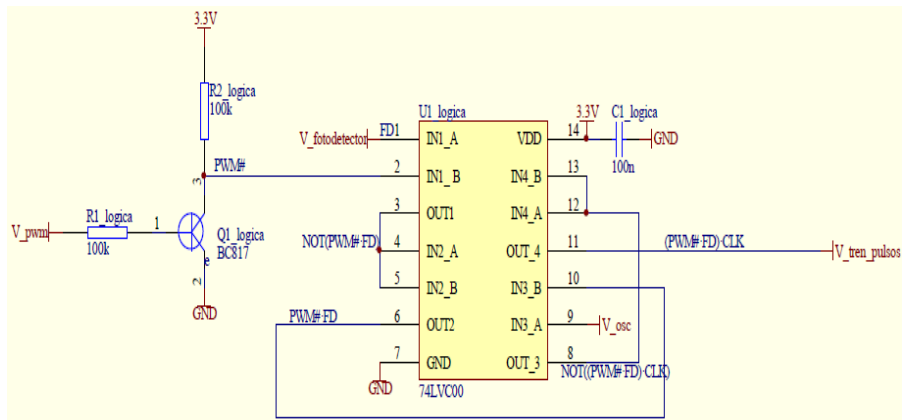
Figure 164. Schematics of the condition circuit.

This block is based on the integrated circuit 74LVC00 (Texas Instruments, USA) which contains 4 NAND logic gates. By using this device, the Boolean function $Y = \overline{A \cdot B}$ o $Y = \bar{A} + \bar{B}$ in positive logic. The operations done in this module are summarized below:

Gate 1. Their inputs are the output photodetector (PO) and the $\overline{PWM}$, its output is $\overline{\overline{PWM} \cdot PO}$ (Figure 165).

Gate 2. Both inputs are the gate 1 output to obtain the previous value without negation, $\overline{PWM} \cdot PO$ (Figure 166).

Gate 3. Its inputs are the gate 2 output and the microcontroller signal clock of 4 MHz, its output is $\overline{(\overline{PWM} \cdot PO) \cdot CLK}$ (Figure 167).

Gate 4. Both inputs are the gate 3 output in order to obtain this result without negation: $(\overline{PWM} \cdot PO) \cdot CLK$ (Figure 168).
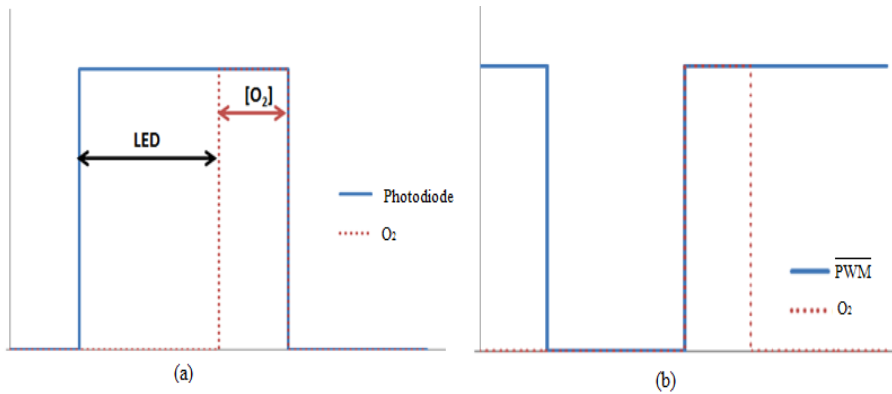
Figure 165. (a) Photodetector output and the interest signal (proportional to the oxygen concentration); (b) PWM signal (in LED absence) and the interest signal (proportional to the oxygen concentration).
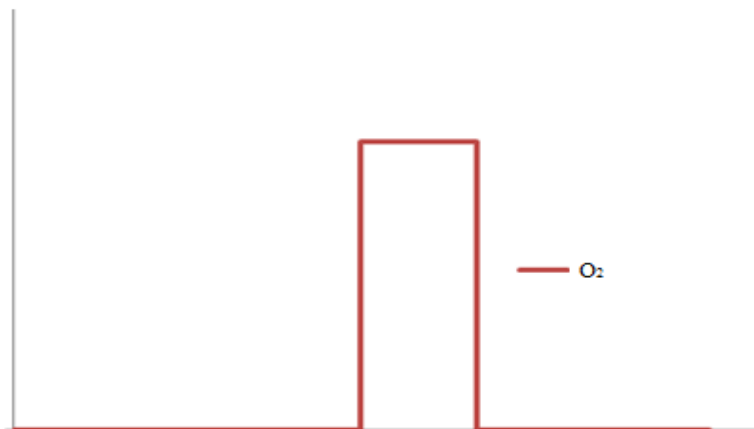
Figure 166. $\overline{PWM} \cdot PO$.
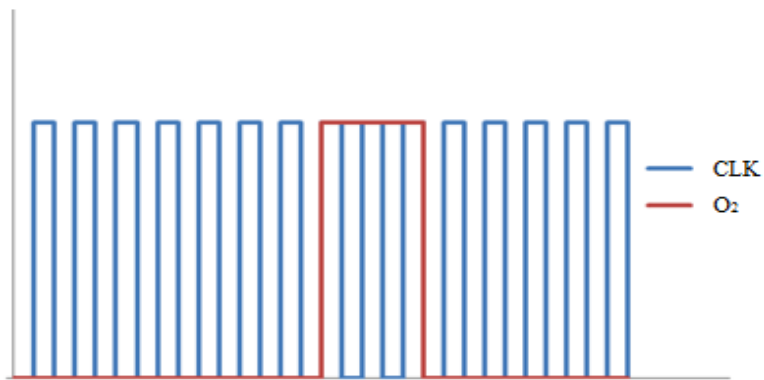
Figure 167. Gate 2 output overlapped with the microcontroller signal clock.
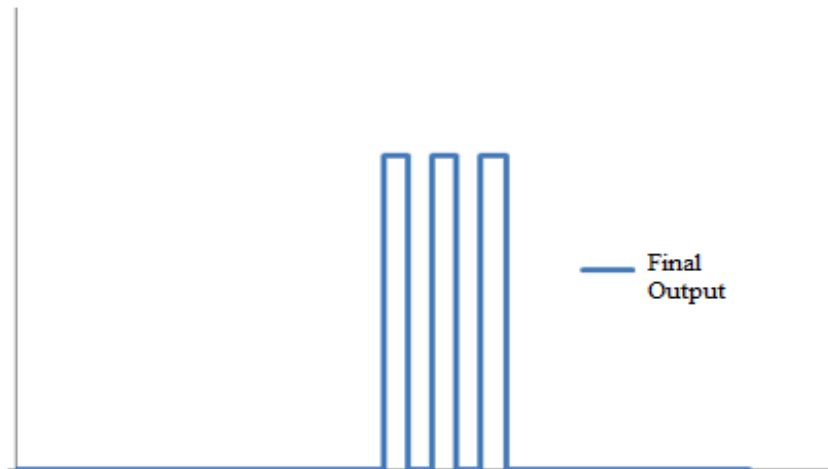
Figure 168. Final output: Product of signals in Figure 167.

Gate 4 output is an impulse train within the time proportional to the oxygen content. A critical factor is the frequency of the microcontroller signal clock because this frequency determines the resolution of the read time.

5.1.3.2 Software

A. Oxygen sensor

The communication between oxygen sensor and microcontroller is done by interruptions. First, interruptions have to be enabled to receive the impulse train as external interruption; then the current source is powered. In order to reduce the counter size, we programmed the counter to be overflowed every 5 ms (this value was equivalent to 2500 time divisions) and we recorded both

counter and overflow numbers. When the integration time (1 s) is expired, the current source and interruptions are disabled.

Summarizing, we need two variables to count the total number of pulses:

- Pulse number in 5 ms (N_1).
- Number of times that the counter is overflowed. The counter is 8 bit length, thus each time that it is overflowed indicates 256 pulses (N_2).

The expression to finally calculate the total pulse number is the following:

$$N = \frac{N_{final} t_{pulse}}{t_{LED}} \cdot t_{integration} \qquad (35)$$

where t_{pulse} is clock period divided by presaler, t_{LED} is the LED illumination time, $t_{integration}$ is the integration time and N_{final} is the number of pulses recorded and it corresponds to $(256 \cdot N_1 + N_2)$. The microcontroller clock works at 16 MHz and each instruction consumes 4 clock cycles, thus the instruction frequency is 4 MHz (250 ns/instruction).

B. Humidity and temperature sensor

The humidity and temperature sensor STH10 works with a proprietary communication standard based on two pin connections: SCK to synchronize the communication between sensor and microcontroller and SDA is a bidirectional data line: to send commands from the microcontroller to the sensor and send the reply from the sensor to the microcontroller. Each parameter can be measured with two different precision (selectable by user):

- Humidity: 8 or 12 bits
- Temperature: 12 or 14 bits

We chose the highest precision measurement. Sensor data must be processed to compensate non-linearity. Regarding humidity, the equation to extract the real value is

$$RH_{linear}(\%) = c_1 + c_2 SO_{RH} + c_2 SO_{RH}^2 \qquad (36)$$

where $c_1 = -4$, $c_2 = 0.0405$, $c_3 = -2.8 \cdot 10^{-6}$ for 12 bits resolution and SO_{RH} is the value directly obtained from the sensor. For temperatures different to 25 ºC, the humidity value requires thermal compensation as follows:

$$RH_{true}(\%) = (T_{°C} - 25)(t_1 + t_2 \cdot SO_{RH}) + RH_{linear} \qquad (\ 37\ )$$

where $t_1 = 0.01$, $t_2 = 8 \cdot 10^{-5}$ for 12 bits resolution.

With regard to temperature, this value is quite linear as follows:

$$T\ (°C) = d_1 + d_2 \cdot SO_T \qquad (\ 38\ )$$

where $d_1 = -40.1$ for $V_{DD} = 5V$ and $d_2 = 0.01$ for 14 bits resolution; SO_T is the value obtained directly from the sensor.

5.1.3.3 Calibration

Thermal dependence in this type of sensitive film has been modelled as a polynomial second order function. This model has been used in two different contexts. Firstly, it has been derived theoretically to justify Stern-Volmer curves, assuming the coexistence of dynamic and static quenching in intensity oxygen sensors. Secondly, an empirical approximation has been developed for calibration purposes. The tested function has been the following:

$$\frac{N_0}{N} = 1 + K_1[O_2] + K_2[O_2]^2 \qquad (\ 39\ )$$

In this equation, K_1 and K_2 are two empirical coefficients. In order to thermally compensate, K_1 y K_2 and N_0 are also modelled by a polynomial second order function and first order function, respectively. To develop this algorithm, at least three values of oxygen concentration have to be known. The first value must be 0%, the last value must be the last value of the oxygen range considered. Despite the extremely good concordance with this model, the calibration curve with thermal compensation requires more parameters to achieve an accurate calibration, concretely 8 parameters are required.

In order to simplify the calibration model, we proposed an empirical function dependently on intensity, lifetime, number of impulses, including cross-sensitivities (Capitan-Vallvey et al. 2007):

$$[O_2] = C_0 + C_1 \begin{Bmatrix} I^{-1/2} \\ \tau^{-1/2} \\ N^{-1/2} \end{Bmatrix} con \begin{array}{l} C_0 = A_0 + A_1 T \\ C_1 = A_2 + A_3 T + A_3 T^2 \end{array} \qquad (40)$$

where T is in Celsius degrees and $[O_2]$ is in volume percentage. This function was applied to experimental data from 11 covered photodetectors and results showed a very good agreement.

Each photodetector was individually characterized from 0 to 24% oxygen concentration in a temperature range from 0 to 45 ℃. The number of impulses N was calculated as the average of 10 replicas at each oxygen concentration and temperature.

The O_2 and N_2 gases had high purity (>99%) and they were provided in gas cylinders by Air Liquid S.A, (Madrid, Spain). Oxygen mixtures were prepared with nitrogen as inert gas. In order to control the flow rates, both gases were introduced in a mixing chamber with a mass flow controlled by computer (Air Liquid S.A, Madrid, Spain) at 760 Torr pressure and 500 cm³/min flow rate with 0.2 % precision.

The oxygen measurements were carried out after the equilibrium between the measurement set-up atmosphere and the gas mixture was reached. All experiments were done at controlled temperature with ±0.5℃ precision. The oxygen concentration can be extracted from the number of impulses, N, as follows:

$$[O_2] = C_0 + C_1 \cdot N^{-\frac{1}{2}} \qquad (41)$$

Firstly, the sensor was studied at ambient conditions, only varying the oxygen concentration. Figure 169 shows these experiments results, where oxygen concentration presents an inverse relationship with the square root of the number of impulses.
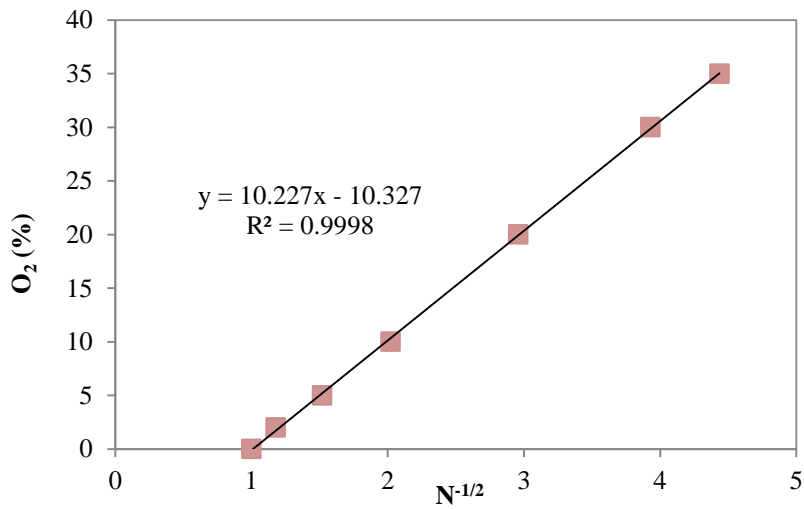
Figure 169. Sensor response at ambient conditions.

Then, the change induced by relative humidity was measured by varying relative humidity at different oxygen concentration at ambient temperature. The number of impulses obtained through this experiment is shown in Figure 170. As can be seen, there is no relationship between these variables, therefore, C_0 and C_1 are independent on the relative humidity.
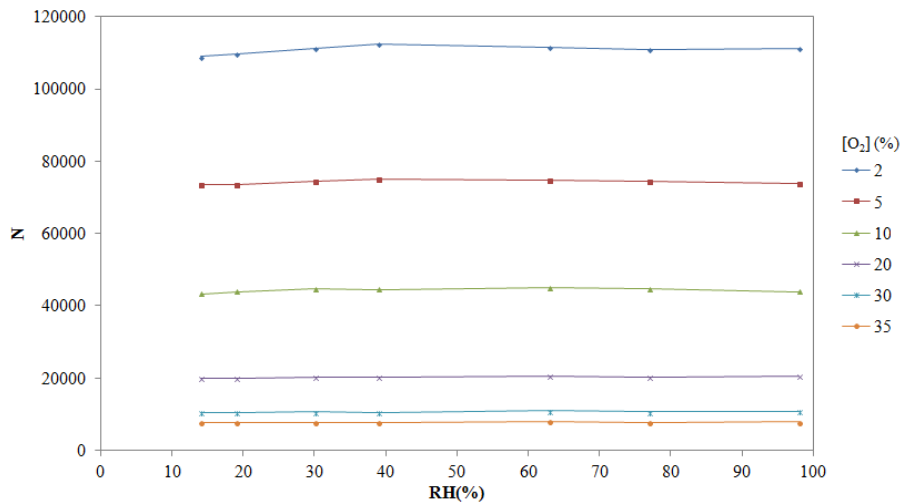
Figure 170. Number of impulses as a function of relative humidity for different oxygen concentrations.

Finally, we studied the interference between temperature and the number of impulses for different oxygen concentrations at ambient humidity.

As shown in Figure 171, there is a deviation in the number of impulses when temperature changes.
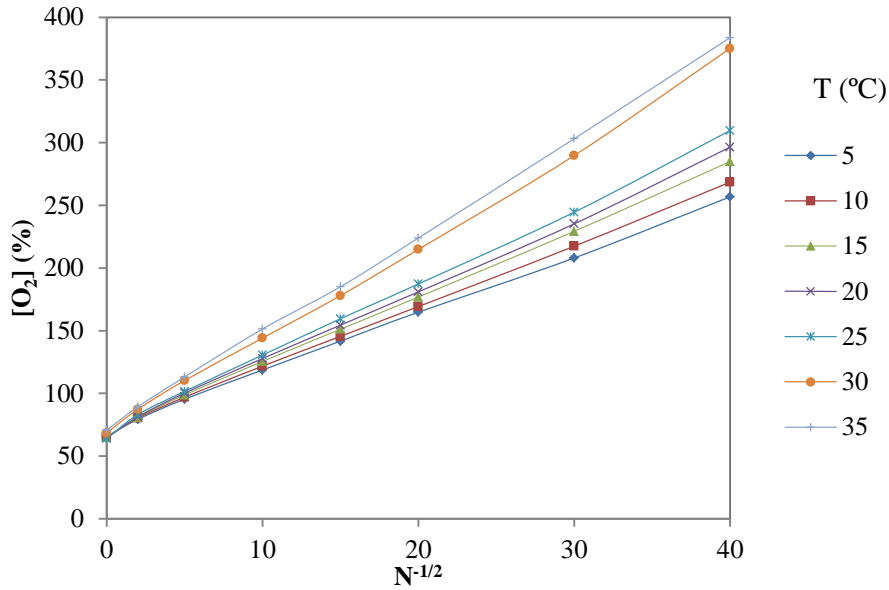
Figure 171. Oxygen concentration as a function of the number of impulses at different temperatures.

From this previous results, we extracted the constants in equation (41). Constant C_0 is modelled by a linear function:

$$C_0 = A_0 + A_1 T \qquad (42)$$
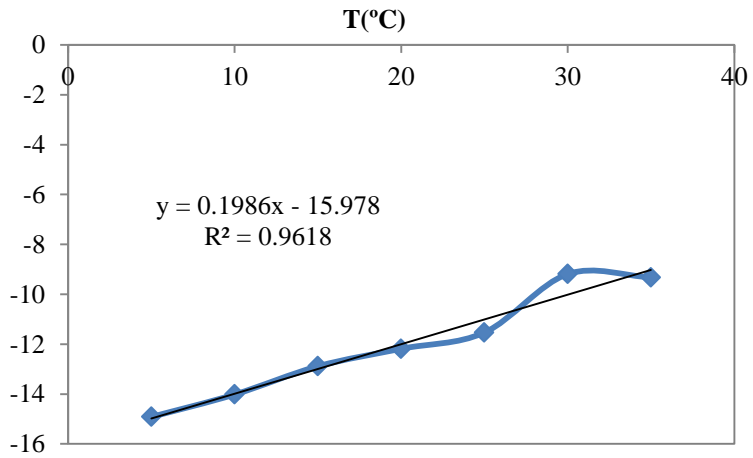
Figure 172. Model of C_0.

Looking at Figure 172, we can extract the function for C_0.

$$C_0 = 0{,}1986T - 15{,}978 \qquad (43)$$

Then, constant C_1 is modelled by a second order function:

$$C_1 = A_2 + A_3T + A_4T^2 \qquad (44)$$
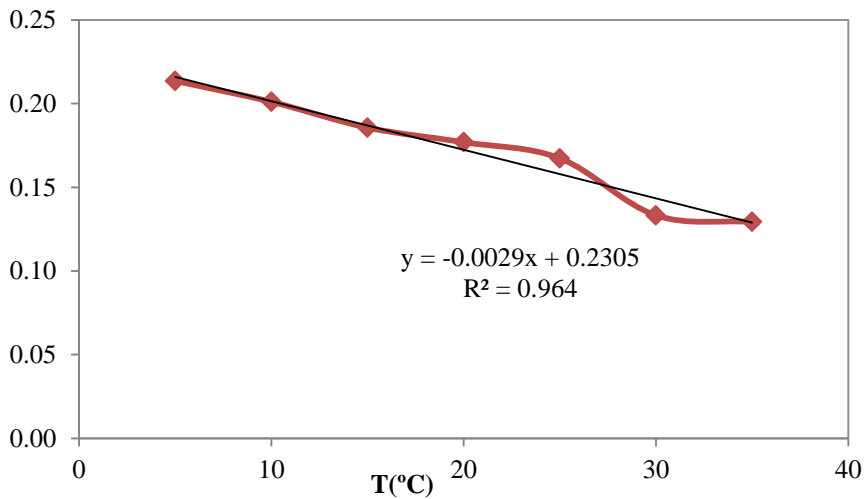
Figure 173. Model of C_1.

Looking at Figure 173, we can observe a quite linear behaviour, thus the expression of C_1 can be approximated as follows:

$$C_1 = A_2 + A_3T + A_4T^2 \approx A_2 + A_3T \qquad\qquad (45)$$

Being the final expression of C_1:

$$C_1 = -0{,}0029T + 0{,}2305 \qquad\qquad (46)$$

5.1.4 Sensing results

Firstly, the sensor was introduced in a flowerpot full of sand with an oxygen diffuser on the backside. Figure 174 shows these measurements where the sensor presents the expected behaviour.
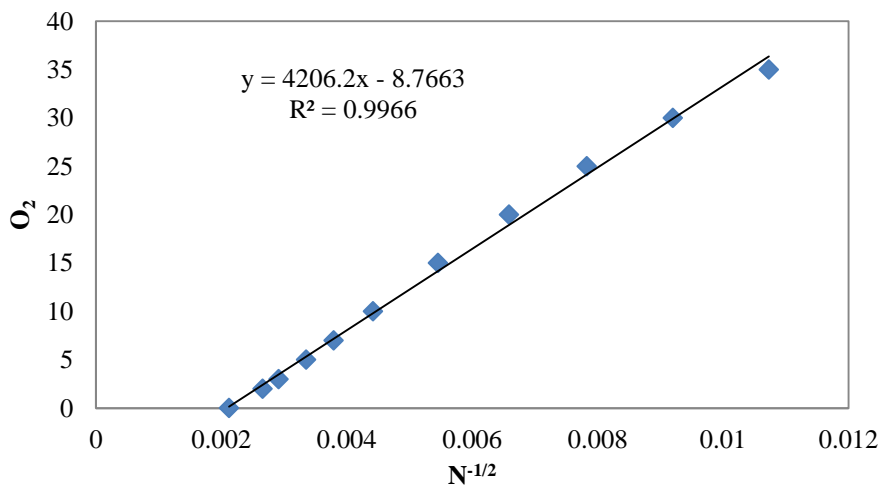
Figure 174. Calibration curve in sand container.

After that, the sensor was characterized during 7 consecutive days inside a holly flowerpot. Data were recorded every 15 s. First, the container was flooded to avoid any gas exchange with the atmosphere and force the plant to consume the oxygen in the roots. Once the system is stabilized, the plant starts to absorb oxygen. The floodgate was opened when the experiment was finished and water was drained. In the latter case, the oxygen in roots showed a fast stabilization to the level of oxygen in the atmosphere, just the time that oxygen took to achieve the sensor probe.

Figure 175 and Figure 176 present the temporal evolution of the number of impulses and the oxygen concentration, respectively. As can be observed,

oxygen is shifted by water when we forced the flood due to water flood expelling all gases in soils.
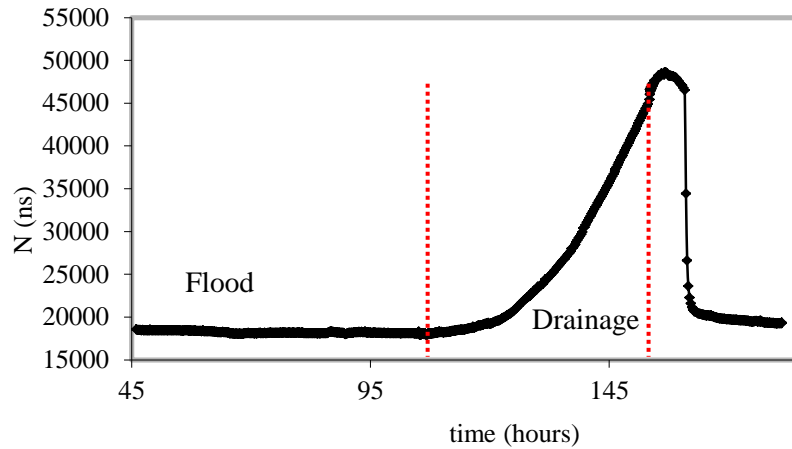
Figure 175. Temporal evolution of the number of impulses.
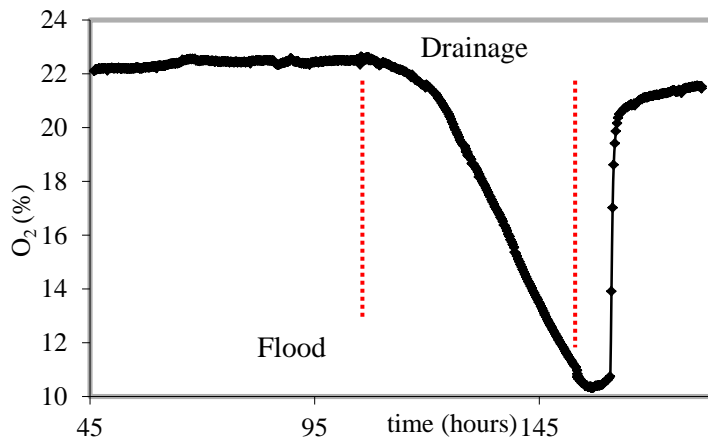
Figure 176. Temporal evolution of oxygen content.

These results are comparable with the ones obtained by Ishii and Kadoya (Ishii and Kadoya 1991) with a zirconia sensor in both flood and drainage stages. This experiment shows the ability of this sensor to measure oxygen variations in soils.

5.2   Passive RFID tags for monitoring temperature and humidity

Over the last years, radio frequency identification (RFID) technology has become increasingly attractive due to its advantages of simultaneous tag reading, wider reading range and faster data transfer in comparison with traditional identification techniques (i.e. barcodes)(Finkenzeller and Müller 2010). The development of RFID and the Electronic Product Code (EPC) standard has become a substitute of popular barcodes in packaging. This new trend, known as intelligent packaging, is able to read not only many packages at the same time but also environmental properties detected by sensors included in the containers. In this sense, a special interest is shown in the capability of tracking the condition of a package through the whole supply chain to certify the product quality has not been degraded in their packages. This added value of this technology justifies its higher cost and complexity with respect to traditional techniques (Zhu, Mukhopadhyay and Kurata 2012). In fact, the field of smart packaging including sensor capabilities opens new challenges in the development of flexible and printed tags compatible with this kind of technologies (Potyrailo et al. 2012a, Virtanen et al. 2011b, Unander, Siden and Nilsson 2011, Schoo and Knoll 2014, Oprea et al. 2009b, Rida et al. 2009). Furthermore, the opportunity of tracking environmental conditions of objects and the communication between them introduces the paradigm of the Internet of Things (IOT) and Wireless Sensors Networks (WSNs) (Akyildiz et al. 2002, Atzori, Iera and Morabito 2010).

Regarding to sensing capabilities, great efforts and very valuable advances have been made in the design of flexible and printed sensors (Andersson et al. 2012, Unander and Nilsson 2009a, Virtanen et al. 2010). Regarding capacitive moisture sensors, different approaches have been followed to include the sensing capability in the capacitor. The most frequent strategy has consisted of depositing a sensing layer over the capacitor electrodes (Molina-Lopez et al. 2012, Starke et al. 2011, Weremczuk et al. 2012). Another method is to directly use the flexible substrate as sensing element, saving fabrication steps compared with the previous strategy, as we have already described in chapter 2.

In this regard, several RFID tags with sensing capabilities, sometimes referred as to smart RFID tags, have been already developed following different strategies. Some authors have associated a change in the analog response of the sensing RFID tag, such as read range or shift of the antenna resonance frequency, to the variation of the monitored magnitude (Amin et al. 2013, Babar et al. 2012, Bhattacharyya, Floerkemeier and Sarma 2010, Cazeca et al. 2013, Daliri et al. 2012, Jacquemod et al. 2010, Li and Kan 2010, Manzari et al. 2012, Merilampi et al. 2011, Nilsson et al. 2012, Virtanen et al. 2011b, Yi et al. 2013). These strategies can be used as threshold tags (Gao et al. 2013) but lead to uncertainties in the source of these variations because there are many factors that can interfere in the tag performance, for instance the path loss between antenna and reader or the spatial and temporal fading. In addition, extra circuitry must be added to the reader in order to measure these parameters. Other approaches are based on microcontroller architectures with RFID chips and different types of sensors: temperature, light, moisture content (Abad et al. 2009, Mattoli et al. 2010); chemical sensing(Eom et al. 2012, Kassal, Steinberg and Steinberg 2013, Martínez-Olmos et al. 2013, Oprea et al. 2009b, Steinberg et al. 2014, Zampolli et al. 2007); printed moisture sensors (Unander and Nilsson 2009b, Unander et al. 2011, Virtanen et al. 2011b, Virtanen et al. 2010); pressure (Fernandez et al. 2012); or built-in sensors, typically temperature sensors (Yin et al. 2010). There are also some examples of single chip architecture without microcontroller unit already reported (Broutas et al. 2012, Catarinucci, Colella and Tarricone 2013, Pletersek, Sok and Trontelj 2012). The main advantage of this strategy compared to the analog reading of the tag is the fact that sensor data are directly processed in the RFID tag. Therefore, the sensor digital data can be transmitted to the reader or stored on the RFID tag for future access. In case of data logging, these strategies require the use of a battery to power periodically the tag. Although the extra components increase the cost of the system, the functionalities incorporated justifies this higher cost.

Here, we present the design, fabrication and characterization of two printed RFID tags with sensing capabilities. These passive tags are printed on a flexible substrate and, with the aim of testing diverse sensor structures, each one includes a different printed capacitive structure which enables to measure the relative humidity. The first tag contains SRE due to their higher

sensitivity than the conventional interdigitated IDE, as shown in section 2.3. The drawback of this approach is the fact that this sensor is defined by inkjet-printing to achieve better pattern resolution and, therefore, two different printing processes are implicated. In order to ease the manufacturing process, we present the second tag. In this particular case, the sensor is fabricated by screen printing but, due to the lower resolution of this printing technique, the sensor size is significantly bigger in order to get a similar capacitance value. As remarkable features, the architecture is based on printing technologies as fabrication process and with only a single chip architecture, where the sensor data, in digital form, can be reliably delivered to the UHF RFID reader. In addition, the chip used here integrates a temperature sensor, and therefore, these tags provide two environmental parameters in every reading.

5.2.1 Smart Tag Architectures

Figure 177 shows the architecture of the two types of printed tag, including the footprints of the different components required. Both tags present a passive architecture based on SL900A RFID chip (AG 2014) (AMS AG, Unterpremstaetten, Austria) compatible with EPC Gen 2 RFID standard. The RFID chip was chosen due to the integration of a Sensor Front End (SFE) that comprises different sensor conditioning stages and 10-bits Analog to Digital Converter (ADC). This extra circuitry has been used to interface the relative humidity capacitive sensor. Furthermore, it includes an on-chip temperature sensor. In this regard we will be able to measure capacitance values of the humidity sensor and, if necessary, perform thermal compensation to the acquired values.

Two types of printed humidity sensors are presented and they can also be seen in Figure 177. In both cases, humidity sensors consist of several capacitive elements in parallel with the aim of achieving a total capacitance of around 36 pF, well above the parasitic capacitance of the RFID chip connections which is about tenths of picofarad. The only difference between these layouts is the footprint of the array of printed sensors, fabricated with different printing techniques, and placed in parallel to sum up a bigger sensor capacitance. The radiofrequency interface consists on a typical dipole antenna resonating at 868 MHz (European Band for RFID UHF) and a RF

Surface Mount Device (SMD) inductor used to match the chip input impedance (Rao, Nikitin and Lam 2005).
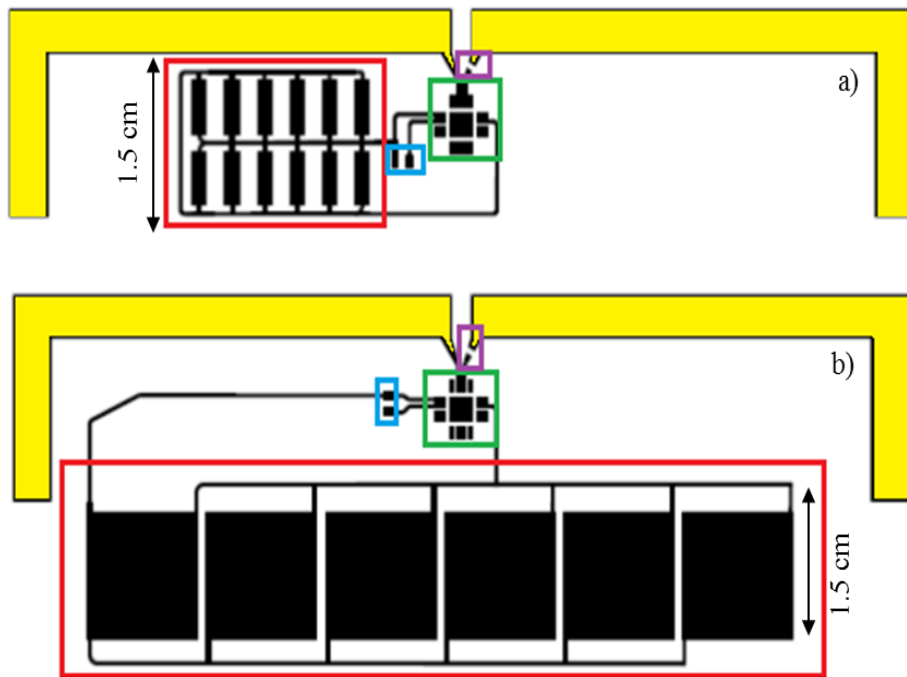
Figure 177. Schematics of the two RFID tags with (a) array of capacitive humidity sensors by inkjet printing and (b) array of capacitive sensor by screen printing (highlighted in red). Both tags include the same antenna design (in yellow) and the same chip RFID (in green). The external matching network has been remarked in purple and the reference capacitance in blue.

Temperature value comes from a conversion in the on-chip A/D converter of the SL900A. Two internal voltage references, V_{ref1} and V_{ref2} individually selectable in steps of 50 mV between 160 and 610 mV, set the lower and upper limits of this converter. These limits are defined as $2 \cdot V_{ref1} - V_{ref2}$ and V_{ref1}. The difference between them defines the input voltage range, $V_{ref2} - V_{ref1}$, and the limits of operation. These voltage references can be set in the user application and, therefore, a concrete resolution and range can be selected by the user. The minimum resolution is 0.18 ºC in a range of 189.9 ºC while a resolution of 0.23 ºC is obtained with the widest range of 237.2 ºC.
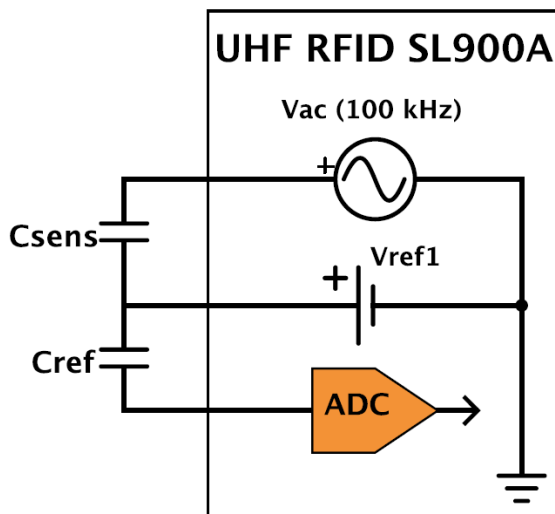
Figure 178. Diagram showing the external capacitive sensor mode of the RFID chip with AC signal excitation.

The printed humidity sensor is directly connected to the SFE of the RFID chip. To read out the capacitance value, the SFE is configured in capacitance mode. In this mode, an external reference capacitor has to be placed in series with the printed sensor as shown in Figure 178. The sensor capacitance is excited with a 100 kHz square wave signal whose amplitude is equal to V_{ref1} voltage. This AC signal is generated with a voltage offset of V_{ref1} so the amplitude signal goes from 0 to $2 \cdot V_{ref1}$. The input voltage on the ADC associated with the capacitance value is:

$$V_{ADC} = V_{REF1} \frac{C_{REF}}{C_{REF} + C_{SENS}} + V_{REF1} \qquad (47)$$

There is no auto ranging capability on the ADC; therefore the reference capacitor has to be properly chosen according to the expected sensor capacitance. According to Equation (47), the term composed by the division of C_{ref} and $C_{ref}+C_{sens}$ governs the input voltage change. At maximum sensing capacitance value ($C_{sens} \gg C_{ref}$) the input voltage should be close to V_{ref1} whereas at minimum sensing capacitance value ($C_{sens} \ll C_{ref}$) the input should be close to $2 \cdot V_{ref1}$. In our concrete case, we are interested in reading a small change in capacitance between two known values, the sensor capacitance at 0% and 100% levels of relative humidity (RH). Sensor capacitance shift causes a change in the $C_{ref}/C_{ref}+C_{sens}$ term. The reference

capacitance should be chosen to maximize this change: the sensor capacitance value at 50% of RH. The selection will cause not to cover the full input range; the term $C_{ref}/C_{ref}+C_{sens}$ will not be never 0 (lower limit) or 1 (upper limit). Taking advantage of V_{ref2} the upper limit of the ADC can be settled to a lower value to maximize the performance of the ADC.

5.2.2 Fabrication processes

All the patterns were printed on a polyimide substrate with 75 µm thickness (Kapton® HN, Dupont^{TM}, Wilmington, DE, USA). We have followed the same strategy as the one presented in chapter 2, no sensing layer was deposited onto the electrodes, being the substrate the only element which changes with the relative humidity. The pre-treatment of the substrate, as well as printing conditions and sintering is detailed in section 2.2.2. The first step before printing was to prepare the substrate to ensure good printability.

The first tag design incorporated an inkjetted printed SRE sensor to measure the relative humidity. For its fabrication, a DMP-2831™ Dimatix printer (Fujifilm Dimatix Inc, Santa Clara, USA) was used for inkjet printing of the electrodes. The employed silver ink was U5603 (SunTronic Technology, San Diego, USA) with a solid content of 20% of silver nanoparticles dispersed in ethanol/ethanediol. The substrate temperature was fixed at 40ºC while printing with the DMP-2831. For minimum area, a drop space of 25 µm was settled in the printer for 50 µm landed diameter drops followed by a sintering step at 120ºC for 60 min. Sintering took place in two different stages; a ramping of the temperature from room temperature to 160ºC at 3ºC/minute, followed by an hour at constant 180 ºC temperature. According to the thickness model presented in section 2.1.2 (see equation (11)), the obtained thickness is (0.43 ± 0.05) µm and the resistivity 23 ± 0.8 µΩcm.

Alternatively, the second tag design will test a screen printed IDE sensor. Screen printed patterns were manufactured with a Serfix III screen printing machine (Seglevint SL, Barcelona, Spain). The screen used to manufacture the tags had a mesh density of 120 Nylon thread per centimetre (T/cm) to fabricate them with only a single-layer screen printed of conductive silver ink CRSN 2442 (Sun Chemical Corporation, Parsippany, USA). With the same criterion as the former case, the minimum spatial resolution for a reliable

fabrication process was 150 μm. Sintering took place at constant 120 ℃ of temperature for 20 min.

Dipole antennas and chip interconnections were manufactured by screen printing on both tag designs. Therefore, the second tag has been completely printed by screen printing, reducing the number of fabrication steps. Finally, we developed a three-step process to do the assembly of the chips and external components to the foil. Firstly, the interconnections between RFID chip and silver pads were made by using the conductive resin H20E (Epoxy Technology, Inc., Billerica, USA). A double layer of 50 μm-thick dry adhesive, AR Clear 8932 (Adhesives Research, Inc. Glen Rock, Pennsylvania, USA), was placed on the bottom part of the chip to fix it to the substrate. Finally, the conductive resin was cured by heating up in an oven at 120℃ for 20 minutes. Moreover, the dry film adhesion improved with temperature, so the heat treatment served also to fix better the chips to the substrate.

5.2.3 Design and Characterization

A. RF Interface

For designing and studying the RF electrical behaviour of the printed antennas, including their surface area roughness and the influence of the substrate, the Advanced Design Simulator (ADS) software (Agilent Technologies, Santa Clara, CA, USA) based on momentum method was used. The antenna has to be designed to resonate at 868 MHz, corresponding to the European UHF RFID band. In order to provide maximum transfer power between the antenna and the RFID chip, conjugate matching between the IC input impedance and the antenna must be fulfilled. The experimental response of an antenna can be calculated through the power reflection coefficient, Γ_{ant}. It describes the quality of power matching between two complex impedances. The power reflection coefficient is defined as:

$$\Gamma_{ant} = \frac{Z_{ant} - Z_{chip}^*}{Z_{ant} + Z_{chip}} \qquad (\,48\,)$$

being Z_{ant} the differential input impedance of the antenna and Z_{chip} the chip impedance measured at the feed point. The RFID chip input impedance was

measured at the minimum operating power level of the RFID chip, -15 dBm. An Infinity RF probe of 800 µm-pitch (Cascade Microtech Inc, Oregon, USA) was used in conjunction with a PM5 probe station (Cascade Microtech Inc, Oregon, USA). The E5071C Vector Network Analyser (VNA) (Agilent Tech., Santa Clara, CA, USA) was used to check the single-ended input impedance. A commercial Impedance Substrate Standard (ISS) provided by the RF probe manufacturer was used for calibration purposes. The input impedance provided by the manufacturer, (31.1-j319) Ω for the QFN package is shifted to (31.1-j286) Ω due to the effect of the mounting capacitance. Therefore an antenna resonating at 868 MHZ with an input differential impedance of (31.1+j286) Ω must be designed to get the maximum power transfer and maximize the reading distance (Rao et al. 2005).

Due to the differential character of the antenna measurement, the S-parameter differential port between port-1 and port-2 was defined through a test fixture included in the VNA. Ultra Miniature Coaxial connectors (U.FL) type (Hirose Electric, Tokyo, Japan) were attached on the antenna feed point for characterization purposes. SMA to U.FL wires were used to connect the antenna to the VNA. A proper calibration is essential to perform reliable measurements. For these purposes, a custom calibration kit was developed using the U.FL connectors. Short, open, load (50 Ω) and thru standards were fabricated using the U.FL connectors making up a full Short-Open-Load-Thru (SOLT) calibration kit. Instead of performing a SOLT calibration with zero delay thru, an unknown thru calibration technique was used. This calibration provides minimum error because it does not take into account the losses associated with the thru standard. It only uses the group delay information to estimate the direct connection between the two ports (Technologies 2002). For the load standard fabrication, two high precision RF resistors (Vishay Intertechnology Inc., Malvern, USA) were placed in parallel to get the 50 Ohms and, in this way, reduce by half the parasitic inductance associated with SMD resistors.

RFID tag tests were performed using a commercial RFID reader compatible with EPC Gen2, DK-UHF RFID HP2 (IDS Microchip AG, Wollerau, Switzerland). The measurement setup was placed in an anechoic chamber to validate the proposed RFID system. The RFID reader power up and drives

the tags using EPC Gen 2 commands. The smart tags operates answering to direct inquiries from the RFID reader, such as setting the different parameters of the RFID chip (SFE configuration, reference voltage levels,…) or getting direct measurement from the ADC converter. The RFID reader was used to check the maximum distance to detect and read out the manufactured RFID tags through a Visual Basic application running in a computer. According to the theory of communication in RFID systems (Rao et al. 2005, Griffin and Durgin 2009), the maximum reading distance is calculated using equation (49).

$$range_{max} = \frac{\lambda}{4\pi} \sqrt{\frac{G_{tag}G_{reader}P_{reader}\tau\,PLF}{S_{tag}}} \qquad (49)$$

S_{tag} is the RFID chip sensitivity; the minimum received power level to activate the tag for the employed RFID chip is -15 dBm. G_{tag} refers to tag antenna gain whose simulated values are obtained by EM with simulation ADS. P_{reader} is the effective radiated power by the reader and G_{reader} the reader antenna gain. The RFID reader antenna is a circular polarized patch antenna A0025 (Poynting antenna, Samrad, South Africa). The transmission power was 26 dBm and the reader antenna gain was 7 dBi at 868 MHz according to the manufacturer. τ is a factor that takes into account the losses related to mismatching between the chip and the antenna (Rao et al. 2005). The polarization mismatch between reader antenna (circular polarization) and the designed antenna tags (linear polarization) has also been included. This is represented as the polarization loss factor (PLF) in Equation 3 and its value is 0.5 (3dB).

B. Sensor

The difference between these tags is the printed technique and, as consequence of this latter, the dimensions. The first prototype includes an array of capacitive sensors based on the serpentine electrodes presented in section 2.3. We chose this design because a higher performance than the traditional interdigitated electrodes has been shown. The manufacturing process is inkjet printing because it provides better resolution. The dimensions of each array element are presented in Table 6 (chapter 2) for a targeted nominal capacitance (for one printed layer) of 2 pF and the final area was 11.65 mm^2 (L = 1.85 mm x W = 6.3 mm) composed of 62 fingers (31

fingers for each electrode) with 50 µm width and inter-spacing (see Figure 23 in chapter 2).

On the other hand, the second tag incorporates an array of interdigitated electrodes manufactured by screen printing. We chose this design for the complete screen printed tag because the manufacturing yield is higher than the serpentine electrodes. The array element dimensions are presented in Table 2 for a targeted nominal capacitance (for one printed layer) of 6 pF and the final area was 2.25 cm^2 (L = 1.5 cm x W = 1.5 cm) composed of 26 fingers (13 fingers for each electrode) with 150 µm width and inter-spacing (see Figure 10 in chapter 2).

Table 35. Physical dimensions of each of the screen printed interdigitated structures.

Parameter	Value	Description
Length	1.5 cm	Length of each finger (y-axis)
Width	150 µm	Width of each finger (x-axis)
Thickness	10 µm	Thickness of electrodes (1 layer) (z-axis)
Number	13	Total number of fingers of the larger electrode
Interspacing	150 µm	Distance between consecutive fingers (y-axis)
Distance	150 µm	Distance between fingers of one electrode and the backbone of the other electrode (x-axis)

The AC electrical characterization for the different fabricated capacitors has been performed by measuring their capacitance and dissipation factor, using the four-wire measurement technique with a precision Impedance Analyser 4294A and an impedance probe kit (4294A1) (Agilent Tech., Santa Clara, CA, USA). The excitation voltage applied in all measurements was $V_{DC} = 0$ and $V_{AC} = 500$ mV at 100 kHz. We have considered this frequency because it is the frequency of the excitation signal of the RFID chip for measuring capacitance changes. The stationary humidity and temperature responses of the tags have been measured in a climatic chamber VCL 4006 (Vötsch Industrietechnik GmbH, Germany). The humidity range varied from 10% RH to 98% RH in a temperature range of + 10 °C to + 95 °C. In the climatic chamber, we included two commercial sensors to monitor the temperature and humidity close to the sensors. These sensors are an analogue humidity sensor HIH4000 (Honeywell International Inc., Illinois, USA) with accuracy

of ±2.5% and a digital thermometer RS Series A1 (RS Amidata S.A., Madrid, Spain) with resolution of 0.1 °C.

5.2.2 Results and discussion

A. Antenna

Figure 4 shows the two smart RFID tags fabricated, with their different components labelled for better understanding. Final dimensions of the screen printed dipole antenna arms are 5.5 mm of width and 79 mm of length each one. In order to optimize the occupied area, the dipole arms have been bent. Input impedance of the dipole at 868 MHz is $(31.1 + j9.4)$ Ω. This dipole was designed to get the same real part of the impedance as the RFID chip, whilst the necessary large inductive part is achieved with a SMD inductor series 3650 of 51 nH and a quality factor of 60 at 900 MHz (TE Connectivity, Ltd., Schaffhausen, Switzerland) placed on one of its arms. The obtained parameters of the antennas by EM simulation at 868 MHz are gain of 0.66 dBi, directivity of 2.40 dBi and efficiency of 66.97%.
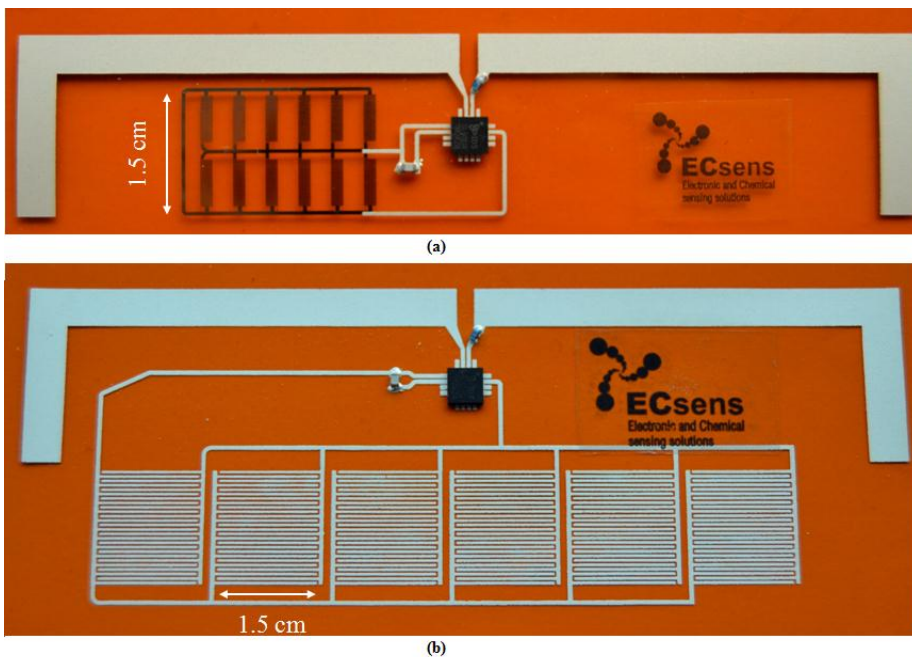
Figure 179. (a) RFID tag with inkjetted serpentine sensors and (b) RFID tag with interdigitated sensors by screen printing.

The comparison between measurements and simulated response of the dipole antenna are in good agreement, as can be seen in Figure 5. The screen printed dipole response is only slightly different from the simulated one. The obtained resonance peak is smaller than the simulated one and a wider response is observed. This could be due to the fact that the obtained resistivity is higher than the simulated value. In these cases, the antenna quality factor will be reduced causing a flatter and wider antenna response.

The measured read range is the maximum distance in which the reader was able to read out the tag including the sensing functionalities. It should be noted that the sensitivity of the RFID chip has a penalty. Chip sensitivity to answer identification inquiries of EPC protocol is -15 dBm whereas the sensitivity for reading out capacitance value is -2.21 dBm. The reason is to the required extra-power to drive the SFE that needs to be collected from the radiated EM field of the reader. According to Equation 3, the read range assuming ideal conditions (perfect matching between chip, $\tau = 1$, and the dipole antenna gain obtained by EM simulation, $G_{tag} = 0.66$ dBi) should be 2.2 meters.

The measured ranges for the printed tags are smaller than the simulated ones, 1.6 meters. These differences could be due to the non-ideal behaviour of the metallic layers in printed electronic that leads to a lower performance than the expected one, affecting the gain and efficiency of the fabricated antennas (Salmerón et al. 2013). Furthermore, extra losses are introduced by the mismatching between the RFID chip and antenna impedance because of the variation of the RFID chip impedance with both working frequency and different powers levels.
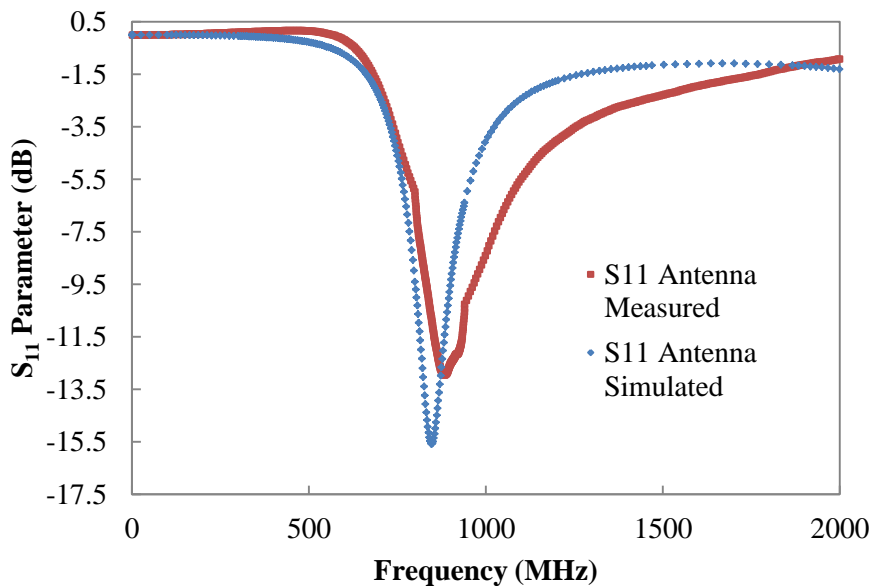
Figure 180. Simulated and measured differential S-parameter magnitude of the screen printed dipole showing minimum return loss at 868.8 MHz.

B. Sensing

The capacitance of the serpentine electrodes has been measured at 100 kHz for different values of relative humidity in ascending and descending mode. The response of one sensor to changes in the relative humidity is directly extracted from the curves obtained with the impedance analyser (Figure 181).

Let's remember that we have built an array of sensors connected in parallel. Then, the total capacitance is the sum of the individual contributions. A total of 12 serpentine capacitors have been printed, therefore, the total expected capacitance is 32.4 pF at dry atmosphere. The sensitivity would also be multiplied by 12, resulting in 100 fF/%RH. The total measured capacitance of the serpentine array at room conditions was 36 pF. The reference capacitance for this array was selected of 33 pF. An SMD capacitor size 0805 with 2% tolerance from Vishay (Vishay Intertechnology, Inc. PA USA) was employed for this purpose.
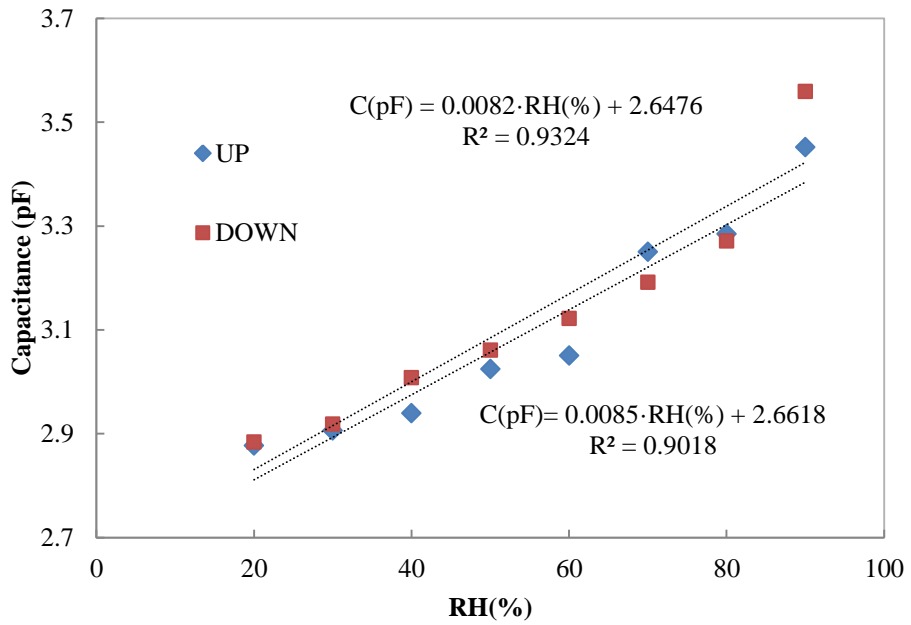
Figure 181. Capacitance vs. Relative humidity for inkjetted printed serpentine electrodes.
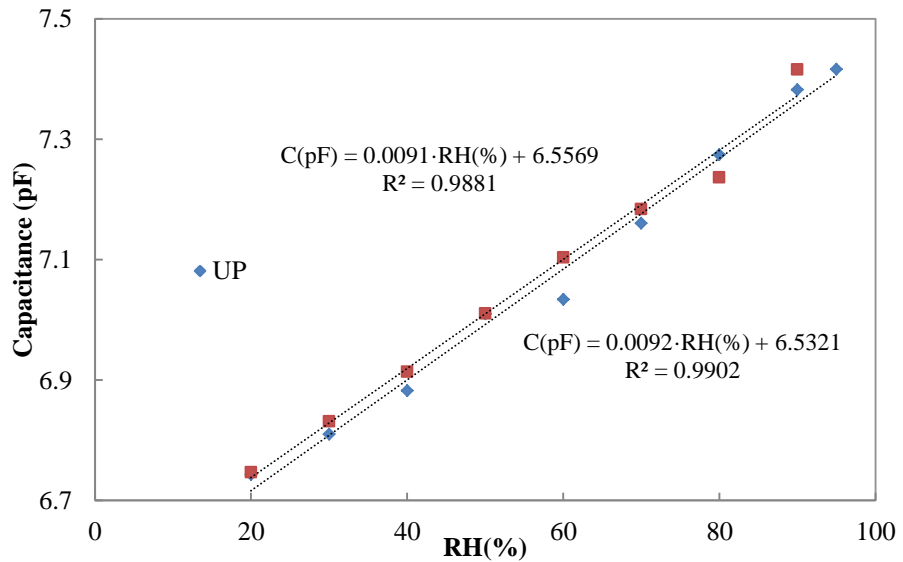
Figure 182. Capacitance vs. Relative humidity for screen printed interdigitated electrodes.

The same characterization was carried out for the interdigitated electrodes manufactured by screen printing. The response of one sensor to changes in the relative humidity is directly extracted from the curves obtained with the impedance analyser (Figure 182). As indicated before, an array of sensors connected in parallel has been implemented. Then, the total capacitance is the sum of the individual contributions. A total of 6 interdigitated capacitors have been printed, therefore, the total expected capacitance is 34.8 pF at dry atmosphere. The sensitivity would be multiplied by 6 as well, resulting in 54 fF/%RH. The number of screen printed IDE sensors was chosen to get a capacitance value similar to the inkjetted sensors array. We measured a total capacitance for this array of 38 pF at room conditions. The SMD 0805 reference capacitance (Vishay Intertechnology, Inc. PA USA) for this tag was selected of 45 pF as an optimum value after studying different capacitors of reference.

C. Tag performance

Temperature measurements are obtained directly from the on-chip sensor and present different errors and accuracy depending on the selected measurement range as mentioned above.

The capacitance sensor is excited with an AC signal from the EXC pin; this square wave travels around the reference voltage V_{ref1} to avoid the generation of negative voltage values. Figure 7 shows two signals read by an oscilloscope MSO9064A (Agilent Tech., Santa Clara, CA, USA), the AC signal varying between 0 and $2 \cdot V_{ref1}$ is shown in red, the signal read by the ADC converter is presented in blue. The selected reference voltage V_{ref1} was 310 mV so the AC signal ranges from 0 to 620 mV.
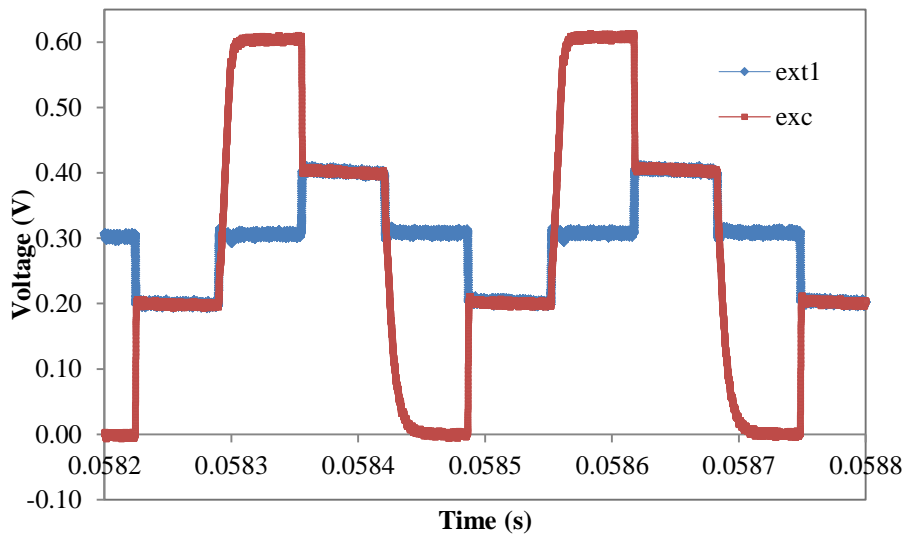
Figure 183.   Signals at the Sensor Front End: red is excitement signal and blue is acquired signal.

The values of the reference voltage and the V_{ref1} determine the ADC levels and the excitation signal amplitude; then we needed to define the proper voltages to obtain the bigger range of reading. After testing the different configurations, we found that below 360 mV the ADC was saturated. From this voltage, the ADC had enough range of reading but voltages higher than 510 mV showed higher deviation, results from ADC present more dispersion. Regarding V_{ref2}, we noticed that the highest range of ADC happened for the lowest voltage (but not ground). Then, we selected for both tags $V_{ref1} = 360$ mV and $V_{ref2} = 160$ mV.

After setting the voltage configuration, we characterized both tags varying the relative humidity at different temperatures. We stored 30 ADC data to know the deviation between measurements. This deviation was lower than 2 LSB of the ADC in all the studied cases. Figure 184 and Figure 185 illustrate the average data obtained by the ADC on both tags. As can be seen in both graphs, the range of sensitivity is concentrated on a range of RH; that is; the whole range of RH cannot be read by just one tag. Looking at the prototype with SRE capacitors, it is not possible to distinguish values below 42.5% and above 75% RH. In the other tag, these limits are 60% and 90% RH.

Therefore, we can assume that the measurement range is about 30% RH independently on the sensor sensitivity or the reference capacitance.
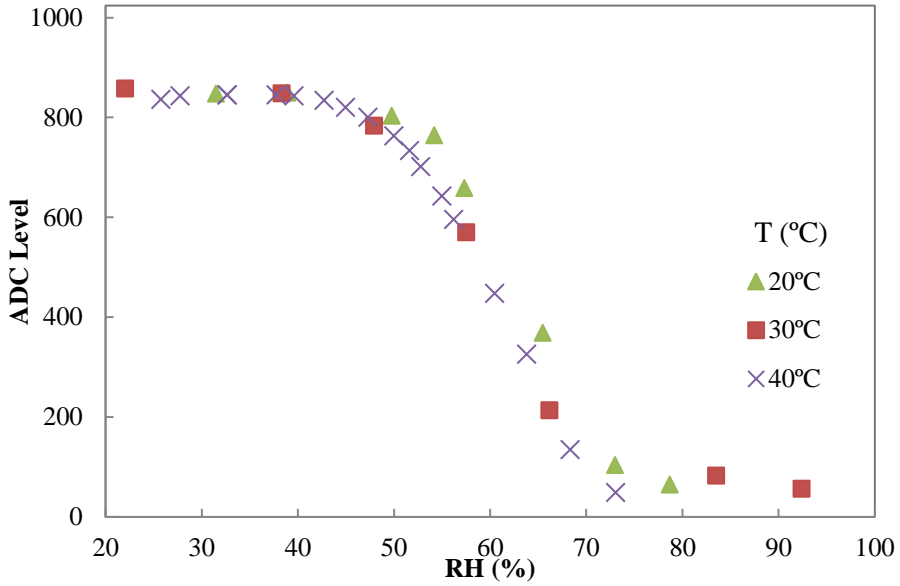
Figure 184. ADC counts of tag with inkjetted serpentine sensor.
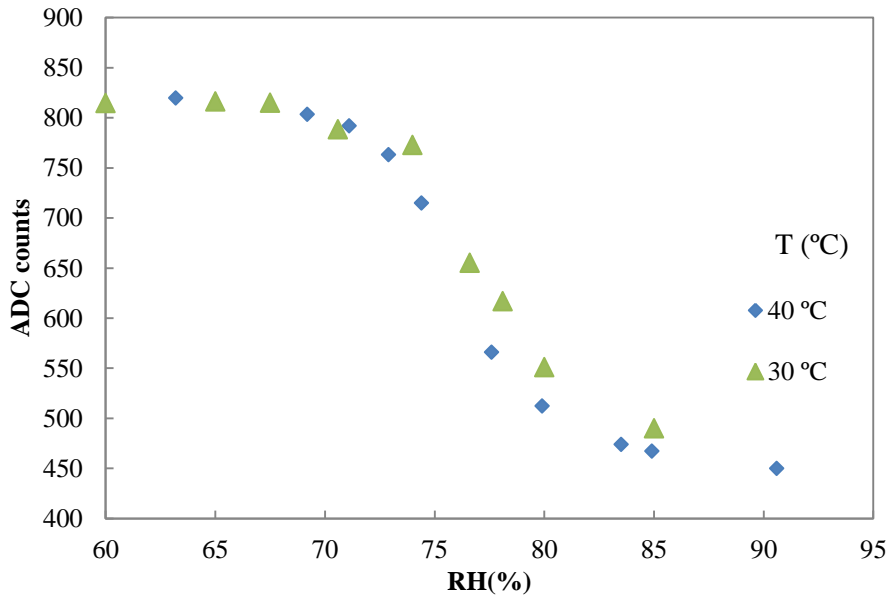
Figure 185. ADC counts of screen printed tag with IDE sensors.

Figure 184 shows an output range approximately from 850 to 85, that is to say, more than 750 counts to be associated to a variation of the 30% RH. Whereas the values in Figure 185 change from about 820 to 450 counts, then only 370 counts can be used to discriminate this variation of the 30% RH. The span available in the former strategy is more than twice the one in the latter approach.

Regarding the tuning of the tag, we can easily select the range of humidity where the tag is going to discriminate values by selecting the suitable value of reference capacitance. For example, we designed the tags for similar values of capacitance at room temperature but their ranges of discrimination are different: the central span of the inkjetted sensors is 58.5 % RH with a reference capacitance of 33 pF whereas this point is found at 75% RH for a reference capacitance of 45 pF.

With respect to the thermal drift, these values are 0.024 %RH/ºC for the inkjetted serpentine structure and 0.044 %RH/ºC for the screen-printed interdigitated structure. This result is in agreement with the results shown in our previous works detailed in chapter 2, where printed sensors on the same substrate had negligible thermal drifts.

5.3   Humidity tag based on the resonance frequency shift

As we have already mentioned, some authors have studied the analog response of the sensing RFID tag: reading range, shift of the antenna resonance frequency, measured level of the backscattered power, etc. These changes have been associated to a variation of the monitored magnitude. Some examples are moisture sensing by means of antenna gain variation [12] and strain and crack sensing [13], among others [14-24]. These strategies can be very useful, e. g., for threshold sensor tags [25], but lead to uncertainties introduced by the wireless link between RFID reader and tag. It is not clear whether a change in the analog response of the tag can be directly related to a change in the monitored magnitude due to other factors playing a role in the link performance such as the path loss between antennas, spatial and

temporal fading, electric interference, non-direct sight between reader and tag, interferences with other objects, etc. On top of that, extra-circuitry must be typically included into the RFID reader to monitor the tag analog response, adding another drawback to this strategy.

Here, we will present passive RFID single-chip architecturetag chip in contrast with more complex architectures. Here, two approaches can be followed. First, the development of a resonant sensor whose resonance frequency directly shifts with the relative humidity in the environment. Resonance peak would be then associated with a concrete level of relative humidity. The second approach is a threshold humidity sensor based on the detection or not of the RFID tag by a reader. For the former approach, the RFID chip could be avoided. Both strategies can be used for other purposes by depositing any layer sensitive to a specific chemical or physical property. Here, we have only studied the change in humidity because no sensing layer was included. Following the strategy of the already explained sensors in chapter 2. We have used Kapton HN as substrate to fabricate this resonator sensor or threshold RFID tag.

5.3.1 Tag architecture

The tag has been designed to resonate at 13.56 MHz (HF band). For numerical simulation, the Advanced Design Simulator (ADS) software (Agilent Technologies, Santa Clara, CA, USA) based on momentum method was used for studying the RF electrical behaviour of the printed antennas including their surface area roughness and the influence of the substrate.

The inductance of a square antenna is given by

$$L_{ant} = 2.34\mu_0 N^2 \frac{d}{1 + 2.75p} \qquad\qquad (\,50\,)$$

where $d = \frac{d_{out} - d_{in}}{2}$ and $p = \frac{d_{out} - d_{in}}{d_{out} - d_{in}}$. The outer diameter is d_{out}, the inner diameter is d_{in}, both in millimetres (see Figure 186); N is the number of turns, $\mu_0 = 4\pi 10^{-7}$ H/m, L is measured in Henry.
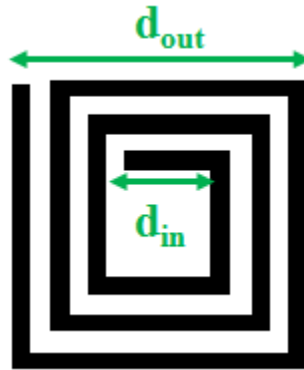
Figure 186. Schematics of a square inductor.

In our case, these geometrical parameters were introduced in the simulator to achieve the desired values.
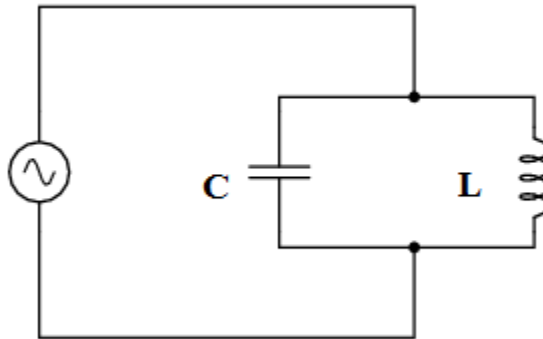
Figure 187. Ideal LC resonator schematic.

The ideal model of a LC resonator is shown in Figure 187. Since we know the equations for determining the reactance of each element at a given frequency, and we look for that point where the two reactances are equal to each other, we can set the two reactance formulae equal to each other and solve for frequency algebraically:

$$X_L = 2\pi f L \ \text{ and } \ X_C = \frac{1}{2\pi f C} \qquad (\ 51\ )$$

Setting the two reactances equal to each other and representing a condition of equal reactance (resonance), we obtain the resonant frequency of a tank circuit, given the values of inductance (L) in Henrys and capacitance (C) in Farads.

$$f_o = \frac{1}{2\pi\sqrt{LC}} \qquad (52)$$

But an inductor is essentially just a coil of wire and so often has a non-negligible resistance. This is most readily modelled as a resistor in series with the inductor. The smaller this resistance, the more ideal the inductor. Therefore, the LC resonator circuit should include this parasitic resistance, as shown in Figure 188.
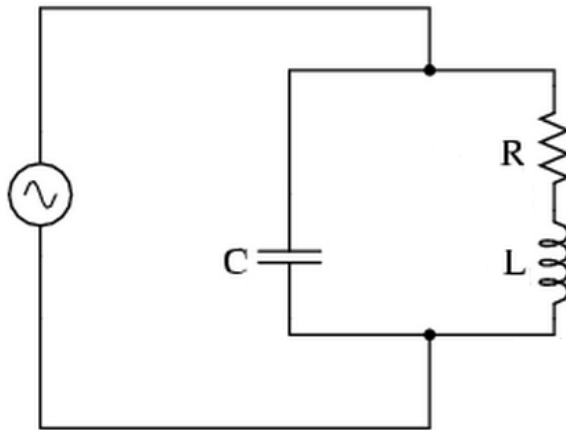
Figure 188. Non-ideal LC resonator schematics.

In this case, we do not have only reactance parts but also a resistance part. In order to find the resonance frequency of this circuit, the imaginary parts of the global impedance should be zero:

$$Z_L = R + j2\pi f L \ and \ Z_C = \frac{1}{j2\pi f C} \qquad (53)$$

In order to ease calculations, we work in admittance mode. Let's remember that admittance is the inverse value of impedance.

$$Y_T = j2\pi f C + \frac{1}{R + j2\pi f L} = j2\pi f C + \frac{R - j2\pi f L}{R^2 + (2\pi f L)^2} \qquad (54)$$

$$Y_T = \frac{R}{R^2 + (2\pi f L)^2} + j2\pi f \left(C - \frac{L}{R^2 + (2\pi f L)^2} \right) \qquad (55)$$

Therefore, if we cancel the imaginary part of eq. (55)

$$2\pi f_o \left(C - \frac{L}{R^2 + (2\pi f_o L)^2} \right) = 0 \qquad (56)$$

Solving for f and simplifying, we obtain us the resonant frequency of a tank circuit, given the values of inductance (L) in Henrys, resistance (R) in Ohms and capacitance (C) in Farads.

$$f_o = \frac{1}{2\pi}\sqrt{\frac{1}{LC} - \frac{R^2}{L}}$$

(57)

In this non-ideal circuit, we can define the quality factor as the relationship between the maximum stored energy and the dissipated energy in each cycle in the circuit. Taking into account that the energy stored in the capacitor is equal to the energy stored in the inductor at resonance frequency,

$$Q = 2\pi \frac{\frac{1}{2}I^2 L}{T \frac{1}{2}I^2 R} = 2\pi \frac{L}{R} f_o$$

(58)

An M24LR64 (STMicroelectronics, Geneva, Switzerland) was selected as the RFID chip. It has a capacitance of approximately 30 pF at f_0 = 13.56 MHz. Without including the parasitic resistance, a value of 4.6 µH for the coil antenna must be achieved to enable resonance at the desired frequency without including external capacitance (Salmerón et al. 2013). In RF mode, using the ISO15693 protocol, the RFID chip is accessed via a 13.56-MHz carrier electromagnetic wave on which incoming data are demodulated from the received amplitude-modulated signal. The first approach we developed was to add to this architecture a printed capacitor in order to know how this new element affects the antenna behaviour.

Now, we will add a sensor capacitance in parallel with the RFID chip to study the behaviour of this tag. Therefore, the analytical expression of the resonance frequency is given by:

$$f_o = \frac{1}{2\pi}\sqrt{\frac{1}{L(C_{chip} + C_{sens})} - \frac{R^2}{L}}$$

(59)

5.3.2 Fabrication process and characterization

For the screen printing technique, we used a Serfix III screen printing machine (Seglevint SL, Barcelona, Spain). The screen used to manufacture the patterns by screen printing had a mesh density of 90 Nylon thread per

centimetre (T/cm) in an aluminium rectangular structure of 50 cm width and 35 cm length. For inkjet printing, a DMP-2831™ Dimatix printer (Fujifilm Dimatix Inc, Santa Clara, USA) was used for inkjet printing of the electrodes.

The selected materials were an ink with a solid content of 20% of silver nanoparticles dispersed in ethanol/ethanediol (U5603 SunTronic Technology, San Diego, USA) for inkjet printing and conductive silver ink CRSN 2442 (Sun Chemical Corporation, Parsippany, USA) for screen printing. All the patterns were printed on a polyimide substrate with 75 µm thickness (Kapton® HN, Dupont™, Wilmington, DE, USA) taking advantage of the fact that its electrical permittivity varies with the relative humidity as shown in section 2.1.3. The pre-treatment of the substrate, as well as printing conditions and sintering is detailed in section 2.2.2. The three-step process to do the assembly of the chips and external components to the foil is detailed in section 5.2.2. The inner and outer ends of the coil have been connected through a small "bridge" manufactured by ink-jet printing and attached using the adhesive epoxy EPO-TEK H20E (Epoxy Technology, Inc., Billerica, USA).

The AC electrical characterization for the different fabricated tags has been performed by measuring their impedance, both magnitude and phase, using the four-wire measurement technique with a precision Impedance Analyser 4294A and an impedance probe kit (4294A1) (Agilent Tech., Santa Clara, CA, USA). The excitation voltage applied in all measurements was $V_{DC} = 0$ and $V_{AC} = 500$ mV from 5 MHz to 40 MHz. We have considered this frequency range because it contains the work frequency of the RFID chip (13.56 MHz) and enough frequencies around it to perceive shifts on the resonance frequency due to variations in the relative humidity. The stationary humidity and temperature responses of the tags have been measured in a climatic chamber VCL 4006 (Vötsch Industrietechnik GmbH, Germany). In the climatic chamber, we included two commercial sensors to monitor the temperature and humidity close to the sensors: an analogue humidity sensor HIH4000 (Honeywell International Inc., Illinois, USA) with accuracy of ±2.5% and a digital thermometer RS Series A1 (RS Amidata S.A., Madrid, Spain) with resolution of 0.1 °C.

RFID tag tests were carried out using a commercial RFID reader compatible with ISO 15693, HF TRF7960 (Texas Instruments). The RFID reader power up and drives the tags using ISO15693 commands.

5.3.3 Results and discussion

Firstly, we measured the change in impedance of every single element, coil and capacitor, for each printing technique. After this study, we characterize the different LC printed tags.

A. Single elements

Figure 189 presents the two coil inductors fabricated. As can be seen, the only difference between then is the printing technique. Figure 190 and Figure 191 show the screen printed coil response to changes in humidity and temperature, respectively. As can be seen, the only appreciable change is in the amplitude of the response with a maximum change of 20 Ω in humidity and 12 Ω in temperature but no frequency shift is perceived. Figure 191 and Figure 193 present the resonance frequency as a function of humidity and temperature curves. There is a small shift in the resonance frequency due to changes in humidity and temperature. The resonance frequency decreases when both magnitudes increases but the maximum change perceived is less than 2 kHz in the ranges of RH and temperature studied.
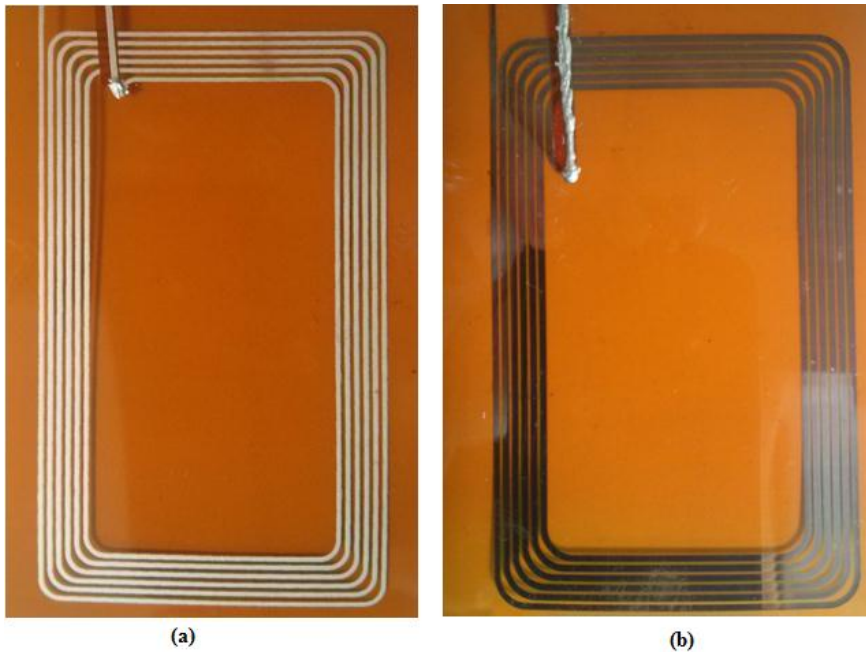
Figure 189. Printed coil inductor by (a) screen printing, (b) inkjet printing.
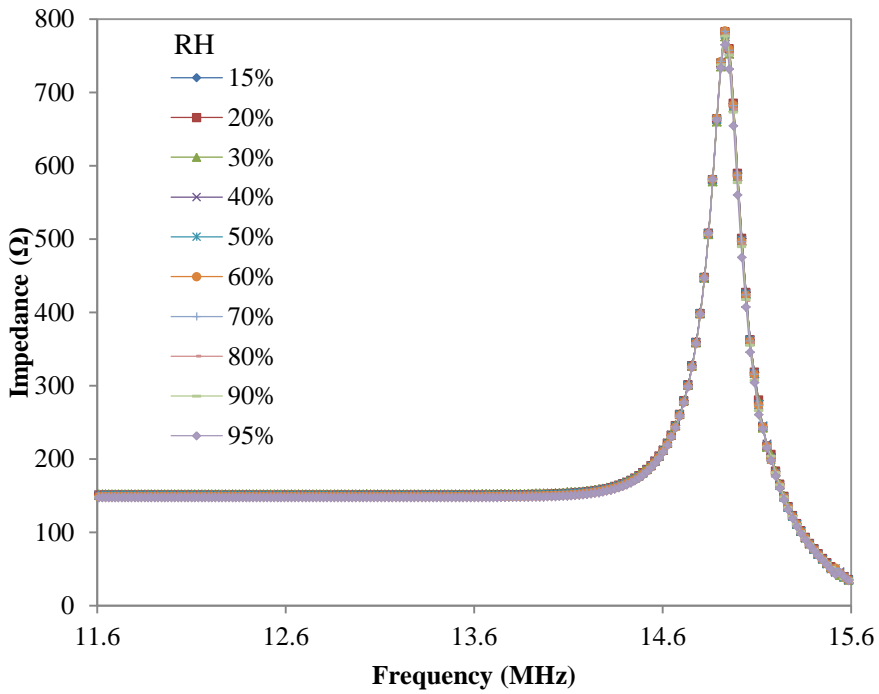
Figure 190. Coil impedance by screen printing as function of frequency at different values of RH.
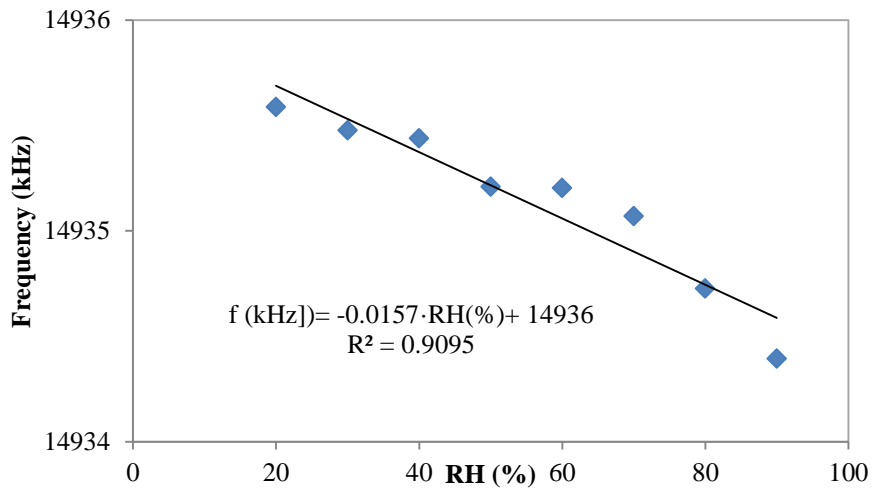
Figure 191. Coil resonance frequency by screen printing as a function of relative humidity.
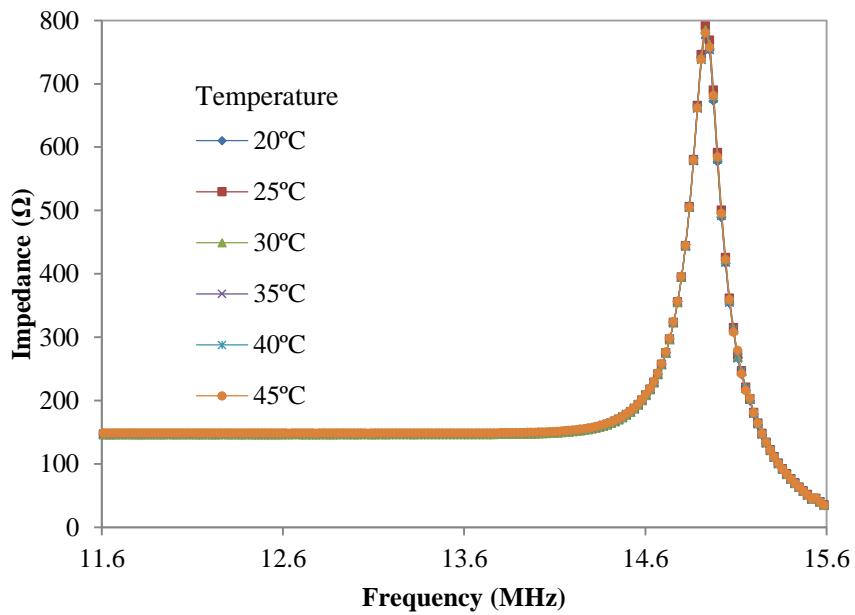
Figure 192. Coil impedance by screen printing as a function of frequency at different temperature values.
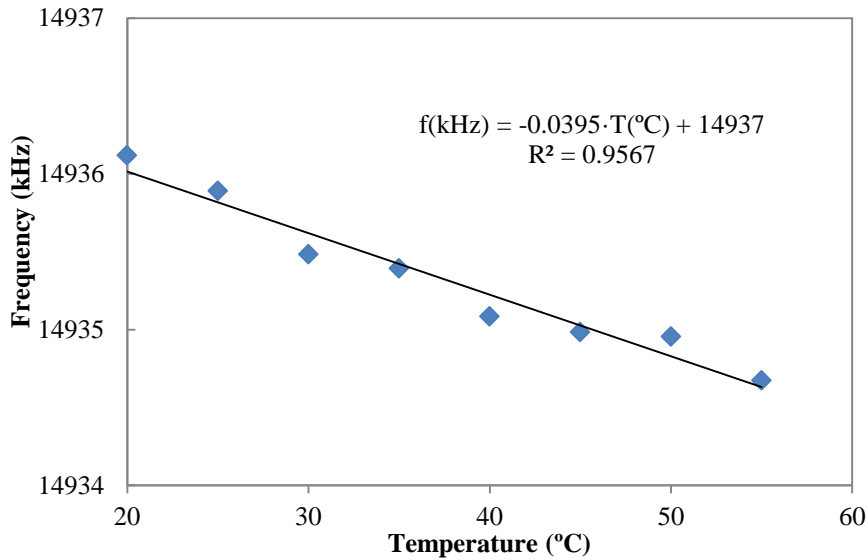
Figure 193. Coil resonance frequency by screen printing as a function of temperature.

The operation of the screen printed antenna tag has been tested with the commercial RFID reader TRF7960 (Texas Instrument, Dallas, TX, USA) with a read range of around 12 cm in vertical direction and 11.2 cm in horizontal one.

Figure 194 presents the impedance of the inkjetted coil as a function of frequency at different values of relative humidity. As we can see, the magnitude not only has reduced its value but also the peak has been widened in comparison with Figure 190. For this reason, we dismissed this option and therefore, the LC tag has been fabricated with screen printed inductances.

On the other hand, the screen printed capacitor was designed in order to get a capacitance value high enough to interfere in the frequency response of the tag. For its ease of fabrication, we chose the interdigitated electrodes. Table 36 contains the physical dimensions of the capacitor with a modelled capacitance of 8 pF at dry atmosphere.
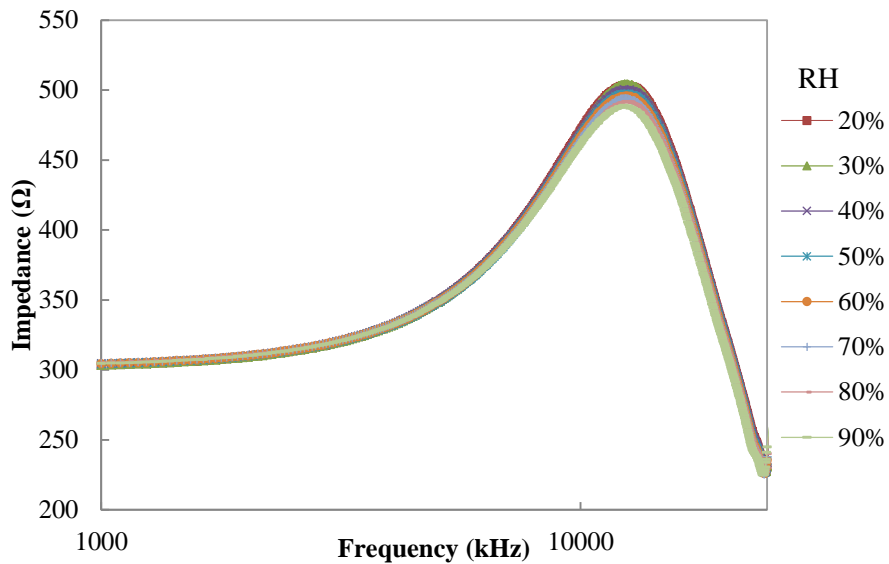
Figure 194. Coil impedance by inkjet printing as a function of frequency at different values of RH.

Figure 195 and Figure 196 present the screen printed capacitor curves in humidity and temperature, respectively. The sensitivity decreases from 11 fF/%RH at 1 MHz to 7.5 fF/%RH at 100 MHz. The thermal dependence is less than -1 fF/ºC in the whole frequency range. The inkjet-printed capacitor is based on serpentine electrodes whose characterization is completely described in section 2.3.

Table 36. Physical dimensions of the capacitive interdigitated structure.

Parameter	Value	Description
Length	1.0 cm	Length of each finger (y-axis)
Width	200 μm	Width of each finger (x-axis)
Thickness	10 μm	Thickness of electrodes (1 layer) (z-axis)
Number	20	Total number of fingers of the larger electrode
Interspacing	200 μm	Distance between consecutive fingers (y-axis)
Distance	200 μm	Distance between fingers of one electrode and the backbone of the other electrode (x-axis)
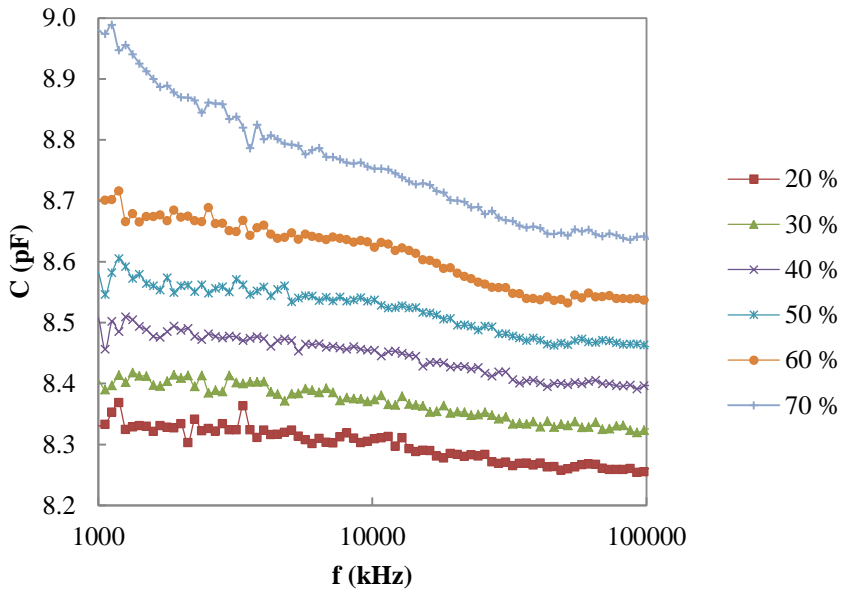
Figure 195. Screen printed capacitance as a function of frequency at different RH values.
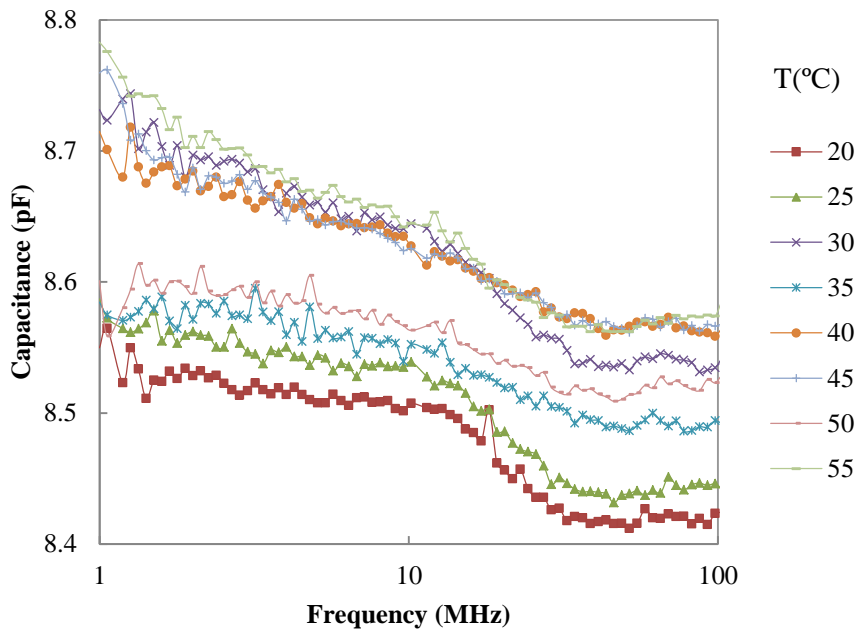
Figure 196. Screen printed capacitance as a function of frequency at different temperature values.

B. LC tags

Then, we characterized a LC tag completely fabricated by screen printing (including one IDE capacitor with specifications in Table 36) as shown in Figure 197. As any of the tag components showed a remarkable variation induced by temperature, we have just studied the tag as a function of RH.
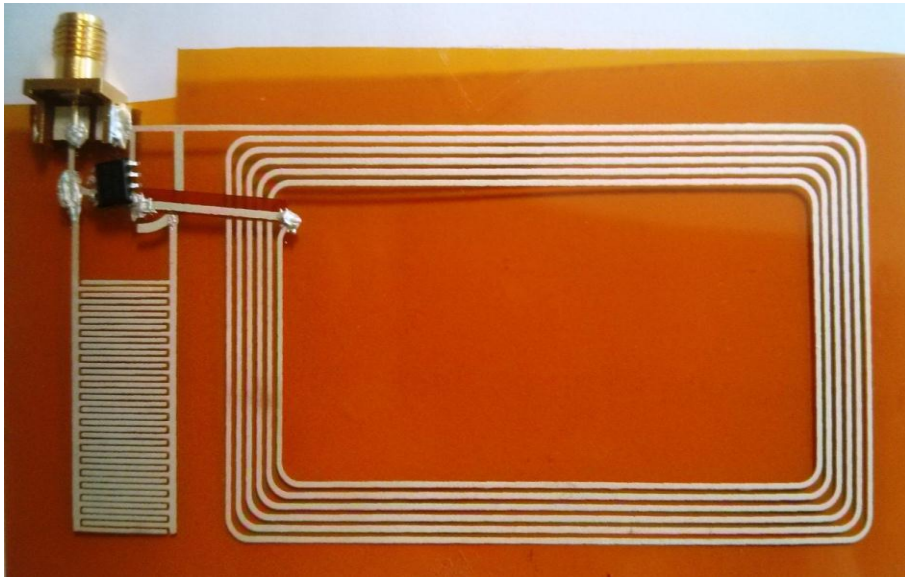
Figure 197. LC tag by screen printing.

The impedance of the screen printed tag at different values of RH is shown in Figure 198. In order to better appreciate the resonance frequency shift, we have zoomed the area where the peak is located and normalized the response, see Figure 199. The resonance frequency is shifted to about 12 MHz because of the added capacitor the change in the resonance frequency varying RH is about 80 kHz (see Figure 200).
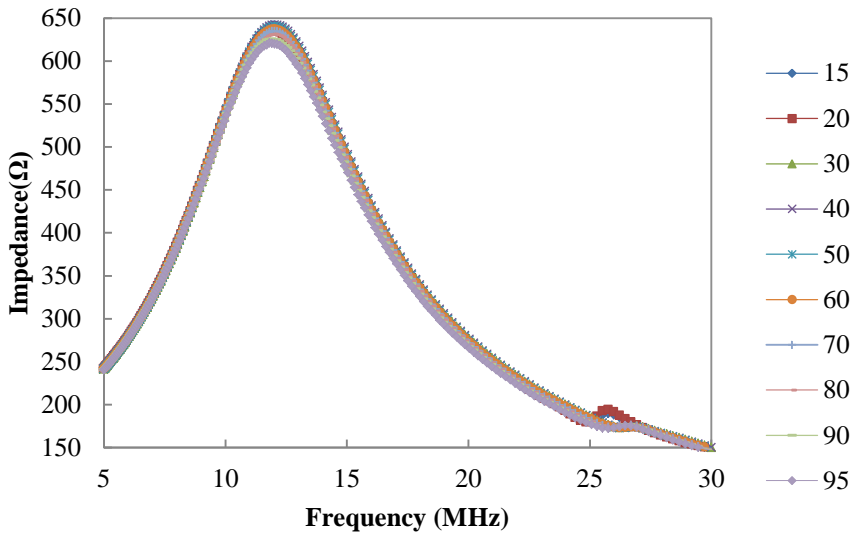
Figure 198. Impedance of the screen printed LC tag as a function of frequency for different RH values.
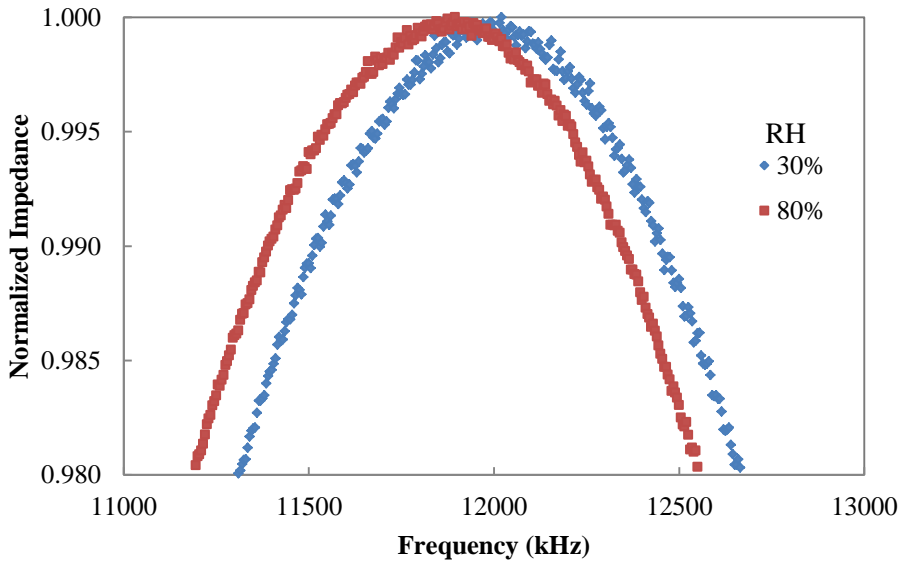
Figure 199. Normalized impedance as a function of frequency for two RH values.
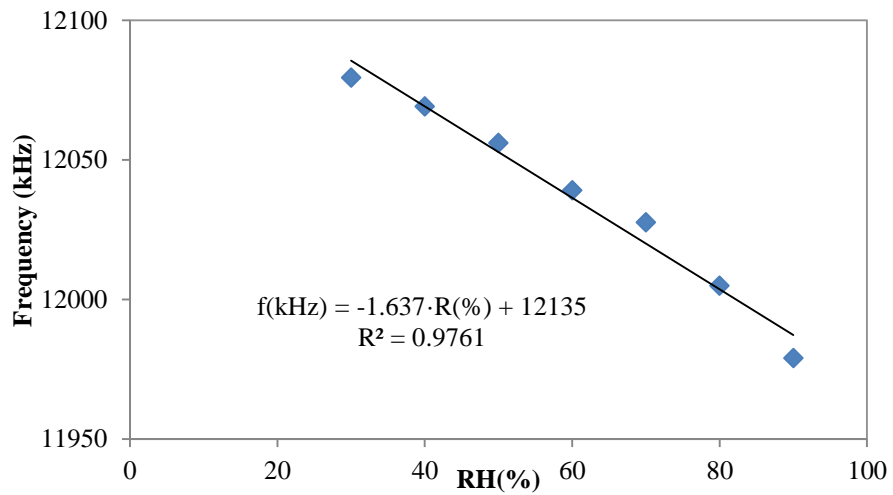
Figure 200. Resonance frequency of the screen printed LC circuit as a function of RH.

Finally, we characterized a hybrid LC tag where the coil inductor was fabricated by screen printing and an array of SRE capacitor was manufactured by inkjet printing (including 12 replicas of SRE capacitor associated in parallel, with specifications in Table 6 in chapter 2) as shown in Figure 201. Here, we have just studied the tag as a function of RH due to the low influence of temperature of each singe element.
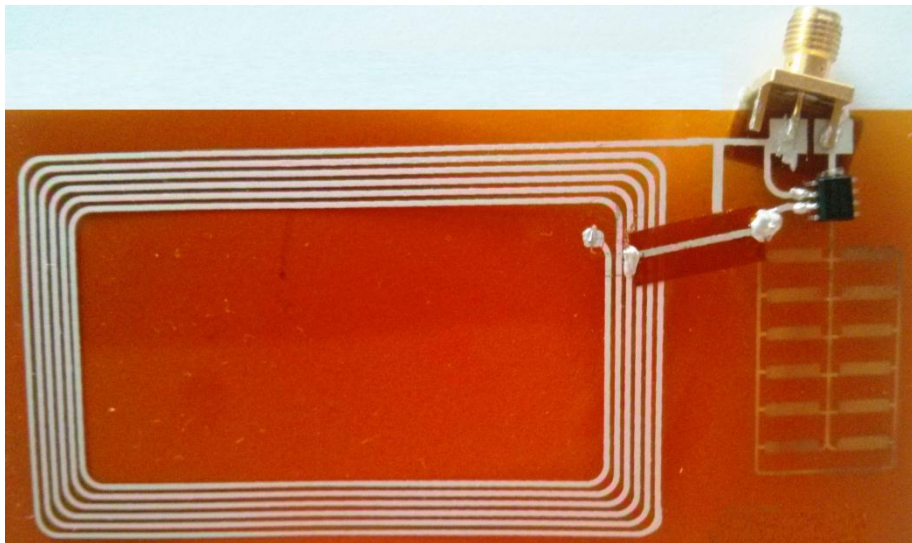
Figure 201. Hybrid LC tag by screen printing (coil) and inkjet printing (capacitors).

The impedance of the screen printed tag at different values of RH is shown in Figure 202 and Figure 198. In order to better appreciate the resonance frequency shift, we have zoomed the area where the peak is located and normalized the response, see Figure 203Figure 199. The resonance frequency is shifted to about 9.5 MHz because of the added capacitors the change in the resonance frequency varying RH is about 300 kHz (see Figure 204).
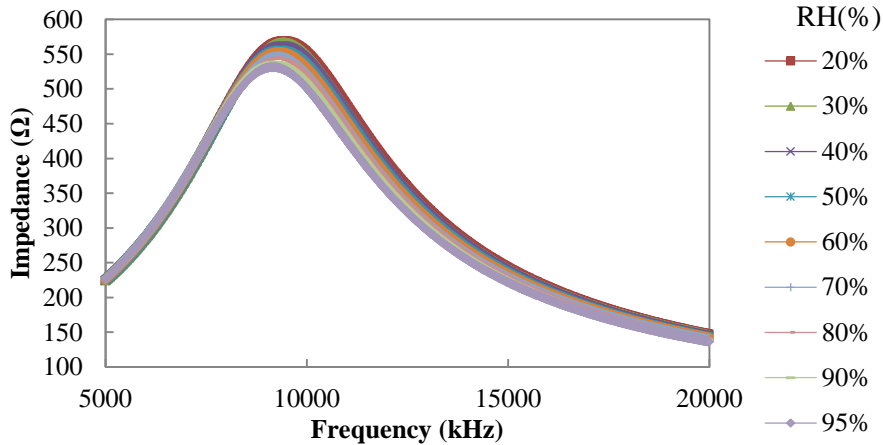
Figure 202. Impedance of the hybrid LC tag as a function of frequency for different RH values.
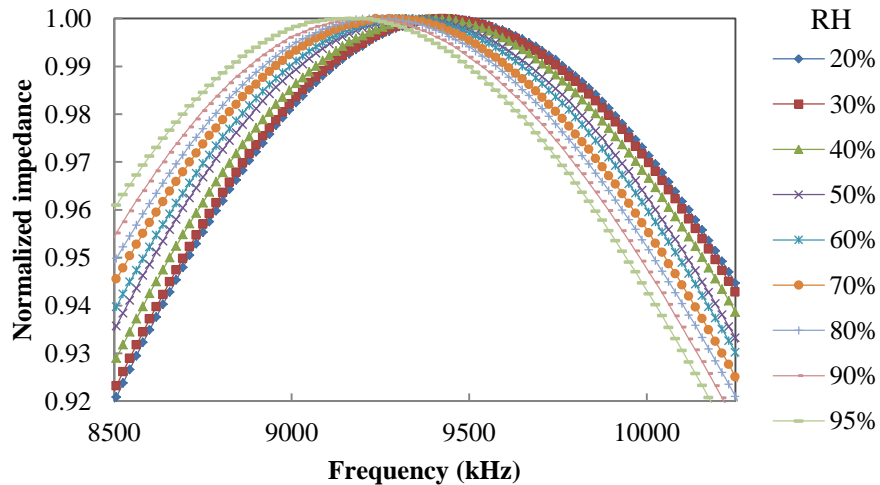
Figure 203. Normalized impedance of hybrid LC tag as a function of frequency for two RH values.
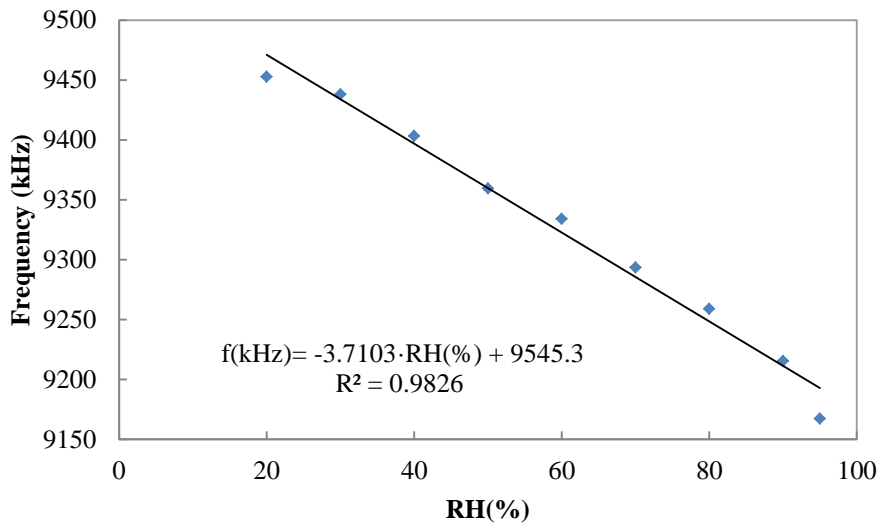
Figure 204. Resonance frequency of the hybrid printed LC circuit as a function of RH.

Further investigation has to be carried out to complete this study but we have obtained a significant change in the resonance frequency. Next steps will be the enhancement of this frequency shift as well as in tuning the tag for the desired RH range. Anyway, this design could be directly used as a resonance humidity sensor by directly measuring the resonance frequency by analog measurements. Actually, we have disconnected the RFID chip to the hybrid LC tag and the shift in the resonance frequency is about 700 kHz.

5.4   Conclusions

In this chapter, we have presented different strategies to design multisensory systems for environmental monitoring. First a commercial sensor, STH15 (Sensirion, Switzerland) was included in a soil probe to monitor different environmental parameters of roots.

The system presented here is a portable device for the measurement of soil properties (moisture, temperature and oxygen concentration) with in-situ data logging. The STH15 sensor data provides humidity and temperature without calibration, small size and a very short response time. The used oxygen sensor provides the following benefits: high immunity to optical and electrical noise, low power consumption, rugged and reliable instrument. This probe has been tested in soil environment showing a good performance.

Regarding the possibilities of continuing this line of work, the inclusion of other sensors in the probe to measure other important environmental parameters in the development of growth plant, such as the determination of ions of interest, would be interesting. The major minerals required by soil plants are phosphorus (P), nitrogen (N), calcium (Ca), iron (Fe) and magnesium (Mg).

On another front, we have presented two prototypes of RFID tags with sensing capabilities. These tags have been fabricated on a polyimide substrate (Kapton HN) by screen printing comprising, apart from the printed sensors, a dipole UFH antenna, a series inductance to match the RFID chip impedance, a reference capacitor necessary for capacitance measurements, and the RFID chip (SL900A). Both tags are able to provide temperature and relative humidity environmental parameters. An on-chip temperature sensor provides temperature data. Taking advantage of the known behaviour of polyimide with relative humidity, two different printed relative humidity sensors, fabricated by inkjet printing and screen printing respectively, have been interfaced to the RFID chip. Capacitance values are obtained in digital form (10 bits) from the integrated ADC of the RFID chip. The tag with the inkjetted printed sensor presents a performance higher than the one obtained with the array of screen printed sensors. The former covers 800 counts of 1024 for a shift in RH from 37% to 70%. The latter covers 220 counts of 1024 for a shift in RH from 57% to 86%. Between these limits of RH, the obtained resolution and associated error are acceptable while out of these range the performance is reduced. The different performance among tags can be explained by the different number of devices (12 inkjetted vs. 6 screen-printed) that affects directly the obtained sensitivity of each array. The different obtained range of RH can be associated with the choice of the reference capacitor, 36 and 39 pF respectively. These capacitors can be tuned to monitor a concrete range of RH. The lack of performance of the ADC can be explained by the fact that the SFE of the RFID chip has been designed to interface different type of sensors, e. g., resistive, and not specific for capacitance.

The drawback of the inkjetted sensor approach is the need of mixing techniques, inkjet and screen printing, implying a complex fabrication with different sintering process and alignment. The screen printed sensors

approach can be fabricated with just one step but a much bigger area is required. Therefore, the tag choice will depend on the restrictions of each application, basically in terms of sensitivity and area. Energy to power up the tag and drive the sensor stage is extracted from the radiated field of the RFID reader. Thus, the proposed tags are passive and composed by a single silicon chip providing a cost-effective solution to monitor environmental properties.

Finally, a RFID tag has been studied as a threshold humidity sensor. The idea is shifting the resonance frequency of the RFID tag to tune the antenna within a specific humidity range. The reader could not read the tag out of this range. For this purpose, we have manufactured an inductor coil and an interdigitated capacitor by screen printing and inkjet printing. Then, we have studied the behaviour of every single element, coil and capacitor, as a function of frequency at different relative humidity (RH) values. The response of coil inductors to humidity were virtually negligible but the quality factor of the inkjetted coil was much lower than the screen printed one and it was strongly affected by RH; therefore we have rejected this option for the final tag. Then, we have characterized a full screen printing LC tag. We found a shift of 100 kHz in the resonance frequency for the whole RH range studied. A hybrid tag with screen printed coil and an array of inkjetted capacitor has also been analysed. In this case, a shift of about 300 kHz in the resonance frequency has been found. Further investigation should be carried out to complete this study but we have obtained a significant change in the resonance frequency. Next steps should be addressed in the enhancement of this frequency shift as well as in tuning the tag for the desired RH range. Anyway, this design could be directly used as a resonance humidity sensor by directly measuring the resonance frequency. Actually, a shift of 700 kHz has been found in the hybrid tag by only disconnecting the RFID chip.

6.   Scientific contributions

6.1   Journal papers

Almudena Rivadeneyra, José Fernández-Salmerón, Manuel Agudo, Juan A López-Villanueva, Luis Fermín Capitan-Vallvey, Alberto J Palma. "Design and characterization of a low thermal drift capacitive humidity sensor by inkjet-printing". Sensors and Actuators B: Chemical. 2014. 195: 123-131.

A Martínez-Olmos, J Fernández-Salmerón, N Lopez-Ruiz, **A Rivadeneyra** Torres, LF Capitan-Vallvey, AJ Palma. "Screen printed flexible radiofrequency identification tag for oxygen monitoring". Analytical Chemistry. 2013. Vol. 85, 22: 11098-11105

José F Salmerón, Francisco Molina-Lopez, Danick Briand, Jason J Ruan, **Almudena Rivadeneyra**, Miguel A Carvajal, LF Capitán-Vallvey, Nico F de Rooij, Alberto J Palma. "Properties and Printability of Inkjet and Screen-Printed Silver Patterns for RFID Antennas". Journal of Electronic Materials. 2014. Vol. 43, 2: 604-617

6.2   Journal papers submissions

José F. Salmerón, Francisco Molina-Lopez, **Almudena Rivadeneyra**, Andrés Vásquez Quintero, L. F. Capitán-Vallvey, Nico F. de Rooij, Jesús Banqueri Ozáez, Danick Briand and Alberto J. Palma. "Printed UHF RFID Smart Tags for Sensing Applications". IEEE Sensors. February, 2014.

Almudena Rivadeneyra, José Fernández-Salmerón, Manuel Agudo-Acemel, Alberto J. Palma, Luis Fermín Capitan-Vallvey, Juan A. López-Villanueva. "Cantilever fabrication by a printing and bonding process". Journal of Microelectromechanical Systems. March, 2014.

Almudena Rivadeneyra, José Fernández-Salmerón, Jesús Banqueri, Juan A. López-Villanueva, Luis Fermín Capitan-Vallvey, Alberto J. Palma. "A novel electrode structure compared with interdigitated electrodes as capacitive sensor". Sensors and Actuator: B. May, 2014.

6.3   International conferences

Rivadeneyra-Torres, Almudena, Fernández-Salmerón, José, Lopez-Villanueva, Juan Antonio, Capitán-Vallvey, Luis Fermín, Palma-Lopez, Alberto J. "Novel capacitive structure: A comparison with Interdigitated Electrodes". The Swiss Conference on Printed Electronics and Functional Materials (e-Swiss). 2013.

Rivadeneyra-Torres, Almudena, Fernández-Salmerón, José, Lopez-Villanueva, Juan Antonio, Capitán-Vallvey, Luis Fermín, Palma-Lopez, Alberto J. "Ink-jet printed humidity sensor on Kapton HN for UHF RFID tags". Large-area, Organic & Printed Electronics Convention (LOPE-C). 2013.

Jose F Salmeron, **Almudena Rivadeneyra Torres**, Jesus Banqueri, Migue A Carvajal, Manuel Agudo. "Design and Characterization of Ink-Jet and Screen Printed HF RFID Antennas". Workshop on RFID Technology (EURASIP RFID), 2012 Fourth International EURASIP. 2012, 119-123.

Almudena Rivadeneyra, Juan A Lopez-Villanueva, Rosemary O'Keeffe, Nathan Jackson, Mike O'Neill, Alan Mathewson. "Frequency response of variants of a cantilever beam". International Conference on Synthesis, Modeling, Analysis and Simulation Methods and Applications to Circuit Design (SMACD). 2012, 177-180

Almudena Rivadeneyra, Fernando Martinez-Marti, Alberto J Palma, Jesus Banqueri, Raul Munoz Bernardo. "Geometrical analysis of a MEMS microphone". International Conference on Synthesis, Modeling, Analysis and Simulation Methods and Applications to Circuit Design (SMACD). 2012, 169-172.

7.   Conclusiones y trabajo futuro

Este trabajo se ha centrado en el diseño de sensores ambientales basados en distintas tecnologías y con diversas aplicaciones. Desde sensores impresos para sensado de humedad hasta micro-palancas para recolección de energía con tecnología MEMS. Además, la mayoría de las estructuras aquí presentadas han sido fabricadas y caracterizadas. Por último, se ha probado la integración de algunos de estos sensores así como de sensores comerciales en sistemas completos de medida.

Primero se han diseñado, modelado y fabricado estructuras capacitivas por impresión de inyección de tinta. La diferencia entre las mismas es la forma de los electrodos: interdigitales, serpentina y espiral. Estas tres configuraciones de electrodos han sido caracterizadas como sensores de humedad. El elemento de detección de estos sensores es directamente el sustrato sobre el que se han definido los electrodos que actúa de dieléctrico. La permitividad eléctrica de dicho material depende directamente de la humedad relativa en el ambiente. El uso directo del substrato como elemento de sensado simplifica enormemente el proceso de fabricación, ya que no es necesaria la impresión de una capa adicional. Además solo se necesita una capa impresa de tinta de plata para definir los electrodos. Los materiales empleados en todos los sensores son Kapton HN como sustrato y tinta de plata SunTronic U5603. Los tres prototipos se caracterizan por su pequeño tamaño y bajo coste en términos de materiales y tiempo de fabricación así como su facilidad y rapidez de integración en etiquetas RFID.

El primer diseño presentado son electrodos interdigitales (IDE) que ocupan menos de 12 mm^2 de sustrato y requieren aproximadamente 23 nl de tinta de plata para una capa impresa con una tasa de éxito de fabricación elevada. Los datos experimentales están en concordancia con los datos obtenidos con el simulador COMSOL Multiphysics, validando el procedimiento de extrapolación para capas impresas de muy poco espesor. Este sensor muestra una respuesta estable en el rango de frecuencias estudiado (100 kHz - 10 MHz), mostrando una sensibilidad de (4.5 ± 0.2) fF/%RH a 100 kHz y (4.2 ± 0.2) fF/%RH a 1 MHz. Además, se ha obtenido una deriva térmica muy baja en dicho rango de frecuencias, con un coeficiente térmico alrededor de (-0.2

± 0.2) fF/ºC a 1 MHz y (-0.4 ± 0.2) fF/ºC a 100 kHz. Por lo tanto, la sensibilidad a la humedad es del orden de 11 veces superior a la deriva térmica a 100 kHz y 21 veces superior a 1 MHz. Este resultado puede significar que se puede prescindir de la compensación en temperatura si se elige adecuadamente la frecuencia de trabajo. En cuanto al tiempo de respuesta del sensor, se ha obtenido un valor de unos 6 min; dicho tiempo podría fácilmente mejorarse si se reduce el espesor del substrato. Por último cabe señalar que la respuesta del sensor prácticamente no ha cambiado como consecuencia del envejecimiento del sensor.

Posteriormente se ha presentado el electrodo serpentina (SRE) y se ha estudiado su potencial como sensor capacitivo en comparación con los electrodos interdigitales conocidos. Se han realizado simulaciones numéricas de la capacitancia de las dos estructuras para analizar las diferencias exclusivamente geométricas entre ellos manteniendo constante el área. Bajo estas condiciones, se ha demostrado la mejora de la capacitancia de los condensadores serpentina con el aumento del número de dedos. Esta mejora ha sido de un 14% con 32 dedos por electrodo y 21% para 180 dedos. El resto de los parámetros dimensionales así como el substrato o la posible capa superior depositada no ha añadido ninguna otra diferencia entre ambas estructuras. Estos resultados numéricos han sido validados a través de la caracterización experimental de sensores capacitivos con electrodos serpentina. Dichos sensores han sido funcionalizados como sensores de humedad siguiendo el mismo proceso de fabricación que los sensores interdigitales anteriormente descritos. En este caso, la tasa de éxito es inferior a los sensores IDE debido a la mayor complejidad de la estructura serpentina. La sensibilidad de los electrodos SRE ha sido de (5.2 ± 0.2) fF/%RH a 1 MHz, mientras que para la sensibilidad del IDE fue de (4.2 ± 0.2) fF/%RH a la misma frecuencia, con una superficie total de 11.65 mm^2 en ambas estructuras. Por otro lado, se ha logrado un comportamiento en humedad prácticamente independiente de la temperatura en el rango de frecuencias de 100 kHz a 2 MHz. Las curvas de calibración encontradas son lineales y con una histéresis comparable con la estructura IDE. Las constantes de tiempo son de aproximadamente 6 min para absorción y desorción de la humedad, similares a los tiempos encontrados para el IDE. Por lo tanto, se ha demostrado un mejor comportamiento de la estructura SRE en comparación con la IDE bajo las mismas condiciones de fabricación y ocupando el mismo

área, siendo una estructura prometedora para múltiples aplicaciones en el campo de la transducción de señales.

En cuanto a los electrodos en forma de espiral, se ha seguido el mismo proceso de fabricación y materiales que en los dos casos anteriores. El área de este sensor fue sólo 5.52 mm^2 con un valor de capacitancia de aproximadamente 1 pF . Estos valores no se pueden comparar directamente con los encontrados para los sensores IDE y SRE por lo que se va a considerar el efecto de dos condensadores de espiral conectados en paralelo. De este modo, el área total sería de 11.05 mm^2 y la capacidad modelada en atmósfera seca de 1.86 pF ya que la capacidad equivalente de dos condensadores conectados en paralelo es igual a la suma de ambos valores. Estos valores sí son comparables con las áreas y capacidades de los sensores IDE y SRE previamente caracterizados. Al estar conectados en paralelo, se puede asumir que la sensibilidad equivalente va a ser también la suma de las sensibilidades individuales, resultando en 4.62 fF/%HR a 1 MHz. Este resultado sugiere que el mayor valor de sensibilidad se encuentra en los condensadores SRE, seguido de electrodos espirales, siendo el sensor IDE el que muestra el menor valor de sensibilidad. El comportamiento en temperatura encontrado es similar al de los electrodos serpentina. La deriva térmica es muy baja, tendiendo a cero a frecuencias inferiores a 2 MHz, mientras que a frecuencias más altas dicha deriva térmica aumenta. La Table 12 resume las principales características de los tres tipos de electrodos estudiados para facilitar su comparación.

Tabla 37. Comparación entre los distintos diseños de electrodos. Por razones de comparación, las características de los electrodos de espiral corresponden a la asociación en paralelo de dos condensadores tipo espiral. * Se esperan resultados similares ya que los materiales empleados son los mismos.

Parámetro	Condensador IDE	Condensador SRE	Condensador Espiral
Área (mm^2)	11.65	11.65	11.05
Capacidad simulada (pF)	1.973	2.256	1.86
Capacidad experimental (pF)	2.053 ± 0.002	2.877 ± 0.003	1.107 ± 0.002
Rango de sensibilidad 100 kHz – 1 MHz (fF/%HR)	4.5 – 4.2	6.2 - 4.7	6.2 - 4.7
Rango deriva térmica 100 kHz – 1 MHz (fF/ºC)	-0.2 – -0.4	0 – 1	0 – 1
Sensibilidad a 1 MHz (fF%HR)	4.2 ± 0.2	5.2 ± 0.2	4.62 ± 0.4
Deriva térmica a 1 MHz	-0.2 ± 0.2	~ 0	~ 0

(fF%°C)			
Tiempo de respuesta (s)	356 ± 3	350 ± 2	--*
Tiempo de desorpción (s)	367 ± 4	365 ± 4	--*
Estabilidad temporal tras 5 meses	< 3% RH	3% RH	--*

Por último, se ha presentado una estructura asimétrica basada en electrodos interdigitales con dichos electrodos situados en distintos planos. La capacidad modelada es de 3.45 pF para una superficie total de 2.2 mm^2 con dedos de 5 μm de espesor. Esta estructura contiene polímero sensible alrededor de todos los ejes de los electrodos y, por lo tanto, si hay una fuerte dependencia entre el espesor de los electrodos y la capacidad obtenida. Por ejemplo, la capacidad obtenida con dedos de 20 μm de espesor es 12 pF.

La fabricación de este dispositivo puede seguir distintos procedimientos. En primer lugar, se puede escoger un sustrato no sensible al analito en estudio para no interferir en los datos o por el contrario escoger un sustrato que también sea sensible al parámetro en estudio para potenciar la sensibilidad total del dispositivo. Otra alternativa es utilizar un substrato metálico para reducir el número de etapas de fabricación. En cuanto a la definición del electrodo superior, se puede imprimir directamente el electrodo superior o transferir los electrodos previamente impresos en otro sustrato. Otra cuestión importante del diseño es el espesor del polímero sensible; además esta capa puede cubrir completamente ambos electrodos, sólo el electrodo inferior o ambos electrodos pueden encontrarte superficialmente al descubierto.

Otro tipo de estructuras que han sido descritas en este trabajo son aquellas que tienen partes móviles. Primero se han detallado dos enfoques de fabricación de estructuras suspendidas mediante técnicas de impresión. El primer proceso de fabricación se ha basado en emplear una capa sacrificial mientras que el segundo enfoque emplea un substrato sacrificial. En este último caso dos materiales diferentes han sido probados como sustrato de sacrificio.

Con respecto al primer enfoque, la fabricación completa de la micro-palanca no se ha logrado pero se han obtenido algunos resultados prometedores. La justificación del uso de una capa sacrificial impresa es lograr una corta distancia entre la micro-palanca y el sustrato bajo ella. Este pequeño espacio

(~ 10 μm) proporciona una mayor capacidad nominal y una mayor sensibilidad cuando se produce cualquier desplazamiento de la palanca. Además, este tipo de estructuras se podría integrar fácilmente como interruptores.

Se han probado distintos materiales como capa sacrificial siendo el candidato mejor encontrado una mezcla de TME, CH y PG. Como materiales conductores, la tinta que mejor resultado ha dado ha sido la tinta de plata de serigrafía. A diferencia de estas tintas probadas, esta tinta se puede imprimir con muy buenos resultados en la solución TME+CH+PG sin aparentemente reaccionar con dicha capa. La principal ventaja de esta mezcla de TME es que se puede eliminar tras el sinterizado de la plata por sublimación. Una posible solución a los materiales conductores que reaccionan con esta capa sacrificial impidiendo la sublimación de dicha capa es insertar una capa estructural, tal como etilcelulosa, entre la capa de sacrificio y los electrodos. Otras alternativas que podrían seguirse son continuar el estudio del PMMA como capa sacrificial o formular la solución de la capa sacrificial con DMHD en vez de NPG. La futura investigación debe centrarse en la mejora de impresión de las distintas capas mediante serigrafía así como la búsqueda de las mejores condiciones de fabricación que permitan la reproducibilidad de este proceso.

En cuanto a los sustratos sacrificiales, se ha presentado un novedoso proceso de fabricación para desarrollar micro-palancas impresas en sustrato flexible. El material estructural y conductor de esta palanca es también tinta de plata para serigrafía. Este proceso reduce el número de etapas de fabricación, reduciendo el tiempo de fabricación. Además, la capa de sacrificio utilizada aquí proporciona una superficie plana facilitando la impresión sobre ella, siendo la rugosidad de esta capa mucho menor que la de las capas impresas ya que se trata de películas comerciales y, por lo tanto, se reduce la probabilidad de fracturas. La principal diferencia entre este procedimiento y los convencionales es el hecho de que la capa de sacrificio se coloca en este caso en la parte superior de la estructura suspendida en lugar de debajo de ella. Esta particularidad resta importancia a la capa de sacrificio durante el proceso de fabricación ya que incluso el espesor de la capa de sacrificio no afecta a la estructura fabricada. Otra peculiaridad de este proceso es el uso de un sustrato flexible proporcionando más versatilidad a este dispositivo. Las

deflexiones de estas micro-palancas se han medido para distintos valores de aceleración a diferentes frecuencias de oscilación. También se ha medido la variación de la capacidad al someter la estructura a ciertos valores de aceleraciones. Como se ha comentado, se han probado dos materiales diferentes como capa sacrificial: PMMA y PVA. El primer prototipo fue desarrollado con la película de PMMA. Aunque su respuesta a la aceleración aplicada, así como la capacidad se midió exitosamente, se detectaron algunas imperfecciones en la homogeneidad de las palancas. Estas alteraciones en la estructura pueden ser causados durante la eliminación de la capa sacrificial de PMMA, ya que es necesario sumergir la estructura en un baño de acetona y si no se controla adecuadamente el tiempo de inmersión la acetona termina reaccionando también con la capa estructural de plata. Posteriormente se ha probado una película de PVA que se puede eliminar con un baño de agua. La estructura resultante mostró un perfil más plano y, por lo tanto, una mejor reproducibilidad así como una mayor tasa de éxito de fabricación.

Otra estructura estudiada con partes móviles ha sido una micro-palanca piezoeléctrica para trabajar como recolector de energía. Esta estructura está pensada para ser fabricada con tecnología MEMS. Con este fin, se ha estudiado cómo afectan los cambios en la geometría a su frecuencia de resonancia. Primeramente, se ha demostrado que el modelado mediante COMSOL Multiphysics de palancas constituidas únicamente de silicio proporciona resultados precisos cuando se compara con dispositivos fabricados con estructura multicapas. Esta simplificación reduce el tiempo de computación para probar las propiedades mecánicas de esta cosechadora. Los resultados muestran que las frecuencias de resonancia se ven afectadas a través de cambios en la geometría de la palanca y estos resultados pueden ser utilizados para diseñar las estructuras a la frecuencia de resonancia deseada. El efecto de estas variaciones sobre el factor de calidad no ha sido muy notorio, se necesitan más estudios al respecto para conocer la influencia correcta sobre dicho factor. Los mismos modelos se pueden actualizar directamente para incluir el elemento piezoeléctrico con el fin de modelar las propiedades piezoeléctricas. Se ha encontrado que el mejor compromiso entre el rendimiento de fabricación y la aproximación de los dos primeros modos de resonancia de la estructura se produce cuando se define una fila de ranuras a 0.5 mm del extremo libre de la palanca con un espesor de 43 μm para silicio de buena calidad y de 38 μm para silicio de baja calidad.

Finalmente, se ha modelado por simulación numérica la respuesta de un micrófono MEMS capacitivo ante variaciones en su geometría. La forma de este micrófono es similar a una seta, siendo la placa suspendida el diafragma sensible a las ondas acústicas. Gracias a los resultados de la simulación, se puede no sólo verificar la validez de los supuestos físicos realizados en la definición del modelo, sino también utilizar las simulaciones para ayudar a determinar los parámetros de diseño que optimicen el rendimiento de los dispositivos, minimizando de este modo el tiempo, el esfuerzo y los gastos necesarios para construir y testear un dispositivo real.

Los resultados muestran que la capacidad se ve afectada por los cambios en su geometría. Los valores más altos de capacidad se alcanzan con mayores diámetros de la membrana, valores menores de altura de la membrana y menores valores de su espesor. No se ha podido fabricar este micrófono pero sería interesante intentar la fabricación de este dispositivo mediante técnicas de impresión tal como el proceso basado en PVA como sustrato de sacrificio.

Por otro lado, se ha presentado un sensor doble con mediciones de capacidad y resistencia. El diseño propuesto se basa en cuatro meandros impresos en sustrato de poliamida. Aunque hay otras geometrías que ofrecen mayor capacidad nominal por unidad de superficie que el aquí mostrado, se optó por este diseño, ya que permite aumentar la funcionalidad del dispositivo mediante la inclusión en la misma zona de un sensor resistivo con la misma huella. El enfoque habitual para proporcionar sensibilidad a la humedad o a cualquier gas es depositar una capa sensible sobre los electrodos, otra posibilidad es utilizar directamente el sustrato como elemento de detección. En este doble sensor se han combinado ambas estrategias en un solo dispositivo; por lo tanto, se concentran prácticamente en la misma área dos sensores diferentes.

Con el fin de funcionalizar este sensor doble o mixto, las dos magnitudes detectadas han sido la humedad y la concentración de tolueno. La humedad relativa se mide a través de cambios en la permitividad eléctrica del sustrato (poliamida), de manera que la capacidad de estos electrodos cambia con la humedad. La concentración de tolueno se deriva de cambios en la resistividad de un polímero basado en grafito depositado sobre los otros electrodos de este sensor; siendo esta parte del sensor resistiva mientras que

la otra parte es capacitiva. Se han caracterizado el comportamiento de las dos partes sensoras ante la humedad relativa, la temperatura y la concentración de tolueno. En cuanto a la parte capacitiva, se encontró una sensibilidad de 5 fF/%HR a 1 MHz. Este valor es comparable a las sensibilidades presentadas anteriormente (Tabla 1) pero en este caso se requiere más área para definir el condensador. La dependencia térmica encontrada ha sido insignificante al igual que ocurrió en las estructuras detalladas anteriormente. Además, el cambio de capacidad en atmósfera saturada de tolueno fue de aproximadamente 1% del valor de la capacidad en condiciones ambientales normales. Con respecto a la parte resistiva, se encontraron dependencias de 0.05 Ω/%HR y 0.1 Ω /ºC. La dependencia a la humedad relativa puede compensarse directamente con el valor de la humedad extraído de la parte capacitiva de este sensor doble. En cuanto a la dependencia térmica de esta resistencia, se requerirá compensación térmica para eliminar su efecto. Hay distintas opciones para hacer frente a este problema, por ejemplo, se podría incluir una termoresistencia en el diseño o si este sensor doble se introduce en una etiqueta RFID muchos de los chips integran directamente un sensor de temperatura (por ejemplo, SL900A). La sensibilidad al tolueno es 0.3 mΩ / ppm de tolueno, midiendo cada 3 minutos, pero se encontró que el valor de resistencia se triplica en atmósfera saturada en tolueno después de 24 horas. Por lo tanto, sería necesario profundizar en el estudio de este polímero sensible para optimizar su respuesta. También se ha encontrado un cambio prometedor en la resistencia a la disolución de agua.

Por este motivo, se ha estudiado la influencia de distintos parámetros controlables durante la fabricación de la resistencia impresa con el fin de encontrar la mejor combinación de ellos en la detección de la concentración de tolueno a muy bajas concentraciones (partes por billón, ppb). En primer lugar, se ha analizado el impacto de la densidad de la malla de serigrafía en la reproducibilidad del proceso de fabricación y el valor nominal de resistencia. En términos de reproducibilidad, se podría concluir que la tinta con el contenido más alto de grafito funciona bastante bien con las dos densidades de malla estudiadas. En caso de usar 43 T/cm de densidad de malla, se obtienen patrones de impresión más fiable. Los patrones impresos con 120 T/cm de densidad de malla siempre resultan en una mayor resistencia que los patrones impresos con densidad de 43 T/cm. Este

resultado podría estar causado por el hecho de que una densidad de malla superior (más fina) obstruye el paso del grafito hacia el sustrato.

A continuación, se ha mostrado la respuesta a la concentración de tolueno constante para diferentes composiciones de polímero. En todos los casos, se observa una respuesta rápida y superior al tolueno que al agua. Las curvas obtenidas con valores nominales de resistencia superiores muestran una respuesta más saturada que la resistencia con valor nominal más bajo. También se observa una relación en la respuesta al agua: el valor nominal más bajo que corresponde a un contenido de grafito superior presenta una menor sensibilidad al agua de los otros patrones.

Por último, se ha estudiado la influencia de los electrodos del sensor; para ello se han fabricado electrodos IDE y SRE ocupando la misma superficie y se han cubierto totalmente con la misma composición de polímero y utilizando la misma densidad de la malla. Se ha encontrado que los electrodos SRE resultan en un 12,7% más resistencia de la configuración del IDE.

Finalmente se han presentado varias estrategias de integración de sensores de humedad en aplicaciones multisensoras completas. En primer lugar se ha incluido un sensor comercial, STH15 (Sensirion, Suiza) en una sonda edáfica para controlar diferentes parámetros ambientales en el entorno cercano a las raíces de las plantas. Se trata de un dispositivo portátil para la medición de las propiedades del suelo (humedad, temperatura y concentración de oxígeno) con el registro de datos in-situ. El sensor STH15 proporciona datos de la humedad y temperatura sin necesidad de calibración. Dicho dispositivo posee un tamaño pequeño y un tiempo de respuesta muy corto, lo cual permite reducir el tamaño de sonda y asegura una respuesta rápida a los cambios en el ambiente. Por otro lado, el sensor de oxígeno utilizado posee las siguientes ventajas: una alta inmunidad al ruido óptico y eléctrico, bajo consumo energético, resistente y fiable. Esta sonda ha sido probada en el entorno de las raíces de una planta de acebo mostrando un buen rendimiento. Respecto a las posibilidades de continuar con esta línea de trabajo, sería interesante la inclusión de otros sensores en la sonda para controlar otros parámetros ambientales importantes en el desarrollo del crecimiento de las

plantas, tales como la salinidad u otros minerales que toman las plantas del suelo son el fósforo, nitrógeno, calcio, hierro y magnesio.

Por otra parte, se han presentado dos prototipos de etiquetas RFID con capacidades sensoras. Estas etiquetas se han fabricado sobre un sustrato de poliamida mediante técnicas de impresión. Aparte de los sensores impresos, posee una antena de dipolo UHF, una inductancia en serie como red de adaptación, un condensador de referencia necesario para las mediciones de capacidad y el chip RFID (SL900A).

Ambas etiquetas son capaces de proporcionar medidas de la temperatura y humedad relativa. La temperatura es proporcionada directamente por el chip RFID que posee integrado un sensor de temperatura. Aprovechando la dependencia conocida de la permitividad relativa de la poliamida con humedad relativa, se han fabricado dos sensores distintos impresos por inyección de tinta y por serigrafía, respectivamente, y se han conectado con la interfaz sensora del chip RFID. Los valores de capacidad se obtienen en formato digital (10 bits) gracias al ADC integrado en el chip de RFID. La etiqueta con el sensor de inyección de tinta presenta un rendimiento más alto que la etiqueta con la matriz de sensores serigrafiados. En el primer caso, se cubren 800 cuentas de 1024 posibles para un cambio en la humedad relativa del 37% al 70 %. En el segundo caso, se utilizan unas 400 cuentas de las 1024 posibles para un cambio en la humedad relativa del 60% al 90%. Entre estos límites de humedad relativa, la resolución obtenida y el error asociado son aceptables, mientras que fuera de dichos valores no es posible discriminar valores de humedad con precisión. El diferente comportamiento de las etiquetas en cuanto al rango de lectura puede explicarse por el número de sensores integrados (12 de inyección de tinta vs. 6 serigrafiados) en cada etiqueta, lo cual afecta directamente a la sensibilidad obtenida en cada matriz. La sintonización del rango de HR se puede asociar con la elección del condensador de referencia, 36 y 45 pF respectivamente. La elección de estos condensadores se puede realizar de forma que la etiqueta se sintonice para monitorizar un rango concreto de HR. El bajo rendimiento del ADC es debido a que el SFE del chip RFID está diseñado para trabajar con diferentes tipos de sensores, por ejemplo, resistivos, y no está específicamente diseñado para capacidad.

El inconveniente de la etiqueta que incluye los sensores de inyección de tinta es la necesidad de mezclar técnicas de impresión, resultando en una fabricación más compleja con distintos procesos de sinterización y alineación. Mientras que la alternativa de sensores serigrafiados permite fabricar toda la etiqueta en un solo paso, a costa de utilizar un área mucho más grande. Por lo tanto, la elección del tipo de etiqueta dependerá de las restricciones de cada aplicación, básicamente en términos de sensibilidad y área. La energía necesaria para alimentar la etiqueta y conducir la etapa de sensor se extrae del campo radiado por el lector RFID. Por lo tanto, las etiquetas propuestas son pasivas y compuestas por un único chip de silicio que proporciona una solución rentable para monitorizar propiedades ambientales.

Por último, se ha estudiado una etiqueta de RFID como sensor de humedad umbral. La idea es cambiar la frecuencia de resonancia de la etiqueta RFID para que la antena esté sintonizada únicamente dentro de un rango de humedad específica. Fuera de este rango de humedad, el lector no es capaz de leer la etiqueta (extraer su identificador). Para este propósito, se han fabricado una inductancia y condensador interdigital por serigrafía e inyección de tinta. A continuación, se ha estudiado el comportamiento de cada elemento, bobina y condensador, como una función de la frecuencia a diferentes valores de humedad relativa. La respuesta de los inductores a la humedad era prácticamente insignificante, pero el factor de calidad de la bobina de inyección fue mucho menor que la serigrafiada, por lo tanto, se ha rechazado esta opción para la etiqueta final.

A continuación, se ha caracterizado una etiqueta LC completamente serigrafiada. El desplazamiento en frecuencia de resonancia encontrado fue de unos 80 kHz para el rango de humedad relativa de estudio. También se probó una estrategia mixta, incluyendo una bobina serigrafiada y una matriz de capacidades de inyección de tinta. En este caso, se ha observado un desplazamiento de la frecuencia de resonancia de unos 300 kHz en el rango de humedad estudiado. Más investigación debe llevarse a cabo para completar este estudio, pero se ha obtenido un cambio significativo en la frecuencia de resonancia. Los siguientes pasos deben ser dirigidos a la mejora de este cambio de frecuencia, así como la sintonización de la etiqueta para el rango de humedad relativa deseada. De todos modos, este diseño

podría ser utilizado directamente como sensor de humedad por medición directa de la frecuencia de resonancia. De hecho, se ha observado un cambio de 700 kHz en la etiquita híbrida con tan solo desconectar el chip RFID.

References

Aachib, M., M. Mbonimpa & M. Aubertin (2004) Measurement and prediction of the oxygen diffusion coefficient in unsaturated media, with applications to soil covers. *Water, air, and soil pollution,* 156**,** 163-193.

Abad, E., F. Palacio, M. Nuin, A. G. d. Zárate, A. Juarros, J. M. Gómez & S. Marco (2009) RFID smart tag for traceability and cold chain monitoring of foods: Demonstration in an intercontinental fresh fish logistic chain. *Journal of Food Engineering,* 93**,** 394-399.

Adam, H., G. Stanisław & I. Folke (1991) Chemical sensors definitions and classification. *Pure Appl. Chem,* 63**,** 1274-1250.

AG, A. 2014. Demo Kit for the SL900A smart EPC sensor tag IC.

Akyildiz, I. F., W. Su, Y. Sankarasubramaniam & E. Cayirci (2002) Wireless sensor networks: a survey. *Computer networks,* 38**,** 393-422.

Almudena Rivadeneyra, J. F.-S., Manuel Agudo, Juan A. López-Villanueva, Luis Fermín Capitan-Vallvey, Alberto J. Palma (2014) Design and characterization of a low thermal drift capacitive humidity sensor by inkjet-printing. *Sensors and Actuators B: Chemical*.

Altenberend, U., A. Oprea, N. Barsan, U. Weimar, N. F. De Rooij, F. Molina-Lopez & D. Briand (2012) 6.2. 1 Inkjet Printed Capacitive Transducers on Flexible Plastic Substrates with Increase Stability: Ag on PET. *Tagungsband***,** 527-531.

Amao, Y. (2003) Probes and polymers for optical sensing of oxygen. *Microchimica Acta,* 143**,** 1-12.

Amin, Y., R. K. Kanth, P. Liljeberg, A. Akram, Q. Chen, L.-R. Zheng & H. Tenhunen. 2013. Printable RFID Antenna with Embedded Sensor and Calibration Functions. In *Progress In Electromagnetics Research Symposium Proceedings, Stockholm, Sweden, Aug. 12-15, 2013*, 567-570. Electromagnetics Academy.

Andersson, H., A. Manuilskiy, T. Unander, C. Lidenmark, S. Forsberg & H. Nilsson (2012) Inkjet printed silver nanoparticle humidity sensor with memory effect on paper. *Sensors Journal, IEEE,* 12**,** 1901-1905.

Andrzejewski, D., I. Klimant & H. Podbielska (2002) Method for lifetime-based chemical sensing using the demodulation of the luminescence signal. *Sensors and Actuators B: Chemical,* 84**,** 160-166.

Anton, S. R. & H. A. Sodano (2007) A review of power harvesting using piezoelectric materials (2003–2006). *Smart Materials and Structures,* 16**,** R1.

Aspar, B. 1996. Characterization of SOI substrates: Application to Recent SIMOX and UNIBOND Wafers. In *Electrochemical Society Proceedings*, 99-111.

Ataka, M., M. Mita, H. Toshiyoshi & H. Fujita. 2013. Electrostatic microactuators in a flexible sheet—Smart MEMS sheet# 2. In *Solid-State Sensors, Actuators and Microsystems (TRANSDUCERS & EUROSENSORS XXVII), 2013 Transducers & Eurosensors XXVII: The 17th International Conference on*, 2341-2344. IEEE.

Atzori, L., A. Iera & G. Morabito (2010) The internet of things: A survey. *Computer networks,* 54**,** 2787-2805.

Babar, A. A., S. Manzari, L. Sydanheimo, A. Z. Elsherbeni & L. Ukkonen (2012) Passive UHF RFID Tag for Heat Sensing Applications. *Antennas and Propagation, IEEE Transactions on,* 60**,** 4056-4064.

Barth, P. W. (1990) Silicon fusion bonding for fabrication of sensors, actuators and microstructures. *Sensors and Actuators A: Physical,* 23**,** 919-926.

Baxter, L. K. 1996. *Capacitive Sensors: Design and Applications*. John Wiley & Sons.

Berger, R., E. Delamarche, H. P. Lang, C. Gerber, J. K. Gimzewski, E. Meyer & H.-J. Güntherodt (1997) Surface stress in the self-assembly of alkanethiols on gold. *Science,* 276**,** 2021-2024.

Berger, R., C. Gerber, J. Gimzewski, E. Meyer & H. Güntherodt (1996) Thermal analysis using a micromechanical calorimeter. *Applied Physics Letters,* 69**,** 40-42.

Berger, R., H. Lang, C. Gerber, J. Gimzewski, J. Fabian, L. Scandella, E. Meyer & H.-J. Güntherodt (1998) Micromechanical thermogravimetry. *Chemical Physics Letters,* 294**,** 363-369.

Bergqvist, J. & J. Gobet (1994) Capacitive microphone with a surface micromachined backplate using electroplating technology. *Microelectromechanical Systems, Journal of,* 3**,** 69-75.

Bhattacharyya, R., C. Floerkemeier & S. Sarma (2010) Low-cost, ubiquitous RFID-tag-antenna-based sensing. *Proceedings of the IEEE,* 98**,** 1593-1600.

Binnig, G., C. F. Quate & C. Gerber (1986) Atomic force microscope. *Physical review letters,* 56**,** 930.

Boltshauser, T., C. Azeredo Leme & H. Baltes (1993) High sensitivity CMOS humidity sensors with on-chip absolute capacitance measurement system. *Sensors and Actuators B: Chemical,* 15**,** 75-80.

Briand, D., F. Molina-Lopez, A. V. Quintero, C. Ataman, J. Courbat & N. F. de Rooij (2011a) Why Going Towards Plastic and Flexible Sensors? *Procedia engineering,* 25**,** 8-15.

Briand, D., A. Oprea, J. Courbat & N. Bârsan (2011b) Making environmental sensors on plastic foil. *Materials Today,* 14**,** 416-423.

Broutas, P., H. Contopanagos, E. D. Kyriakis-Bitzaros, D. Tsoukalas & S. Chatzandroulis (2012) A low power RF harvester for a smart passive sensor tag with integrated antenna. *Sensors and Actuators a-Physical,* 176**,** 34-45.

Bustillo, J. M., R. T. Howe & R. S. Muller (1998) Surface micromachining for microelectromechanical systems. *Proceedings of the IEEE,* 86**,** 1552-1574.

Butler, W. J. & M. Milkovic. 1981. Pressure and temperature sensor. Google Patents.

Calvert, P. (2001) Inkjet printing for materials and devices. *Chemistry of Materials,* 13**,** 3299-3305.

Capitan-Vallvey, L., L. Asensio, J. Lopez-Gonzalez, M. Fernandez-Ramos & A. Palma (2007) Oxygen-sensing film coated photodetectors for portable instrumentation. *Analytica chimica acta,* 583**,** 166-173.

Castille, C., I. Dufour & C. Lucat (2010) Longitudinal vibration mode of piezoelectric thick-film cantilever-based sensors in liquid media. *Applied Physics Letters,* 96**,** 154102-154102-3.

Catarinucci, L., R. Colella & L. Tarricone (2013) Enhanced UHF RFID Sensor-Tag. *IEEE Microwave and Wireless Components Letters,* 23**,** 49-51.

Cazeca, M. J., J. Mead, J. Chen & R. Nagarajan (2013) Passive wireless displacement sensor based on RFID technology. *Sensors and Actuators a-Physical,* 190**,** 197-202.

Cohn, M. B. & R. T. Howe. 2000. Wafer-to-wafer transfer of microstructures using break-away tethers. Google Patents.

Colvin Jr, A. E. 1996. Fluorescent optical sensor. Google Patents.

---. 1999. Flourescence sensing device. Google Patents.

Colvin Jr, A. E., G. A. Dale, P. S. Zerwekh, J. C. Lesho & R. W. Lynn. 2001. Optical-based sensing devices. Google Patents.

Courbat, J., Y. Kim, D. Briand & N. de Rooij. 2011. Inkjet printing on paper for the realization of humidity and temperature sensors. In *Solid-State Sensors, Actuators and Microsystems Conference (TRANSDUCERS), 2011 16th International*, 1356-1359. IEEE.

Covington, J., S. Tan, J. Gardner, A. Hamilton, T. Koickal & T. Pearce. 2003. Combined smart chemFET/resistive sensor array. In *Sensors, 2003. Proceedings of IEEE*, 1120-1123. IEEE.

Cremer, L. & M. Heckl (1988) Structure-borne sound: structural vibrations and sound radiation at audio frequencies. *Berlin and New York, Springer-Verlag, 1988, 590 p. Translation.,* 1.

Crowley, K., A. Morrin, R. L. Shepherd, G. G. Wallace, M. R. Smyth & A. J. Killard (2010) Fabrication of polyaniline-based gas sensors using piezoelectric inkjet and screen printing for the detection of hydrogen sulfide. *Sensors Journal, IEEE,* 10**,** 1419-1426.

Chang, C.-P. & C.-L. Yuan (2009) The fabrication of a MWNTs–polymer composite chemoresistive sensor array to discriminate between chemical toxic agents. *Journal of materials science,* 44**,** 5485-5493.

Cho, N.-B., T.-H. Lim, Y.-M. Jeon & M.-S. Gong (2008) Humidity sensors fabricated with photo-curable electrolyte inks using an ink-jet printing technique and their properties. *Sensors and Actuators B: Chemical,* 130**,** 594-598.

Choi, D.-H., C.-H. Han, H.-D. Kim & J.-B. Yoon (2011) Liquid-based electrostatic energy harvester with high sensitivity to human physical motion. *Smart Materials and Structures,* 20**,** 125012.

Choi, W., Y. Jeon, J.-H. Jeong, R. Sood & S.-G. Kim (2006) Energy harvesting MEMS device based on thin film piezoelectric cantilevers. *Journal of Electroceramics,* 17**,** 543-548.

Daliri, A., A. Galehdar, S. John, C. H. Wang, W. S. T. Rowe & K. Ghorbani (2012) Wireless strain measurement using circular microstrip patch antennas. *Sensors and Actuators a-Physical,* 184**,** 86-92.

Dally, J. W., W. F. Riley & K. G. McConnell (1993) Instrumentation for engineering measurements.

de Vargas-Sansalvador, I. M. P., A. Martinez-Olmos, A. J. Palma, M. D. Fernández-Ramos & L. F. Capitán-Vallvey (2011) Compact optical instrument for simultaneous determination of oxygen and carbon dioxide. *Microchimica acta,* 172**,** 455-464.

Derby, B. (2010) Inkjet printing of functional and structural materials: fluid property requirements, feature stability, and resolution. *Annual Review of Materials Research,* 40**,** 395-414.

Djuric, S. M., L. F. Nagy, M. S. Damnjanovic, N. M. Djuric & L. D. Zivanov (2011) A novel application of planar-type meander sensors. *Microelectronics International,* 28**,** 41-49.

Dubourg, G., L. Fadel-Taris, I. Dufour, C. Pellet & C. Ayela (2011) Collective fabrication of all-organic microcantilever chips based on a hierarchical combination of shadow-masking and wafer-bonding processing methods. *Journal of Micromechanics and Microengineering,* 21**,** 095021.

Duffy, D. C., J. C. McDonald, O. J. Schueller & G. M. Whitesides (1998) Rapid prototyping of microfluidic systems in poly (dimethylsiloxane). *Analytical chemistry,* 70**,** 4974-4984.

Dupont[TM] (Kapton® polyimide film datasheet) Kapton Datasheet.

Dziedzic, A., L. J. Golonka, J. Kozlowski, B. W. Licznerski & K. Nitsch (1997) Thick-film resistive temperature sensors. *Measurement Science and Technology,* 8**,** 78.

Ehrfeld, W., P. Bley, F. Gotz, P. Hagmann, A. Maner, J. Mohr, H. Moser, D. Munchmeyer, W. Schelb & D. Schmidt. 1987. Fabrication of microstructures using the LIGA process. In *Proc. IEEE Micro Robots and Teleoperators Workshop*.

Emam, M. (2008) Finite element analysis of composite piezoelectric beam using comsol.

Eom, K. H., M. C. Kim, S. Lee & C. w. Lee (2012) The Vegetable Freshness Monitoring System Using RFID with Oxygen and Carbon Dioxide Sensor. *International Journal of Distributed Sensor Networks,* 2012**,** 1-6.

Fedder, G. K. 2003. MEMS fabrication. In *2013 IEEE International Test Conference (ITC)*, 691-691. IEEE Computer Society.

Fernandez, I., A. Asensio, I. Gutierrez, J. Garcia, I. Rebollo & J. de No (2012) Study of the communication distance of a MEMS Pressure Sensor Integrated in a RFID Passive Tag. *Advances in Electrical and Computer Engineering,* 12**,** 15-18.

Finkenzeller, K. & D. Müller. 2010. *RFID Handbook: Fundamentals and Applications in Contactless Smart Cards, Radio Frequency Identification and Near-Field Communication*. Wiley.

Fraden, J. 2004. *Handbook of modern sensors: physics, designs, and applications*. Springer.

---. 2010. Chemical sensors. In *Handbook of Modern Sensors*, 569-606. Springer.

Fuller, S. B., E. J. Wilhelm & J. M. Jacobson (2002) Ink-jet printed nanoparticle microelectromechanical systems. *Microelectromechanical Systems, Journal of,* 11**,** 54-60.

Galaxy, I. (1994) Photothermal spectroscopy with femtojoule sensitivity using a micromechanical device. *Nature,* 372**,** 3.

Ganji, B. A. & B. Y. Majlis (2009) Design and fabrication of a new MEMS capacitive microphone using a perforated aluminum diaphragm. *Sensors and Actuators A: Physical,* 149**,** 29-37.

Gao, J., J. Siden, H.-E. Nilsson & M. Gulliksson (2013) Printed Humidity Sensor With Memory Functionality for Passive RFID Tags. *IEEE Sensors Journal,* 13**,** 1824-1834.

Gimzewski, J., C. Gerber, E. Meyer & R. Schlittler (1994) Observation of a chemical reaction using a micromechanical sensor. *Chemical Physics Letters,* 217**,** 589-594.

Griffin, J. D. & G. D. Durgin (2009) Complete link budgets for backscatter-radio and RFID systems. *Antennas and Propagation Magazine, IEEE,* 51**,** 11-25.

Griffiths, D. J. & R. College. 1999. *Introduction to electrodynamics*. prentice Hall Upper Saddle River, NJ.

Gründler, P. (2007) Conductivity sensors and capacitive sensors. *Chemical sensors: An introduction for scientists and engineers***,** 123-132.

Hagleitner, C., A. Hierlemann, D. Lange, A. Kummer, N. Kerness, O. Brand & H. Baltes (2001) Smart single-chip gas sensor microsystem. *Nature,* 414**,** 293-296.

Harrey, P., B. Ramsey, P. Evans & D. Harrison (2002) Capacitive-type humidity sensors fabricated using the offset lithographic printing process. *Sensors and Actuators B: Chemical,* 87**,** 226-232.

Hartmann, P. & M. J. P. Leiner. 2001. Optochemical sensor. Google Patents.

Hauser, P. C., C. L. C. Liang & B. Muller (1995) A solid-state instrument for fluorescence chemical sensors using a blue light-emitting diode of high intensity. *Measurement Science and Technology,* 6**,** 1081.

Hierlemann, A., O. Brand, C. Hagleitner & H. Baltes (2003) Microfabrication techniques for chemical/biosensors. *Proceedings of the IEEE,* 91**,** 839-863.

Hierlemann, A. & R. Gutierrez-Osuna (2008) Higher-order chemical sensing. *Chemical reviews,* 108**,** 563-613.

Ho, C. K., M. T. Itamura, M. Kelley & R. C. Hughes (2001) Review of chemical sensors for in-situ monitoring of volatile contaminants. *SANDIA REPORT, SAND2001-0643*.

Hohm, D. & R. Gerhard-Multhaupt (1984) Silicon-dioxide electret transducer. *The Journal of the Acoustical Society of America,* 75**,** 1297-1298.

Horowitz, S., T. Nishida, L. Cattafesta & M. Sheplak (2007) Development of a micromachined piezoelectric microphone for aeroacoustics applications. *The Journal of the Acoustical Society of America,* 122**,** 3428-3436.

Horsley, D. 2002. Method of fabricating suspended microstructures. Google Patents.

Hossein-Babaei, F., S. Hosseini-Golgoo & A. Amini (2009) Extracting discriminative information from the Padé-Z-transformed responses of a temperature-modulated chemoresistive sensor for gas recognition. *Sensors and Actuators B: Chemical,* 142**,** 19-27.

Hu, X. & W. Yang (2010) Planar capacitive sensors–designs and applications. *Sensor Review,* 30**,** 24-39.

Huang, X., W.-H. Yeo, Y. Liu & J. A. Rogers (2012) Epidermal differential impedance sensor for conformal skin hydration monitoring. *Biointerphases,* 7**,** 1-9.

Igreja, R. & C. Dias (2004) Analytical evaluation of the interdigital electrodes capacitance for a multi-layered structure. *Sensors and Actuators A: Physical,* 112**,** 291-301.

--- (2006) Dielectric response of interdigital chemocapacitors: The role of the
          sensitive layer thickness. *Sensors and Actuators B: Chemical,* 115**,**
          69-78.

Ionescu, R. (1998) Combined Seebeck and resistive SnO< sub> 2</sub> gas
          sensors, a new selective device. *Sensors and Actuators B: Chemical,*
          48**,** 392-394.

Ishii, T. & K. Kadoya (1991) Continuous measurement of oxygen
          concentration in citrus soil by means of a waterproof zirconia oxygen
          sensor. *Plant and soil,* 131**,** 53-58.

J.F. Salmeron, F. M.-L., D. Briand, J.J. Ruan, Al. Rivadeneyra, Miguel A.
          Carvajal, L. F. Capitán-Vallvey, N.F. de Rooij, A.J. Palma (2013)
          Properties and Printability of Ink-jet and Screen Printed Silver
          Patterns for RFID Antennas. *Journal of Electronic Materials*.

Jacquemod, G., M. Nowak, E. Colinet, N. Delorme & F. Conseil (2010)
          Novel architecture and algorithm for remote interrogation of battery-
          free sensors. *Sensors and Actuators A: Physical,* 160**,** 125-131.

Jalkanen, T., E. Makila, A. Maattanen, J. Tuura, M. Kaasalainen, V.-P.
          Lehto, P. Ihalainen, J. Peltonen & J. Salonen (2012) Porous silicon
          micro-and nanoparticles for printed humidity sensors. *Applied
          Physics Letters,* 101**,** 263110-263110-4.

Janata, J. 1985. *Solid state chemical sensors*. Academic Press.

Janata, J. 2009. *Principles of chemical sensors*. Springer.

Jo, B.-H., L. M. Van Lerberghe, K. M. Motsegood & D. J. Beebe (2000)
          Three-dimensional micro-channel fabrication in
          polydimethylsiloxane (PDMS) elastomer. *Microelectromechanical
          Systems, Journal of,* 9**,** 76-81.

Judy, J. W. (2001) Microelectromechanical systems (MEMS): fabrication,
          design and applications. *Smart materials and Structures,* 10**,** 1115.

Kalantar-zadeh, K. & B. Fry (2008) Sensor Characteristics and Physical
          Effects. *Nanotechnology-Enabled Sensors***,** 13-62.

Kassal, P., I. M. Steinberg & M. D. Steinberg (2013) Wireless smart tag with
          potentiometric input for ultra low-power chemical sensing. *Sensors
          and Actuators B: Chemical,* 184**,** 254-259.

Ke, M.-T., M.-T. Lee, C.-Y. Lee & L.-M. Fu (2009) A MEMS-based
          benzene gas sensor with a self-heating wo3 sensing layer. *Sensors,* 9**,**
          2895-2906.

Keller, C. & M. Ferrari. 1994. Milli-scale polysilicon structures. In *Proc. Solid-State Sensor and Actuator Workshop*, 12-16.

Kim, Y., H. Kim & H.-J. Yoo (2010) Electrical characterization of screen-printed circuits on the fabric. *Advanced Packaging, IEEE Transactions on,* 33**,** 196-205.

Koester, D., A. Cowen, R. Mahadevan, M. Stonefield & B. Hardy (2003) PolyMUMPs design handbook. *V10. 0*.

Kovacs, G. T. 1998. *Micromachined transducers sourcebook*. WCB/McGraw-Hill New York.

Laermer, F. & A. Schilp. 1996. Method for anisotropic plasma etching of substrates. Google Patents.

Lakhmi, R., H. Debéda, I. Dufour & C. Lucat (2010) Force sensors based on screen-printed cantilevers. *Sensors Journal, IEEE,* 10**,** 1133-1137.

Lakhmi, R., H. Debeda, M. Maglione, I. Dufour & C. Lucat (2013) Study of Screen-Printed PZT Cantilevers Both Self-Actuated and Self-Read-Out. *International Journal of Applied Ceramic Technology*.

Lam, E., H. Li & M. Schmidt. 2009. Silver nanoparticle structures realized by digital surface micromachining. In *Solid-State Sensors, Actuators and Microsystems Conference, 2009. TRANSDUCERS 2009. International*, 1698-1701. IEEE.

Lang, H., M. Baller, R. Berger, C. Gerber, J. Gimzewski, F. Battiston, P. Fornaro, J. Ramseyer, E. Meyer & H. Güntherodt (1999) An artificial nose based on a micromechanical cantilever array. *Analytica Chimica Acta,* 393**,** 59-65.

Lavergne, T., S. Durand, M. Bruneau, N. Joly & D. Rodrigues (2010) Dynamic behavior of the circular membrane of an electrostatic microphone: Effect of holes in the backing electrode. *The Journal of the Acoustical Society of America,* 128**,** 3459-3477.

Leach, W. M. 2003. *Introduction to electroacoustics and audio amplifier design*. Kendall/Hunt Publishing Company.

Lee, S.-K. & I. Okura (1997) Porphyrin-doped sol-gel glass as a probe for oxygen sensing. *Analytica chimica acta,* 342**,** 181-188.

Li, X. Y. & E. C. Kan (2010) A wireless low-range pressure sensor based on P(VDF-TrFE) piezoelectric resonance. *Sensors and Actuators a-Physical,* 163**,** 457-463.

Lippitsch, M. E., J. Pusterhofer, M. J. Leiner & O. S. Wolfbeis (1988) Fibre-optic oxygen sensor with the fluorescence decay time as the information carrier. *Analytica Chimica Acta,* 205**,** 1-6.

Lonergan, M. C., E. J. Severin, B. J. Doleman, S. A. Beaber, R. H. Grubbs & N. S. Lewis (1996) Array-based vapor sensing using chemically sensitive, carbon black-polymer resistors. *Chemistry of Materials,* 8**,** 2298-2312.

Lorenz, H., M. Despont, N. Fahrni, N. LaBianca, P. Renaud & P. Vettiger (1997) SU-8: a low-cost negative resist for MEMS. *Journal of Micromechanics and Microengineering,* 7**,** 121.

Lorwongtragool, P., E. Sowade, T. Dinh, O. Kanoun, T. Kerdcharoen & R. Baumann. 2012. Inkjet printing of chemiresistive sensors based on polymer and carbon nanotube networks. In *Systems, Signals and Devices (SSD), 2012 9th International Multi-Conference on*, 1-4. IEEE.

Lucat, C., P. Ginet, C. Castille, H. Debéda & F. Ménil (2008) Microsystems elements based on free-standing thick-films made with a new sacrificial layer process. *Microelectronics Reliability,* 48**,** 872-875.

Maas, D., B. Bustgens, J. Fahrenberg, W. Keller, P. Ruther, W. Schomburg & D. Seidel. 1996. Fabrication of microcomponents using adhesive bonding techniques. In *Micro Electro Mechanical Systems, 1996, MEMS'96, Proceedings. An Investigation of Micro Structures, Sensors, Actuators, Machines and Systems. IEEE, The Ninth Annual International Workshop on*, 331-336. IEEE.

Madou, M. J. 2002. *Fundamentals of microfabrication: the science of miniaturization*. CRC press.

Mamishev, A., A. Takahashi, Y. Du, B. Lesieutre & M. Zahn. 2002. Assessment of performance of fringing electric field sensor arrays. In *Electrical Insulation and Dielectric Phenomena, 2002 Annual Report Conference on*, 918-921. IEEE.

Mamishev, A. V., K. Sundara-Rajan, F. Yang, Y. Du & M. Zahn (2004) Interdigital sensors and transducers. *Proceedings of the IEEE,* 92**,** 808-845.

Manzari, S., C. Occhiuzzi, S. Nawale, A. Catini, C. Di Natale & G. Marrocco (2012) Humidity Sensing by Polymer-Loaded UHF RFID Antennas. *IEEE Sensors Journal,* 12**,** 2851-2858.

Martinez-Olmos, A., I. de Vargas-Sansalvador, A. Palma, J. Banqueri, M. Fernandez-Ramos & L. Capitán-Vallvey (2011) Multisensor probe for soil monitoring. *Sensors and Actuators B: Chemical,* 160**,** 52-58.

Martínez-Olmos, A., J. Fernández-Salmerón, N. Lopez-Ruiz, A. Rivadeneyra Torres, L. F. Capitan-Vallvey & A. Palma (2013) Screen printed flexible radiofrequency identification tag for oxygen monitoring. *Analytical chemistry,* 85**,** 11098-11105.

Mattoli, V., B. Mazzolai, A. Mondini, S. Zampolli & P. Dario (2010) Flexible tag datalogger for food logistics. *Sensors and Actuators a-Physical,* 162**,** 316-323.

Mayr, T., T. Abel, B. Enko, S. Borisov, C. Konrad, S. Köstler, B. Lamprecht, S. Sax, E. J. List & I. Klimant (2009) A planar waveguide optical sensor employing simple light coupling. *Analyst,* 134**,** 1544-1547.

Merilampi, S., T. Björninen, L. Ukkonen, P. Ruuskanen & L. Sydänheimo (2011) Embedded wireless strain sensors based on printed RFID tag. *Sensor Review,* 31**,** 32-40.

Miller, L. M., E. Halvorsen, T. Dong & P. K. Wright (2011) Modeling and experimental verification of low-frequency MEMS energy harvesting from ambient vibrations. *Journal of Micromechanics and Microengineering,* 21**,** 045029.

Mohd Syaifudin, A., S. Mukhopadhyay & P. Yu (2012) Modelling and fabrication of optimum structure of novel interdigital sensors for food inspection. *International Journal of Numerical Modelling: Electronic Networks, Devices and Fields,* 25**,** 64-81.

Molina-Lopez, F., D. Briand & N. de Rooij (2012) All additive inkjet printed humidity sensors on plastic substrate. *Sensors and Actuators B: Chemical,* 166**,** 212-222.

--- (2013a) Decreasing the size of printed comb electrodes by the introduction of a dielectric interlayer for capacitive gas sensors on polymeric foil: Modeling and fabrication. *Sensors and Actuators B: Chemical,* 189**,** 89-96.

Molina-Lopez, F., A. V. Quintero, G. Mattana, D. Briand & N. de Rooij (2013b) Large-area compatible fabrication and encapsulation of inkjet-printed humidity sensors on flexible foils with integrated thermal compensation. *Journal of Micromechanics and Microengineering,* 23**,** 025012.

Multiphysics, C. 2008. Structural Mechanics Module. Reference Guide,
         Vers.

---. 2012. 4.3 User's Guide. COMSOL.

Nakano, S., T. Sekitani, T. Yokota & T. Someya (2008) Low operation
         voltage of inkjet-printed plastic sheet-type micromechanical
         switches. *Applied Physics Letters,* 92**,** 053302-053302-3.

Nilsson, H.-E., T. Unander, J. Siden, H. Andersson, A. Manuilskiy, M.
         Hummelgard & M. Gulliksson (2012) System Integration of
         Electronic Functions in Smart Packaging Applications. *Components,*
         Packaging and Manufacturing Technology, IEEE Transactions on,
         2**,** 1723-1734.

Ning, Y., A. Mitchell & R. Tait (1996) Fabrication of a silicon
         micromachined capacitive microphone using a dry-etch process.
         Sensors and Actuators A: Physical, 53**,** 237-242.

O'Keeffe, R., N. Jackson, F. Waldron, M. O'Niell, K. McCarthy & A.
         Mathewson. 2013. Investigation into modelling power output for
         MEMS energy harvesting devices using COMSOL Multiphysics R.
         In *Thermal, Mechanical and Multi-Physics Simulation and*
         Experiments in Microelectronics and Microsystems (EuroSimE),
         2013 14th International Conference on, 1-6. IEEE.

Oikonomou, P., A. Botsialas, K. Manoli, D. Goustouridis, E. Valamontes, M.
         Sanopoulou, I. Raptis & G. Patsis (2012) Chemocapacitor
         performance modeling by means of polymer swelling optical
         measurements. *Sensors and Actuators B: Chemical,* 171**,** 409-415.

Oprea, A., N. Bârsan, U. Weimar, M.-L. Bauersfeld, D. Ebling & J.
         Wöllenstein (2008) Capacitive humidity sensors on flexible RFID
         labels. *Sensors and Actuators B: Chemical,* 132**,** 404-410.

Oprea, A., J. Courbat, N. Bârsan, D. Briand, N. De Rooij & U. Weimar
         (2009a) Temperature, humidity and gas sensors integrated on plastic
         foil for low power applications. *Sensors and Actuators B: Chemical,*
         140**,** 227-232.

Oprea, A., J. Courbat, N. Bârsan, D. Briand, N. F. de Rooij & U. Weimar
         (2009b) Temperature, humidity and gas sensors integrated on plastic
         foil for low power applications. *Sensors and Actuators B: Chemical,*
         140**,** 227-232.

Pabst, O., J. Perelaer, E. Beckert, U. Schubert, R. Eberhardt & A. Tünnermann. 2011. Inkjet printing of electroactive polymer actuators on polymer substrates. In *SPIE Smart Structures and Materials+ Nondestructive Evaluation and Health Monitoring*, 79762H-79762H-6. International Society for Optics and Photonics.

Palma, A. J., J. López-González, L. J. Asensio, M. D. Fernández-Ramos & L. F. Capitán-Vallvey (2007a) Microcontroller-based portable instrument for stabilised optical oxygen sensor. *Sensors and Actuators B: Chemical,* 121**,** 629-638.

Palma, A. J., J. López-González, L. J. Asensio, M. D. Fernández-Ramos & L. F. Capitán-Vallvey (2007b) Open air calibration with temperature compensation of a luminescence quenching-based oxygen sensor for portable instrumentation. *Analytical chemistry,* 79**,** 3173-3179.

Park, E., J. Jeon, V. Subramanian & T.-J. Liu. 2012. Inkjet-printed microshell encapsulation: a new zero-level packaging technology. In *Micro Electro Mechanical Systems (MEMS), 2012 IEEE 25th International Conference on*, 357-360. IEEE.

Park, E. S., Y. Chen, T.-J. K. Liu & V. Subramanian. 2011. Inkjet-printed micro-electro-mechanical switches. In *Electron Devices Meeting (IEDM), 2011 IEEE International*, 29.2. 1-29.2. 4. IEEE.

Pederson, M., W. Olthuis & P. Bergveld (1998) High-performance condenser microphone with fully integrated CMOS amplifier and DC-DC voltage converter. *Microelectromechanical Systems, Journal of,* 7**,** 387-394.

Petersen, K. E. (1982) Silicon as a mechanical material. *Proceedings of the IEEE,* 70**,** 420-457.

Peterson, J. I., R. V. Fitzgerald & D. K. Buckhold (1984) Fiber-optic probe for in vivo measurement of oxygen partial pressure. *Analytical chemistry,* 56**,** 62-67.

Pletersek, A., M. Sok & J. Trontelj (2012) Monitoring, control and diagnostics using RFID infrastructure. *J Med Syst,* 36**,** 3733-9.

Potyrailo, R. A., N. Nagraj, Z. Tang, F. J. Mondello, C. Surman & W. Morris (2012a) Battery-free radio frequency identification (RFID) sensors for food quality and safety. *J Agric Food Chem,* 60**,** 8535-43.

Potyrailo, R. A., N. Nagraj, Z. Tang, F. J. Mondello, C. Surman & W. Morris (2012b) Battery-free Radio Frequency Identification (RFID) Sensors

for Food Quality and Safety. *Journal of agricultural and food chemistry,* 60**,** 8535-8543.

Potyrailo, R. A., C. Surman, S. Go, Y. Lee, T. Sivavec & W. G. Morris (2009) Development of radio-frequency identification sensors based on organic electronic sensing materials for selective detection of toxic vapors. *Journal of Applied Physics,* 106**,** 124902-124902-6.

Precision, L. 2006. Capacitive sensor operation and optimization. Tech. rep. http://www. lionprecision. com/tech-library/technotes/cap-0020-% sensor-theory. html.

Quintero, A. V., F. Molina-Lopez, G. Mattana, D. Briand & N. de Rooij. 2013. Self-standing printed humidity sensor with thermo-calibration and integrated heater. In *Solid-State Sensors, Actuators and Microsystems (TRANSDUCERS & EUROSENSORS XXVII), 2013 Transducers & Eurosensors XXVII: The 17th International Conference on*, 838-841. IEEE.

R. Ghodssi, P. L. 2011. *MEMS Materials and Processes Handbook.* Berlin: Springer.

Rao, K. V. S., P. V. Nikitin & S. F. Lam (2005) Antenna design for UHF RFID tags: a review and a practical application. *Antennas and Propagation, IEEE Transactions on,* 53**,** 3870-3876.

Reddy, A., B. Narakathu, M. Atashbar, M. Rebros, E. Rebrosova & M. Joyce (2011) Fully printed flexible humidity sensor. *Procedia Engineering,* 25**,** 120-123.

Rida, A., L. Yang, R. Vyas & M. M. Tentzeris (2009) Conductive inkjet-printed antennas on flexible low-cost paper-based substrates for RFID and WSN applications. *Antennas and Propagation Magazine, IEEE,* 51**,** 13-23.

Rivadeneyra, A., J. Fernández-Salmerón, M. Agudo, J. López-Villanueva, L. Capitan-Vallvey & A. Palma (2014) Design and characterization of a low thermal drift capacitive humidity sensor by inkjet-printing. *Sensors and Actuators B: Chemical*.

Rivadeneyra, A., J. A. Lopez-Villanueva, R. O'Keeffe, N. Jackson, M. O'Neill & A. Mathewson. 2012. Frequency response of variants of a cantilever beam. In *Synthesis, Modeling, Analysis and Simulation Methods and Applications to Circuit Design (SMACD), 2012 International Conference on*, 177-180. IEEE.

Roberts, J., N. Jackson & M. Smith. 2006. *Tree roots in the built environment*. The Stationery Office.

Ruan, J. J., R. A. Lockhart, P. Janphuang, A. V. Quintero, D. Briand & N. de Rooij (2013) An Automatic Test Bench for Complete Characterization of Vibration-Energy Harvesters.

Sahm, M., A. Oprea, N. Bârsan & U. Weimar (2007) Water and ammonia influence on the conduction mechanisms in polyacrylic acid films. *Sensors and Actuators B: Chemical,* 127**,** 204-209.

Salmerón, J. F., F. Molina-Lopez, D. Briand, J. J. Ruan, A. Rivadeneyra, M. A. Carvajal, L. Capitán-Vallvey, N. F. de Rooij & A. J. Palma (2013) Properties and Printability of Inkjet and Screen-Printed Silver Patterns for RFID Antennas. *Journal of Electronic Materials***,** 1-14.

--- (2014) Properties and Printability of Inkjet and Screen-Printed Silver Patterns for RFID Antennas. *Journal of Electronic Materials,* 43**,** 604-617.

Schäferling, M., M. Wu, J. Enderlein, H. Bauer & O. S. Wolfbeis (2003) Time-resolved luminescence imaging of hydrogen peroxide using sensor membranes in a microwell format. *Applied spectroscopy,* 57**,** 1386-1392.

Scheeper, P., A. Van der Donk, W. Olthuis & P. Bergveld (1992) Fabrication of silicon condenser microphones using single wafer technology. *Microelectromechanical Systems, Journal of,* 1**,** 147-154.

Schoo, C. & M. Knoll (2014) Self-writing smart labels for humidity monitoring. *Sensors and Actuators A: Physical,* 205**,** 1-5.

Serra, N. 2012. Epoxy-graphite Resistive Composites: Formulation, Characterization and Applications. ÉCOLE POLYTECHNIQUE FÉDÉRALE DE LAUSANNE.

Serra, N., T. Maeder, O. Gentsch & P. Ryser (2011) Fabrication of polymer-based micro devices: Formulation and study of the paste. *Sensors and Actuators A: Physical,* 172**,** 336-340.

Serra, N., T. Maeder, C. Jacq, Y. Fournier & P. Ryser. 2009. Screen-printed polymer-based microfluidic and micromechanical devices based on evaporable compounds. In *Microelectronics and Packaging Conference, 2009. EMPC 2009. European*, 1-5. IEEE.

Shivok, T. J. 2007. MEMS POLYMUMPS-based miniature microphone for directional sound sensing. DTIC Document.

Skotadis, E., D. Mousadakos, K. Katsabrokou, S. Stathopoulos & D. Tsoukalas (2013) Flexible polyimide chemical sensors using platinum nanoparticles. *Sensors and Actuators B: Chemical,* 189**,** 106-112.

Soeda, J., T. Uemura, Y. Mizuno, A. Nakao, Y. Nakazawa, A. Facchetti & J. Takeya (2011) High Electron Mobility in Air for N, N′-1H, 1H-Perfluorobutyldicyanoperylene Carboxydi-imide Solution-Crystallized Thin-Film Transistors on Hydrophobic Surfaces. *Advanced Materials,* 23**,** 3681-3685.

Starke, E., A. Turke, M. Krause & W.-J. Fischer. 2011. Flexible polymer humidity sensor fabricated by inkjet printing. In *Solid-State Sensors, Actuators and Microsystems Conference (TRANSDUCERS), 2011 16th International*, 1152-1155. IEEE.

Steinberg, M. D., P. Kassal, B. Tkalčec & I. Murković Steinberg (2014) Miniaturised wireless smart tag for optical chemical analysis applications. *Talanta,* 118**,** 375-381.

Su, J.-J., L. Beardslee & O. Brand. 2013. Combined chemoresistive and chemocapacitive microsensor structures. In *Solid-State Sensors, Actuators and Microsystems (TRANSDUCERS & EUROSENSORS XXVII), 2013 Transducers & Eurosensors XXVII: The 17th International Conference on*, 258-261. IEEE.

Su, P.-G., C.-T. Lee & C.-Y. Chou (2009) Flexible NH< sub> 3</sub> sensors fabricated by< i> in situ</i> self-assembly of polypyrrole. *Talanta,* 80**,** 763-769.

Subramanian, V., J. Chang & F. Liao. 2013. Printed Organic Chemical Sensors and Sensor Systems. In *Applications of Organic and Printed Electronics*, 157-177. Springer.

Suganuma, K. (2014) Introduction to printed electronics.

Sukhija, M. & T. Nagsarkar. 2010. *Circuits and Networks: Analysis, Design, and Synthesis*. Oxford University Press.

Technologies, A. 2002. Applying Error Correction to Network Analyzer Measurements. AN 1287-3. Agilent Technologies

Tibbitts, T. W. (1979) Humidity and plants. *BioScience,* 29**,** 358-363.

Unander, T. & H.-E. Nilsson (2009a) Characterization of printed moisture sensors in packaging surveillance applications. *Sensors Journal, IEEE,* 9**,** 922-928.

Unander, T. & H.-E. Nilsson (2009b) Characterization of Printed Moisture
        Sensors in Packaging Surveillance Applications. *IEEE Sensors
        Journal,* 9**,** 922-928.

Unander, T., J. Siden & H.-E. Nilsson (2011) Designing of RFID-Based
        Sensor Solution for Packaging Surveillance Applications. *IEEE
        Sensors Journal,* 11**,** 3009-3018.

Urrestarazu, M. & M. U. Gavilán. 2004. *Tratado de cultivo sin suelo*. Mundi-
        Prensa Libros.

Virtanen, J., L. Ukkonen, T. Bjorninen, A. Z. Elsherbeni & L. Sydanheimo
        (2011a) Inkjet-printed humidity sensor for passive UHF RFID
        systems. *Instrumentation and Measurement, IEEE Transactions on,*
        60**,** 2768-2777.

Virtanen, J., L. Ukkonen, T. Bjorninen, A. Z. Elsherbeni & L. Sydänheimo
        (2011b) Inkjet-Printed Humidity Sensor for Passive UHF RFID
        Systems. *IEEE Transactions on Instrumentation and Measurement,*
        60**,** 2768-2777.

Virtanen, J., L. Ukkonen, T. Bjorninen & L. Sydanheimo. 2010. Printed
        humidity sensor for UHF RFID systems. In *Sensors Applications
        Symposium (SAS), 2010 IEEE*, 269-272. IEEE.

Wallis, G. & D. I. Pomerantz (2003) Field assisted glass-metal sealing.
        Journal of Applied Physics, 40**,** 3946-3949.

Wang, X.-B., Y. Huang, X. Wang, F. F. Becker & P. Gascoyne (1997)
        Dielectrophoretic manipulation of cells with spiral electrodes.
        Biophysical journal, 72**,** 1887-1899.

Watkins, A. N., B. R. Wenner, J. D. Jordan & F. V. Bright. 2001. Sensing
        device with sol-gel derived film on the light source. Google Patents.

Watkins, A. N., B. R. Wenner, J. D. Jordan, W. Xu, J. N. Demas & F. V.
        Bright (1998) Portable, low-cost, solid-state luminescence-based O2
        sensor. *Applied spectroscopy,* 52**,** 750-754.

Wei, Y., R. Torah, K. Yang, S. Beeby & J. Tudor. 2012a. A novel fabrication
        process for capacitive cantilever structures for smart fabric
        applications. In *Design, Test, Integration and Packaging of
        MEMS/MOEMS (DTIP), 2012 Symposium on*, 136-139. IEEE.

---. 2012b. A novel fabrication process to realise piezoelectric cantilever
        structures for smart fabric sensor applications. In *Sensors, 2012
        IEEE*, 1-4. IEEE.

--- (2012c) Screen printed capacitive free-standing cantilever beams used as a motion detector for wearable sensors. *Procedia Engineering,* 47**,** 165-169.

Wei, Y., R. Torah, K. Yang, S. Beeby & J. Tudor (2013a) A novel fabrication process to release a valveless micropump on a flexible substrate.

Wei, Y., R. Torah, K. Yang, S. Beeby & J. Tudor (2013b) Screen printing of a capacitive cantilever-based motion sensor on fabric using a novel sacrificial layer process for smart fabric applications. *Measurement Science and Technology,* 24**,** 075104.

Weremczuk, J., G. Tarapata & R. S. Jachowicz (2012) The ink-jet printing humidity sorption sensor—modelling, design, technology and characterization. *Measurement Science and Technology,* 23**,** 014003.

Wohler, A., K. Mohri, C. Schulz & B. Weigand (2011) Flow structures in subsonic-to-supersonic mixing processes using different injector geometries. _ *EUCASS* _.

Xia, Y. & G. M. Whitesides (1998) Soft lithography. *Annual review of materials science,* 28**,** 153-184.

Xie, K., Y. Lai, X. Guo & R. J. Campbell (2010) A three phase serpentine micro electrode array for AC electroosmotic flow pumping. *Microsystem technologies,* 16**,** 1825-1830.

Yang, C.-T. (2010) The sensitivity analysis of a mems microphone with different membrane diameters. *Journal of Marine Science and Technology,* 18**,** 790-796.

Yang, T.-Y., J.-J. Huang, C.-Y. Liu & H.-Y. Wang. 2011. A CMOS-MEMS Humidity Sensor. In *Proceedings of International Conference on Circuits, System and Simulation (ICCSS 2011)*.

Yi, X., C. Cho, J. Cooper, Y. Wang, M. M. Tentzeris & R. T. Leon (2013) Passive wireless antenna sensor for strain and crack sensing—electromagnetic modeling, simulation, and testing. *Smart Materials and Structures,* 22**,** 085009.

Yin, J., J. Yi, M. K. Law, Y. X. Ling, M. C. Lee, K. P. Ng, B. Gao, H. C. Luong, A. Bermak, M. Chan, W. H. Ki, C. Y. Tsui & M. Yuen (2010) A System-on-Chip EPC Gen-2 Passive UHF RFID Tag With Embedded Temperature Sensor. *IEEE Journal of Solid-State Circuits,* 45**,** 2404-2420.

Yokota, T., S. Nakano, T. Sekitani & T. Someya (2008) Plastic
    complementary microelectromechanical switches. *Applied Physics
    Letters,* 93**,** 023305.

Zampolli, S., I. Elmi, E. Cozzani, G. C. Cardinali, A. Scorzoni, M. Cicioni,
    S. Marco, F. Palacio, J. M. Gómez-Cama, I. Sayhan & T. Becker
    (2007) Ultra-low-power components for an RFID Tag with physical
    and chemical sensors. *Microsystem Technologies,* 14**,** 581-588.

Zhang, X. X., S. J. Peng & J. L. Zou (2012) Air Damping Effects of MEMS
    Parallel-Plate Structure Using ANSYS Thin Film Analysis.
    Advanced Materials Research, 403**,** 4588-4592.

Zhu, X., S. K. Mukhopadhyay & H. Kurata (2012) A review of RFID
    technology and its managerial applications in different industries.
    Journal of Engineering and Technology Management, 29**,** 152-167.